



Jorge Diogo
Marques Laranjeira

Investigação por teoria do funcional da densidade
de novas nanoestruturas de carbono obtidas por
polimerização de C_{60}

Density functional theory investigation of novel
carbon nanostructures obtained from C_{60}
polymerization



**Jorge Diogo
Marques Laranjeira**

**Investigação por teoria do funcional da densidade
de novas nanoestruturas de carbono obtidas por
polimerização de C_{60}**

**Density functional theory investigation of novel
carbon nanostructures obtained from C_{60}
polymerization**

Tese apresentada à Universidade de Aveiro para cumprimento dos requisitos necessários à obtenção do grau de Doutor em Física, realizada sob a orientação científica do Doutor Leonel Marques Vitorino Joaquim, Professor Auxiliar do Departamento Física da Universidade de Aveiro e do Doutor Manuel Melle-Franco, Investigador Principal do Departamento de Química da Universidade de Aveiro.

This work was supported by Fundação para a Ciência e a Tecnologia (FCT) through national funds and the PhD grant SFRH/BD/139327/2018.

"Without physics there is no life"

Reference to a taxi driver in Minneapolis made by Richard R. Martin

o júri / the jury

presidente / president

Doutor João Paulo Davim Tavares da Silva,
Professor Catedrático, Universidade de Aveiro.

vogais / examiners committee

Doutor José Luís Rodrigues Júlio Martins,
Professor Catedrático, Universidade de Lisboa;

Doutor Marcos Mandado Alonso,
Professor Catedrático, Universidade de Vigo;

Doutora Maria Helena Sousa Soares de Oliveira Braga,
Professora Associada, Universidade do Porto;

Doutor Manuel Melle-Franco,
Investigador Principal, Ciceco - Universidade de Aveiro (orientador);

Doutora Estelina Lora da Silva,
Investigadora Júnior, Universidade do Porto.

Acknowledgements

First of all, I would like to express my gratitude to professor Leonel Marques for supervising this work, for his interest in the topics that we discussed even those outside of his scope, without his effort and availability this thesis would not be possible. I also appreciate his patience and will to teach me. I'm truly grateful for his guidance in the last 8 years.

Manuel Melle-Franco, who co-supervised this work, was also crucial, always opening doors to cooperate with other researchers and guiding me through some tough calculations, pointing me in the best direction to solve our problems. His contribution to this thesis and my personal development is incalculable.

Although not a supervisor, and not having any obligation to this work, Karol Strutyński acted numerous times as a supervisor guiding me in some practical aspects of calculations and other issues. His constant friendship and availability were a pillar where I could lean in some harsh times. Karol is without a doubt a role model for any human being, always available to help everybody around him with a smile.

To professor Emilio Martínez-Núñez for his availability to supervise for one and a half months during the difficult pandemic period. I'm very grateful for all the knowledge passed about AutoMeKin and also for the opportunity to play a bit with the chemistry virtual reality setup.

I must also acknowledge professor Ion Errea for the availability to supervise me for three months teaching me the amazing world of phonon physics, electron-phonon coupling mediated superconductivity and the SSCHA code. During this time he was always available for any questions, even those that I already should have known, making indeed an amazing teacher. I would also like to acknowledge his whole group, in particular, Đorđe Dancić, Francesco Belli and Martin Gutierrez, for their help with some issues and also their friendship through my time in San Sebastian.

Professor Manuel Barroso for all his friendship and guidance on how to properly use high-performance computing resources and other computing issues in general.

Professor Maria Rosário Correia for guiding me numerous times across the last 10 years. Firstly, for helping me choose the proper time to do my first Erasmus+ program. Also for giving me the amazing opportunity of helping to write a high school book of solutions for physics and lately, for guiding me on how to be a good teacher through the last four, years with valuable thoughts and discussions about experimental issues of electromagnetism and the Portuguese educational system. An amazing teacher who is concerned with all her students.

Ricardo Batalha and Diamantino Silva for their friendship and help with programming issues and some tricky illustrations done in blender. Daniel Pereira for his friendship and English review of this document.

To Yuriy Skorokhod for his friendship and for teaching me all of what I know about the Paris-Edinburgh large-volume press.

To Nuno Fortunato who has been an amazing friend since I started my academic path. Always available to discuss density functional theory issues and other matters.

To the Kids that kept me company through the past 5 years, Francisco Teixeira, Mauricio Ferreira and Diana Pereira. Thank you for the weird discussions.

I also feel the need to acknowledge my second home for the last decade, the physics department and all the knowledge and opportunities that I got there. A small word of appreciation towards the director, professor João Miguel Dias, for his constant availability to help those who help the department and will to improve it.

Finally, I would like to thank my family. My brother, Hugo Laranjeira, for his advice on countless issues and for his friendship and his trust. My father, Artur Laranjeira, for his high standards even without knowing what they mean. My mother, Maria Teresa Claro, for all her help and support.

Palavras-Chave

Carbono, Fulereo, Teoria do funcional da densidade, Supercondutividade, Clatratos, Propriedades elásticas, Dispersão de fonões, Estrutura eletrônica

Resumo

Os numerosos alótropos de carbono apresentam um extenso conjunto de propriedades e, no entanto, estamos ainda longe de conhecer todas as formas que o carbono pode adotar. Recentemente, uma profusão de novos alótropos de carbono puro, apresentando novas propriedades, foram descobertos e estudados, aumentando ainda mais o interesse nestas estruturas. Algumas fases poliméricas de C_{60} , obtidas por tratamentos a alta pressão e alta temperatura do monômero de C_{60} , integram este conjunto de novas formas de carbono. No entanto, a baixa resolução dos seus padrões de difração de raios-x impede a determinação das suas estruturas cristalinas. O objetivo desta tese é utilizar ferramentas teóricas, nomeadamente a teoria do funcional da densidade (em inglês "density functional theory", DFT), para estudar possíveis estruturas cristalinas dos polímeros de C_{60} e suas propriedades, de forma a clarificar os resultados experimentais. Desta forma, vários modelos estruturais foram desenvolvidos e estudados.

Os primeiros modelos que vamos discutir foram construídos para elucidar a estrutura cristalina de uma fase polimérica cúbica de faces centradas (cfc), obtida por síntese a alta pressão (9.5 GPa) e alta temperatura (823 K). Nestes modelos estruturais ordenados, as moléculas foram colocadas inicialmente numa rede cfc, adotando uma de duas orientações moleculares padrão. Ligações poliméricas do tipo 56/56 cicloadição 2+2 são estabelecidas entre moléculas vizinhas que possuam orientações distintas, não havendo ligação entre moléculas vizinhas com a mesma orientação. Este comportamento é análogo à interação antiferromagnética. Os modelos estruturais obtidos não conseguem explicar o padrão cfc experimental, uma vez que, após otimização estrutural, nenhum deles apresenta uma métrica cúbica ou originam reflexões de super-estrutura não observadas experimentalmente. No entanto, eles permitem-nos concluir que o polímero cfc experimental deverá ter uma estrutura frustrada, onde as moléculas estão ligadas a aproximadamente oito das suas doze vizinhas através da ligação 56/56 cicloadição 2+2, de uma forma análoga ao modelo de Ising antiferromagnético numa rede cfc com interações entre primeiros vizinhos. A estrutura eletrônica e o módulo volumétrico das estruturas ordenadas foram também calculadas, indicando um comportamento metálico e um módulo volumétrico moderado (aproximadamente 100 GPa), em acordo com o observado experimentalmente.

A estrutura em clatrato do C_{60} polimerizado foi outro modelo estrutural proposto. Esta estrutura foi construída considerando que as moléculas numa rede cfc são ligadas a todas as suas doze vizinhas através de uma nova ligação, a 5/5 cicloadição 2+3, dupla. Como consequência do estabelecimento destas ligações poliméricas, novas gaiolas de C_{60} são geradas nos interstícios octaédricos e novas gaiolas de C_{24} são também geradas nos interstícios tetraédricos da rede cfc. Esta nova estrutura clatrato apresenta um comportamento semicondutor, um módulo volumétrico de 268 GPa e uma dureza estimada de 21.6 GPa. Poderá eventualmente ser preparada experimentalmente, desde que o caminho termodinâmico pressão-temperatura apropriado para a sua síntese seja encontrado. A nova estrutura clatrato apresenta um pico intenso na densidade de estados eletrónicos, localizado na banda de condução, aproximadamente a 0.7 eV acima do nível de Fermi. Assim, uma dopagem eletrónica apropriada induzirá um comportamento metálico nesta estrutura, o que, aliado ao facto dela conter apenas carbono, um elemento leve capaz de formar ligações covalentes fortes, poderá possibilitar o aparecimento de supercondutividade. Esta possibilidade foi explorada através da dopagem da estrutura clatrato com diferentes átomos (Li, Be, Na, Mg, Al, K, Ca, Ga, Ge) inseridos numa das duas gaiolas disponíveis, C_{60} ou C_{24} . As curvas de dispersão de fonões calculadas mostraram que a maioria das estruturas dopadas é dinamicamente instável, com exceção do $Li@C_{24}$, $Na@C_{24}$, $Ga@C_{24}$ e do $Be@C_{60}$. Estas quatro estruturas são metálicas e apresentam mesmo supercondutividade, mas as suas temperaturas críticas, calculadas recorrendo à teoria de Eliashberg, são inferiores a 2 K.

Com o objetivo de conhecer melhor os possíveis tipos de ligação polimérica, uma pesquisa sistemática de dímeros de C_{60} foi realizada automaticamente. Para isso recorremos ao programa AutoMeKin, um software de química quântica usado para determinar possíveis produtos de uma reação. Para complementar esta pesquisa de dímeros, considerámos sistematicamente possíveis combinações entre diferentes configurações moleculares e também uma análise extensa da literatura. Todos os dímeros hipotéticos foram, subsequentemente, sujeitos a uma otimização pelo método de DFT, incorporando correções de van der Waals. Como resultado deste estudo, o número de dímeros de C_{60} conhecidos foi aumentado de doze para quarenta e um. Alguns destes dímeros são estáveis somente quando a polarização de spin é considerada nas funções de onda. Os resultados obtidos neste estudo são extremamente pertinentes, já que a presença do mesmo tipo de ligação num dímero e num polímero de C_{60} envolve uma distância entre as moléculas aproximadamente igual nos dois casos, o que poderá ser bastante útil na identificação dos novos tipos de ligações presentes nas fases poliméricas de C_{60} .

Para concluir o nosso trabalho, estudámos sistematicamente o módulo volumétrico e a estrutura eletrónica de várias fases poliméricas de C_{60} . As estruturas estudadas, que vão desde o monómero de C_{60} (0D) até à estrutura em clatrato do C_{60} polimerizado 3D, apresentam propriedades eletrónicas e elásticas que dependem fortemente do número de carbonos sp^3 nessas estruturas. O aumento do número de carbonos com hibridização sp^3 leva a um decréscimo monótono da compressibilidade e, num primeiro estágio, a uma diminuição do hiato eletrónico até à observação de comportamento metálico. O subsequente aumento do número de carbonos sp^3 origina uma reabertura do hiato eletrónico, num comportamento semicondutor reentrante.

Keywords

Carbon, Fullerene, Density functional theory, Superconductivity, Clathrates, Elastic properties, Phonon dispersion, Electronic structure

Abstract

Allotropes of carbon present a vast range of properties, yet we are far from knowing all the possible carbon allotropes. In recent years, a profusion of pure-carbon allotropes with new properties have been studied, fostering strong interest in carbon structures. Some polymerized C_{60} phases obtained through high-pressure high-temperature treatments of the monomer C_{60} fullerite are among them. However, the low resolution of their x-ray diffraction patterns precluded the determination of their crystal structures. Hence, the objective of this thesis is to employ theoretical approaches, mainly density functional theory (DFT), in the study of possible polymerized fullerite structures and their properties, in order to clarify the experimental phases. We have developed several structural models and studied them using DFT techniques.

The first models that we will discuss were constructed to elucidate the structure of a face-centered cubic (fcc) polymerized fullerite phase obtained at 9.5 GPa and 823 K. In these models, the molecules are in either one of two standard orientations and they were initially ascribed to a face-centered cubic lattice. Polymeric bonds of the 56/56 2+2 cycloaddition type are formed between neighboring molecules differently oriented but not between molecules having the same orientation. This is analogous to the antiferromagnetic interaction. These ordered polymerized structural models cannot explain the experimental fcc diffraction pattern, because they do not exhibit a cubic metric upon DFT relaxation or because they display reflections not observed experimentally. Nevertheless, these results allowed us to conclude that the fcc polymer should have a frustrated structure in which each molecule is bonded to nearly eight out of twelve nearest neighbors, analogous to the fcc Ising antiferromagnet with near-neighbor interactions. We have also computed the electronic structures and the bulk moduli for these ordered structural models, indicating a metallic behavior and a moderate bulk modulus (around 100 GPa), in agreement with the experimental results.

Another structural model that we have proposed is the polymerized fullerite clathrate structure. This structure was constructed by considering each molecule in the fcc lattice to be bonded to its twelve nearest neighbors with a new kind of bond, the double 5/5 2+3 cycloaddition. As a consequence of this bonding, the octahedral interstitial sites are enclosed by new C_{60} cages, exactly equal to the original molecules, and the tetrahedral interstitial sites are enclosed by new C_{24} cages. This new clathrate structure presents semiconducting behavior, a moderate bulk modulus of 268 GPa and an estimated hardness of 21.6 GPa. It may be prepared experimentally once a proper thermodynamic path is found. Furthermore, it displays a strong peak in the electronic density of states (DOS) located in the conduction band, ~ 0.7 eV above the Fermi level. Thus, appropriate electron doping is expected to induce metallicity in this structure, possibly even superconductivity, given that it is formed by a light element, such as carbon, that can form strong covalent bonds. This possibility was promptly explored by doping the clathrate structure with guest atoms (Li, Be, Na, Mg, Al, K, Ca, Ga, Ge) inserted in either the C_{60} cages or the C_{24} cages. Calculation of the phonon dispersion curves have shown that most of the structures were dynamically unstable, excepting $Li@C_{24}$, $Na@C_{24}$, $Ga@C_{24}$ and $Be@C_{60}$. These four stable structures are metallic and had their superconducting critical temperatures computed through Eliashberg theory, yielding very low values, below 2K.

We have also performed an automatic search of C_{60} dimers with the aim of getting more insight into other possible polymeric bonding schemes. To this end, we have employed the AutoMeKin package, a quantum chemistry software used to compute reaction products. In order to complete our dimer search, we have also systematically considered different combinations of molecular configurations and an extensive literature analysis. All the possible bonding schemes were then optimized at DFT level, including van der Waals corrections. With this approach, we have increased the universe of known dimers from twelve to forty-one. Some of these dimers are only stable when spin-polarized wave functions are considered. Relevant to our subsequent investigations, the observed distance between the two C_{60} molecules is about the same in the new dimers and in C_{60} polymers having the same bond, thus, allowing identification of bonding types occurring in fullerite polymers and facilitating their modeling.

To conclude our work, comparative studies of the electronic structure and the bulk moduli of several polymerized fullerite structures were performed. These structures, ranging from the 0D monomeric fullerite to the 3D polymerized fullerite clathrate, show electronic and elastic properties that depend critically on the number of sp^3 carbons possessed by the polymerized structures. Increasing the number of sp^3 carbons leads initially to a decrease of the electronic bandgap until metallicity is observed. A further increase in the number of sp^3 carbons induces a bandgap reopening, in a reentrant fashion. Regarding their compressibilities, the polymerized structures naturally show a monotonous decrease with the increase of the number of sp^3 carbons.

Contents

Contents	i
List of Figures	iii
List of Tables	v
List of Publications	vii
List of Abbreviations	viii
1 Introduction	1
1.1 Recent computational efforts in predicting crystal structures	3
1.1.1 Crystal structure prediction	4
1.1.1.1 The problem of applying CSP to C_{60} polymers	4
1.1.2 Finding structures through permutation of atoms with DFT optimization: the carbon clathrates case	5
1.1.3 Molecular dynamics	6
1.2 C_{60} crystalline phases obtained through HPHT treatments	6
1.2.1 C_{60} solid structure at room conditions	7
1.2.2 C_{60} at low temperatures and pressures	8
1.2.3 C_{60} dimerization	9
1.2.3.1 Other C_{60} bonding schemes	10
1.2.4 Pressure induced polymerized C_{60} structures	11
1.2.4.1 1D orthorhombic polymerized phase	11
1.2.4.2 2D polymerized phases	12
1.2.4.3 3D polymerized phases	14
1.2.5 Properties of C_{60} polymerized phases	16
1.2.5.1 Electronic structure of polymerized C_{60} phases	17
1.2.5.2 Bulk moduli of polymerized C_{60} phases	18
1.3 Thesis outline and objectives	19
1.3.1 List of individual contributions	21
2 Computational methods	33
2.1 Atomic structure of materials	33
2.1.1 Crystalline structure	33
2.1.2 Point group symmetry	34
2.2 Electronic structure calculation: A many-body problem	34
2.2.1 Born-Oppenheimer approximation	35
2.2.2 Density functional theory	35
2.2.2.1 Hohenberg-Kohn theorems	35

2.2.2.2	Kohn-Sham formulation: DFT as a single-body problem . . .	36
2.2.3	Implementing DFT	38
2.2.3.1	Exchange-Correlation functionals	38
2.2.3.2	Wave functions expansion	40
2.2.3.3	Pseudopotentials for plane waves	42
2.3	Crystalline lattice vibrations	42
2.4	Superconductivity mediated by electron-phonon interaction	43
3	A1 - Bonding frustration in the 9.5 GPa fcc polymeric C₆₀	49
4	A2 - Three-dimensional C₆₀ polymers with ordered binary-alloy-type structures	55
5	A3 - Three-dimensional fcc C₆₀ polymer	69
6	A4 - C₆₀+C₆₀ molecular bonding revisited and expanded	75
7	A5 - Clathrate structure of polymerized fullerite C₆₀	97
8	A6 - Superconductivity in the doped polymerized fullerite clathrate from first principles	113
9	Polymeric C₆₀ electronic structure evolution	133
9.1	A7 - C ₆₀ structures: Structural, electronic and elastic properties	133
9.2	A8 - Reentrant semiconducting behavior in polymerized fullerenes with increasing sp ³ content	138
10	Conclusions	155

List of Figures

1.1	C_{60} pressure-temperature diagram sketch. Figure after Álvarez-Murga et al. [16].	2
1.2	AIRSS predicted phase diagram of carbon. Image adapted from [33].	5
1.3	An example of clathrate structure (a) and the two polyhedral cages that constitute this clathrate (b). Image taken from [4].	6
1.4	From a regular icosahedron to a truncated icosahedron.	7
1.5	C_{60} molecular structure showing disorder between the two standard orientations (one indicated by bold lines and other by dashed lines). Figure from [88]. . . .	7
1.6	Four C_{60} molecules with the same standard configuration, at position (000), $(\frac{1}{2}\frac{1}{2}0)$, $(\frac{1}{2}0\frac{1}{2})$ and $(00\frac{1}{2})$, as in the room conditions fcc model ignoring disorder (molecular rotation) with $Fm\bar{3}$ space group. The rods indicate the $\langle 111 \rangle$ cubic directions where the rotation is to be performed to obtain the sc phase structures. Figure from [87].	8
1.7	Relative orientation of neighboring C_{60} molecules. (a) P configuration. (b) H configuration. Figure adapted from [87].	9
1.8	Low-temperature low-pressure phase diagram of C_{60} . The fcc to sc and the sc to orientational glass phases are indicated. The percentage of H configuration is indicated. Figure from [92].	9
1.9	Two C_{60} molecules bonded via 66/66 2+2 cycloaddition. Figure adapted from [93].	10
1.10	Theoretical dimers. (a) Single bond dimer. (b) 56/56 2+2 cycloaddition dimer. (c) 56/65 2+2 cycloaddition dimer.	10
1.11	C_{60} dimers (a) 3+3 cycloaddition between hexagons. (b) double 4+4 cycloaddition, each 4+4 cycloaddition is drawn with darker lines. Figure from [101]. . .	11
1.12	Low-dimensional polymerized C_{60} structures. The dark spheres, in the top panel, indicate molecules bonded to each other forming polymerized chains and layers, which are shown in detail in the bottom panel. Figure from [92]. . . .	12
1.13	(a) Tetragonal C_{60} phase polymeric layer ascribed to the tetragonal axis. (b) Relationship between the tetragonal cell and the fcc cell. Figure from [16]. . .	13
1.14	(a) Rhombohedral C_{60} phase polymerized layer. (b) The polymerized layer having molecules in other orientation. (c) ABC stacking of (a) oriented layers. (d) ABC stacking of (b) oriented layers. (e) Combined stacking model. Figure adapted from [16].	14
1.15	3D cuboidal polymerized C_{60} structure. Figure adapted from [19].	15
1.16	3D polymerized structure with the $R\bar{3}$ symmetry reported by Yamanaka et al. (a) (a,b) polymerized plane with C_{60} molecules bonded via 5/5 3+3 cycloaddition between pentagons. Red atoms are involved in 56/65 2+2 cycloadditions that bond to neighboring molecules belonging to adjacent (a,b) polymerized planes. (b) Bonding schemes. Figure adapted from [18].	16

1.17	Electronic band structures of low-dimensional polymers calculated using DFT within LDA. (a) 2D rhombohedral structure. (b) 2D tetragonal structure. Figures from [67, 68].	17
2.1	Scheme depicting the self-consistent loop used to solve the Kohn-Sham equations.	38

List of Tables

1.1	Crystallographic data of 1D orthorhombic phase.	12
1.2	Crystallographic data of 2D tetragonal phase for different P-T paths (P-T meaning applying first pressure and then temperature and T-P in the reverse way). T-tetragonal phase, R-rhombohedral phase.	13
1.3	Crystallographic data of 2D rhombohedral phase. T-tetragonal phase and R-rhombohedral phase.	14
1.4	Bulk moduli of polymerized C ₆₀ phases with known structure.	19
2.1	Crystal lattices primitive unit cell specifications.	34

List of Publications

Here a list of publications already published or to be submitted to scientific journals (with some pre-printed version available at Arxiv) is presented. It includes one publication I co-authored which is not part of this thesis.

1. J. Laranjeira, L. Marques, M. Mezouar, M. Melle-Franco, and K. Strutyński, Bonding Frustration in the 9.5 GPa fcc polymeric C_{60} , *Physica Status Solidi - Rapid Research Letters* 11 (2017), 1700343.
2. J. Laranjeira, L. Marques, N. Fortunato, M. Melle-Franco, K. Strutyński and M. Barroso, Three-dimensional C_{60} polymers with ordered binary-alloy-type structures, *Carbon* 137 (2018) 511–518.
3. J. Laranjeira, L. Marques, M. Melle-Franco, K. Strutyński, M. Mezouar and M. Barroso, Three-dimensional fcc C_{60} polymer, *Materials Letters: X* 4 (2019) 100026.
4. J. Laranjeira, L. Marques, C_{60} structures: Structural, electronic and elastic properties, *Materials Today Communications* 23 (2020) 100906.
5. V. Milotti, C. Berkmann, J. Laranjeira, W. Cui, K. Cao, Y. Zhang, U. Kaiser, K. Yanagi, M. Melle-Franco, L. Shi, T. Pichler and P. Ayala, Unravelling the complete Raman response of graphene nanoribbons discerning the signature of edge passivation, *Small Methods* 6 (2022) 2200110.
6. J. Laranjeira, L. Marques, M. Melle-Franco, K. Strutyński and M. Barroso, Clathrate structure of polymerized fullerite C_{60} , *Carbon* 194 (2022) 297-302.
7. J. Laranjeira, K. Strutyński, L. Marques, E. Martínez-Nuñez and M. Melle-Franco, $C_{60}+C_{60}$ molecular bonding revisited and expanded, pre-print version at arXiv:2302.06901 (2023), to be submitted.
8. J. Laranjeira, I. Errea, Đ. Dangić, L. Marques, M. Melle-Franco and K. Strutyński, Superconductivity in the doped polymerized fullerite clathrate from first principles, pre-print version at arXiv:2302.06897 (2023), to be submitted.
9. J. Laranjeira, L. Marques, M. Melle-Franco and K. Strutyński, Reentrant semiconducting behavior in polymerized fullerites with increasing sp^3 content, pre-print version at arXiv:2302.13395 (2023), to be submitted.

List of Abbreviations

fcc face-centered cubic	1
sc simple cubic	1
2D two-dimensional	1
1D one-dimensional	2
3D Three-dimensional	2
nn nearest neighbors	2
DFT density functional theory	3
HPHT high-pressure high-temperature	2
CSP crystal structure prediction	3
USPEX Universal Structure Predictor: Evolutionary Xtallography	3
CALYPSO Crystal structure AnaLYsis by Particle Swarm Optimization	3
AIRSS Ab Initio Random Structure Searching	3
MD Molecular dynamics	6
LDA local density approximation	17
GGA general gradient approximation	18

DOS density of states	17
EOS equation of state	18
VASP Vienna Ab initio Simulation Package	19
QE QUANTUM ESPRESSO	19
DFPT density functional perturbation theory	19
HSE Heyd-Scuseria-Ernzerhof	20
AMK AutoMeKin	20
T_c superconducting critical temperature	44
PBE Perdew-Burke-Ernzerhof	39
LCAO linear combination of atomic orbitals	40

Chapter 1

Introduction

Carbon, being one of the most abundant elements in nature [1], has a vast plethora of allotropes with different dimensionalities and physical properties [2–56]. Such flexibility is the result of the different hybridization states (sp^1 , sp^2 , sp^3) that valence orbitals of carbon can present and, concomitantly, the distinct number of bonding geometries that this atom can adopt. For instance, the well-known graphite, graphene, carbon nanotubes and fullerenes have all their carbon sp^2 -hybridized, while in diamond all carbon atoms are sp^3 -hybridized. Sp^1 -hybridization is observed in linear acetylenic carbons, for instance [2].

This large flexibility that carbon presents can be exploited to synthesize new pure-carbon materials with fascinating physical properties, such as superhardness [36–48] or even softness, as the case of graphite. It also allows for tunable electronic behavior with structures ranging from insulator, like diamond, to semi-metallic, such as graphite. Furthermore, carbon-based structures have also shown other exotic properties, as superconductivity [49–55] and topological electronic properties [30, 31]. These outstanding properties and tuning possibilities allow for a considerable amount of technological applications. For instance, graphdiynes, a family of carbon allotropes, have applications ranging from catalysis to energy storage, among others [56]. Another example is a few layer graphene, which can be used as a transistor [11]. The discovery of these fascinating properties and possible applications, fostered the interest in finding new carbon allotropes, which may present properties, or combinations of properties, that are even more impressive and more suitable for technological applications than those exhibited by the already known carbon allotropes. Thus, huge efforts, both computational [31–37] and experimental [12–16, 43], have been dedicated to find new carbon or carbon-based structures. In some of these studies, metastable forms of carbon, like fullerenes or nanotubes, have been used as precursors to synthesize, or to theoretically predict, new carbon structures with remarkable properties [14–19, 57], making them a viable option as building blocks for new carbon structures. As an example, quite recently C_{60} molecules have been used as building blocks to prepare two-dimensional (2D) layers: these layers were produced from the exfoliation of a polymer synthesized by facile reaction of C_{60} and magnesium at atmospheric pressure [12].

Experimental research activities that lead to a considerable amount of structures constructed using metastable precursors have been initiated by the synthesis of the C_{60} fullerene in macroscopic amounts by Krätschmer et al. [58], a few years after the discovery of the C_{60} molecule by Kroto et al. [59]. For the discovery of C_{60} , Kroto and coworkers were awarded the 1996 Nobel Prize in Chemistry [60]. At ambient conditions, fullerite C_{60} is a van der Waals solid with a face-centered cubic (fcc) structure where the molecules are rotating freely [61]. This structure has $Fm\bar{3}m$ space group and has a lattice parameter of 14.17 Å [16]. At 255 K fullerite undergoes a first-order phase transition to a simple cubic (sc) structure, space group $Pa\bar{3}$, with a lattice parameter of 14.04 Å. The C_{60} molecules in the sc structure are also

held together through van der Waals interactions but now the molecules are frozen in specific orientations and are not freely rotating [62].

It is well-known that high-pressure conditions can modify the carbon hybridization state and, hence, its coordination number [7]. Therefore, high-pressure high-temperature (HPHT) methods have been used to prepare novel carbon materials displaying outstanding physical properties. In the particular case of C_{60} , the application of pressure decreases the intermolecular distances and hinders the molecular rotational motion, while temperature induces rotational motion, though with limited amplitude. Thus, applying simultaneously pressure and temperature allows the C_{60} molecules to adopt the correct orientation, at reduced distances, between nearest neighbors (nn), fostering the formation of polymerized C_{60} phases. In other words, it facilitates the assembly of C_{60} molecules as building blocks in new carbon structures. Several C_{60} polymerization products have been produced in early studies through HPHT methods [10, 63]. The first HPHT induced polymerization of C_{60} was reported, in 1994, by Iwasa et al. [63].

At moderate temperatures, below 1000 K, and at pressures below 8 GPa, low-dimensional C_{60} polymers are formed: the one-dimensional (1D) orthorhombic phase [10, 64] and both 2D rhombohedral and tetragonal phases [10, 65–68]. Polymerized chains grow along the shortest lattice parameter of the 1D orthorhombic phase, the tetragonal phase has square polymerized layers formed, while the rhombohedral phase has triangular layers. The polymerized layers, or chains, are kept together through van der Waals interactions. These low-dimensional polymerized phases have a common type of intermolecular covalent bond, 66/66 2+2 cycloadditions, which connects neighboring molecules by their intramolecular double bonds [3]. A sketch of C_{60} pressure-temperature diagram is shown in figure 1.1.

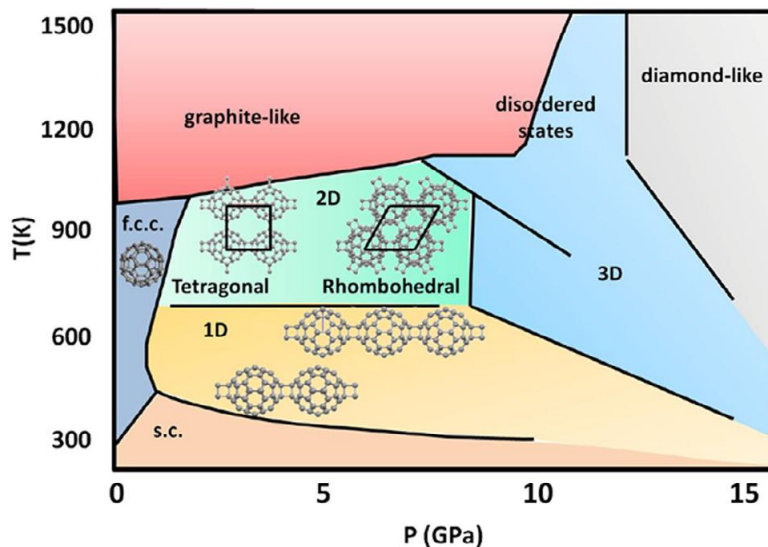


Figure 1.1: C_{60} pressure-temperature diagram sketch. Figure after Álvarez-Murga et al. [16].

Three-dimensional (3D) polymerized networks of C_{60} are formed above 8 GPa. They exhibit astonishing physical properties for pure carbon phases, such as electron conductivity and low-compressibility, together with low density [10, 16, 19, 38–41, 69–71]. In particular, C_{60} samples subjected to 13 GPa and to temperatures above 1000 K have shown higher bulk moduli than diamond [69]. Quite recently, the ultra-hardness of these systems resurged stunningly in several works [38–41]. Although there have been numerous studies of polymerized C_{60} phases, little is known about their crystal structures. The samples synthesized until now are poorly crystallized and heterogeneous, with multiple phases coexisting. This originates x-ray

diffraction patterns with poor-resolution, preventing the structure determination and even a clear identification of the experimental phases. New bonding types are needed to be involved in such 3D polymerized structures, since 66/66 2+2 cycloaddition bonds alone cannot form 3D polymerized C₆₀ in ABC-stacked lattices. New types of bonding, such as the 6/6 3+3 cycloaddition [19], have been proposed based on both experimental data and computational simulations. Nevertheless, a considerable amount of effort, both on the experimental and computational sides, is still needed to get a correct and comprehensive picture of the pressure effects on C₆₀. Hence, the main objective of this thesis is to shed light on structural and other physical properties of 3D polymerized C₆₀ phases using density functional theory (DFT) techniques.

During this PhD project, we have attempted to resolve the crystal structure of 3D C₆₀ polymers by combining low-resolution x-ray diffraction data with computational modeling, using DFT. To find the crystal structures, we have taken into account all the possible information from the experimental diffraction pattern (basically the overall symmetry and lattice parameters) to build possible structural models. These structural models were then optimized using DFT. With this methodology, we successfully found the structure of a 3D C₆₀ polymer phase experimentally synthesized, as well as, some other structures of interest, including a polymerized C₆₀ clathrate that may be synthesized through HPHT treatments, once the appropriate thermodynamic path is found. After the discovery of interesting polymerized structures, we often studied their mechanical, electronic and other relevant properties using again DFT methods.

In the remainder of this introductory chapter, we will present some recent developments in the research of carbon structures using computational methods. Then we will present the state-of-the-art on polymerized C₆₀ phases synthesized at HPHT before outlining the thesis, by giving a brief summary of the articles that constitute it.

1.1 Recent computational efforts in predicting crystal structures

Since quite early, computational techniques have shown the capacity to be an important tool to understand C₆₀ based materials and their properties. In particular, DFT studies have been crucial in the interpretation of the photoemission spectra of C₆₀, allowing for an accurate understanding of the origin of its peaks [72, 73] and, thus, showing the potential of DFT techniques to facilitate the study of these and other materials. This capability was properly highlighted with half of the 1998 Nobel Prize in Chemistry being awarded to W. Kohn for his development of DFT [74].

In the last decades, several approaches have been used to predict new carbon structures. For instance, crystal structure prediction (CSP) algorithms, such as Ab Initio Random Structure Searching (AIRSS) [75, 76], Universal Structure Predictor: Evolutionary Xtallography (USPEX) [32, 77] and Crystal structure AnaLYsis by Particle Swarm Optimization (CALYPSO) [78], have been responsible for proposing several novel carbon crystalline structures [4, 32–36, 44, 79]. All these methods are interfaced with DFT codes to allow for the optimization of proposed structures. Another path to predict carbon structures, has been to build models and then use DFT to check their stability [5, 6, 18, 19, 29–31, 37, 50, 57]. Another way is to run molecular dynamics simulations, which are usually also proceeded by a subsequent DFT optimization [18, 80, 81]. The aim of the present section is to show the importance of computational methods in the research of new carbon allotropes, as well as, to enumerate the reasons why some of these methods have not been employed to our problem.

1.1.1 Crystal structure prediction

CSP algorithms use mathematical operations to construct new structures. At the beginning of a calculation, one may give initial structures and/or define constraints, such as lattice parameters and the number of atoms in the cell. After this step, a DFT calculation is usually performed to assess the stability of the proposed structure. All the structures that pass this step are saved and may then be used, by the program, to produce new structures. These codes can perform several complementary operations, like the random motion of atoms, mixing two different structures, generating a new structure based on the previous constraints, among others. These algorithms usually accelerate the discovery of new structures, several carbon allotropes being predicted by them in recent years. Nevertheless, this acceleration comes at a computational cost that needs to be taken into account, as we shall discuss in the next subsection.

AIRSS program was used to predict a carbon nanostructure that was named chiral structure framework [34]. This structure is only slightly more unstable than diamond, 112 meV per atom, belonging to the $P6_122$ space group and having an electronic bandgap very close to that of diamond.

Another CSP code that, right since its genesis, was used to predict several carbon structures is USPEX [32]. In 2009, Li et al. [36] predicted a new carbon structure, which they named M-carbon: the structure can be seen as a distorted form of graphite, where the sheets are translated and buckled. It has $C2/m$ symmetry and the carbon atoms are all in sp^3 hybridization, showing elastic properties identical to diamond. M-carbon structure fits quite well experimental data of cold compressed graphite, up to ~ 14 GPa [43]. In 2011, Lyakhov and Oganov reported five more carbon nanostructures predicted with USPEX [44]. They also compared their hardness to those of diamond, chiral structure framework [34], M-carbon [36] and bct4-carbon [37], concluding that diamond is the hardest carbon structure but all the others are almost as hard. Also in 2011, another paper from USPEX [79] added three more structures to the carbon family, being all of them slightly less hard than diamond and impressively some of them are less dense than diamond. USPEX has also been used to predict a 2D form of carbon, phantagraphene, which is formed by pentagonal, hexagonal and heptagonal rings [35].

CSP methods have also been employed to study the phase diagram of carbon. In particular, Martinez-Canales et al. [33] performed such a study using AIRSS that corroborated a previously reported phase transition sequence, where diamond transforms into BC8, at 0.99 TPa, and BC8 would undergo a subsequent phase transition to a sc lattice at 2.9 TPa. BC8 structure was previously proposed in the 1980s [82] by using a known silicon structure framework and making the permutation of the silicon atoms by carbons. Above 2.9 TPa, the authors proposed a new phase diagram with the following phase transformations: sc, simple hexagonal, fcc, double hexagonal close-packed, body-centered cubic, with transition pressures of 6.4, 21, 270, and 650 TPa, respectively. The proposed phase diagram of carbon is presented in figure 1.2.

1.1.1.1 The problem of applying CSP to C_{60} polymers

The previous results show the relevance that CSP can have in predicting carbon structures, which in some cases correspond to experimentally synthesized phases [13, 36, 83]. Nonetheless, CSP tools have their drawbacks. For instance, to avoid interaction between adjacent cores (primitive cells) a supercell of 64 atoms was used to find M-carbon [36]. In our study, the C_{60} molecules are the structural building blocks, consisting of a very large number of atoms, and, since CSP codes are interfaced with DFT packages, the application of these methods to our problem would render such a computation impossible at an affordable computational cost.

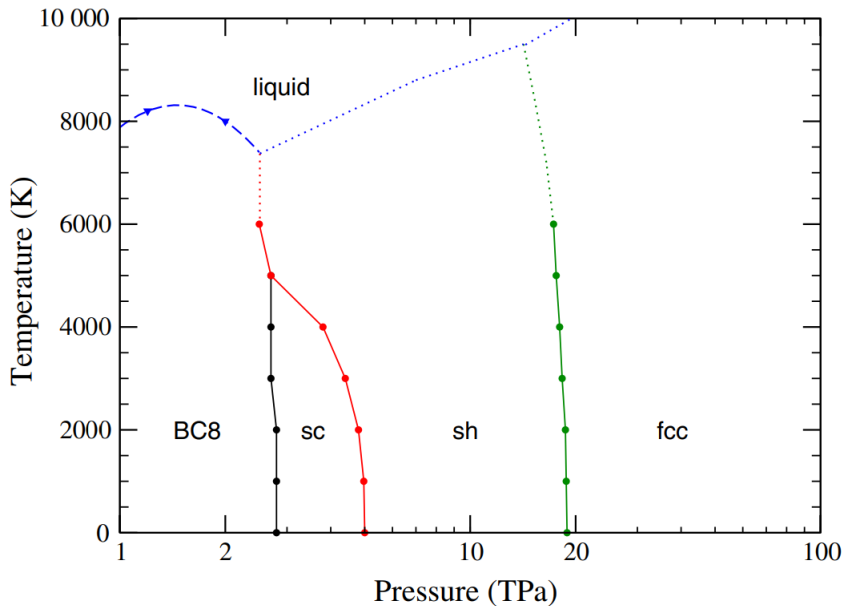


Figure 1.2: AIRSS predicted phase diagram of carbon. Image adapted from [33].

Furthermore, USPEX uses different kinds of operations to design crystal structures, such as the combination of two initial unit cells, which often breaks the C_{60} molecules, being thus unsuitable for our study. The random change of cell vectors and/or atomic positions, which, for a system with a high number of atoms, will again increase the computational load at an impossible rate to keep up with our resources. AIRSS and CALYPSO suffer from similar problems and, therefore, we have not used them to predict C_{60} polymers.

1.1.2 Finding structures through permutation of atoms with DFT optimization: the carbon clathrates case

Clathrates are open framework structures constituted by a continuum of face-sharing polyhedral cages, which may or may not contain guest species [4–7, 17, 29], see figure 1.3 for an example. Guest-free carbon clathrates are thought to show outstanding physical properties themselves, like superhardness [4, 5], and they could also be doped in order to tune other properties [6, 29]. Good electrical conductivity and bad thermal conductivity may arise together in doped carbon clathrates due to the incoherent scatter of thermal phonons in the rattling modes of the guest species [84]. Another possibility for doped carbon clathrates is to show high superconducting critical temperatures, since this property is enhanced by the lightness of the carbon atoms and strength of covalent bonds [49, 50].

Carbon clathrate structures may be some of those whose prediction recurring to DFT has been more intensive, with their structures being taken as analogues of clathrate structures formed by group IV elements [5, 6, 29], i.e. changing the group IV atoms to carbons in the previously known clathrate structure. In this sense, Wang and coworkers [31] have proposed a body-centered tetragonal structure, belonging to the $I/4mmm$ space group, that was constructed swapping each C-C bond in the bct- C_4 [37] by a benzene ring and subsequent DFT optimization. This structure was named bct- C_{40} and presents a very curious electronic structure that the authors classify as a topological nodal-net semimetal. Although most carbon clathrates have been studied by this simple atomic permutation and DFT calculations, CSP packages have also been used to predict carbon clathrates with CALYPSO finding a

new carbon clathrate structure [4], seen in figure 1.3. More relevantly, mixed carbon boron clathrates have been synthesized, guided by initial theoretical predictions, and their crystal structures were determined by x-ray diffraction combined with CSP results [13, 83]. Even though a lot of effort has been poured into strategies to synthesize pure carbon clathrates, they have not yet been experimentally realized. C_{60} has been thought to be a good precursor for the synthesis of carbon clathrates, however, all the structures determined up to now are not clathrates [7, 17].

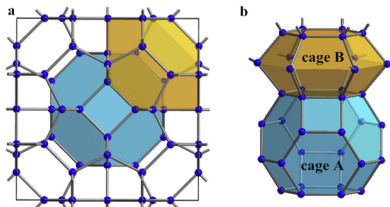


Figure 1.3: An example of clathrate structure (a) and the two polyhedral cages that constitute this clathrate (b). Image taken from [4].

1.1.3 Molecular dynamics

Molecular dynamics (MD) is another computational technique that has been used to study carbon structures. In particular, MD has been used to follow the transformation of a given carbon structure into a new one through the simulation of temperature and/or pressure application. As an example, the bct- C_4 structure was predicted by applying 20 GPa to a (10,10) carbon nanotube system via MD. The final structure had its stability checked via DFT methods and consists of rings with only four carbon atoms bonded extending in a 3D network and having all its carbons sp^3 -hybridized [37].

New C_{60} polymers have also been studied employing MD, see Yamagami and Saito [80, 81] and Yamanaka et al. [18] for examples. These works will be briefly discussed in the next section, nevertheless all of them fail to capture the detailed structural properties of the experimental phases. At the end of 2022, Zhao et al. published an MD study employing a machine learning fitted potential (GAP20 [85]) that yielded impressive results, fitting the experimental data and proving the validity of such methods to simulate carbon nanostructures with accuracies close to those of DFT, but at a fraction of the computational cost [86]. The authors have studied the pressure-temperature phase diagram of C_{60} , being able to accurately identify different regions, for instance, the region where diamond-like phases arise. Unfortunately, they have done all their studies above 1000 K, missing most of the regions where the C_{60} polymers form. This opens a promising path to study polymerized C_{60} structures but, regrettably, arrived too late to impact the work done by us.

1.2 C_{60} crystalline phases obtained through HPHT treatments

The C_{60} molecule is a highly symmetrical molecule with its sixty atoms located at the vertices of a truncated icosahedron and having $m\bar{3}5$ point symmetry (I_h in Schönflies notation). A regular icosahedron is a geometric solid with twenty equilateral triangular-shaped faces, thirty edges and twelve vertices, if we slice a plane perpendicular to the vector that connects the icosahedron center to each vertex a truncated icosahedron is obtained. Figure 1.4 illustrates this procedure, where the final geometrical solid has twelve pentagons and twenty hexagons making a total of thirty-two faces, ninety edges and sixty vertices.

The hexagons in the C_{60} molecule are not regular, as they have two different edge lengths. The bonds belonging to both a hexagon and a pentagon are the longer ones (1.45 Å) and have a smaller double-bond character, while the ones fusing two hexagons are shorter bonds (1.40 Å) having higher double bond character [61]. The hexagonal faces are perpendicular to three-fold rotation axes and the pentagonal faces are perpendicular to five-fold rotational axes [62]. The molecule has a center of symmetry and its double bonds are perpendicular to a two-fold rotation axis, which has, in addition, a perpendicular mirror plane.

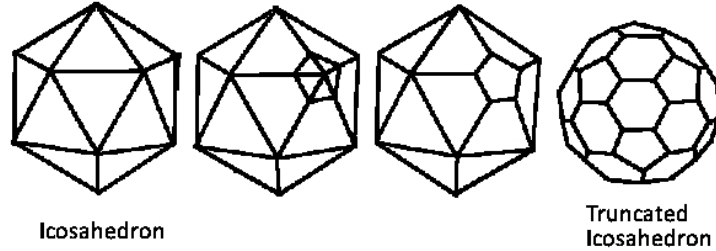


Figure 1.4: From a regular icosahedron to a truncated icosahedron.

When C_{60} molecules are ascribed to a cubic lattice, they may adopt one of two standard orientations [62]. In the standard orientations, the three cubic axes of the lattice are orthogonal to double bonds, i.e. they are aligned to the molecular two-fold axes. One standard orientation can be converted into the other through a 90° rotation around any $\langle 100 \rangle$ direction or by a 75.5° rotation around any $\langle 111 \rangle$ direction. Although the two standard orientations are not the only ones adopted by C_{60} in its ordered polymers, they play a crucial role in several polymers [87] including the experimental phase that we will explore in three of our papers, A1 to A3.

1.2.1 C_{60} solid structure at room conditions

The C_{60} solid structure at room temperature can be interpreted as an ABC stacking of interacting spheres held by van der Waals forces. Constructing an fcc lattice with C_{60} molecules in the same standard orientation leads to a crystalline structure belonging to the $Fm\bar{3}$ space group, the five-fold symmetry being incompatible with crystal symmetry [88]. X-ray diffraction intensities indicate an orientational molecular disorder. This disorder can be achieved by the superposition of the two standard orientations, as shown in figure 1.5, leading to $Fm\bar{3}m$ symmetry. Nuclear magnetic resonance spectroscopy data shows that molecules are rotating, indicating that the disorder is higher than the simple disorder between the two standard orientations. A model where C_{60} is viewed as a spherical shell of charge (complete orientational disorder) is in better agreement with the x-ray diffraction intensities [62].

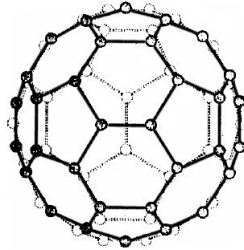


Figure 1.5: C_{60} molecular structure showing disorder between the two standard orientations (one indicated by bold lines and other by dashed lines). Figure from [88].

1.2.2 C_{60} at low temperatures and pressures

The disordered state at room conditions cannot be the ground state of fullerene C_{60} since it has a very large entropy. Thus, by lowering the temperature orientational molecular order must be reached [62]. Indeed, at 255 K there is a first-order phase transition from the fcc phase to an sc phase, symmetry $Pa\bar{3}$, with the four molecules in the fcc conventional lattice becoming orientationally nonequivalent [62]. Starting from the fcc with the four molecules adopting one of the two standard orientations, the sc phase is built by rotating the four molecules around different $\langle 111 \rangle$ cubic directions by the same angle [87], see figure 1.6. This rotation has to be done clockwise and the angle could be either 98° or 38° . When the angle is 98° six double bonds align with six pentagonal faces, from the six neighboring molecules, see figure 1.7(a). On the other hand, when the angle is 38° six double bonds align with six hexagonal faces, see figure 1.7(b). These configurations are called P and H, respectively, and both configurations minimize the intermolecular electronic repulsion. One configuration can be transformed into another through a rotation of 60° degrees around the $\langle 111 \rangle$ cubic directions or through a rotation of $\sim 42^\circ$ around the $\langle 110 \rangle$ cubic directions. The latter is the most probable, as it is energetically preferred [87].

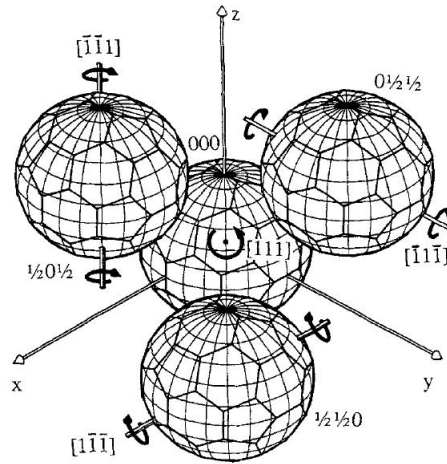


Figure 1.6: Four C_{60} molecules with the same standard configuration, at position (000) , $(\frac{1}{2}\frac{1}{2}0)$, $(\frac{1}{2}0\frac{1}{2})$ and $(00\frac{1}{2})$, as in the room conditions fcc model ignoring disorder (molecular rotation) with $Fm\bar{3}$ space group. The rods indicate the $\langle 111 \rangle$ cubic directions where the rotation is to be performed to obtain the sc phase structures. Figure from [87].

Although the P configuration at room pressure is energetically slightly more favorable [89], these two configurations, P and H, coexist in the sc phase. In this phase, the molecules are continuously jumping between P and H configurations. Hence, some structural disorder is kept [87]. The majority of the molecules in the sc phase have P configuration and the ratio of P and H configuration is a function of temperature and pressure. At 250 K (and room pressure), the sc phase has a maximum number of molecules in the H configuration. The temperature decrease results in an increase in the percentage of the most favorable P configuration, from $\sim 60\%$ to a maximum of $\sim 84\%$. At 90 K a second-order phase transition occurs, below which the ratio of P and H configurations are constant as the thermal energy becomes insufficient to allow conversion of H into P configuration and the system becomes an orientational glass [87, 89].

The volume of the H configuration is 1 % smaller than the volume of P configuration [90] and, thus, the H configuration becomes energetically more favorable at high-pressure [91]. At

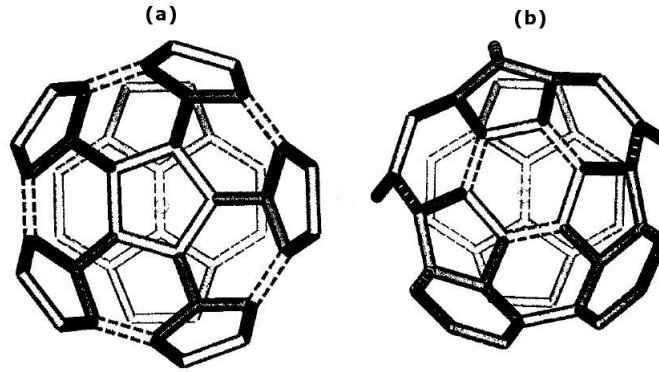


Figure 1.7: Relative orientation of neighboring C_{60} molecules. (a) P configuration. (b) H configuration. Figure adapted from [87].

150 K and ~ 0.2 GPa, a percentage of 50 % of H configuration is achieved, which increases upon further pressure rise [90]. Figure 1.8 shows the low-temperature low-pressure C_{60} phase diagram, illustrating the rise of number of molecules in the H configuration with pressure.

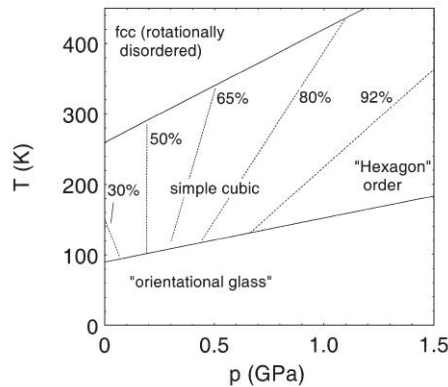


Figure 1.8: Low-temperature low-pressure phase diagram of C_{60} . The fcc to sc and the sc to orientational glass phases are indicated. The percentage of H configuration is indicated. Figure from [92].

1.2.3 C_{60} dimerization

In 1993, C_{60} dimerization was reported by Rao et al. [93]. To synthesize this dimer, fullerite C_{60} was irradiated at room temperature with either visible or ultra-violet light, leading to a new solid structure where molecules are covalently bonded, through 66/66 2+2 cycloaddition. Although the molecules are now forming dimers, the fcc lattice is kept on average. Later Davydov et al. [94] produced pressure-induced dimerization. The 66/66 2+2 cycloaddition reaction, involved in C_{60} dimerization, occurs when two new covalent single bonds are formed from two previous covalent double bonds, creating a square ring of bonds, as shown in figure 1.9. The name of these reactions is given according to the number of atoms that each reacting molecule has in the newly generated square ring [95], hence 2+2. The 66/66 indicates the molecular relative position, in this case meaning that two hexagons of one molecule (6) are

pointing to identical hexagons in the neighboring molecule.

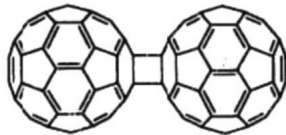


Figure 1.9: Two C_{60} molecules bonded via 66/66 2+2 cycloaddition. Figure adapted from [93].

1.2.3.1 Other C_{60} bonding schemes

C_{60} molecules can be bonded via other chemical schemes. In theoretical studies, Scuseria [96] considered dimerization via the previous 66/66 2+2 cycloaddition and via a single bond, see figure 1.10(a), concluding that the lowest energy dimer is the one formed via 66/66 2+2 cycloaddition. Such result was later experimentally confirmed, as all the high-pressure polymerized C_{60} structures, obtained below 8 GPa, only exhibit 66/66 2+2 cycloadditions.

Twelve C_{60} dimers have been theoretically studied up to now [3, 96–100]. Among these bonding possibilities in dimers are the four 2+2 cycloadditions, the two possibilities of bridging two molecules connecting all the atoms from facing hexagons (having six intermolecular bonds), and the one possibility of bonding all the atoms from two facing pentagons (forming five intermolecular bonds). From these early studies, 56/56 2+2 cycloaddition bonds are of particular interest because of its participation in 3D C_{60} polymers. Besides the 66/66 alignment, possible 2+2 cycloaddition bonds are formed between intramolecular hexagon-pentagon (56) bonds (single bonds), with two additional possibilities. In the first case 56/56, molecules align their pentagons and their hexagons, shown in figure 1.10(b). In the second case 56/65, the pentagon of one molecule aligns with the hexagon of the other, as seen in figure 1.10(c). Another 2+2 cycloaddition bonding configuration where a double bond from one molecule is facing a single bond from another 66/56 is also possible. The 56/65 bonding patterns have already been used to build C_{60} crystal structures [18] and all the 2+2 cycloadditions were previously considered in dimers [3], showing the relevance of these bonding schemes. In this thesis, we have used the 56/56 2+2 cycloadditions to elucidate a 3D C_{60} polymer phase that is discussed in the papers A1 to A3.

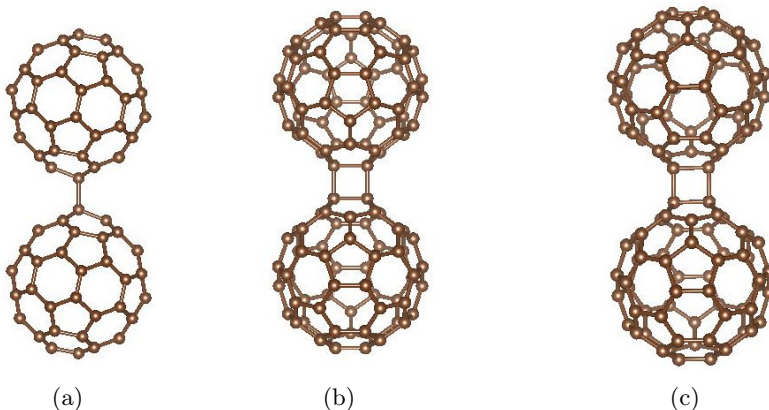


Figure 1.10: Theoretical dimers. (a) Single bond dimer. (b) 56/56 2+2 cycloaddition dimer. (c) 56/65 2+2 cycloaddition dimer.

Aside from theoretical studies on dimers, research conducted to find polymerized structures

has unveiled more C_{60} bonding types. Yamanaka et al. [19] reported that a 3+3 cycloaddition between hexagons is involved in the 3D cuboidal phase. In this 3+3 cycloaddition, two non-adjacent atoms from one hexagon are bonded to the same atoms in the neighboring molecule, see figure 1.11(a). The 3D cuboidal structure have also another new type of bonding, the double 66/66 4+4 cycloaddition, shown in figure 1.11(b), involving four covalent bonds [19, 101]. Yamanaka et al. [18] has proposed a 3+3 cycloaddition between pentagons to occur in another 3D polymerized phase.

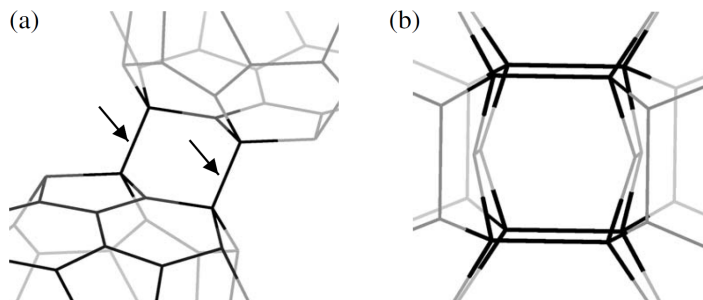


Figure 1.11: C_{60} dimers (a) 3+3 cycloaddition between hexagons. (b) double 4+4 cycloaddition, each 4+4 cycloaddition is drawn with darker lines. Figure from [101].

The distance between the centers of mass of C_{60} molecules linked by a given polymeric bond is about the same on dimers and on bulk polymers. For instance, the distance between molecular centers of mass in the low-dimensional polymers, where the molecules are bonded via 66/66 2+2 cycloaddition, range from 9.02 and 9.18 Å [10, 16], while it has a calculated value of ~ 9.1 Å in the dimer. Hence, the search for possible C_{60} dimers with new molecular bonding schemes could bring more insights to the investigations of C_{60} polymers, in particular, in identifying the bonding types involved and in elucidating the crystal structures. Based on this assumption, we have explored the possible bonding schemes in C_{60} dimers, expanding the universe of known dimers to forty-one. This work is presented in article A4.

1.2.4 Pressure induced polymerized C_{60} structures

As mentioned before, below 8 GPa of pressure, three low-dimensional polymers are synthesized via HPHT treatments of fullerite C_{60} : the 1D orthorhombic, 2D tetragonal and rhombohedral polymers. Above this pressure, 3D C_{60} polymers are obtained. The polymerization process is known to start with the formation of dimers, which grow, upon temperature rise, to form higher oligomers and finally an extended polymer structure is created.

The low-dimensional polymerized structures can easily be seen as distortions of the fcc structure. The 1D orthorhombic phase can be achieved by compressing the fcc structure along one $\langle 110 \rangle$ cubic direction. Similarly, in the 2D tetragonal and rhombohedral phases the (100) and (111) cubic planes are to be compressed, respectively. These distortions of the fcc lattice are illustrated in figure 1.12.

1.2.4.1 1D orthorhombic polymerized phase

The 1D orthorhombic phase is prepared at pressures lower than 2 GPa and temperatures between 500 K and 700 K. Table 1.1 summarizes the lattice parameters reported for this structure, as well as, the proposed space groups and pressure-temperature conditions of synthesis.

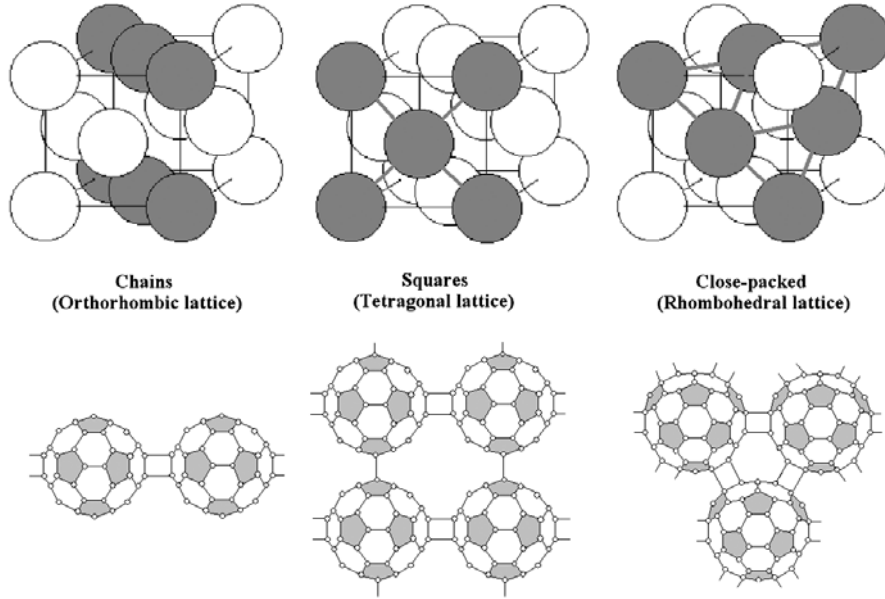


Figure 1.12: Low-dimensional polymerized C_{60} structures. The dark spheres, in the top panel, indicate molecules bonded to each other forming polymerized chains and layers, which are shown in detail in the bottom panel. Figure from [92].

Table 1.1: Crystallographic data of 1D orthorhombic phase.

Report on	Phase	space group	$a(\text{\AA})$	$b(\text{\AA})$	$c(\text{\AA})$	$P(\text{GPa})$	$T(\text{K})$	Refs.
Powder	O	Immm	9.26	9.88	14.22	2.0	573	[10]
Powder	O	Immm	9.09	9.83	14.72	1.5	723	[64]
Single Crystal	O	Pmnn	9.14	9.90	14.66	1.2	585	[102]

1.2.4.2 2D polymerized phases

Two-dimensional polymerized phases are synthesized under pressures ranging from 2 to 8 GPa and temperatures between 500 and 900 K. The two phases often coexist, although above 4 GPa the rhombohedral phase is dominant. The first sample of these 2D polymers was produced by Núñez-Regueiro et al. [10], using 3 GPa and 873 K. The sample contained 65 % of rhombohedral phase and 35 % of tetragonal phase.

The tetragonal structure can be thought to be formed by creating intermolecular bonds between the polymeric chains in the plane defined by the a and b tetragonal axes (along two $[110]$ cubic directions), as shown in figure 1.13(a). The interaction between polymerized sheets is of van der Waals nature. Figure 1.13(b) shows the crystallographic relationship between the body-centered tetragonal cell and the fcc cell.

The first reported 2D tetragonal structure was indexed to the orthorhombic space group Immm [10], this structure is labeled as T. In this structure the polymeric stacked layers, with ABAB... stacking-type, have the same orientation. Later, Davydov et al. [103] proposed a different structure with tetragonal space group $P4_2/mmc$, the difference from the previous structure is that the B stacked-layer is rotated by 90° , around the tetragonal c axis, with respect to the A layer, this structure is labeled as T'. Later, Chen and Yamanaka [65] obtained again the T structure from a single crystalline sample. Table 1.2 summarizes all the data from different groups.

The synthesis of phases T and T' depends on the values of pressure and temperature, but

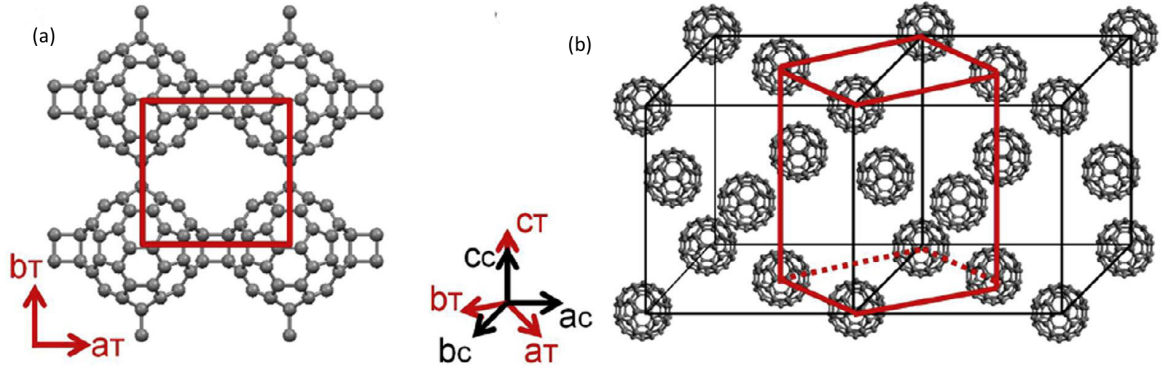


Figure 1.13: (a) Tetragonal C₆₀ phase polymeric layer ascribed to the tetragonal axis. (b) Relationship between the tetragonal cell and the fcc cell. Figure from [16].

Table 1.2: Crystallographic data of 2D tetragonal phase for different P-T paths (P-T meaning applying first pressure and then temperature and T-P in the reverse way). T-tetragonal phase, R-rhombohedral phase.

Path	Report on	Phase	space group	$a(\text{\AA})$	$b(\text{\AA})$	$c(\text{\AA})$	$P(\text{GPa})$	$T(\text{K})$	Refs.
P-T	Powder	35%T-65%R	Immm	9.09	9.09	14.95	3.0	873	[10]
	Powder	65%T'-35%R	P4 ₂ /mmc	9.097	9.097	15.04	2.2	873	[103]
	single crystal	T	Immm	9.026	9.083	15.07	2.5	773	[65]
T-P	Powder	90%T'	P4 ₂ /mmc	9.097	9.097	15.04	2.2	873	[103, 104]
	single crystal	75%T'-25%R dimers	P4 ₂ /mmc	9.02	9.02	14.934	2.0	700	[105, 106]
	single crystal	84%T'-16%T	84% P4 ₂ /mmc 16% Immm	9.064	9.064	15.039	2.2	873	[107]

also on the pressure-temperature path. If the temperature is applied before the pressure (T-P path) the rotational freedom is increased and, thus, the subsequent application of pressure allows the C₆₀ molecules to shorten intermolecular distances. Hence, the reorientation of molecules from one layer to another is allowed, which in turn allows the layers to be rotated, forming the T' phase. On the other hand, if the pressure is applied first (P-T path) the molecular rotation is blocked and subsequent heating is not enough to allow molecular rotation, thus the T phase is obtained.

In the rhombohedral structure, the polymerization occurs in a given (111) fcc plane, resulting in triangular polymerized layers that interact with each other via van der Waals forces. Figures 1.14(a) and 1.14(b) show possible polymerized layers in which molecules are differently oriented.

There are various proposed ways to explain how the polymerized layers organize themselves in the crystal. The ABC stacking can be performed with the polymerized layers having the same orientation in the crystal, shown in figure 1.14(a), and with molecules of adjacent layers facing each other through pentagons, as seen in figure 1.14(c). Another possibility is to consider differently oriented polymerized layers, figure 1.14(b), rotated 60° around the three-fold molecular axis from the previous orientation. The molecules of adjacent layers are now facing each other through hexagons while before they were facing through their pentagons. Based on their samples, Nuñez-Regueiro et al. [10] have considered a random mixture of the two orientations (figure 1.14(e)), while Davydov et al. [103] has considered an ordered structure having only the second orientation.

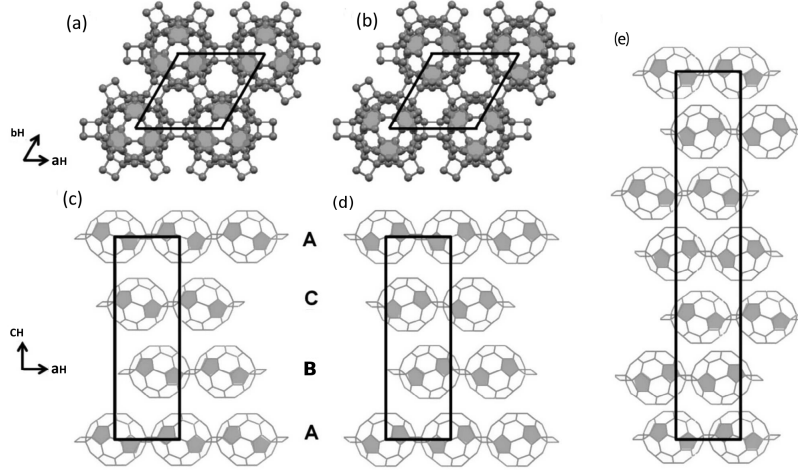


Figure 1.14: (a) Rhombohedral C₆₀ phase polymerized layer. (b) The polymerized layer having molecules in other orientation. (c) ABC stacking of (a) oriented layers. (d) ABC stacking of (b) oriented layers. (e) Combined stacking model. Figure adapted from [16].

Table 1.3: Crystallographic data of 2D rhombohedral phase. T-tetragonal phase and R-rhombohedral phase.

Report on	Phase	space group	$a(\text{\AA})$	$c(\text{\AA})$	$P(\text{GPa})$	$T(\text{K})$	Refs.
Powder	R	R $\bar{3}m$	9.22	24.6	5 – 7.5	773 – 1073	[108, 109]
Powder	18%T-82%R	R $\bar{3}m$	9.19	24.5	4 – 5	873 – 973	[10, 110]
single crystal	75%T-25%R	R $\bar{3}m$	9.19	24.5	2.2	700	[105, 106]
Powder	R	R $\bar{3}m$	9.175	24.568	6	873	[111, 112]
single crystal	R	R $\bar{3}m$	9.175	24.568	5	773	[65, 113]

1.2.4.3 3D polymerized phases

As referred previously, 3D C₆₀ polymers are synthesized above 8 GPa. In 1995, Blank et al. [109, 114] reported the first 3D C₆₀ polymers. They also reported possible symmetries for the structures, although they were not able to solve the crystal structures. Marques et al. [25] also reported 3D polymerized C₆₀ phases but the low-resolution of the x-ray precluded, once again, the structure determination. Based on the 2D tetragonal structure, Okada and coworkers [115] constructed a theoretical model of a 3D C₆₀ polymer and used DFT to study it. In 2000, Serebryanaya and Chernozatonskii [116] reported a joint work, combining experimental data and computer simulations (molecular mechanics), and proposed a structural model for a 3D C₆₀ polymer. In this model, the molecules lose some of their intramolecular double bonds in order to create a new intermolecular bond. This structural model is highly questionable, as we have computed the energy's second-order derivative, after structural relaxation, and got negative phonon frequencies, which shows the invalidity of the model and, therefore, this proposal will not be taken into consideration. Our calculation will be described in one of our articles A5.

Motivated by previous works [25, 115, 116], Burgos et al. [23] performed combined force field and DFT structural studies of 3D polymerized phases proposing three theoretical structural models, based on body-centered cubic packing of molecules, instead of the experimentally observed fcc packing. In 2006, Yamanaka et al. [19] proposed the 3D cuboidal phase, which is obtained from a topochemical compression of the 2D tetragonal phase. Later, in 2008, another 3D polymerized structure was proposed by the same group [18]. We have also contributed

here with the unveiling of a new 3D C_{60} phase structure which is discussed in three of our papers A1 to A3.

The 3D cuboidal phase proposed by Yamanaka et al. [19] was synthesized by compressing the 2D tetragonal phase at 15 GPa and 873 K. The experimental lattice parameters are $a = 7.86 \text{ \AA}$, $b = 8.59 \text{ \AA}$ and $c = 12.73 \text{ \AA}$. The structure has an Immm space group, where the C_{60} molecules are deformed into a cuboidal shape. Each molecule is connected to eight neighboring molecules, in adjacent (a,b) planes, through 6/6 3+3 cycloaddition forming a body-centered cell as shown in figure 1.15. Additional 66/66 4+4 cycloaddition bonds are formed along the lattice direction a .

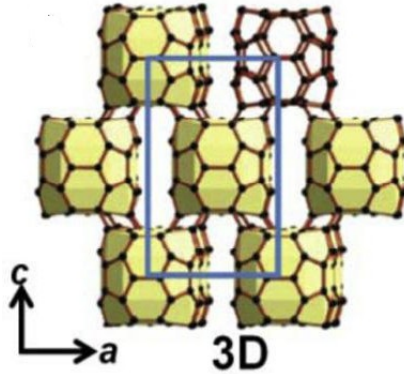


Figure 1.15: 3D cuboidal polymerized C_{60} structure. Figure adapted from [19].

Compared to the precursor 2D tetragonal structure, the a cell parameter strongly decreases, from 9.1 \AA to around 7.86 \AA . Along the b parameter this decrease is also substantial, from 9.1 \AA to 8.59 \AA . The previous 66/66 2+2 cycloaddition bonds were broken in (a,b) plane and the distance between these previously bonded atoms is increased to 2.47 \AA , since they are pushed inside the C_{60} cage.

DFT studies yielded optimized lattice parameters different from the experimental ones, $a = 8.581 \text{ \AA}$, $b = 8.510 \text{ \AA}$ and $c = 13.132 \text{ \AA}$ [71], although the overall molecular deformation and space group are kept. Yang et al. [71] also modeled other two structures, based on the initially proposed structure, but these models also failed to describe the experimental data. The important difference between experimental [19] and DFT optimized [71] lattice parameters propelled new computational studies [80, 101]. Zipoli and Bernasconi [101] studied three new variants of the original 3D cuboidal structure, through DFT calculations. These structures kept the 6/6 3+3 cycloaddition bonds between molecules belonging to different (a,b) planes and added in-plane double 66/66 4+4 cycloaddition or 66/66 2+2 cycloaddition bonds. All their attempts fail to correctly describe the experimentally observed lattice parameters. Finally, Yamagami and Saito [80] using tight-binding molecular dynamics found a 3D polymerized structure at 20 GPa with lattice parameters close to those of the 3D cuboidal phase. This structure is similar to the 3D cuboidal structure although it contains in-plane bonds. There is a considerable difference between DFT and tight-binding molecular dynamics accuracies, thus the latter method can be used as a first approach in the research of novel C_{60} polymerized phases but once an interesting crystal structure is found, DFT calculations must be carried out to ensure their correctness.

Another 3D polymer produced at 15 GPa and 773-873 K was reported by Yamanaka et al. [18]. Once again, low-resolution x-ray diffraction patterns hampered the full determination of its crystal structure, making computational methods necessary for clarifying it. Although the experimental diffraction pattern was indexed in fcc lattice, the structure proposed by Yamanaka

et al., shown in figure 1.16, belongs to the space group $R\bar{3}$. In this structure, the molecules form triangular polymerized layers involving 5/5 3+3 cycloadditions between pentagons of neighboring molecules. Adjacent layers are bonded via 56/65 2+2 cycloadditions, also shown in figure 1.16. The experimental lattice parameters are $a = 8.44 \text{ \AA}$ and $c = 20.67 \text{ \AA}$, and the computational ones $a = 8.46 \text{ \AA}$ and $c = 21.39 \text{ \AA}$. Although the a lattice parameters are close to each other, the c parameters have a difference of 0.7 \AA . Furthermore, we have performed DFT relaxations in this polymerized structure with our results yielding quite different lattice parameters, as described in our paper A8.

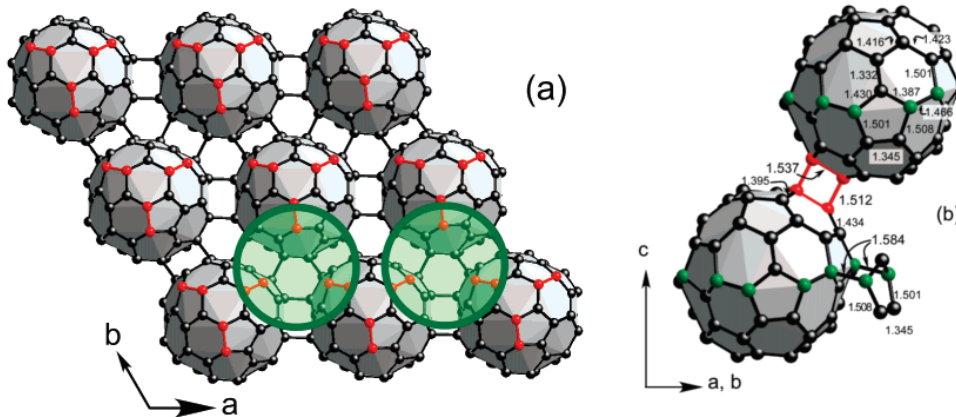


Figure 1.16: 3D polymerized structure with the $R\bar{3}$ symmetry reported by Yamanaka et al. (a) (a,b) polymerized plane with C_{60} molecules bonded via 5/5 3+3 cycloaddition between pentagons. Red atoms are involved in 56/65 2+2 cycloadditions that bond to neighboring molecules belonging to adjacent (a,b) polymerized planes. (b) Bonding schemes. Figure adapted from [18].

1.2.5 Properties of C_{60} polymerized phases

The C_{60} molecule was predicted to have a very high bulk modulus, which suggested that polymerized C_{60} crystals could be less compressible than diamond [117]. Indeed, the creation of intermolecular covalent bonds increases the bulk modulus of C_{60} samples [23, 27, 69–71, 101, 115, 118–121]. The low-dimensional 1D and 2D polymers had their bulk modulus determined through x-ray diffraction studies. Their values, ranging from 20 GPa to 40 GPa [118–120], are larger than that of the van der Waals monomeric phase, but lower than those of the 3D polymers [23, 27, 38, 41, 69–71, 101, 115, 121]. Amorphous phases obtained from HPHT compression and displaying bulk moduli higher than diamond, have been reported by Blank et al. [69] and also recently by another group [38]. The former results are involved in controversy since for similar pressures and temperatures, Brazkhin et al. [70] reported bulk modulus lower than diamond, while the samples of Zhang et al. [38] have been obtained at higher pressures. This low compressibility is accompanied by low density, the reported densities being below 3.3 g/cm^3 , which is lower than the density of diamond, 3.5 g/cm^3 .

At room conditions, fullerite C_{60} is known to be a semiconductor. The electronic bandgap of C_{60} decreases upon polymerization [67, 68, 113, 122, 123]. Furthermore, in 3D C_{60} polymers metallic behavior is observed [19, 71, 80, 101, 115, 124]. However, it is expected that the semiconducting behavior reappears in 3D C_{60} polymers with high sp^3 -hybridized carbons content, since the full- sp^3 carbon structures are known to be semiconducting or even insulating. The evolution of the bandgap with the content of sp^3 carbons in C_{60} polymers is explored in detail in articles A7 and A8.

1.2.5.1 Electronic structure of polymerized C_{60} phases

Tight-binding studies on the low-dimensional structures [122] indicated that the electronic gap would decrease with the increase of the number of covalent bonds. In this study, the calculation of electronic bandgap was performed for a molecule, a linear polymerized chain and the 2D tetragonal and rhombohedral structures. As mentioned above, the C_{60} molecule has the higher bandgap, while the 2D rhombohedral structure has the lower.

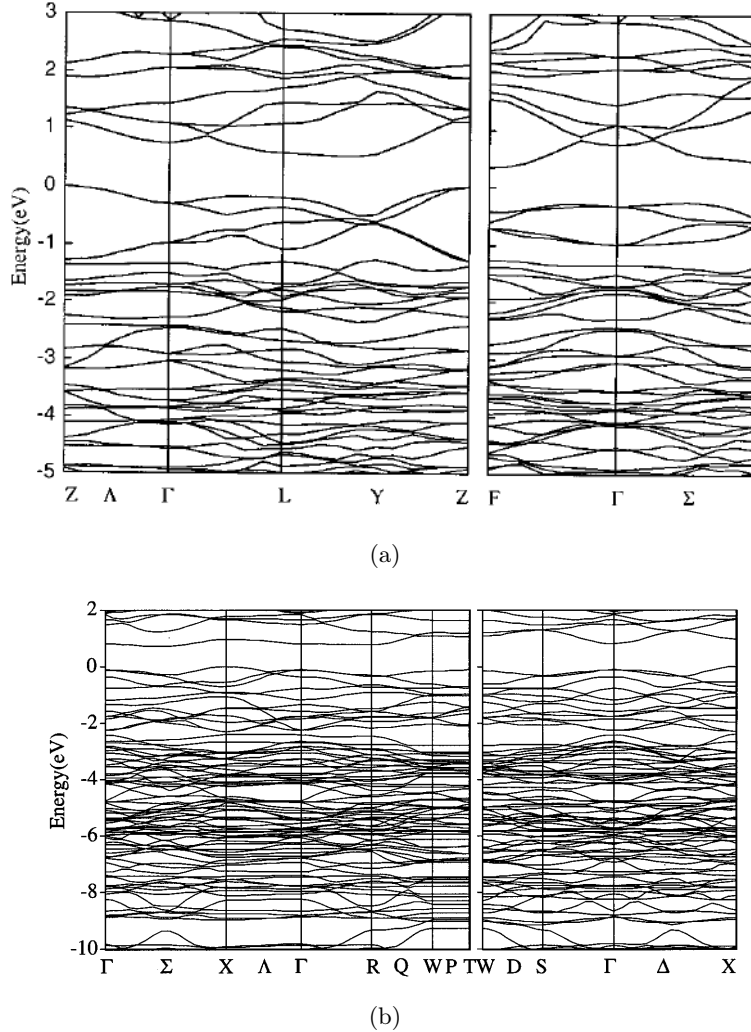


Figure 1.17: Electronic band structures of low-dimensional polymers calculated using DFT within LDA. (a) 2D rhombohedral structure. (b) 2D tetragonal structure. Figures from [67, 68].

Saito and coworkers [67, 68, 113, 123] calculated the electronic band structures, shown in figure 1.17, and density of states (DOS), using DFT within the local density approximation (LDA). These calculations confirmed the tight-binding results. As can be seen in figure 1.17(a), the 2D rhombohedral structure has an indirect bandgap of 0.35 eV, between the bottom of the conduction band, at the F point, and the top of the valence band at the Z point [67]. Figure 1.17(b) shows that 2D tetragonal structure C_{60} is also an indirect bandgap semiconductor, with a bandgap of 0.72 eV found between the top of the valence band at the X point, and the bottom of the conduction band at the Σ point. Both these values are smaller than the one computed for the fullerite monomer, 1.06 eV [68]. Both the 2D polymerized phases show

dispersion along the Λ line, indicating that these systems have a 3D electronic character. Although in the mentioned studies the bandgap is not reported for the 1D orthorhombic structure, Saito et al. [123] mention that it is higher than for the 2D tetragonal structure and lower than for the fullerite monomer. They also mention that the bandgap of this 1D structure is strongly dependent on the relative orientation of the C_{60} chains. It must be mentioned that DFT calculations using LDA or general gradient approximation (GGA) exchange-correlation functionals usually underestimate electronic bandgaps [68, 125]. Therefore, the real bandgap values for these systems would be larger than the reported values but the trend observed between the different polymerized phases should be obeyed.

Increasing the polymerization degree in the polymerized C_{60} samples induces metallic behavior. Experiments confirmed this in the electronically-conductive 3D cuboidal polymer [19], also confirmed by DFT calculations [19, 71, 101]. In opposite, the 3D rhombohedral phase [18] displays experimental semiconductive behavior and the DFT-LDA calculation of the electronic bandgap gives 0.5 eV, larger than the gap found for the 2D rhombohedral phase. In this structure, each molecule is highly bonded to its twelve nearest neighbors, thus, there should be a threshold of the degree of polymerization, above which the polymers will no longer display metallic behavior. Nevertheless, this bandgap reopening should also be dependent on the unit cell volume, since a smaller volume will allow more interaction of π orbitals that drive metallic behavior. Sato and coworkers [124] made some high-energy-resolution electron energy-loss spectroscopy measurements in both the 3D cuboidal and the 3D rhombohedral phases, confirming the previous results: the 3D cuboidal phase is metallic while the 3D rhombohedral phase is a semiconductor. Zipoli et al. [101] pointed out the importance of spin-polarized DFT calculations, since several of the 3D polymerized structures studied by them developed antiferromagnetic ground states. In some cases, the appearance of an antiferromagnetic ground state is accompanied by the opening of the electronic gap. The observation of magnetic effects is surprising since the 3D polymerized C_{60} structures are pure-carbon systems.

1.2.5.2 Bulk moduli of polymerized C_{60} phases

X-ray diffraction patterns of the 1D and 2D polymerized C_{60} phases were recorded at different pressures, providing the dependence of lattice volumes on pressure. This dependence was then fitted with the Birch-Murnaghan equation of state (EOS) [126] and the experimental bulk modulus determined [118–120]. Table 1.4 reports the bulk moduli for the polymerized C_{60} phases with defined structures and it is to be noticed that the trend (bulk modulus increase with increasing polymerization degree) does not hold for the 2D rhombohedral phase. We should, nevertheless, look carefully at these results since the bulk modulus derivative is considered to be the same in all the 2D polymers ($B'_0 = 10.6$), being determined for the fcc monomer and assumed to be typical of van der Waals solids [119, 120]. In addition, the 2D tetragonal phase obtained by Kawasaki et al. [120] contained a small amount of 2D rhombohedral phase.

As expected, all of the reported bulk moduli for 3D polymers are higher than the reported values for the 2D polymers. The 3D cuboidal polymerized phase had its bulk modulus calculated using DFT by two different groups [71, 101]. Both groups reported a bulk modulus around 150 GPa (see table 1.4), which is well above the reported value for the low-dimensional polymerized phases, as one would expect for a 3D polymer. As a general trend, the rise in the number of polymeric bonds and, concomitantly, in the number of sp^3 carbons, increases, as expected, the bulk moduli displayed by C_{60} polymers. Other factors should also play a significant role in the elastic properties exhibited by the polymers, such as the type of polymeric bond involved. In the article of section 9.1 we have extended these results.

Table 1.4: Bulk moduli of polymerized C_{60} phases with known structure.

	Structure	B_0 (GPa)	B_0'	Refs.
Experiment	room conditions fcc	14.4	10.6	[119]
	1D orthorhombic	22	13	[118]
	2D tetragonal	34.8	10.6	[119]
	2D tetragonal	29.9	10.6	[120]
	2D rhombohedral	28.1	10.6	[120]
Theory	cuboidal phase	152	-	[71]
	cuboidal phase	156	-	[101]

1.3 Thesis outline and objectives

Our main objective in this work was to assign crystalline structures obtained from computational studies to 3D C_{60} polymers synthesized under HPHT treatments of the molecule. This task is extremely difficult because, as explained in the first article presented here (chapter 3), samples recovered from HPHT treatments display the x-ray diffraction patterns with low-resolution, even when synchrotron radiation is employed, rendering impossible the structure determination by traditional crystallographic methods. Nevertheless, some information, like the overall symmetry and lattice parameters, can be extracted from the patterns. Thus, one has some starting parameters to build structural models, which were subsequently relaxed using DFT techniques, in order to evaluate if the constructed model is energetically stable, and if it can explain the experimental phase. After finding interesting polymerized structures, we move towards other objectives, namely the understanding of their properties. With this regard, we have computed properties for all relevant structures using DFT or DFT-based methods. For example, we calculated elastic properties, electronic structures, phonon dispersion curves, Raman and infrared spectra, and superconducting critical temperatures.

Through this thesis, several DFT packages have been used, namely Vienna Ab initio Simulation Package (VASP), QUANTUM ESPRESSO (QE), CRYSTAL17 and Gaussian09. Each of these software packages, and their different approaches to DFT, have their advantages and weaknesses. Thus, a small chapter dedicated to DFT, its different formulations (plane waves or linear combination of atomic orbitals), as well as, some post-DFT methods, such as density functional perturbation theory (DFPT) are given. Hence, chapter 2 aims to give a short, yet comprehensive, insight into these, and related, topics without diving in too much detail. If the reader wishes to get a deeper knowledge of these subjects, we point him some references from the already extensive literature on the subject [127–131]. In particular, we recommend the book from R. Martin [127].

From chapters 3 to 9 we present our papers, one per chapter, excepting chapter 9 where we present two papers, since they involve the same subject: the electronic bandgaps of the polymerized C_{60} structures, though tackled from different approaches. Then, in chapter 10 we present some concluding remarks and future steps to be taken. We labeled the articles from A1 to A8 in order of appearance in this thesis. The author of this thesis has also contributed to another work, as coauthor, which is outside of the scope of this thesis, since it involves studies on encapsulated nanoribbons inside nanotubes, and, thus, is not presented in this work.

Chapters 3 to 9 include a set of articles, from which we will give a short description in the following:

Article A1 “Bonding frustration in the 9.5 GPa fcc polymeric C_{60} ”, is included in the third chapter. Here we proposed a model to describe an experimental phase of 3D polymerized C_{60} obtained under 9.5 GPa and 550 °C. From the x-ray diffraction pattern, we could only extract

the fcc symmetry and lattice parameters of 12.79 Å at 9.5 GPa and 13.19 Å at room conditions. As the experimental phase has fcc symmetry, we start building models with fullerene molecules in either one of the two standard orientations compatible with this symmetry. We discovered that no polymeric bond would be formed between neighboring molecules having the same standard orientation, (even if in the initial model the atoms from neighboring molecules were pulled out in such a way that they would be in covalent bonding distance) but, when the two molecules have different standard orientations, a 56/56 2+2 cycloaddition polymeric bond would form (in the paper this bond is erroneously named 56/65 2+2 cycloaddition with the notation being corrected in subsequent publications). Thus, we could map the bond formation (or no bond formation) to an "antiferro" interaction (or "ferro" interaction) and conclude that the fcc polymer has a frustrated structure, similar to fcc Ising antiferromagnet with nearest-neighbor interactions.

In paper A2 “Three-dimensional C₆₀ polymers with ordered binary-alloy-type structures”, we extended our number of structural models, constructing two new models based on the binary-alloy fcc type structures and the 56/56 2+2 cycloaddition polymeric bonds. The two new models corroborated the previous article. We also computed all their electronic structures, finding out that metallic behavior is exhibited by these 3D polymerized structures. Later, in article A8, we will see that for one of the structures this is not entirely true and when we compute the electronic structure with a hybrid functional, the Heyd-Scuseria-Ernzerhof (HSE), the bandgap opens, making it effectively a short bandgap semiconductor.

Article A3, “Three-dimensional fcc C₆₀ polymer”, is the last paper entirely about the frustrated fcc polymerized C₆₀ phase and the models that we have used to describe it. Here we have computed the bulk moduli of the four structures presented in the last two papers. We have also found that they agree with an estimation of the experimental bulk modulus, concluding that indeed the bonding type should be correct and that the bulk modulus rises with the number of intermolecular bonds. We have also extended the hypothesis of existing a linear relationship between the number of 2+2 cycloaddition bonds and the lattice volume per molecule, reaching the conclusion that, in the experimental fcc polymer, each molecule is bonded to 7.6 nm, in agreement with the eight "antiferro" interactions in the ground state configurations of the frustrated fcc Ising antiferromagnet.

In an attempt to find new bonding schemes that could improve the models constructed to elucidate 3D C₆₀ polymers, we started studying possible bonding schemes in fullerene dimers. This study is particularly relevant because, for the low-dimensional polymers, the distance between the molecules in a crystal is similar to the bonding distance found in a dimer having the same bonding scheme. This path is explored in article A4 “C₆₀+C₆₀ molecular bonding revisited and expanded”. We have used AutoMeKin (AMK) [132–134] to perform an automatic search for dimers. AMK is a quantum chemistry tool designed to find reaction paths, the fullerene dimers being the biggest systems studied with it. Forty-one stable bonding configurations were found, with thirty of them being completely new in the literature. We have also commented on the possibility of some new bonding schemes being present in the already published experimental phases.

Having these new bonding schemes, we have tried to construct new structures. From all the models that we built, we have noticed a particular model, which has an amazing crystal structure. This structure is presented in the paper A5 “Clathrate structure of polymerized fullerite C₆₀”. To the best of our knowledge, it is the first C₆₀ polymer that is composed of a continuum of polyhedral cages forming a clathrate, these cages are the C₆₀ icosahedral cage itself and a C₂₄ sodalite-type cage. To construct such a model a new bonding scheme is used, the double 5/5 2+3 cycloaddition, which was also found using AMK, described in article A4. As a consequence of all the nn being bonded through this bonding scheme in the fcc lattice,

new C_{60} cages are generated at the octahedral interstitial sites that are exactly equal to the original C_{60} cages located at the fcc lattice points. Also, in the tetrahedral interstitial sites, the C_{24} sodalite-type cages are formed. Because, upon transformation, the octahedral sites turn out to be symmetrically equivalent to the lattice points, the clathrate lattice is sc and the full structure is described with only thirty atoms in the unit cell (half of a C_{60} molecule). In this work, we also compute the elastic properties, electronic structure, phonon spectra and Raman and infrared spectra. These last two spectra and the x-ray diffraction patterns are compared with those simulated for structures corresponding to experimental phases. The comparison was also done for the bulk modulus where experimental data is available. The results indicate that some experimental polymerized phases could consist of carbon clathrates related to the one described. We have also compared the enthalpy of this structure with other structures.

Regarding its electronic structure, the clathrate structure of C_{60} is a short bandgap semiconductor with three nearly-flat bands located at around 0.7 eV above the Fermi level, which originates a strong peak in the electronic DOS. Thus, doping this clathrate structure with three electrons could move the Fermi level to the DOS peak, driving metallicity and possible superconductivity. This is the path explored in article A6 "Superconductivity in the doped polymerized fullerite clathrate from first principles", where the doping of the clathrate structure with various monovalent, divalent, and trivalent atoms, have been explored, through the calculation of their electronic band structure and phonon dispersion curves have been computed. We have also computed the superconducting critical temperatures for the four stable doped structures, however, they have quite low critical temperatures, barely reaching 2 K.

In chapter 9 we present two articles, both of which dealing with the evolution of the bandgap with the number of sp^3 carbons in polymerized C_{60} structures. Article A7 " C_{60} structures: Structural, electronic and elastic properties", compares the electronic bandgaps and the bulk moduli of several C_{60} polymers possessing different content of sp^3 carbon. This paper shows evidence that the bulk modulus increases with the number of sp^3 carbons while the electronic bandgap decreases. This work was performed in the early stages of our research and thus does not represent the full picture of the electronic bandgap evolution with the number of sp^3 carbons. Hence, we have performed a new study presented in article A8 "Reentrant semiconducting behavior in polymerized fullerites with increasing sp^3 content", where we found a reentrant semiconducting behavior in the C_{60} polymerized structures with the growing number of sp^3 carbons. In this article we have increased the level of theory used, resulting in more accurate bandgaps.

In the last chapter, we present some concluding remarks and future work.

1.3.1 List of individual contributions

The statutes of the University of Aveiro, regarding the format of Ph.D. thesis, require that the author must discriminate his contribution to each of the articles presented here. Apart from experimental work, presented in the first article, the author of this thesis has participated in all the stages of their preparation, except supervision, and it would be redundant to describe it for each paper. His crucial role in the work described in these articles is illustrated by the fact that he is the first author in all of them. This does not mean that the contribution of the other authors were not important for the development of the papers integrating this thesis, elevating their quality and helping the author to overcome many problems. For instance, the main supervisor of this thesis was instrumental in the writing process of most articles, improving them considerably after the first draft written by the author.

Bibliography

- [1] H. Suess and H. Urey. Abundances of the elements. *Reviews of Modern Physics*, 28(1): 53–74, 1956. doi: 10.1103/RevModPhys.28.53.
- [2] R. Lagow, J. Kampa, H.-C. Wei, S. Battle, J. Genge, D. Laude, C. Harper, R. Bau, R. Stevens, J. Haw, and E. Munson. Synthesis of linear acetylenic carbon: The "sp" carbon allotrope. *Science*, 267(5196):362–367, 1995. doi: 10.1126/science.267.5196.362.
- [3] D. Strout, R. Murry, C. Xu, W. Eckhoff, G. Odom, and G. Scuseria. A theoretical study of buckminsterfullerene reaction products: $C_{60}+C_{60}$. *Chemical Physics Letters*, 214(6): 576–582, 1993. doi: 10.1016/0009-2614(93)85686-I.
- [4] Z. Li, M. Hu, M. Ma, Y. Gao, B. Xu, J. He, D. Yu, Y. Tian, and Z. Zhao. Superhard super-strong carbon clathrate. *Carbon*, 105:151–155, 2016. doi: 10.1016/j.carbon.2016.04.038.
- [5] X. Blase, Philippe Gillet, A. San Miguel, and P. Mélinon. Exceptional ideal strength of carbon clathrates. *Physical Review Letters*, 92(21):215505, 2004. doi: 10.1103/PhysRevLett.92.215505.
- [6] D. Connétable. First-principles calculations of carbon clathrates: Comparison to silicon and germanium clathrates. *Physical Review B*, 82(7):075209, 2010. doi: 10.1103/PhysRevB.82.075209.
- [7] D. Machon, V. Pischedda, S. Le Floch, and A. San-Miguel. Perspective: High pressure transformations in nanomaterials and opportunities in material design. *Journal of Applied Physics*, 124(16):160902, 2018. doi: 10.1063/1.5045563.
- [8] C. Pei and L. Wang. Recent progress on high-pressure and high-temperature studies of fullerenes and related materials. *Matter Radiat. at Extremes*, 4(2):028201, 2019. doi: 10.1063/1.5086310.
- [9] B. Sundqvist. Carbon under pressure. *Physics Reports*, 909:1–73, 2021. doi: 10.1016/j.physrep.2020.12.007.
- [10] M. Núñez–Regueiro, L. Marques, J.-L. Hodeau, O. Béthoux, and M. Perroux. Polymerized fullerite structures. *Physical Review Letters*, 74(2):278–281, 1995. doi: 10.1103/PhysRevLett.74.278.
- [11] K. Novoselov, A. Geim, S. Morozov, D. Jiang, Y. Zhang, S. Dubonos, I. Grigorieva, and A. Firsov. Electric field effect in atomically thin carbon films. *Science*, 306(5696): 666–669, 2004. doi: 10.1126/science.1102896.
- [12] X. Hou, L. and Cui, B. Guan, S. Wang, R. Li, Y. Liu, D. Zhu, and J. Zheng. Synthesis of a monolayer fullerene network. *Nature*, 606(7914):507, 2022. doi: 10.1038/s41586-022-04771-5.
- [13] T. Strobel, L. Zhu, P. Guńka, G. M. Borstad, and M. Guerette. A lanthanum-filled carbon–boron clathrate. *Angewandte Chemie International Edition*, 60(6):2877–2881, 2020. doi: 10.1002/anie.202012821.
- [14] H.-T. Huang, L. Zhu, M. Ward, T. Wang, B. Chen, B. Chaloux, Q. Wang, A. Biswas, J. Gray, B. Kuei, G. Cody, A. Epshteyn, V. Crespi, J. Badding, and T. Strobel. Nanoarchitecture through strained molecules: Cubane-derived scaffolds and the smallest carbon

- nanotherads. *Journal of the American Chemical Society*, 142(42):17944–17955, 2020. doi: 10.1021/jacs.9b12352.
- [15] Y. Zhang, M. Yao, M. Du, Z. Yao, Y. Wang, J. Dong, Z. Yang, B. Sundqvist, É. Kováts, S. Pekker, and B. Liu. Negative volume compressibility in sc3n@c80 -cubane cocrystal with charge transfer. *Journal of the American Chemical Society*, 142(16):7584–7590, 2020. doi: 10.1021/jacs.0c01703.
- [16] M. Álvarez–Murga and J.-L. Hodeau. Structural phase transitions of C_{60} under high-pressure and high-temperature. *Carbon*, 82:381–407, 2015. doi: <http://dx.doi.org/10.1016/j.carbon.2014.10.083>.
- [17] S. Yamanaka. Silicon clathrates and carbon analogs: high pressure synthesis, structure, and superconductivity. *Dalton Transactions*, 39(8):1901–1915, 2010. doi: 10.1039/B918480E.
- [18] S. Yamanaka, N. S. Kini, A. Kubo, S. Jida, and H. Kuramoto. Topochemical 3D polymerization of C_{60} under high pressure at elevated temperatures. *Journal of the American Chemical Society*, 130:4303–4309, 2008. doi: 10.1021/ja076761k.
- [19] S. Yamanaka, A. Kubo, K. Inumaru, K. Komaguchi, N. Kini, T. Inoue, and T. Irifune. Electron conductive three-dimensional polymer of cuboidal C_{60} . *Physical Review Letters*, 96(7):076602, 2006. doi: 10.1103/PhysRevLett.96.076602.
- [20] L. Chernozatonskii, N. Serebryanaya, and B. Mavrin. The superhard crystalline three-dimensional polymerized C_{60} phase. *Chemical Physics Letters*, 316(3):199–204, 2000. doi: 10.1016/S0009-2614(99)01288-9.
- [21] Y. Sato, M. Terauchi, and S. Yamanaka. Electronic structures of three-dimensional C_{60} polymers studied by high-energy-resolution electron energy-loss spectroscopy based on transmission electron microscopy. *Chemical Physics Letters*, 626:90–95, 2015. doi: 10.1016/j.cplett.2015.03.017.
- [22] S. Berber, E. Osawa, and D. Tománek. Rigid crystalline phases of polymerized fullerenes. *Physical Review B*, 70(8):085417, 2004. doi: 10.1103/PhysRevB.70.085417.
- [23] E. Burgos, E. Halac, R. Weht, H. Bonadeo, E. Artacho, and P. Ordejón. New superhard phases for three-dimensional C_{60} -based fullerites. *Physical Review Letters*, 85(11):2328–2331, 2000. doi: 10.1103/PhysRevLett.85.2328.
- [24] V. Brazhkin, A. Lyapin, S. Popova, R. Voloshin, Y. Antonov, S. Lyapin, Y. Kluev, A. Naletov, and N. Mel'nik. Metastable crystalline and amorphous carbon phases obtained from fullerite c_{60} by high-pressure-high-temperature treatment. *Physical Review B*, 56(18):11465–11471, 1997. doi: 10.1103/PhysRevB.56.11465.
- [25] L. Marques, M. Mezouar, J.-L. Hodeau, M. Núñez-Regueiro, N. Serebryanaya, V. Ivdenko, V. Blank, and G. Dubitsky. "debye-scherrer ellipses" from 3D fullerene polymers: An anisotropic pressure memory signature. *Science*, 283(5408):1720–1723, 1999. doi: 10.1126/science.283.5408.1720.
- [26] A. Lyapin, Y. Katayama, and V. Brazhkin. Order versus disorder: In situ high-pressure structural study of highly polymerized three-dimensional C_{60} fullerite. *Journal of Applied Physics*, 126(6):065102, 2019. doi: 10.1063/1.5111370.

- [27] M. Mezouar, L. Marques, J.-L. Hodeau, V. Pischedda, and M. Núñez-Regueiro. Equation of state of an anisotropic three-dimensional C₆₀ polymer: The most stable form of fullerene. *Physical Review B*, 68(19):193414, 2003. doi: 10.1103/PhysRevB.68.193414.
- [28] Y. Zhao, C. Qian, V. Gladkikh, and F. Ding. Simulated pressure-temperature carbon structure map obtained through uniaxial compression of bulk C₆₀. *Carbon*, 202:554–560, 2023. doi: 10.1016/j.carbon.2022.11.007.
- [29] D. Connétable, V. Timoshevskii, B. Masenelli, J. Beille, J. Marcus, B. Barbara, A. Saitta, G.-M. Rignanese, P. Mélinon, S. Yamanaka, and X. Blase. Superconductivity in doped *sp*³ semiconductors: The case of the clathrates. *Physical Review Letters*, 91(24):247001, 2003. doi: 10.1103/PhysRevLett.91.247001.
- [30] J. Wang, H. Weng, S. Nie, Z. Fang, Y. Kawazoe, and C. Chen. Body-centered orthorhombic c₁₆: A novel topological node-line semimetal. *Physical Review Letters*, 116(19):195501, 2016. doi: 10.1103/PhysRevLett.116.195501.
- [31] J. Wang, S. Nie, H. Weng, Y. Kawazoe, and C. Chen. Topological nodal-net semimetal in a graphene network structure. *Physical Review Letters*, 120(2):026402, 2018. doi: 10.1103/PhysRevLett.120.026402.
- [32] A. Oganov and C. Glass. Crystal structure prediction using ab initio evolutionary techniques: Principles and applications. *The Journal of Chemical Physics*, 124:244704, 2006. doi: 10.1063/1.2210932.
- [33] M. Martinez-Canales, C. Pickard, and R. Needs. Thermodynamically stable phases of carbon at multiterapascal pressures. *Physical Review Letters*, 108(4):045704, 2012. doi: 10.1103/PhysRevLett.108.045704.
- [34] C. Pickard and R. Needs. Hypothetical low-energy chiral framework structure of group 14 elements. *Physical Review B*, 81(1):014106, 2010. doi: 10.1103/PhysRevB.81.014106.
- [35] Z. Wang, X.-F. Zhou, X. Zhang, Q. Zhu, H. Dong, M. Zhao, and A. Oganov. Phagraphene: A low-energy graphene allotrope composed of 5–6–7 carbon rings with distorted dirac cones. *Nano Letters*, 15(9):6182–6186, 2015. doi: 10.1021/acs.nanolett.5b02512.
- [36] Q. Li, Y. Ma, A. Oganov, H. Wang, H. Wang, Y. Xu, T. Cui, H.-K. Mao, and G. Zou. Superhard monoclinic polymorph of carbon. *Physical Review Letters*, 102(17):175506, 2009. doi: 10.1103/PhysRevLett.102.175506.
- [37] K. Umemoto, R. Wentzcovitch, S. Saito, and T. Miyake. Body-centered tetragonal c₄: A viable *sp*³ carbon allotrope. *Physical Review Letters*, 104(12):125504, 2010. doi: 10.1103/PhysRevLett.104.125504.
- [38] S. Zhang, Z. Li, K. Luo, J.g He, Y. Gao, A. V. Soldatov, V. Benavides, K. Shi, A. Nie, B. Zhang, W. Hu, M. Ma, Y. Liu, B. Wen, G. Gao, B. Liu, Y. Zhang, D. Yu, X.-F. Zhou, Z. Zhao, B. Xu, L. Su, G. Yang, O. Chernogorova, and Y. Tian. Discovery of carbon-based strongest and hardest amorphous material. *National Science Review*, 9(1), 2021. doi: 10.1093/nsr/nwab140.
- [39] Y. Shang, Z. Liu, J. Dong, M. Yao, Z. Yang, Q. Li, C. Zhai, F. Shen, X. Hou, L. Wang, N. Zhang, W. Zhang, R. Fu, J. Ji, X. Zhang, H. Lin, Y. Fei, B. Sundqvist, W. Wang, and B. Liu. Ultrahard bulk amorphous carbon from collapsed fullerene. *Nature*, 599(7886):599–604, 2021. doi: 10.1038/s41586-021-03882-9.

- [40] H. Tang, X. Yuan, Y. Cheng, H. Fei, F. Liu, T. Liang, Z. Zeng, T. Ishii, M.-S. Wang, T. Katsura, H. Sheng, and H. Gou. Synthesis of paracrystalline diamond. *Nature*, 599(7886):605–610, 2021. doi: 10.1038/s41586-021-04122-w.
- [41] S. Zhang, Y. Wu, K. Luo, B. Liu, Y. Shu, Y. Zhang, L. Sun, Y. Gao, M. Ma, Z. Li, B. Li, P. Ying, Z. Zhao, W. Hu, V. Benavides, O. Chernogorova, A. Soldatov, J. He, D. Yu, B. Xu, and Y. Tian. Narrow-gap, semiconducting, superhard amorphous carbon with high toughness, derived from C₆₀ fullerene. *Cell Reports Physical Science*, 2(9):100575, 2021. doi: 10.1016/j.xcrp.2021.100575.
- [42] Q. Wei, C. Zhao, M. Zhang, H. Yan, Y. Zhou, and R. Yao. A new superhard carbon allotrope: Orthorhombic c20. *Physics Letters A*, 382(25):1685–1689, 2018. doi: 10.1016/j.physleta.2018.04.024.
- [43] W. Mao, H. k. Mao, P. Eng, T. Trainor, M. Newville, C. c. Kao, D. Heinz, J. Shu, Y. Meng, and R. Hemley. Bonding changes in compressed superhard graphite. *Science*, 302(5644):425–427, 2003. doi: 10.1126/science.1089713.
- [44] A. Lyakhov and A. Oganov. Evolutionary search for superhard materials: Methodology and applications to forms of carbon and tio₂. *Physical Review B*, 84(9):092103, 2011. doi: 10.1103/PhysRevB.84.092103.
- [45] Q. Zhu, Q. Zeng, and A. Oganov. Systematic search for low-enthalpy sp³ carbon allotropes using evolutionary metadynamics. *Physical Review B*, 85(20):201407, 2012. doi: 10.1103/PhysRevB.85.201407.
- [46] Q. Huang, D. Yu, B. Xu, W. Hu, Y. Ma, Y. Wang, Z. Zhao, B. Wen, J. He, Z. Liu, and Y. Tian. Nanotwinned diamond with unprecedented hardness and stability. *Nature*, 510:250, 2014. doi: 10.1038/nature13381.
- [47] Y. Tian, B. Xu, D. Yu, Y. Ma, Y. Wang, Y. Jiang, W. Hu, C. Tang, Y. Gao, K. Luo, Z. Zhao, L. Wang, B. Wen, J. He, and Z. Liu. Ultrahard nanotwinned cubic boron nitride. *Nature*, 493:385–388, 2013. doi: 10.1038/nature11728.
- [48] X. Yang, M. Yao, X. Wu, Sh. Liu, S. Chen, K. Yang, R. Liu, T. Cui, B. Sundqvist, and B. Liu. Novel superhard sp³ carbon allotrope from cold-compressed c₇₀ peapods. *Physical Review Letters*, 118(24):245701, 2017. doi: 10.1103/PhysRevLett.118.245701.
- [49] S. Di Cataldo, S. Qulaghasi, G. Bachelet, and L. Boeri. High- T_c superconductivity in doped boron-carbon clathrates. *Physical Review B*, 105(6):064516, 2022. doi: 10.1103/PhysRevB.105.064516.
- [50] S. Lu, H. Liu, I. Naumov, S. Meng, Y. Li, J. Tse, B. Yang, and R. Hemley. Superconductivity in dense carbon-based materials. *Physical Review B*, 93(10):104509, 2016. doi: 10.1103/PhysRevB.93.104509.
- [51] Y. Takano, T. Takenouchi, S. Ishii, S. Ueda, T. Okutsu, I. Sakaguchi, H. Umezawa, H. Kawarada, and M. Tachiki. Superconducting properties of homoepitaxial cvd diamond. *Diamond and Related Materials*, 16(4):911–914, 2007. doi: 10.1016/j.diamond.2007.01.027.
- [52] T. Weller, M. Ellerby, S. Saxena, R. Smith, and N. Skipper. Superconductivity in the intercalated graphite compounds C₆Yb and C₆Ca. *Nature Physics*, 1(1):3, 2005. doi: 10.1038/nphys0010.

- [53] O. Gunnarsson. Superconductivity in fullerides. *Reviews of Modern Physics*, 69(2): 575–606, 1997. doi: 10.1103/RevModPhys.69.575.
- [54] T. Palstra, O. Zhou, Y. Iwasa, P. Sulewski, R. Fleming, and B. Zegarski. Superconductivity at 40k in cesium doped C_{60} . *Solid State Communications*, 93(4):327–330, 1995. doi: 10.1016/0038-1098(94)00787-X.
- [55] Y. Cao, V. Fatemi, S. Fang, K. Watanabe, T. Taniguchi, E. Kaxiras, and P. Jarillo-Herrero. Unconventional superconductivity in magic-angle graphene superlattices. *Nature*, 556(7699):43, 2018. doi: 10.1038/nature26160.
- [56] H. Yu, Y. Xue, and Y. Li. Graphdiyne and its assembly architectures: Synthesis, functionalization, and applications. *Advanced Materials*, 31(42):1803101, 2019. doi: 10.1002/adma.201803101.
- [57] M. Hu, Z. Zhao, F. Tian, A. Oganov, Q. Wang, M. Xiong, C. Fan, B. Wen, J. He, D. Yu, H.-T. Wang, B. Xu, and Y. Tian. Compressed carbon nanotubes: A family of new multifunctional carbon allotropes. *Scientific Reports*, 3(1):1331, 2013. doi: 10.1038/srep01331.
- [58] W. Krätschmer, L. Lamb, K. Fostiropoulos, and D. Huffman. Solid C_{60} : a new form of carbon. *Nature*, 347:354–358, 1990. doi: 10.1038/347354a0.
- [59] H. Kroto, J. Heath, S. O’Brien, R. Curl, and R. Smalley. C_{60} : Buckminsterfullerene. *Nature*, 318:162–163, 1985. doi: 10.1038/318162a0.
- [60] The nobel prize in chemistry 1996:the discovery of carbon atoms bound in the form of a ball is rewarded. 1996, . url: <https://www.nobelprize.org/prizes/chemistry/1996/press-release/>, Retrieved December 21, 2022.
- [61] A. Harris and R. Sachidanandam. Orientational ordering of icosahedra in solid C_{60} . *Physical Review B*, 46(8):4944–4957, 1992. doi: 10.1103/PhysRevB.46.4944.
- [62] P. Heiney. Structure, dynamics and ordering transition of solid C_{60} . *Journal of Physics and Chemistry of Solids*, 53:1333–1352, 1992. doi: [http://dx.doi.org/10.1016/0022-3697\(92\)90231-2](http://dx.doi.org/10.1016/0022-3697(92)90231-2).
- [63] Y. Iwasa, T. Arima, R. Fleming, T. Siegrist, O. Zhou, R. Haddon, L. Rothberg, K. Lyons, H. Carter, A. Hebard, R. Tycko, G. Dabbagh, J. Krajewski, G. Thomas, and T. Yagi. New phases of C_{60} synthesized at high pressure. *Science*, 264:1570–1572, 1994. doi: 10.1126/science.264.5165.1570.
- [64] V. Agafonov, V. Davydov, L. Kashevarova, A. Rakhmanina, A. Kahn-Harari, P. Dubois, R. Céolin, and H. Szwarc. ‘low-pressure’ orthorhombic phase formed from pressure-treated C_{60} . *Chemical Physics Letters*, 267:193–198, 1997. doi: [http://dx.doi.org/10.1016/S0009-2614\(97\)00072-9](http://dx.doi.org/10.1016/S0009-2614(97)00072-9).
- [65] X. Chen and S. Yamanaka. Single-crystal x-ray structural refinement of the ‘tetragonal’ C_{60} polymer. *Chemical Physics Letters*, 360:501–508, 2002. doi: 10.1016/S0009-2614(02)00827-8.
- [66] X. Chen, S. Yamanaka, K. Sako, Y. Inoue, and M. Yasukawa. First single-crystal x-ray structural refinement of the rhombohedral C_{60} polymer. *Chemical Physics Letters*, 356: 291–297, 2002. doi: [http://dx.doi.org/10.1016/S0009-2614\(02\)00332-9](http://dx.doi.org/10.1016/S0009-2614(02)00332-9).

- [67] S. Okada and S. Saito. Rhombohedral C_{60} polymer: A semiconducting solid carbon structure. *Physical Review B*, 55(7):4039–4041, 1997. doi: 10.1103/PhysRevB.55.4039.
- [68] S. Okada and S. Saito. Electronic structure and energetics of pressure-induced two-dimensional C_{60} polymers. *Physical Review B*, 59(3):1930–1936, 1999. doi: 10.1103/PhysRevB.59.1930.
- [69] V. Blank, S. Buga, G. Dubitsky, N. Serebryanaya, M. Popov, and B. Sundqvist. High-pressure polymerized phases of C_{60} . *Carbon*, 36(4):319–343, 1998. doi: 10.1016/S0008-6223(97)00234-0.
- [70] V. Brazhkin, A. Lyapin, S. Popova, Y. Klyuev, and A. Naletov. Mechanical properties of the 3D polymerized, sp^2 – sp^3 amorphous, and diamond-plus-graphite nanocomposite carbon phases prepared from C_{60} under high pressure. *Journal of Applied Physics*, 84(1):219–226, 1998. doi: 10.1063/1.368021.
- [71] J. Yang, J. Tse, and T. Iitaka. First-principles investigation on the geometry and electronic structure of the three-dimensional cuboidal C_{60} polymer. *The Journal of Chemical Physics*, 127:134906, 2007. doi: 10.1063/1.2771162.
- [72] J. Weaver, J. Martins, T. Komeda, Y. Chen, T. Ohno, G. Kroll, N. Troullier, R. Hauffer, and R. Smalley. Electronic structure of solid c_{60} : Experiment and theory. *Physical Review Letters*, 66(13):1741–1744, 1991. doi: 10.1103/PhysRevLett.66.1741.
- [73] N. Troullier and J. Martins. Structural and electronic properties of c_{60} . *Physical Review B*, 46(3):1754–1765, 1992. doi: 10.1103/PhysRevB.46.1754.
- [74] The nobel prize in chemistry 1998:development of computational methods in chemistry awarded. 1998, . url: <https://www.nobelprize.org/prizes/chemistry/1998/press-release/>, Retrieved December 21, 2022.
- [75] C. Pickard and R. Needs. High-pressure phases of silane. *Physical Review Letters*, 97(4):045504, 2006. doi: 10.1103/PhysRevLett.97.045504.
- [76] C. Pickard and R. Needs. Ab initio random structure searching. *Journal of Physics: Condensed Matter*, 23(5):053201, 2011. doi: 10.1088/0953-8984/23/5/053201.
- [77] C. Glass, A. Oganov, and N. Hansen. Uspex—evolutionary crystal structure prediction. *Computer Physics Communications*, 175:713–720, 2006. doi: <http://dx.doi.org/10.1016/j.cpc.2006.07.020>.
- [78] M. Hu, Y. Pan, K. Luo, J. He, D. Yu, and B. Xu. Three dimensional graphdiyne polymers with tunable band gaps. *Carbon*, 91:518–526, 2015. doi: 10.1016/j.carbon.2015.05.027.
- [79] Q. Zhu, A. Oganov, M. Salvadó, P. Perterra, and A. Lyakhov. Denser than diamond: Ab initio search for superdense carbon allotropes. *Physical Review B*, 83(19):193410, 2011. doi: 10.1103/PhysRevB.83.193410.
- [80] Y. Yamagami and S. Saito. Polymerized sp^2 – sp^3 hybrid metallic phase of C_{60} as obtained via constant-pressure molecular dynamics. *Physical Review B*, 79(4):045425, 2009. doi: 10.1103/PhysRevB.79.045425.
- [81] Yamagami Y. and Saito S. Simple-cubic three-dimensional C_{60} polymer. *Physica E: Low-dimensional Systems and Nanostructures*, 43(3):661–668, 2011. doi: 10.1016/j.physe.2010.07.024.

- [82] M. Yin. Si-iii (bc-8) crystal phase of si and c: Structural properties, phase stabilities, and phase transitions. *Physical Review B*, 30(4):1773–1776, 1984. doi: 10.1103/PhysRevB.30.1773.
- [83] L. Zhu, G. Borstad, H. Liu, P. Guńka, M. Guerette, J.-A. Dolyniuk, Y. Meng, E. Greenberg, V. Prakapenka, B. Chaloux, A. Epshteyn, R. Cohen, and T. Strobel. Carbon-boron clathrates as a new class of sp^3 -bonded framework materials. *Science Advances*, 6(2), 2020. doi: 10.1126/sciadv.aay8361.
- [84] C. Perottoni and J. da Jornada. The carbon analogues of type-i silicon clathrates. *Journal of Physics: Condensed Matter*, 13:5981, 2001. doi: 10.1088/0953-8984/13/26/313.
- [85] P. Rowe, V. Deringer, P. Gasparotto, G. Csányi, and A. Michaelides. An accurate and transferable machine learning potential for carbon. *The Journal of Chemical Physics*, 153(3):034702, 2020. doi: 10.1063/5.0005084.
- [86] Y. Zhao, C. Qian, V. Gladkikh, and F. Ding. Diagram of new carbon materials derived by high-temperature and high-pressure treatment of C_{60} bulk. *Carbon*, 2022. doi: 10.1016/j.carbon.2022.11.007.
- [87] J. Copley, W. David, and D. Neumann. Structure and dynamics of buckyballs. *Neutron News*, 4:20–28, 1993. doi: 10.1080/10448639308218960.
- [88] R. Fleming, T. Siegrist, P. Marsh, B. Hessen, A. Kortan, D. Murphy, R. Haddon, R. Tycko, G. Dabbagh, A. Mujsce, M. Kaplan, and S. Zahurak. Diffraction symmetry in crystalline, close-packed C_{60} . *MRS Proceedings*, 206, 1990. doi: 10.1557/PROC-206-691.
- [89] W. David, R. Ibberson, T. Dennis, J. Hare, and K. Prassides. Structural phase transitions in the fullerene C_{60} . *Europhysics Letters*, 18(3):219–225, 1992. doi: 10.1209/0295-5075/18/3/006.
- [90] W. David and R. Ibberson. High-pressure, low-temperature structural studies of orientationally ordered C_{60} . *Journal of Physics: Condensed Matter*, 5(43):7923–7928, 1993. doi: 10.1088/0953-8984/5/43/005.
- [91] H. Schober and B. Renker. Pressure dependence of the external mode spectrum of solid C_{60} . *Physical Review B*, 59(5):3287–3290, 1999. doi: 10.1103/PhysRevB.59.3287.
- [92] B. Sundqvist. Polymeric fullerene phases formed under pressure. In K. Prassides, editor, *Fullerene-based materials: structures and properties*. Springer, 2004. ISBN 9783540201069.
- [93] A. Rao, P. Zhou, K.-A. Wang, G. Hager, J. Holden, Y. Wang, W.-T. Lee, X.-X. Bi, P. Eklund, D. Cornett, M. Duncan, and I. Amster. Photoinduced polymerization of solid C_{60} films. *Science*, 259:955–957, 1993. doi: 10.1126/science.259.5097.955.
- [94] V. Davydov, L. Kashevarova, A. Rakhmanina, V. Senyavin, O. Pronina, N. Oleynikov, V. Agafonov, R. Céolin, H. Allouchi, and H. Szwarc. Pressure-induced dimerization of fullerene C_{60} : a kinetic study. *Chemical Physics Letters*, 333:224–229, 2001. doi: [http://dx.doi.org/10.1016/S0009-2614\(00\)01379-8](http://dx.doi.org/10.1016/S0009-2614(00)01379-8).
- [95] J. Coyle. *Introduction to Organic Photochemistry*. Wiley, 1986. ISBN 9780471909750.
- [96] G. Scuseria. What is the lowest-energy isomer of the C_{60} dimer? *Chemical Physics Letters*, 257:583–586, 1996. doi: [http://dx.doi.org/10.1016/0009-2614\(96\)00599-4](http://dx.doi.org/10.1016/0009-2614(96)00599-4).

- [97] G. Adams, J. Page, O. Sankey, and M. O’Keeffe. Polymerized c_{60} studied by first-principles molecular dynamics. *Physical Review B*, 50(23):17471–17479, 1994. doi: 10.1103/PhysRevB.50.17471.
- [98] F.-L. Liu and X.-X. Zhao. Two intact c_{60} cages linked by six carbon–carbon single bonds. *Journal of Molecular Structure: THEOCHEM*, 804(1):117–121, 2007. doi: 10.1016/j.theochem.2006.10.018.
- [99] S. Ōsawa, E. Ōsawa, and Y. Hirose. Doubly bonded c_{60} dimers and congeners: Computational studies of structures, bond energies and transformations. *Fullerene Science and Technology*, 3(5):565–585, 1995. doi: 10.1080/153638X9508543808.
- [100] N. Matsuzawa, M. Ata, D. Dixon, and G. Fitzgerald. Dimerization of c_{60} : The formation of dumbbell-shaped c_{120} . *The Journal of Physical Chemistry*, 98(10):2555–2563, 1994. doi: 10.1021/j100061a009.
- [101] F. Zipoli and M. Bernasconi. First principles study of three-dimensional polymers of C_{60} : Structure, electronic properties, and raman spectra. *Physical Review B*, 77(11):115432, 2008. doi: 10.1103/PhysRevB.77.115432.
- [102] R. Moret, P. Launois, P.-A. Persson, and B. Sundqvist. First x-ray diffraction analysis of pressure polymerized C_{60} single crystals. *Europhysics Letters*, 40(1):55, 1997. doi: 10.1209/epl/i1997-00424-4.
- [103] V. Davydov, L. Kashevarova, A. Rakhmanina, V. Agafonov, H. Allouchi, R. Ceolin, A. Dzyabchenko, V. Senyavin, and H. Szwarc. Tetragonal polymerized phase of C_{60} . *Physical Review B*, 58(22):14786–14790, 1998. doi: 10.1103/PhysRevB.58.14786.
- [104] V. Davydov, L. Kashevarova, A. Rakhmanina, V. Senyavin, R. Céolin, H. Szwarc, H. Allouchi, and V. Agafonov. Spectroscopic study of pressure-polymerized phases of C_{60} . *Physical Review B*, 61(18):11936–11945, 2000. doi: 10.1103/PhysRevB.61.11936.
- [105] R. Moret, P. Launois, T. Wågberg, and B. Sundqvist. High-pressure synthesis, structural and raman studies of a two-dimensional polymer crystal of C_{60} . *European Physical Journal B*, 15:253–263, 2000. doi: 10.1007/s100510051123.
- [106] R. Moret, T. Wågberg, and B. Sundqvist. Influence of the pressure–temperature treatment on the polymerization of C_{60} single crystals at 2GPa–700K. *Carbon*, 43:709–716, 2005. doi: <http://dx.doi.org/10.1016/j.carbon.2004.10.039>.
- [107] B. Narymbetov, V. Agafonov, V. Davydov, L. Kashevarova, A. Rakhmanina, A. Dzyabchenko, V. Kulakov, and R. Céolin. The crystal structure of the 2D polymerized tetragonal phase of C_{60} . *Chemical Physics Letters*, 367:157–162, 2003. doi: 10.1016/S0009-2614(02)01526-9.
- [108] Y. Iwasa, T. Arima, L. Rothberg, R. Fleming, O. Zhou, K. Lyons, S.-W. Cheong, R. Haddon, A. Hebard, and G. Thomas. Pressure-induced cross-linking of C_{60} . *Synthetic Metals*, 70:1407–1408, 1995. doi: [http://dx.doi.org/10.1016/0379-6779\(94\)02898-9](http://dx.doi.org/10.1016/0379-6779(94)02898-9).
- [109] V. Blank, S. Buga, N. Serebryanaya, G. Dubitsky, S. Sulyanov, M. Popov, V. Denisov, A. Ivlev, and B. Mavrin. Phase transformations in solid C_{60} at high-pressure-high-temperature treatment and the structure of 3D polymerized fullerenes. *Physics Letters A*, 220:149–157, 1996. doi: [http://dx.doi.org/10.1016/0375-9601\(96\)00483-5](http://dx.doi.org/10.1016/0375-9601(96)00483-5).

- [110] L. Marques, J.-L. Hodeau, M. Núñez–Regueiro, and M. Perroux. Pressure and temperature diagram of polymerized fullerite. *Physical Review B*, 54(18):12633–12636, 1996. doi: 10.1103/PhysRevB.54.R12633.
- [111] V. Davydov, V. Agafonov, A. Dzyabchenko, R. Céolin, and H. Szwarc. Packing models for high-pressure polymeric phases of C₆₀. *Journal of Solid State Chemistry*, 141:164–167, 1998. doi: <http://dx.doi.org/10.1006/jssc.1998.7938>.
- [112] A. Dzyabchenko, V. Agafonov, and V. Davydov. Theoretical molecular packings and the structural model of solid-phase polymerization of fullerene C₆₀ under high pressures. *Crystallography Reports*, 44:18–24, 1999.
- [113] T. Miyake and S. Saito. Geometry and electronic structure of rhombohedral C₆₀ polymer. *Chemical Physics Letters*, 380:589–594, 2003. doi: <http://dx.doi.org/10.1016/j.cplett.2003.09.067>.
- [114] V. Blank, S. Buga, N. Serebryanaya, V. Denisov, G. Dubitsky, A. Ivlev, B. Mavrin, and M. Popov. Ultrahard and superhard carbon phases produced from C₆₀ by heating at high pressure: structural and raman studies. *Physics Letters A*, 205(2):208–216, 1995. doi: 10.1016/0375-9601(95)00564-J.
- [115] S. Okada, S. Saito, and A. Oshiyama. New metallic crystalline carbon: Three dimensionally polymerized C₆₀ fullerite. *Physical Review Letters*, 83(10):1986–1989, 1999. doi: 10.1103/PhysRevLett.83.1986.
- [116] N. Serebryanaya and L. Chernozatonskii. Modelling and interpretation of the experimental data on the 3D polymerized C₆₀ fullerenes. *Solid State Communications*, 114(10):537–541, 2000. doi: 10.1016/S0038-1098(00)00085-5.
- [117] R. Ruoff and A. Ruoff. Is C₆₀ stiffer than diamond? *Nature*, 350(6320):663–664, 1991. doi: 10.1038/350663b0.
- [118] R. Papoular, V. Dmitriev, V. Davydov, A. Rakhmanina, and H. Allouchi and V. Agafonov. Study of the orthorhombic polymeric phase of C₆₀ under high pressure using synchrotron x-ray powder diffraction. *Fullerenes, Nanotubes and Carbon Nanostructures*, 18(4-6):392–395, 2010. doi: 10.1080/1536383X.2010.487438.
- [119] J. Léger, J. Haines, V. Davydov, and V. Agafonov. Irreversible amorphization of tetragonal two-dimensional polymeric C₆₀ under high pressure. *Solid State Communications*, 121(5):241–244, 2002. doi: 10.1016/S0038-1098(01)00503-8.
- [120] S. Kawasaki, A. Yao, Y. Matsuoka, S. Komiyama, F. Okino, H. Touhara, and K. Suito. Elastic properties of pressure-polymerized fullerenes. *Solid State Communications*, 125(11):637–640, 2003. doi: 10.1016/S0038-1098(02)00873-6.
- [121] A. Lyapin, Y. Katayama, and V. Brazhkin. Order versus disorder: In situ high-pressure structural study of highly polymerized three-dimensional C₆₀ fullerite. *Journal of Applied Physics*, 126(6):065102, 2019. doi: 10.1063/1.5111370.
- [122] V. Belavin, L. Bulusheva, A. Okotrub, and D. Tomanek. Stability, electronic structure and reactivity of the polymerized fullerite forms. *Journal of Physics and Chemistry of Solids*, 61(12):1901–1911, 2000. doi: 10.1016/S0022-3697(00)00079-2.

- [123] S. Saito, K. Umemoto, and T. Miyake. *Electronic Structure and Energetics of Fullerites, Fullerenes, and Fullerene Polymers*, pages 41–57. Springer Berlin Heidelberg, Berlin, Heidelberg, 2004. ISBN 978-3-540-39821-9. doi: 10.1007/b94378.
- [124] Y. Sato, M. Terauchi, and S. Yamanaka. Electronic structures of three-dimensional C₆₀ polymers studied by high-energy-resolution electron energy-loss spectroscopy based on transmission electron microscopy. *Chemical Physics Letters*, 626:90–95, 2015. doi: 10.1016/j.cplett.2015.03.017.
- [125] H. Xiao, J. Tahir-Kheli, and W. Goddard. Accurate band gaps for semiconductors from density functional theory. *The Journal of Physical Chemistry Letters*, 2(3):212–217, 2011. doi: 10.1021/jz101565j.
- [126] F. Birch. Finite elastic strain of cubic crystals. *Physical Review*, 71(11):809–824, 1947. doi: 10.1103/PhysRev.71.809.
- [127] R. Martin. *Electronic Structure: Basic Theory and Practical Methods*. Cambridge University Press, 2004. ISBN 9780511805769. doi: 10.1017/CBO9780511805769.
- [128] M. Springborg. *Methods of Electronic-Structure Calculations: From Molecules to Solids*. Wiley, 2000. ISBN 978-0-471-97975-3.
- [129] D. Sholl and J. Steckel. *Density Functional Theory: A Practical Introduction*. Wiley, 2009. ISBN 9780470447703.
- [130] K. Capelle. A bird’s-eye view of density-functional theory. *Brazilian Journal of Physics*, 36:1318, 2006. doi: 10.1590/S0103-97332006000700035.
- [131] M. Holthausen W. Koch. *A Chemist’s Guide to Density Functional Theory, Second Edition*. Wiley, 2001. ISBN 9783527303724. doi: 10.1002/3527600043.
- [132] E. Martínez-Núñez. An automated method to find transition states using chemical dynamics simulations. *Journal of Computational Chemistry*, 36(4):222–234, 2015. doi: 10.1002/jcc.23790.
- [133] E. Martínez-Núñez. An automated transition state search using classical trajectories initialized at multiple minima. *Physical Chemistry Chemical Physics*, 17(22):14912–14921, 2015. doi: 10.1039/C5CP02175H.
- [134] A. Rodríguez, R. Rodríguez-Fernández, S. Vázquez, G. Barnes, J. Stewart, and E. Martínez-Núñez. tsscds2018: A code for automated discovery of chemical reaction mechanisms and solving the kinetics. *Journal of Computational Chemistry*, 39(23):1922–1930, 2018. doi: 10.1002/jcc.25370.

Chapter 2

Computational methods

Throughout the work done in this thesis, we have used ab initio simulation techniques to find structures that would fit our experimental data and to compute the properties of those structures. We have employed mainly density functional theory (DFT) to obtain the electronic ground state of our proposed structures and then move the atoms to their equilibrium positions using the minimization algorithms included in the DFT packages. Thus, this chapter is dedicated to a brief description of this technique as well as some others that have DFT as a basis, allowing the computation of physical properties, such as superconductive behavior and Raman spectra among others. Accordingly to what was previously mentioned, the idea behind this chapter is to give a comprehensive summary of all these topics without diving into too much detail. Most of the knowledge presented here is based upon very well know textbooks in the field [1–5]. Whenever we used different sources, proper references will be made. Of all the papers presented in this thesis, the one where we employed more computational techniques in order to predict different properties is presented in article A5.

2.1 Atomic structure of materials

As stated in the introductory chapter, there are different dimensionalities among materials and carbon allotropes are well known for this. There are also periodic materials, where atoms have short and long-range order, and amorphous materials, where atoms only present short-range order. We need to deepen a bit these concepts if we want to simulate such materials.

Amorphous materials are outside of the scope of this work, where we focus on well-crystallized experimental structures, thus we will ignore them. Important concepts for our work are dimensionality, periodicity and symmetry, hence we will briefly discuss them before moving to the methods themselves.

2.1.1 Crystalline structure

We may define a crystalline lattice as an infinite repetition of a unit cell across three non coplanar vectors, \vec{a}_1 , \vec{a}_2 and \vec{a}_3 . Then any position on the crystal lattice, \vec{R} , will be equivalent to the position, \vec{R}' , if we shift it by a combination of these vectors:

$$\vec{R}' = \vec{R} + n_1\vec{a}_1 + n_2\vec{a}_2 + n_3\vec{a}_3. \quad (2.1)$$

\vec{a}_1 , \vec{a}_2 and \vec{a}_3 are known as lattice vectors and n_1 , n_2 and n_3 are any integers.

There are only seven types of possible primitive unit cells (cell which holds the lowest number of atoms possible to describe a particular crystal). These seven unit cells are classified

Crystal lattice family	Cell constraints
triclinic	none
monoclinic	$\beta = 90^\circ$
orthorhombic	$\alpha = \beta = \gamma = 90^\circ$
rhombohedral	$a = b = c, \alpha = \beta = \gamma \neq 90^\circ$
hexagonal	$a = b, \alpha = \beta = 90^\circ, \gamma = 120^\circ$
tetragonal	$a = b, \alpha = \beta = \gamma = 90^\circ$
cubic	$a = b = c, \alpha = \beta = \gamma = 90^\circ$

Table 2.1: Crystal lattices primitive unit cell specifications.

accordingly to their six degrees of freedom. Three lattice parameters, $a = |\vec{a}_1|$, $b = |\vec{a}_2|$ and $c = |\vec{a}_3|$, and three angles, α (defined between \vec{a}_2 and \vec{a}_3), β (defined between \vec{a}_1 and \vec{a}_3) and γ (defined between \vec{a}_1 and \vec{a}_2). These seven crystal lattices are summarized in table 2.1.

2.1.2 Point group symmetry

Until now we have seen that a crystalline structure is invariant regarding certain translations, accordingly to their primitive cell lattice. Nevertheless, similarly to molecules, crystals also present point group symmetry elements such as mirror planes, inversions and rotations. Unlike molecules, the rotations allowed are restricted to one, two, three, four and six-fold.

Whenever a crystalline structure is considered, symmetry elements can be created by joining point group operations with translations. For instance, we can form glide planes by applying a mirror plane and then a translation. A screw axis is generated by joining a rotation with a subsequent translation.

There are only two hundred and thirty possible combinations between the crystal primitive lattices and the allowed point groups. These two hundred and thirty unique combinations are known as space groups.

2.2 Electronic structure calculation: A many-body problem

The time-independent Schrödinger equation is used to describe any stationary quantum physics problem

$$\hat{H}|\Psi\rangle = E|\Psi\rangle, \quad (2.2)$$

where \hat{H} is the system's Hamiltonian, E its energy and its wave function Ψ . In order to find the wave function of any quantum physics problem its Hamiltonian needs to be settled. Excluding relativistic and spin effects, a system made of several atoms (i.e. nuclei and electrons) is described by the following time-independent Hamiltonian

$$\hat{H} = -\frac{\hbar^2}{2m_e} \sum_i \nabla_i^2 - \sum_{i,I} \frac{Z_I e^2}{|\vec{r}_i - \vec{R}_I|} + \frac{1}{2} \sum_{i \neq j} \frac{e^2}{|\vec{r}_i - \vec{r}_j|} - \sum_I \frac{\hbar^2}{2M_I} \nabla_I^2 + \frac{1}{2} \sum_{I \neq J} \frac{Z_I Z_J e^2}{|\vec{R}_I - \vec{R}_J|}, \quad (2.3)$$

where \hbar is the Plack constant, m_e is the electron mass, Z_I is the I th nuclei charge, M_I the I th nuclei mass, \vec{r}_i the i th electron position and \vec{R}_I the I th Nuclei position. i, j are electron indexes and I, J are nucleus indexes.

For simplicity, let us adopt atomic units (a.u.) $\hbar = m_e = e = 1$. Then the equation will have the following form

$$\hat{H} = -\frac{1}{2} \sum_i \nabla_i^2 - \sum_{i,I} \frac{Z_I}{|\vec{r}_i - \vec{R}_I|} + \frac{1}{2} \sum_{i \neq j} \frac{1}{|\vec{r}_i - \vec{r}_j|} - \sum_I \frac{1}{2M_I} \nabla_I^2 + \frac{1}{2} \sum_{I \neq J} \frac{Z_I Z_J}{|\vec{R}_I - \vec{R}_J|}, \quad (2.4)$$

$$= \hat{T}_e + \hat{V}_{e,n} + \hat{V}_{e,e} + \hat{T}_n + \hat{V}_{n,n}. \quad (2.5)$$

The Hamiltonian is composed of various contributions. The first term corresponds to the electron's kinetic energy \hat{T}_e . The second one is the electron-nuclei Coulomb interaction, $\hat{V}_{e,n}$. $\hat{V}_{e,e}$ is the electron-electron Coulomb repulsion, and \hat{T}_n the nuclei kinetic energy. The last term is the nuclei-nuclei Coulomb interaction $\hat{V}_{n,n}$.

Apart from specific cases, like the Hydrogen atom, solving the Schrödinger equation for the Hamiltonian 2.5 is a many-body problem, which is impossible to solve analytically. Nevertheless, this Hamiltonian is the cornerstone of solid-state physics ab initio calculations since it describes our system from first principles without any prior knowledge of the problem. The many-body problem is quite complex and solving it is one of the main problems in solid-state physics. Indeed there are recent works with new approaches to tackle this issue [6–8], nevertheless one of the most widespread and proven methods to solve the problem is DFT.

2.2.1 Born-Oppenheimer approximation

We still need to perform a small, yet extremely important, approximation before employing DFT to equation 2.5, the Born-Oppenheimer approximation. This approximation effectively decouples the nuclear and electronic degrees of freedom assuming that, as the nuclei mass is much larger than the electron one, the time scales of their dynamics are much different, thus we can assume that the nucleus remains static during the electronic motion, and we can describe our electronic system ignoring all the nuclei-nuclei terms. By doing this approximation the nuclear kinetic energy becomes zero, the nuclei-nuclei Coulomb repulsion is transformed into a constant and the electron-nuclei interaction can be described by an external potential. Thus, we can describe the nuclear effect on our system as an external potential, \hat{V}_{ext} . Hence, for the electronic system, equation 2.5, can be written simple as

$$\hat{H}_e = \hat{T}_e + \hat{V}_{e,e} + \hat{V}_{\text{ext}}. \quad (2.6)$$

2.2.2 Density functional theory

Although we have simplified our problem, it is still very complex. DFT further simplifies it. As the name implies, the first approach that is taken when employing this technique is to use the electronic density instead of the position of each electron to describe our system. This approach reduces our problem from $3N$ variables, with N being the total number of electrons, to a three-variable problem, with the electronic density defined as

$$n(\vec{r}) = N \int d^3 r_2 \int d^3 r_3 \dots \int d^3 r_N \Psi^*(\vec{r}, \vec{r}_2, \vec{r}_3, \dots, \vec{r}_N) \Psi(\vec{r}, \vec{r}_2, \vec{r}_3, \dots, \vec{r}_N). \quad (2.7)$$

2.2.2.1 Hohenberg-Kohn theorems

The two Hohenberg-Kohn theorems are the basis of DFT, being built on top of equations 2.6 and 2.7. The first theorem states that for any system of interacting particles in an external potential, $\hat{V}_{\text{ext}}(\vec{r})$, this potential is defined by the ground state density $n_0(\vec{r})$, apart from a constant. As a consequence, if the electronic ground state density, $n_0(\vec{r})$, is known, the

Hamiltonian 2.6 is completely determined and, thus it is possible to calculate the wave functions for all states, including the ground state one, $\Psi_0(\vec{r})$, that corresponds to that ground state density.

The second theorem is the final one responsible for the technique's name. It states that a universal energy functional, $E[n]$, in terms of the system electronic density can be defined in such a way that for a particular $\hat{V}_{\text{ext}}(\vec{r})$ the global minimum of this functional is the ground state energy of the system, being the density that minimizes this system the ground state density $n_0(\vec{r})$. Thus the ground state energy is given by:

$$E_0[n] = \min_{\Psi \rightarrow n_0} \langle \Psi | \hat{T}_e + \hat{V}_{e,e} + \hat{V}_{\text{ext}} | \Psi \rangle. \quad (2.8)$$

If instead of the ground state density any other density, $n(r)$, is used, then the produced wave function will no longer be the ground state one and the energy found will be larger than the ground state one. As the kinetic and Coulomb operators are system independent, we can write our energy functional as:

$$E_0[n] = \min_{\Psi \rightarrow n} \langle \Psi | \hat{T}_e + \hat{V}_{e,e} | \Psi \rangle + \int d^3r n(\vec{r}) v_{\text{ext}}(\vec{r}), \quad (2.9)$$

where $\int d^3r n(r) v_{\text{ext}}(r) = V_{\text{ext}}[n]$ is the only system dependent functional. Thus, the energy functional is defined as:

$$E[n] = T_e[n] + V_{e,e}[n] + V_{\text{ext}}[n]. \quad (2.10)$$

2.2.2.2 Kohn-Sham formulation: DFT as a single-body problem

Until now we have applied the DFT formalism to a many-body problem. Kohn and Sham assumed that one could describe the many-body interacting problem with an auxiliary system of non-interacting particles. By solving the equations one finds the ground state density and energy of the original interacting system with the accuracy limited only by the approximations in the exchange–correlation functional.

Let us start by decomposing the kinetic functional, $T_e[n]$, into the kinetic energy of non-interacting particles, $T_s[n]$ and what is left, $T_c[n]$.

$$T_e[n] = T_s[n] + T_c[n]. \quad (2.11)$$

It is impossible to know $T_c[n]$. Nevertheless, as the total kinetic energy of non-interacting particles is the individual particle's kinetic energy sum, we can write it as a sum of the single-particle orbitals of a non-interacting system, $\phi_i(\vec{r})$,

$$T_s = -\frac{1}{2} \sum_i^N \int d^3r \phi_i^*(\vec{r}) \nabla^2 \phi_i(\vec{r}). \quad (2.12)$$

All the orbitals $\phi_i(\vec{r})$ are functionals of the electronic density, $n(\vec{r})$, hence $T_s = T_s[\{\phi_i[n]\}]$, with the electronic density defined in terms of single-particle wave functions as

$$n(\vec{r}) = \sum_i^N |\phi_i(\vec{r})|^2. \quad (2.13)$$

One may also define the exchange–correlation energy functional as

$$E_{\text{xc}}[n] = T_c[n] + V_{e,e}[n] - V_H[n], \quad (2.14)$$

$V_H[n]$ being the Hartree potential functional given by

$$V_H[n] = \frac{1}{2} \int d^3\vec{r} d^3\vec{r}' \frac{n(\vec{r})n(\vec{r}')}{|\vec{r} - \vec{r}'|}. \quad (2.15)$$

Thus, we can rewrite the energy functional in equation 2.10 in the following form

$$E[n] = T_s[\{\phi_i[n]\}] + V_H[n] + E_{xc}[n] + V_{ext}[n]. \quad (2.16)$$

If we could know the $E_{xc}[n]$ functional then we could find the exact ground state density and energy for the many-body electron problem by solving the Kohn-Sham equations. Unfortunately, one of the major drawbacks from DFT is that the exchange-correlation functional, E_{xc} , is unknown. Nevertheless, several approximations have been done through the years with a variable degree of success.

We will briefly discuss them later in subsection 2.2.3.1.

The new energy functional, equation 2.16, has a term which is not directly dependent on the electron density, $T_s[\{\phi_i[n]\}]$ and thus we cannot simply minimize the energy functional regarding its density, n . Kohn and Sham gave the solution, minimizing equation 2.16 with respect to the electronic density, using the chain rule

$$\frac{\delta E[n]}{\delta \phi_i(\vec{r})} = \frac{T_s[\{\phi_i[n]\}]}{\delta \phi_i(\vec{r})} + \left[\frac{V_H[n]}{\delta n(\vec{r})} + \frac{E_{xc}[n]}{\delta n(\vec{r})} + \frac{V_{ext}[n]}{\delta n(\vec{r})} \right] \frac{\delta n(\vec{r})}{\delta \phi_i(\vec{r})} = 0. \quad (2.17)$$

Using equations 2.12 and 2.13 one can find that

$$\frac{T_s[\{\phi_i[n]\}]}{\delta \phi_i(\vec{r})} = -\frac{1}{2} \nabla^2 \phi_i(\vec{r}), \quad \frac{\delta n(\vec{r})}{\delta \phi_i(\vec{r})} = \phi_i(\vec{r}). \quad (2.18)$$

If we consider that the system of non interacting particles is in an effective potential $v_{\text{eff}}(\vec{r})$ given by

$$v_{\text{eff}}(\vec{r}) = \frac{V_H[n]}{\delta n(\vec{r})} + \frac{E_{xc}[n]}{\delta n(\vec{r})} + \frac{V_{ext}[n]}{\delta n(\vec{r})}. \quad (2.19)$$

Then our auxiliary system Schrödinger equation will be

$$\left[-\frac{\nabla^2}{2} + v_{\text{eff}}(\vec{r}) \right] \phi_i(\vec{r}) = \epsilon_i \phi_i(\vec{r}). \quad (2.20)$$

Equations 2.19 and 2.20 are known as the Kohn-Sham equation and solving them is a nonlinear problem. They allow to map the many-body interacting problem into a set of independent particles that interact with an external potential. To solve these equations in a practical way, one starts using an electronic density guess, $n(\vec{r})$ to calculate the correspondent effective potential $v_{\text{eff}}(\vec{r})$. Afterward, equation 2.20 is solved to get the single-particle wave functions, $\phi_i(\vec{r})$, that are then used to get the new density recurring to equation 2.13. The calculation is then restarted with the new density (or a mixture of the new and old density) and the procedure is repeated until the changes in the density are smaller than a user-defined threshold. Hence we create a self-consistency loop, with the procedure as shown in a simplified manner in scheme 2.1.

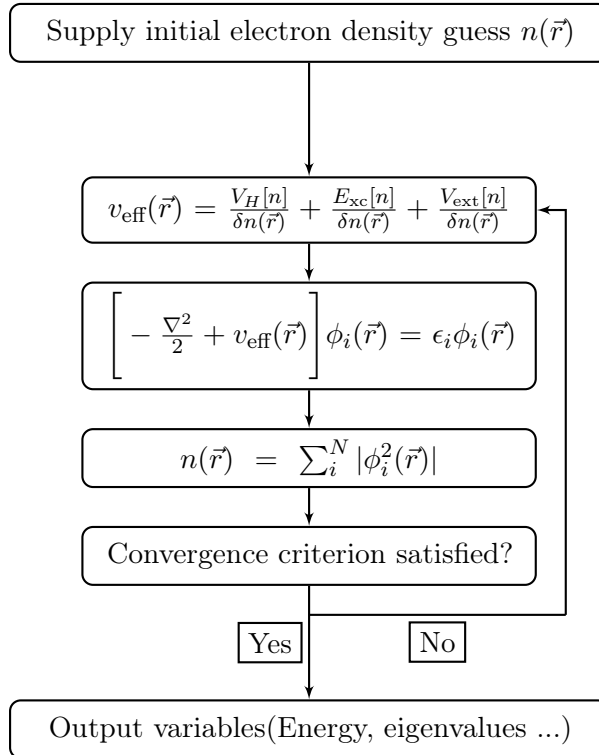


Figure 2.1: Scheme depicting the self-consistent loop used to solve the Kohn-Sham equations.

2.2.3 Implementing DFT

We have discussed how DFT transforms a many-body Schrödinger equation into a set of solvable independent particle Schrödinger equations. In principle, the equations derived up to now would lead to the exact ground state energy of the interacting system. Nevertheless, there are approximations that need to be done in order to solve the derived Kohn-Sham equations. We need to find a way to numerically compute our independent single-particle wave functions and to approximate the exchange-correlation functional. In this section, we will briefly discuss the practical implementations and approximations that are used in DFT calculations.

2.2.3.1 Exchange-Correlation functionals

As stated above, the exact form of the exchange-correlation functional, E_{xc} is not known.

Fortunately, when compared to other functionals in the Kohn-Sham Hamiltonian, it yields much smaller values allowing us to reasonably approximate it. There are different approximations with different complexities and accuracies. The biblical concept of the "Jacob's ladder" is usually used as an analogy with the exchange-correlation functionals. Each rung of the ladder is equivalent to a type of functional and, as we climb each rung, we get closer to "god", i.e. closer to the real solution to our problem. Relevant for this work is the first rung of this ladder, which corresponds to the local density approximation (LDA), the second one which corresponds to the general gradient approximations (GGA), the third rung correspondent to meta-(GGA) functionals and the fourth rung where the Hybrid GGA functionals are found.

An exchange-correlation in the limit of the homogeneous electron gas was proposed since the genesis of the Kohn-Sham theory. By its nature, it would have a local character, i.e. it would only depend on the electron density at each position $n(\vec{r})$, and could be described by the following integral

$$E_{\text{xc}}^{\text{LDA}}[n] = \int d^3\vec{r} n(\vec{r}) \epsilon_{\text{xc}}^{\text{hom}}(n(\vec{r})). \quad (2.21)$$

Parameterizations for the exchange-correlation energy of the homogeneous electron gas, $\epsilon_{\text{xc}}^{\text{hom}}$, have been given with great success.

The next step to improve our exchange-correlation functional is to consider that, besides local density at each point \vec{r} , it also depends on how the density changes with \vec{r} , thus one needs to look to the density gradient, $\nabla n(\vec{r})$. These approximations are called General Gradient approximations (GGA) and are described by the following exchange-correlation functional:

$$E_{\text{xc}}^{\text{GGA}}[n] = \int d^3\vec{r} n(\vec{r}) \epsilon_{\text{xc}}(n(\vec{r}), |\nabla n(\vec{r})|). \quad (2.22)$$

Several parameterizations to the GGA exchange-correlation energy, $\epsilon_{\text{xc}}(n(\vec{r}), |\nabla n(\vec{r})|)$, were given, with the most commonly used among condensed matter physicists being Perdew-Burke-Ernzerhof (PBE) [9, 10].

Meta-(GGA) improves further our exchange-correlation functional by considering not only the local density at each point \vec{r} and how it changes with \vec{r} but also taking into account the local kinetic energy density:

$$E_{\text{xc}}^{\text{meta-GGA}}[n] = \int d^3\vec{r} n(\vec{r}) \epsilon_{\text{xc}}(n(\vec{r}), |\nabla n(\vec{r})|, \tau(\vec{r})). \quad (2.23)$$

where the kinetic energy density is defined as the following summation over all occupied Kohn-Sham orbitals $\phi(\vec{r})$:

$$\tau(\vec{r}) = \frac{1}{2} \sum_i^{\text{occ}} (\nabla \phi(\vec{r}))^2 \quad (2.24)$$

While working on this thesis we have recurred to TPSS meta-GGA functional [11] to compute energies in molecular systems, C_{60} dimers present in article 6.

The last functionals that we must mention are the Hybrid GGA (commonly named only by Hybrid functionals). A common problem arising from the exchange-correlation functionals is the overestimation of the exchange contribution over the correlation one. Hence, a possible solution is to use an exact number for the exchange (which we can calculate using Hartree-Fock theory) and keep approximating the correlation. Indeed the HSE hybrid functional is based on the PBE functional but then, a bit of exact Hartree-Fock exchange is mixed [12]. In a very simple way, the HSE exchange-correlation functional will have the form

$$E_{\text{xc}}^{\text{HSE}}[n] = E_c^{\text{PBE}}[n] + aE_x^{\text{PBE}}[n] + bE_x^{\text{HF}}[n], \quad (2.25)$$

being $a + b = 1$ and $E_c^{\text{PBE}}[n]$ the PBE correlation, $E_x^{\text{PBE}}[n]$ the PBE exchange and $E_x^{\text{HF}}[n]$ the exact Hartree-Fock exchange. This leads to more accurate energies and electronic bandgaps but more expensive calculations are required.

In addition, all the described functionals provide robust descriptions of metallic, ionic and covalent interactions, nevertheless, they fail to properly represent van der Waals interactions. Although in some cases this is not relevant because van der Waals forces are much weaker than the other mentioned interactions, they play an important role in layered materials, biological macromolecules, and molecular crystals [13–15]. For instance, in the case of graphite, the interlayer distance, where no covalent bonds are observed, must be computed with this correction to be reproduced accurately [16]. Thus, this interaction is particularly relevant if our structures present any crystalline directions without covalent bonds, such as graphite or, relevantly, all the low dimensional C_{60} polymers. Hence, we employed Stefan Grimme's D3

van der Waals correction [17, 18] with Becke–Johnson damping [19], in articles A4 and A8, and Tkatchenko-Scheffler method with iterative Hirshfeld partitioning [20, 21], in article A7. These corrections are characterized by the addition of a nonlocal correlation dispersion term to the exchange–correlation functional after the electronic convergence is achieved. For the PBE the corrected functional will have the form:

$$E_{xc}^{PBE-disp}[n] = E_{xc}^{PBE}[n] + E_c^{disp}[n]. \quad (2.26)$$

In this work, we have used most of the times PBE, since it yields good accuracy for the bond lengths and overall geometry at an affordable computational load [22]. As PBE systematically underestimates electronic bandgaps between the valence and conduction electronic levels, we have used HSE (in particular HSE06) to get more accurate values [23] whenever we found it relevant. Other functionals, namely B3LYP, were also employed in one of our works, article A4, as they yield more accurate electronic gaps and energies, respectively.

2.2.3.2 Wave functions expansion

In practice, we need to find a way to numerically compute the Kohn-Sham equations, thus a way to compute the set of single-particle wave functions. In this thesis several DFT packages were used to tackle different problems, among the ones used in the works presented here are VASP [24–26], QE [27, 28], Gaussian09 [29] and Crystal17 [30]. The first two programs use plane waves basis, to expand the single-particle wave functions, excelling in computing crystalline materials, the last two programs expand the wave functions in linear combination of atomic orbitals (LCAO) being more suitable to compute isolated molecules or lower dimensional systems, i.e. 1D and 2D systems.

Plane waves: a periodic boundary condition implementation

The Bloch theorem states that the solutions to a periodic system Schrödinger equation can have the following form:

$$\phi_{\vec{K}}(\vec{r}) = e^{i\vec{K}\cdot\vec{r}} u_{\vec{K}}(\vec{r}). \quad (2.27)$$

where \vec{K} is the position vector in the reciprocal space and $u_{\vec{K}}(\vec{r})$ a periodic function such that $u_{\vec{K}}(\vec{r}) = u_{\vec{K}}(\vec{r} + n_1\vec{a}_1 + n_2\vec{a}_2 + n_3\vec{a}_3)$, \vec{a}_1, \vec{a}_2 and \vec{a}_3 being the crystalline lattice vectors and n_1, n_2 and n_3 any integer numbers.

Thus, we can solve our Schrödinger equation for each reciprocal lattice \vec{K} point, which is useful, since implementing DFT in the reciprocal space is more practical from a numerical point of view. Nevertheless, now we are presented with the impossible task of integrating over all the reciprocal space vectors, \vec{K} . To overcome this issue usually one defines a discrete number of \vec{K} vectors accordingly to the work of [31]. The higher the number of K points, the more accurate the result gets. In practice, one needs to converge the K points number to be sure that the results are accurate and also avoid computational time waste. Since the reciprocal space is proportionally inverse to the real space, as the lattice vectors increase, fewer K points are required to describe the system accurately. The number of K points may further be reduced using symmetry operations within the first Brillouin Zone.

There is still a problem regarding the periodic function $u_{\vec{K}}$ expansion. This function can be expanded in plane waves itself:

$$u_{\vec{K}}(\vec{r}) = \sum_{\vec{G}} c_{\vec{G}} e^{i\vec{G}\cdot\vec{r}}, \quad (2.28)$$

where $c_{\vec{G}}$ is a coefficient and $\vec{G} = m_1\vec{b}_1 + m_2\vec{b}_2 + m_3\vec{b}_3$ with m_1 , m_2 and m_3 integer numbers and, \vec{b}_1 , \vec{b}_2 and \vec{b}_3 the reciprocal lattice vectors defined as:

$$\vec{b}_1 = 2\pi \frac{\vec{a}_2 \times \vec{a}_3}{\vec{a}_1 \cdot (\vec{a}_2 \times \vec{a}_3)}, \quad \vec{b}_2 = 2\pi \frac{\vec{a}_3 \times \vec{a}_1}{\vec{a}_2 \cdot (\vec{a}_3 \times \vec{a}_1)}, \quad \vec{b}_3 = 2\pi \frac{\vec{a}_1 \times \vec{a}_2}{\vec{a}_3 \cdot (\vec{a}_1 \times \vec{a}_2)}, \quad (2.29)$$

with \vec{a}_1 , \vec{a}_2 and \vec{a}_3 the real space lattice vectors. Hence, we can write our single-particle wave functions as

$$\phi_{\vec{K}}(\vec{r}) = \sum_{\vec{G}} c_{\vec{K}+\vec{G}} e^{i(\vec{K}+\vec{G})\cdot\vec{r}}. \quad (2.30)$$

We can take this equation as a solution of Schrödinger equation with kinetic energy

$$T = \frac{1}{2} |\vec{K} + \vec{G}|^2. \quad (2.31)$$

As solutions with lower energy are more important than solutions with higher energies we can truncate our kinetic energy to the value:

$$T_{\text{cut}} = \frac{1}{2} G_{\text{cut}}^2. \quad (2.32)$$

Hence, the equation 2.30 is summed until this reciprocal lattice vector cutoff

$$\phi_{\vec{K}}(\vec{r}) = \sum_{|\vec{G}+\vec{K}| < G_{\text{cut}}} c_{\vec{K}+\vec{G}} e^{i(\vec{K}+\vec{G})\cdot\vec{r}}. \quad (2.33)$$

As a consequence, we need to define a kinetic energy cutoff. Similarly to the \vec{K} points as higher the value as accurate the result but it also turns the calculation more expensive. Once again one should converge this cutoff value.

Linear combination of atomic orbitals

As the name implies here we solve our Schrödinger equation recurring to a linear combination of atomic orbitals to expand our wave functions. To perform this task we need to define a set of L basis functions $\varphi_{\mu}(\vec{r})$ and expand them linearly

$$\phi_i(\vec{r}) = \sum_{\mu=1}^L c_{\mu i} \varphi_{\mu}(\vec{r}). \quad (2.34)$$

Here $c_{\mu i}$ are constants that weight differently for distinct function $\varphi_{\mu}(r)$. If $L = \infty$, the set of basis functions would be complete and we could express completely every function $\phi_i(r)$. Nevertheless, this is computationally impossible and thus, a finite L is used. Usually, $\varphi_{\mu}(r)$ are Gaussian functions.

With LCAO the Kohn-Sham nonlinear problem is transformed into a linear one. Furthermore, and in opposition to plane waves, we do not need to define an energy cutoff but we need to define the basis set. A major drawback is that now we may have basis set superposition errors (BSSE). Superposition errors occur due to the necessary finiteness of the atomic basis sets. So that the basis set of neighboring molecules or atoms augment the original basis set, bringing the energy system down. With plane waves superposition errors are impossible to occur as calculations with this method are equivalent to a complete basis set.

Although plane waves based software packages are intrinsically suitable for periodic boundary conditions problems, we can still use them to compute finite systems. To perform

this task we just need to use a big enough cell so the molecule does not interact with its periodic images. This is highly inefficient and thus is better to use a LCAO program if possible.

Similarly, an LCAO program can compute periodic boundary conditions systems but usually they converge slower than plane waves programs and we need to converge our problem regarding the basis set, which may be tricky. There may also be basis set superposition problems and, more problematically, if used in a periodic calculation, the LCAO basis can become linearly dependent leading to SCF convergence problems. Hence, in this thesis, we have used mainly VASP for most crystalline geometric optimizations and electronic structure computations (band structure and DOS). If we were working in a system with lower dimensionality we used mostly Crystal17.

2.2.3.3 Pseudopotentials for plane waves

When the wave functions are expanded in plane waves the pseudopotential approximation is used. In a material, the core and valence electrons of an atom have very distinct roles. The core electrons are usually tightly bound to the nucleus, being extremely localized, while valence electrons are responsible for most properties of the material, like the electronic structure or even the covalent bonding between atoms. Being tightly bound, core electrons remain invariant with respect to the environment where the nucleus is located. Additionally, considering them explicitly may create numerical issues since highly localized electrons need a high energy cutoff to describe their rapidly changing wave functions. Thus, it is common to separate valence from core electrons and treat the core electrons joined with the nucleus in an effective "nucleus", i.e. in a pseudopotential.

Nowadays there are several approaches to pseudopotentials. In all calculations performed with VASP we have used projector augmented-wave [32] pseudopotentials while in QE we have used ultrasoft pseudopotentials [33].

2.3 Crystalline lattice vibrations

Raman and infrared spectra are among several observables where one needs to consider that the nuclei are not frozen, but instead, they are vibrating around equilibrium positions.

Let us consider a system with I nuclei of mass M_I and positions $\vec{R}_{I\alpha}$, α being the Cartesian coordinate. Periodic boundary conditions need to be applied to a large supercell with $p = 1, \dots, N_p$ cells defined by \vec{R}_p real space vectors. Within the Born-Oppenheimer approximation, the total electronic energy for this system at equilibrium is given by DFT, let us define it as E_0 . We can expand this energy in a Taylor series, stopping in the second term and obtaining the harmonic approximation

$$E = E_0 + \frac{1}{2} \sum_{\substack{I\alpha p \\ I'\alpha'p'}} \frac{\partial^2 E}{\partial \vec{R}_{I\alpha p} \partial \vec{R}_{I'\alpha'p'}} \Delta \vec{R}_{I\alpha p} \Delta \vec{R}_{I'\alpha'p'}, \quad (2.35)$$

with $\Delta \vec{R}_{I\alpha p} = \vec{R}_{I\alpha p} - \vec{R}_{I\alpha p}^0$, where $\vec{R}_{I\alpha p}^0$ is the equilibrium position and $\vec{R}_{I\alpha p}$ a slightly moved position with regard to the equilibrium one.

In equation 2.35 the first-order derivatives vanish since we are at an equilibrium position where the forces should be 0. The matrix of the energy second derivatives is known as Hessian and is constituted by the "interatomic nuclear force constants". The discrete Fourier transform of this matrix gives the Dynamical matrix:

$$D_{I\alpha I'\alpha'}(\vec{q}) = \frac{1}{\sqrt{M_I M_{I'}}} \sum_{p'} \frac{\partial^2 E}{\partial \vec{R}_{I\alpha} \partial \vec{R}_{I'\alpha' p'}} e^{i\vec{q} \cdot \vec{R}_p}, \quad (2.36)$$

where \vec{R}_p is a real space vector being \vec{q} the reciprocal space momentum vector. The dynamical matrix is hermitian and thus only admits real eigenvalues, $\omega_{\vec{q}\nu}^2$, such that

$$\sum_{I'\alpha'} D_{I\alpha I'\alpha'}(\vec{q}) \vec{e}_{I'\alpha'\nu}(\vec{q}) = \omega_{\vec{q}\nu}^2 \vec{e}_{I\alpha\nu}(\vec{q}), \quad (2.37)$$

with $\nu = 1, \dots, N_n$ with N_n the number of nuclei in the primitive unit cell. Each $\omega_{\vec{q}\nu}$ corresponds to a vibration frequency in the reciprocal space point \vec{q} and normal mode ν associated with an eigenvector $\vec{e}_{I\alpha\nu}(\vec{q})$. Thus, finding the phonon dispersion curves becomes an eigenvalue problem.

We have treated our problem for periodic systems, nevertheless the same approach can be performed to a molecular system where the dynamical matrix will be simplified to

$$D_{I\alpha I'\alpha'} = \frac{1}{\sqrt{M_I M_{I'}}} \frac{\partial^2 E}{\partial \vec{R}_{I\alpha} \partial \vec{R}_{I'\alpha'}}. \quad (2.38)$$

As we have mentioned above, the energy first-order derivatives of a system where the nuclei are in their groundstate positions are 0. Nevertheless, this also happens if our nuclei are in a saddle point. Thus, it is extremely important to compute the dynamical matrixes of our system and ensure that all our matrix elements are non-negative.

One very simple way to evaluate the dynamical matrix is to consider a specific q point and, starting from the equilibrium structure with energy E_0 , consider all the possible displacements of each nucleus for this specific q point. The copy of the same atom in a different unit cell can move differently and thus one needs to use a supercell to perform this calculation in all the high symmetry q points. The big supercells needed, renders this calculation computationally expensive. This is the so-called "Frozen Phonon" approach. We used this approach to compute phonon dispersion curves with VASP and phonopy [34] packages.

In QE a more mathematically cumbersome, yet more computationally efficient, method to compute the dynamical matrix is used, namely, density functional perturbation theory.

In this thesis, we have computed Raman and infrared spectra with techniques such as those described above [35, 36]. The intensities of these spectra were computed through couple perturbed Kohn Sham theory as implemented in Crystal17, due to its proven accuracy and computational efficiency [37, 38].

2.4 Superconductivity mediated by electron-phonon interaction

Conventional superconducting behavior is described by the electron-phonon interaction, which Hamiltonian can be written as follows:

$$\hat{H}_{e-ph} = \frac{1}{\sqrt{N_p}} \sum_{\substack{\vec{K}, \vec{q} \\ mn\nu}} g_{mn\nu}(\vec{K}, \vec{q}) \hat{c}_{m\vec{K}+\vec{q}}^\dagger \hat{c}_{n\vec{K}} (\hat{a}_{\vec{q}\nu} + \hat{a}_{-\vec{q}\nu}^\dagger), \quad (2.39)$$

where we make use of the Bosonic and Fermionic creation and annihilation operators, $\hat{a}^\dagger, \hat{a}, \hat{c}^\dagger, \hat{c}$ respectively. $g_{mn\nu}(\vec{K}, \vec{q})$ are the electron-phonon matrix elements, which are needed to predict superconducting behavior. We may obtain them by calculating the following:

$$g_{mn\nu}(\vec{K}, \vec{q}) = \langle u_{m\vec{K}+\vec{q}} | \Delta_{\vec{q}\nu} v_{\text{eff}} | u_{n\vec{K}} \rangle, \quad (2.40)$$

where $u_{n\vec{K}}$ and $u_{m\vec{K}+\vec{q}}$ are Bloch periodic functions and the phonon-induced variation of the effective potential felt by the electron, $\Delta_{\vec{q}\nu}v_{\text{eff}}$, is given by

$$\Delta_{\vec{q}\nu}v_{\text{eff}} = \frac{1}{\sqrt{2\omega_{\vec{q}\nu}}} \sum_{I\alpha} \sqrt{\frac{1}{M_I}} e_{I\alpha\nu}(\vec{q}) \sum_p e^{-i\vec{q}\cdot(\vec{r}-\vec{R}_p)} \left. \frac{\partial V_{\text{eff}}}{\partial R_{I\alpha}} \right|_{\vec{r}=\vec{R}_p}. \quad (2.41)$$

It is possible to compute these quantities with QE via density functional perturbation theory: for more details we point the reader to Giustino's review on the electron-phonon interaction [39] and to Grimvall's book [40].

Once we compute $g_{mn\nu}(\vec{K}, \vec{q})$ it becomes possible to calculate the superconducting critical temperature (T_c) using the Eliashberg formalism and the McMillan-Allen-Dynes equation. The isotropic Eliashberg spectral function is given by

$$\alpha^2 F(\omega) = \frac{1}{N_f} \int \frac{d\vec{K} d\vec{q}}{V_{BZ}^2} \sum_{mn\nu} |g_{mn\nu}(\vec{K}, \vec{q})|^2 \delta(\epsilon_{n\vec{K}} - \epsilon_F) \delta(\epsilon_{n\vec{K}+\vec{q}} - \epsilon_F) \delta(\omega - \omega_{\vec{q}\nu}). \quad (2.42)$$

where N_f is the electronic density of states (DOS) at the Fermi level, V_{BZ} is the first Brillouin zone volume, $\epsilon_{n\vec{K}}$ the energy of the band n at the wave vector \vec{K} and ϵ_F the energy of the Fermi level. $\omega_{\vec{q}\nu}$ is the frequency of phonon ν at \vec{q} wave vector.

Then, the electron-phonon coupling constant, λ , can be computed as well as the phonon frequency logarithmic average

$$\lambda = 2 \int_0^\infty \frac{\alpha^2 F(\omega)}{\omega} d\omega, \quad \omega_{\log} = \exp \left[\frac{2}{\lambda} \int_0^\infty \frac{\alpha^2 F(\omega)}{\omega} \log(\omega) d\omega \right], \quad (2.43)$$

The superconducting critical temperature can right away be approximated by the McMillan-Allen-Dynes equation

$$k_B T_c = \frac{\omega_{\log}}{1.2} \exp \left[- \frac{1.04(1 + \lambda)}{\lambda - \mu^*(1 + 0.62\lambda)} \right], \quad (2.44)$$

where k_B is the Boltzmann constant and μ^* is an empirical parameter that describes the Coulomb repulsion, which usually is chosen to be between 0.1 and 0.2. Thus, the T_c obtained through this method usually presents considerable uncertainty.

A better way to compute superconducting temperatures is through the Migdal-Eliashberg equations, where one computes the superconducting gap function, Δ_I , and finds T_c from the highest temperature where $\Delta_I \neq 0$. More details are also given in Giustino's review [39]. Both the McMillan-Allen-Dynes equation and Migdal-Eliashberg equations were used in article A6.

Bibliography

- [1] R. Martin. *Electronic Structure: Basic Theory and Practical Methods*. Cambridge University Press, 2004. ISBN 9780511805769. doi: 10.1017/CBO9780511805769.
- [2] M. Springborg. *Methods of Electronic-Structure Calculations: From Molecules to Solids*. Wiley, 2000. ISBN 978-0-471-97975-3.
- [3] D. Sholl and J. Steckel. *Density Functional Theory: A Practical Introduction*. Wiley, 2009. ISBN 9780470447703.

- [4] K. Capelle. A bird's-eye view of density-functional theory. *Brazilian Journal of Physics*, 36:1318, 2006. doi: 10.1590/S0103-97332006000700035.
- [5] M. Holthausen W. Koch. *A Chemist's Guide to Density Functional Theory, Second Edition*. Wiley, 2001. ISBN 9783527303724. doi: 10.1002/3527600043.
- [6] V. Tapilin. A new method of solving the many-body schrödinger equation. *Journal of Structural Chemistry*, 58(1):1–8, 2017. doi: 10.1134/S0022476617010012.
- [7] Y.-H. Chen and S. Chao. Solving many-body schrödinger equations with kinetic energy partition method. *Annals of Physics*, 388:54–68, 2018. doi: 10.1016/j.aop.2017.11.002.
- [8] R. Hong, Y.-X. Xiao, J. Hu, A.-C. Ji, and S.-J. Ran. Functional tensor network solving many-body schrödinger equation. *Physical Review B*, 105(16):165116, 2022. doi: 10.1103/PhysRevB.105.165116.
- [9] J. Perdew, K. Burke, and M. Ernzerhof. Generalized gradient approximation made simple. *Physical Review Letters*, 77(18):3865–3868, 1996. doi: 10.1103/PhysRevLett.77.3865.
- [10] J. Perdew, K. Burke, and M. Ernzerhof. Erratum: Generalized gradient approximation made simple. *Physical Review Letters*, 78(7):1396–1396, 1997. doi: 10.1103/PhysRevLett.78.1396.
- [11] Jianmin Tao, John P Perdew, Viktor N Staroverov, and Gustavo E Scuseria. Climbing the density functional ladder: Nonempirical meta-generalized gradient approximation designed for molecules and solids. *Physical review letters*, 91(14):146401, 2003.
- [12] J. Heyd, G. Scuseria, and M. Ernzerhof. Hybrid functionals based on a screened coulomb potential. *The Journal of Chemical Physics*, 118(18):8207–8215, 2003. doi: 10.1063/1.1564060.
- [13] T. Bučko, S. Lebègue, J. Hafner, and J. Ángyán. Tkatchenko-scheffler van der waals correction method with and without self-consistent screening applied to solids. *Physical Review B*, 87:064110, 2013. doi: 10.1103/PhysRevB.87.064110.
- [14] G. Román-Pérez and J. Soler. Efficient implementation of a van der waals density functional: Application to double-wall carbon nanotubes. *Physical Review Letters*, 103:096102, Aug 2009. doi: 10.1103/PhysRevLett.103.096102.
- [15] H. Rydberg, M. Dion, N. Jacobson, E. Schröder, P. Hyldgaard, S. Simak, D. Langreth, and B. Lundqvist. Van der waals density functional for layered structures. *Physical Review Letters*, 91:126402, 2003. doi: 10.1103/PhysRevLett.91.126402.
- [16] C. Rêgo, L. Oliveira, P. Tereshchuk, and J. Silva. Comparative study of van der waals corrections to the bulk properties of graphite. *Journal of Physics: Condensed Matter*, 27(41):415502, sep 2015. doi: 10.1088/0953-8984/27/41/415502.
- [17] S. Grimme, J. Antony, S. Ehrlich, and H. Krieg. A consistent and accurate ab initio parametrization of density functional dispersion correction (dft-d) for the 94 elements h-pu. *The Journal of Chemical Physics*, 132(15):154104, 2010. doi: 10.1063/1.3382344.
- [18] S. Grimme, S. Ehrlich, and L. Goerigk. Effect of the damping function in dispersion corrected density functional theory. *Journal of Computational Chemistry*, 32(7):1456–1465, 2011. doi: <https://doi.org/10.1002/jcc.21759>.

- [19] A. Becke and E. Johnson. A density-functional model of the dispersion interaction. *The Journal of Chemical Physics*, 123(15):154101, 2005. doi: 10.1063/1.2065267.
- [20] A. Tkatchenko and M. Scheffler. Accurate molecular van der waals interactions from ground-state electron density and free-atom reference data. *Physical Review Letters*, 102:073005, 2009. doi: 10.1103/PhysRevLett.102.073005.
- [21] T. Bučko, S. Lebègue, J. Hafner, and J. Ángyán. Improved density dependent correction for the description of london dispersion forces. *Journal of Chemical Theory and Computation*, 9(10):4293–4299, 2013. doi: 10.1021/ct400694h.
- [22] D. Rappoport, N. Crawford, F. Furche, and K. Burke. *Approximate Density Functionals: Which Should I Choose?* John Wiley & Sons, Ltd, 2009. ISBN 9780470862100. doi: 10.1002/0470862106.ia615.
- [23] P. Borlido, J. Schmidt, A. Huran, F. Tran, M. Marques, and S. Botti. Exchange-correlation functionals for band gaps of solids: benchmark, reparametrization and machine learning. *npj Computational Material*, 6(1):96, 2020. doi: 10.1038/s41524-020-00360-0.
- [24] G. Kresse and J. Hafner. *Ab initio* molecular dynamics for liquid metals. *Physical Review B*, 47(1):558–561, 1993. doi: 10.1103/PhysRevB.47.558.
- [25] G. Kresse and J. Hafner. *Ab initio* molecular-dynamics simulation of the liquid-metal–amorphous-semiconductor transition in germanium. *Physical Review B*, 49(20):14251–14269, 1994. doi: 10.1103/PhysRevB.49.14251.
- [26] G. Kresse and J. Furthmüller. Efficiency of ab-initio total energy calculations for metals and semiconductors using a plane-wave basis set. *Computational Materials Science*, 6:15–50, 1996. doi: 10.1016/0927-0256(96)00008-0.
- [27] P. Giannozzi, S. Baroni, N. Bonini, M. Calandra, R. Car, C. Cavazzoni, D. Ceresoli, G. Chiarotti, M. Cococcioni, I. Dabo, A. Dal Corso, S. de Gironcoli, S. Fabris, G. Fratesi, R. Gebauer, U. Gerstmann, C. Gougoussis, A. Kokalj, M. Lazzeri, L. Martin-Samos, N. Marzari, F. Mauri, R. Mazzarello, S. Paolini, A. Pasquarello, L. Paulatto, C. Sbraccia, S. Scandolo, G. Sclauzero, A. Seitsonen, A. Smogunov, P. Umari, and R. Wentzcovitch. Quantum espresso: a modular and open-source software project for quantum simulations of materials. *Journal of Physics: Condensed Matter*, 21(39):395502, 2009. doi: 10.1088/0953-8984/21/39/395502.
- [28] P. Giannozzi, O. Andreussi, T. Brumme, O. Bunau, M. Nardelli, M. Calandra, R. Car, C. Cavazzoni, D. Ceresoli, M. Cococcioni, N. Colonna, I. Carnimeo, A. Dal Corso, S. de Gironcoli, P. Delugas, R. DiStasio, A. Ferretti, A. Floris, G. Fratesi, G. Fugallo, R. Gebauer, U. Gerstmann, F. Giustino, T. Gorni, J. Jia, M. Kawamura, H.-Y. Ko, A. Kokalj, E. Küçükbenli, M. Lazzeri, M. Marsili, N. Marzari, F. Mauri, N. Nguyen, H.-V. Nguyen, A. Otero de-la Roza, L. Paulatto, S. Poncé, D. Rocca, R. Sabatini, B. Santra, M. Schlipf, A. Seitsonen, A. Smogunov, I. Timrov, T. Thonhauser, P. Umari, N. Vast, X. Wu, and S. Baroni. Advanced capabilities for materials modelling with quantum espresso. *Journal of Physics: Condensed Matter*, 29(46):465901, 2017. doi: 10.1088/1361-648X/aa8f79.
- [29] M. Frisch, G. Trucks, H. Schlegel, G. Scuseria, M. Robb, J. Cheeseman, G. Scalmani, V. Barone, G. Petersson, H. Nakatsuji, X. Li, M. Caricato, A. Marenich, J. Bloino, B. Janesko, R. Gomperts, B. Mennucci, H. Hratchian, J. Ortiz, A. Izmaylov, J. Sonnenberg,

- D. Williams-Young, F. Ding, F. Lipparini, F. Egidi, J. Goings, B. Peng, A. Petrone, T. Henderson, D. Ranasinghe, V. Zakrzewski, J. Gao, N. Rega, G. Zheng, W. Liang, M. Hada, M. Ehara, K. Toyota, R. Fukuda, J. Hasegawa, M. Ishida, T. Nakajima, Y. Honda, O. Kitao, H. Nakai, T. Vreven, K. Throssell, J. Montgomery, J. Peralta, F. Ogliaro, M. Bearpark, J. Heyd, E. Brothers, K. Kudin, V. Staroverov, T. Keith, R. Kobayashi, J. Normand, K. Raghavachari, A. Rendell, J. Burant, S. Iyengar, J. Tomasi, M. Cossi, J. M. Millam, M. Klene, C. Adamo, R. Cammi, J. Ochterski, R. Martin, K. Morokuma, O. Farkas, J. Foresman, , and D. Fox. Gaussian 09 revision A.02. Gaussian Inc. Wallingford CT, 2016.
- [30] R. Dovesi, A. Erba, R. Orlando, C. Zicovich-Wilson, B. Civalleri, L. Maschio, M. Rérat, S. Casassa, J. Baima, S. Salustro, and B. Kirtman. Quantum-mechanical condensed matter simulations with crystal. *WIREs Computational Molecular Science*, 8(4):e1360, 2018. doi: 10.1002/wcms.1360.
- [31] H. Monkhorst and J. Pack. Special points for brillouin-zone integrations. *Physical Review B*, 13(12):5188–5192, 1976. doi: 10.1103/PhysRevB.13.5188.
- [32] P. Blöchl. Projector augmented-wave method. *Physical Review B*, 50(24):17953–17979, 1994. doi: 10.1103/PhysRevB.50.17953.
- [33] D. Vanderbilt. Soft self-consistent pseudopotentials in a generalized eigenvalue formalism. *Physical Review B*, 41(11):7892–7895, 1990. doi: 10.1103/PhysRevB.41.7892.
- [34] A. Togo and I. Tanaka. First principles phonon calculations in materials science. *Scripta Materialia*, 108:1–5, 2015. doi: 10.1016/j.scriptamat.2015.07.021.
- [35] F. Pascale, C. Zicovich-Wilson, F. López Gejo, B. Civalleri, R. Orlando, and R. Dovesi. The calculation of the vibrational frequencies of crystalline compounds and its implementation in the crystal code. *Journal of Computational Chemistry*, 25(6):888–897, 2004. doi: 10.1002/jcc.20019.
- [36] C. Zicovich-Wilson, F. Pascale, C. Roetti, V. Saunders, R. Orlando, and R. Dovesi. Calculation of the vibration frequencies of α -quartz: The effect of hamiltonian and basis set. *Journal of Computational Chemistry*, 25(15):1873–1881, 2004. doi: 10.1002/jcc.20120.
- [37] L. Maschio, B. Kirtman, M. Rérat, R. Orlando, and R. Dovesi. Ab initio analytical raman intensities for periodic systems through a coupled perturbed hartree-fock/kohn-sham method in an atomic orbital basis. i. theory. *The Journal of Chemical Physics*, 139(16):164101, 2013. doi: 10.1063/1.4824442.
- [38] L. Maschio, B. Kirtman, M. Rérat, R. Orlando, and R. Dovesi. Ab initio analytical raman intensities for periodic systems through a coupled perturbed hartree-fock/kohn-sham method in an atomic orbital basis. ii. validation and comparison with experiments. *The Journal of Chemical Physics*, 139(16):164102, 2013. doi: 10.1063/1.4824443.
- [39] F. Giustino. Electron-phonon interactions from first principles. *Reviews of Modern Physics*, 89(1):015003, 2017. doi: 10.1103/RevModPhys.89.015003.
- [40] G. Grimvall. *The Electron-phonon Interaction in Metals*. Science Education and Future Human Needs Series. North-Holland Publishing Company : sole distributors for the U.S.A. and Canada, Elsevier North-Holland, 1981. ISBN 9780444861054.

Chapter 3

A1 - Bonding frustration in the 9.5 GPa fcc polymeric C₆₀

© 2017 John Wiley & Sons, Inc.
Reprinted with permission.

Bonding Frustration in the 9.5 GPa fcc Polymeric C₆₀

Jorge Laranjeira, Leonel Marques,* Mohamed Mezouar, Manuel Melle-Franco, and Karol Strutyński

We argue that the face-centered cubic (fcc) polymeric C₆₀ phase obtained at 9.5 GPa can be mapped onto the classical frustrated Ising fcc antiferromagnet. Extensive density functional theory (DFT) calculations show that at 9.5 GPa 56/65 2+2 cycloaddition polymeric bonds are formed between neighboring molecules having different standard orientations but do not form when they have the same standard orientation. These “antiferromagnetic” bonds cannot be fully satisfied in the fcc lattice of the polymeric phase, resulting in a frustrated structure. By analyzing the ground state configurations of the frustrated Ising fcc antiferromagnet, a picture of the polymeric frustrated structure was obtained.

At high pressure, fullerite C₆₀ displays a plethora of phases in which the molecules form polymeric structures with bonding extending in different dimensionalities (for a recent review see Ref. [1]). This rich behavior attracted considerable interest and resulted in vast amount of experimental and theoretical work. [1–13] For pressures up to 8 GPa the scenario is well known and researchers agreed on main issues: ordered 1D chain polymers are formed at 1–2 GPa and 2D square and triangular layered polymers are formed at increasing pressures, all of these structures being based on the 66/66 2+2 cycloaddition (66/66 means that the polymerization reaction occurs between the intramolecular double bonds common to two hexagons). [2,3] At about 800 °C, the molecular structure collapses and transforms into new disordered carbon phases. [4,5] Above 8 GPa 3D polymerized phases are obtained, which indicates the presence of new types of polymeric bonds since 3D polymerized structures based only on the 66/66 2+2 cycloaddition bonds cannot be formed in a ABC-stacked lattice. [6–11] Several of such phases have been reported but only overall lattice parameters

have been given. [6–8] The exception are two phases prepared at 15 GPa and 600 °C, the cuboidal phase obtained from the compression of the 2D tetragonal phase and an fcc phase obtained by compressing C₆₀ pristine. [9–11] However, there are concerns about their proposed structures since they are not well reproduced in theoretical calculation. [10,12,13] Thus, much effort is still needed to clarify the structures of the 3D C₆₀ polymeric phases and their pressure-temperature stability domain.

We have obtained an fcc C₆₀ phase at 9.5 GPa and 550 °C. It is the same hard phase reported previously by Talyzin et al.

whose crystal structure is unknown. [14] Herein, we describe DFT investigations on the structure of this phase, which eventually led to the proposed frustrated structure. Synchrotron diffraction patterns collected during the high pressure synthesis are also presented.


Experimental Details: In situ diffraction studies were conducted at the ID27 beamline of the European Synchrotron Radiation Facility (ESRF), employing a Paris-Edinburgh press equipped with sintered diamond anvils. Sublimed C₆₀ powders purchased from MER Corporation (Tucson AZ, USA) were compressed to 9.5 GPa and subsequently heated to 550 °C, remaining 30 min in these conditions; heating was then stopped and the pressure was slowly released back to ambient conditions. A detailed description of the radial diffraction geometry used is given elsewhere. [15] A monochromatic beam ($\lambda = 0.53396$ Å) was used and the 2D angle dispersive diffraction images were collected in a MAR345 image plate detector. Diffraction data were processed using FIT2D program. [16] DFT optimizations of atomic positions and lattice constants were performed using the VASP software package. [17] The generalized gradient approximation was used for the exchange-correlation with the Perdew–Burke–Ernzerhof functional, [18] an energy cutoff of 520 eV and a $6 \times 6 \times 6$ k-point mesh were employed. Geometry optimizations were stopped when the energy change was less than 10^{-5} eV.

Results and Discussion: Integrated intensity diffraction 1D profiles obtained at different points of the pressure-temperature cycle is shown in **Figure 1**. In addition to the peak shifting to larger 2θ angles reflecting a compressed structure, high pressure and high temperature conditions also induce peak broadening. The patterns are indexed on fcc lattices, with unit cell constants of 12.79 Å at 9.5 GPa and 13.19 Å at room conditions for the recovered sample (at the end of the cycle). As was mentioned, this new fcc phase was previously obtained by Talyzin et al. at 13 GPa and 560 °C. [14] These pressure-temperature conditions

J. Laranjeira, Dr. L. Marques
Departamento de Física and CICECO
Universidade de Aveiro
3810-193 Aveiro, Portugal
E-mail: lmarques@ua.pt

Dr. M. Mezouar
European Synchrotron Radiation Facility, BP220
38043 Grenoble, France

Dr. M. Melle-Franco, Dr. K. Strutyński
Departamento de Química and CICECO
Universidade de Aveiro
3810-193 Aveiro, Portugal

 The ORCID identification number(s) for the author(s) of this article can be found under <https://doi.org/10.1002/pssr.201700343>.

DOI: 10.1002/pssr.201700343

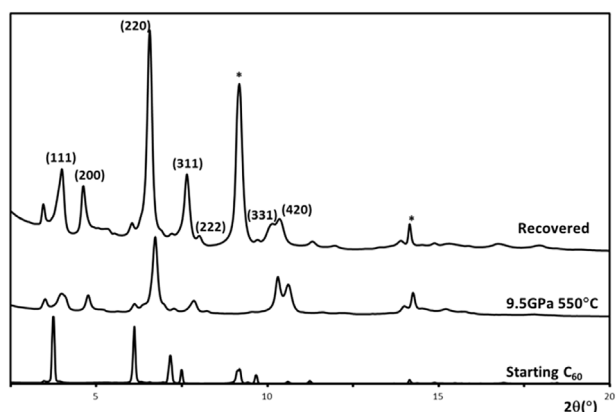


Figure 1. Integrated intensity diffraction 1D profiles obtained at different pressure–temperature conditions. Non-indexed peaks come from the amorphous-epoxy gasket and from the sample container h-BN (indicated by *).

are markedly different from ours; the reason for this difference is not understood. Talyzin et al. made an extensive characterization of the phase but no structural model was proposed.^[14]

As the polymeric phase has fcc symmetry, we have started investigating, via DFT methods, possible structures formed by molecules in their standard orientations, which are compatible with cubic symmetry.^[19] Each C_{60} molecule can adopt one of the two standard orientations, shown in **Figure 2a)** and denoted + and –. One standard orientation can be converted into the other through a 90° rotation about any $\langle 100 \rangle$ axes or through a rotation of $\approx 75.5^\circ$ about any $\langle 111 \rangle$ axes. We have found that polymeric bonds of the 56/65 2+2 cycloaddition type (56 means intramolecular single bond fusing a hexagon and a pentagon and which are involved in the polymerization reaction) were established between neighboring molecules with different standard orientations, + and – (see **Figure 2b)**. Interestingly,

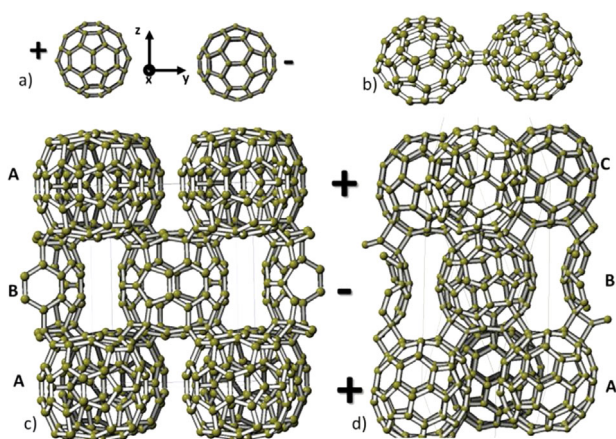


Figure 2. a) The two molecular standard orientations; b) 65/56 polymeric bond established between molecules in different standard orientations; c) ordered tetragonal optimized structure having “antiferromagnetic” polymeric bonds between the AB-stacked (001) planes; d) ordered rhombohedral optimized structure having “antiferromagnetic” polymeric bonds between the ABC-stacked (111) planes.

no polymeric bonds are formed between neighboring molecules with the same standard orientation, meaning that the polymeric bond corresponds to a + – “antiferromagnetic” interaction.

We now describe two of such ordered structures based on the molecular standard orientations that have been investigated. The first structure involves “antiferromagnetic” molecular ordering, + –, in the AB-stacked (001) fcc planes, and are described by the tetragonal space group $P4_2/mnm$ (see **Figure 2c)**. A second structure involves “antiferromagnetic” molecular ordering in the ABC-stacked (111) fcc planes, and belongs to the space group $R-3c$ (see **Figure 2d)**. The first case corresponds to the ordered structure of the binary alloy $AuCu$,^[20] whereas the last case corresponds to the ordered antiferromagnetic low-temperature structure of the simple oxide MnO .^[21] The starting structures subjected to DFT optimizations, although having tetragonal and rhombohedral symmetries, have their lattice constants constrained to the experimental cubic metrics (12.79 Å at high pressure and 13.19 Å at ambient pressure), with a unique near-neighbor (NN) distance to either “ferromagnetic”, ++ and – –, or “antiferromagnetic”, + –, connections. Each molecule of the starting structures is undeformed excepting the atoms pointing to each of the twelve neighboring molecules (either having + or – orientations), which were pulled out in order to have an intermolecular covalent distance of ≈ 1.5 Å.

Initial and optimized lattice constants are given in **Table 1**. They changed during the optimization evolving from the cubic metrics to distortions according to the structure symmetry. The exception is the tetragonal structure at high pressure, for which the lattice constants remained almost unchanged (this agreement is discussed later). For all other cases the c/a ratio of the optimized structures is smaller than those of the initial structures with cubic metrics, reflecting the existence of polymeric bonds between the “antiferromagnetic” ordered (001) or (111) planes and the absence of bonding within these planes. The optimized structures, whose atomic positions are given as Supporting Information, are shown in detail in **Figure 2c,d)**. Polymeric bonds remained between molecules with different orientations, + –, belonging to the different (001) or (111) planes, but no bonds survived between similarly oriented molecules within these planes. The structure optimization at ambient pressure was also computed, with the same results, using the high-pressure optimized structure as the starting model.

These ordered structures, having lattice distortions from cubic symmetry, cannot explain the observed fcc lattice. However, they give important clues to understand the 9.5 GPa polymeric structure, in particular, showing that the polymeric

Table 1. Initial and optimized lattice constants (in Å). Hexagonal 3R lattice parameters are given for the rhombohedral structure, in which the unit cell is doubled along c .

Structure	Initial (ambient)	Optimized (ambient)	Initial (9.5 GPa)	Optimized (9.5 GPa)
$P4_2/mnm$	$a = b = 9.33$; $c = 13.20$	$a = b = 9.32$; $c = 12.87$	$a = b = 9.01$; $c = 12.74$	$a = b = 9.07$; $c = 12.72$
$R-3c$	$a = b = 9.33$; $c = 22.85 \times 2$	$a = b = 9.52$; $c = 22.35 \times 2$	$a = b = 9.01$; $c = 22.07 \times 2$	$a = b = 9.19$; $c = 22.01 \times 2$

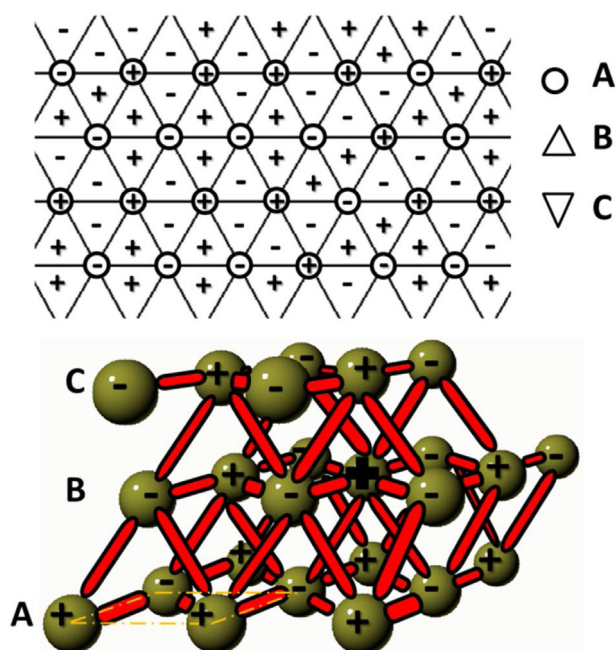


Figure 3. Top: one of the ground state configurations for the fcc antiferromagnetic Ising model viewed perpendicularly to the ABC-stacked layers, after Danielian.^[23] Bottom: polymeric bonding pattern according to the previous configuration (each sphere corresponds to a C_{60} molecule).

bond is analogue to the antiferromagnetic interaction. Thus, this polymeric system can be mapped onto the classical antiferromagnetic Ising model with NN interaction. This model is extensively studied and is used currently to describe magnetic systems, binary alloys and orientational glasses.^[22] When applied to an fcc lattice, it leads to a frustrated system, characterized by frustrated antiferromagnetic interactions and a degenerate ground state. Thus, the fcc polymeric phase must have a frustrated structure in which each molecule cannot establish polymeric bonds to all of its twelve NN. The ground state multiplicity of the frustrated Ising fcc antiferromagnet, as well as, its configurations were first determined by Danielian.^[23] One of the ground state configurations is depicted in **Figure 3**: each site has eight antiferromagnetic bonds and four frustrated ferromagnetic bonds. The polymeric structure mapped onto the ground state configuration is depicted in **Figure 3**, bottom. Each molecule is bonded to eight NN and the resulting bonding network extends throughout the space forming a 3D polymerized structure. We note that also an average of 8 bonds per molecule was obtained by Talyzin et al.,^[14] by extrapolating to the new phase the volume decrease of about 20 \AA^3 per new polymeric bond observed in low-pressure ($P < 8 \text{ GPa}$) polymers.

The more general ground state is disordered, containing a huge number of configurations, but a few of these configurations are ordered. The tetragonal structure discussed previously, containing eight “antiferromagnetic” polymeric bonds, is one of such ordered configurations. This is probably the reason its optimized lattice constants match the experimental values at high pressure. However, when the pressure is released to ambient conditions its relaxation is anisotropic according to the structure symmetry, while the experimental

frustrated structure, containing a huge number of configurations, remains cubic.

The C_{60} polymer structure probably does not match perfectly the ground state configurations of the frustrated antiferromagnetic Ising model, because a variable number of molecules could flip the orientations of the ground state configurations. The excited states created in this way have a number of bonds per molecule slightly smaller than the eight bonds characterizing the ground states. The variable number of flipping molecules, inducing a variable number of bonds per molecule, is in agreement with the variation of lattice constants in different points of the sample reported by Talyzin et al.^[14] Finally, the assumption of an equal number of molecules in each standard orientation needs a justification. The polymerization process in C_{60} is known to be started by forming dimers before higher oligomers and extended polymers are formed. In the present case the dimerized, $+ -$, state imply the same number of $+$ and $-$ molecules.

In conclusion, an fcc polymeric C_{60} phase was obtained at 9.5 GPa and 550 °C. Its structure can be explained by the frustration of “antiferromagnetic” polymeric bonds in the fcc lattice, mapping the frustrated Ising fcc antiferromagnet. The present work should revive investigations on the structures of other 3D polymeric phases which still remain unknown.

Supporting Information

Supporting Information is available from the Wiley Online Library or from the author.

Acknowledgements

Part of this work was developed within the scope of the project CICECO-Aveiro Institute of Materials, POCI-01-0145-FEDER-007679 (FCT Ref. UID/CTM/50011/2013), financed by national funds through the FCT/MEC and when appropriate co-financed by FEDER under the PT2020 Partnership Agreement (L. Marques, J. Laranjeira, M. Melle-Franco, and K. Strutyński). We warmly thank Jean-Louis Hodeau, Institut Néel, Grenoble, France, for his help during the synchrotron diffraction experiments.

Conflict of Interest

The authors declare no conflict of interest.

Keywords

density functional calculations, fullerenes, geometrical frustration, high-pressure synthesis, X-ray diffraction

Received: September 27, 2017
Revised: October 13, 2017
Published online: November 3, 2017

- [1] M. Álvarez-Murga, J.-L. Hodeau, *Carbon* **2015**, *82*, 381.
- [2] M. Núñez-Regueiro, L. Marques, J.-L. Hodeau, O. Béthoux, M. Perroux, *Phys. Rev. Lett.* **1995**, *74*, 278.
- [3] V. Agafonov, V. Davydov, L. Kashevarova, A. Rakhmanina, A. Kahn-Harari, P. Dubois, R. Céolin, H. Szwarc, *Chem. Phys. Lett.* **1997**, *267*, 193.

- [4] C. Lepoittevin, M. Álvarez-Murga, L. Marques, M. Mezouar, J.-L. Hodeau, *Carbon* **2013**, 52, 278.
- [5] O. Chernogorova, I. Potapova, E. Drozdova, V. Sirotinkin, A. Soldatov, A. Vasiliev, E. Ekimov, S. Sulyanov, N. Lvova, *Appl. Phys. Lett.* **2014**, 104, 043110.
- [6] L. Marques, M. Mezouar, J.-L. Hodeau, M. Nunez-Regueiro, N. Serebryanaya, V. Ivdenko, V. Blank, G. Dubitsky, *Science* **1999**, 283, 1720.
- [7] V. Brazhkin, A. Lyapin, S. Popova, Y. Klyuev, A. Naletov, *J. Appl. Phys.* **1998**, 84, 219.
- [8] S. Buga, V. Blank, Å. Fransson, N. Serebryanaya, S. Sundqvist, *J. Phys. Chem. Solids* **2002**, 63, 331.
- [9] S. Yamanaka, A. Kubo, K. Inumaru, K. Komaguchi, N. Kini, T. Inoue, T. Irifune, *Phys. Rev. Lett.* **2006**, 96, 076602.
- [10] S. Yamanaka, N. Kini, A. Kubo, S. Jida, H. Kuramoto, *J. Am. Chem. Soc.* **2008**, 130, 4303.
- [11] Y. Sato, M. Terauchi, S. Yamanaka, *Chem. Phys. Lett.* **2015**, 626, 90.
- [12] J. Yang, J. Tse, T. Iitaka, *J. Chem. Phys.* **2007**, 127, 134906.
- [13] F. Zipoli, M. Barnasconi, *Phys. Rev. B* **2008**, 77, 115432.
- [14] A. Talyzin, F. Langenhorst, N. Dubrovinskaia, S. Dub, L. Dubrovinsky, *Phys. Rev. B* **2005**, 71, 115424.
- [15] L. Marques, M. Mezouar, M. Núñez-Regueiro, J.-L. Hodeau, *Phys. Rev. B* **2003**, 68, 193408.
- [16] A. Hammersley, S. Svensson, M. Hanfland, A. Fitch, D. Hausermann, *High Press. Res.* **1996**, 14, 235.
- [17] G. Kresse, J. Furthmüller, *Phys. Rev. B* **1996**, 54, 11169.
- [18] J. Perdew, K. Burke, M. Ernzerhof, *Phys. Rev. Lett.* **1996**, 37, 3865.
- [19] P. Heiney, *J. Phys. Chem. Solids* **1992**, 53, 1333.
- [20] D. de Fontaine, *Solid State Phys.* **1979**, 34, 73.
- [21] G. Shull, W. Strauser, E. Wollan, *Phys. Rev.* **1951**, 83, 333; A. Goodwin, M. Tucker, M. Dove, D. Keen, *Phys. Rev. Lett.* **2006**, 96, 47209.
- [22] J. Lebowitz, D. Phani, D. Styer, *J. Stat. Phys.* **1985**, 38, 413.
- [23] A. Danielian, *Phys. Rev. Lett.* **1961**, 6, 670; A. Danielian, *Phys. Rev.* **1964**, 133, A1344.

SUPPORTING INFORMATION

Bonding Frustration in the 9.5 GPa fcc Polymeric C₆₀

[Phys. Status Solidi RRL, DOI 10.1002/pssr.201700343 (2017)]

J. Laranjeira¹, L. Marques^{*1}, M. Mezouar², M. Melle-Franco³, and K. Strutyński³

¹ Departamento de Física and CICECO, Universidade de Aveiro, 3810-193 Aveiro, Portugal

² European Synchrotron Radiation Facility, BP220, 38043 Grenoble, France

³ Departamento de Química and CICECO, Universidade de Aveiro, 3810-193 Aveiro, Portugal

* E-Mail: lmarques@ua.pt

Optimized ordered structures:

P4₂/mnm

atom	Room conditions			9.5GPa		
	x	y	z	x	y	z
C(1)	-0.44444	-0.44444	0.24578	-0.44366	-0.44366	0.24294
C(2)	0.25711	0.25711	0.05548	0.26543	0.26543	0.05583
C(3)	0.31908	-0.21062	0.00000	-0.17299	-0.28390	0.50000
C(4)	-0.29941	-0.47775	0.26428	-0.29695	-0.47742	0.26449
C(5)	-0.18691	0.36119	0.38881	-0.17901	0.35709	0.38860
C(6)	-0.16263	-0.37503	0.40900	-0.15543	-0.37243	0.40886
C(7)	-0.22279	-0.34376	0.30460	-0.21953	-0.34249	0.30524
C(8)	-0.25081	0.37169	0.28120	-0.24820	0.37078	0.28213
C(9)	-0.14299	0.48167	0.44361	-0.13652	0.48100	0.44352
Lattice parameters	a(angs)	B(angs)	c(angs)	a(angs)	b(angs)	c(angs)
	9.32	9.32	12.87	9.07	9.07	12.72

R-3c

atom	Room conditions			9.5GPa		
	x	y	z	x	y	z
C(1)	-0.29835	-0.21593	0.20223	0.38462	0.12785	0.03613
C(2)	-0.49425	-0.23340	0.24144	0.17723	0.10514	0.07455
C(3)	-0.24363	-0.15471	0.17239	0.43740	0.18988	0.00585
C(4)	-0.36297	-0.38463	0.20214	0.31592	-0.04643	0.03577
C(5)	-0.37651	-0.00595	0.20932	0.29718	0.33982	0.04301
C(6)	0.41190	-0.14309	0.24722	0.07550	0.19082	0.07999
C(7)	0.49315	0.01303	0.22492	0.15811	0.35206	0.05826
C(8)	-0.32915	0.04537	0.18036	0.34378	0.39215	0.01372
C(9)	0.43432	0.07271	0.17207	0.09800	0.41571	0.00545
C(10)	-0.37050	-0.14482	0.22078	0.30829	0.19991	0.05467
Lattice parameters	a(angs)	B(angs)	c(angs)	a(angs)	b(angs)	c(angs)
	9.52	9.52	44.70	9.19	9.19	44.02

Chapter 4

A2 - Three-dimensional C₆₀ polymers with ordered binary-alloy-type structures

© 2018 Elsevier Ltd.
Reprinted with permission.



Three-dimensional C₆₀ polymers with ordered binary-alloy-type structures

Jorge Laranjeira^a, Leonel Marques^{a,*}, Nuno M. Fortunato^{a,1}, Manuel Melle-Franco^b, Karol Strutyński^b, Manuel Barroso^c

^a Departamento de Física and CICECO, Universidade de Aveiro, 3810-193 Aveiro, Portugal

^b Departamento de Química and CICECO, Universidade de Aveiro, 3810-193 Aveiro, Portugal

^c Departamento de Física and I3N, Universidade de Aveiro, 3810-193 Aveiro, Portugal

ARTICLE INFO

Article history:

Received 28 March 2018

Received in revised form

15 May 2018

Accepted 29 May 2018

Available online 30 May 2018

Keywords:

DFT calculations

Fullerene polymers

Ordered binary-alloy structures

ABSTRACT

Three-dimensional (3D) C₆₀ polymer structures with each molecule in one of the two standard orientations, A or B, and analogue to ordered binary-alloy-type structures - AuCuI, Au₃Cu, CuPt, “A₂B₂”-, have been investigated by first principles density functional theory (DFT) methods. In all the studied structures, 56/56 2 + 2 cycloaddition polymeric bonds are formed between differently oriented neighboring molecules, but not between similarly oriented neighboring molecules, supporting our previous interpretation for the intermolecular covalent bonding as analogous to an Ising-type antiferromagnetic interaction. Optimized lattice constants and atomic positions were calculated at room and high pressure, as well as, the respective electronic structures. All the investigated structures are metallic, a trend common to the previously proposed 3D C₆₀ polymers.

© 2018 Elsevier Ltd. All rights reserved.

1. Introduction

Fullerite C₆₀ is a Van der Waals molecular solid with face centered cubic (fcc) structure at room temperature [1]. Its compression above 1 GPa (GPa) at moderate temperatures induces the formation of intermolecular bonds leading to polymers of different dimensionalities [2–12]. One-dimensional (1D) polymerized chains and 2-dimensional (2D), quadratic and triangular, polymerized layers are obtained at increasing pressures up to 8 GPa. All these low-dimensional polymer structures have a unique and common polymeric bond, 66/66 2 + 2 cycloaddition, a square ring established between the intramolecular double bonds joining the molecular hexagons [13]. Three-dimensional (3D) polymers are obtained above 8 GPa and different bonding architectures have been proposed, to explain both experimental [5–12] and computer simulations results [14–19].

These 3D polymers exhibit remarkable physical properties such as electron conductivity, low-compressibility and super-hardness [2–12]. 1D and 2D polymers are semiconductors with an

electronic band gap smaller than the C₆₀ monomer, which decreases with the increasing number of polymer bonds on each molecule [20–23]. On the other hand, 3D polymers usually show metallic behavior, despite the large quantity of sp³ carbons [8–10,14–18].

The poor crystallinity of the 3D C₆₀ polymers limits the accuracy of their x-ray crystal structures and, moreover, structural models are still lacking for some of these polymers. Thus, the prediction of new 3D polymer structures, and the underlying bonding schemes, is much awaited. In this regard, we have recently shown that the 3D polymer obtained at 9.5 GPa involves another type of intermolecular bond, 56/56 2 + 2 cycloaddition, connecting intramolecular single bonds of neighboring molecules [11]. In this polymer, each molecule adopts one of the two standard orientations, A or B, which are characterized by the alignment of three molecular two-fold axes along the Cartesian axes (see Fig. 1). This C₆₀ system can be mapped onto the antiferromagnetic Ising model, where one orientation A corresponds to spin up and the other orientation B corresponds to spin down. Actually, this model was already applied to alkali-metal fulleride superconductor, in which the molecules also adopt the standard orientations, to study the mechanism of orientational ordering in its ground state [24,25]. The recent discovery of unconventional superconductivity has reinvigorated the interest in these materials [26].

The antiferromagnetic Ising model is being used, other than in

* Corresponding author.

E-mail address: lmarques@ua.pt (L. Marques).

¹ present address: Department of Materials and Geosciences, TU Darmstadt, Darmstadt, 64287, Germany.

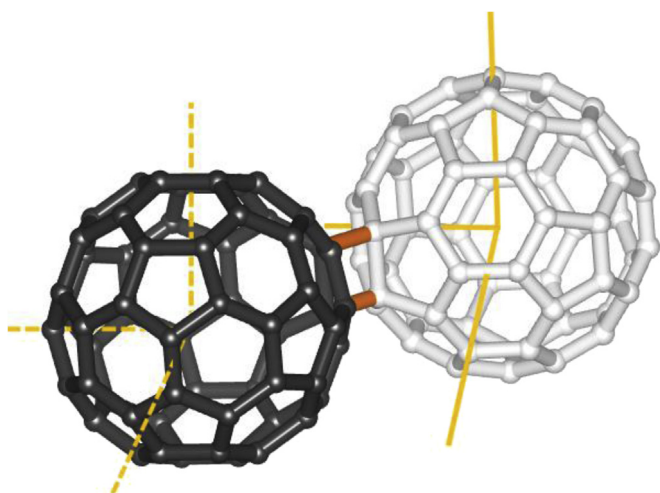


Fig. 1. Molecules in the two standard orientations, A and B, where three two-fold molecular axes (at the center of intramolecular double-bonds) are aligned along the three Cartesian axes (yellow solid and dashed lines). A 56/56 cycloaddition bond (in orange) is formed between the two differently oriented molecules. (A colour version of this figure can be viewed online.)

molecular and magnetic systems, to describe ordering in binary alloys, in particular to predict their stable ordered structures [27,28]. The most common ordered binary-alloy structures served as prototypes for us to construct several ordered C_{60} structures, with each molecule in one of the two standard orientations, A or B, extending our preliminary work on two of such structures. In all the studied structures 56/56 2 + 2 cycloaddition bonds are formed between inequivalent oriented molecules but not between similarly oriented molecules. The polymeric 56/56 2 + 2 cycloaddition bond is, thus, analogous to the Ising antiferromagnetic interaction strongly supporting our initial claim that this “antiferromagnetic” bond is involved in the 9.5 GPa 3D C_{60} polymer, although the fcc lattice experimentally observed points to a non-ordered/frustrated structure [11]. DFT optimized crystal structures and electronic structures are presented and discussed.

2. Methods

DFT calculations were performed within the Perdew-Burke-Ernzerhof (PBE) generalized gradient approximation (GGA) [29] with the plane wave (PW) Vienna ab initio simulation package (VASP) [30]. Electron-core interactions for carbon were described by the projector augmented wave pseudo-potentials supplied with VASP. Each self-consistent-field cycle was stopped once the energy difference between two consecutive steps was smaller than 10^{-5} eV; the k-points were converged within 10^{-5} meV/atom.

The crystal structures investigated in this study are shown in Fig. 2. The optimization of two of such structures, AuCuI-type and CuPt-type, was already reported by us [11]. Lattice constants and atomic positions were simultaneously optimized. A $6 \times 6 \times 6$ k-point mesh was used for all the structures, except for the large “ A_2B_2 ” structure, where a $4 \times 4 \times 4$ grid was employed. Optimizations were stopped once all forces were smaller than 0.01 eV/Å and a Gaussian smearing with standard deviation of 0.2 was used. An energy cutoff of 520 eV was employed.

The electronic density of states (DOS) was calculated using a $12 \times 12 \times 10$ k-point mesh for all the structures, except the large “ A_2B_2 ” structure, where a smaller, $10 \times 10 \times 10$ grid, was employed. The tetrahedron method with Blöchl corrections was used for smearing and an energy cutoff of at least 400 eV was employed.

The band structure calculations were made with 20 k-points between high-symmetric k-points (identified in the Supplementary data), employing an energy cutoff of at least 400 eV.

This methodology was also tested on other C_{60} high pressure polymers yielding similar results to a previous study [14]. Calculations on the AuCuI-type structure with spin polarization gave the same crystal and electronic structures as the non-magnetic calculations.

3. Results and discussion

3.1. Structural optimization

The investigations performed herein concern structures constructed with molecules in either one of the two standard orientations, A or B (see Fig. 1). We have used starting lattice constants corresponding to the experimental fcc metrics, $a = 13.19$ Å at room pressure and $a = 12.74$ Å at 9.5 GPa, the pressure where the polymeric 56/56 2 + 2 cycloaddition bonds presumably form [11]. Also, in the initial structural models the molecules were undeformed with exception of those atoms closer to the nearest neighboring molecules which were pulled out about 0.2 Å in order for them to lie at a covalent distance, ≈ 1.55 Å, from the closer atoms of the neighboring molecules. Note that using an alternative initial structural model with molecules fully undeformed in a compressed fcc lattice, so that the closest atoms of neighboring molecules lie also at a covalent distance, yields the same optimized structures.

Optimized lattice constants at room pressure and at 9.5 GPa are shown in Table 1. Optimized atomic coordinates for each structure are given in the Supplementary data section. Fig. 2 shows the optimized 3D polymer structures, with the corresponding alloy-type structures shown as insets. Structures 2(a) and 2(b) involve orientational antiferromagnetic ordering of ferromagnetic ordered (001) and (111) fcc planes, and are thus analogous to ordered AuCuI and to ordered CuPt alloy structures, respectively [28]. They are described by $P4_2/mnm$ and $R\bar{3}c$ space groups, respectively. Structure 2(c) involves stacking of antiferromagnetic ordered (001) fcc planes, doubling the fcc cell constant along the c axis. This structure is not adopted by any known binary-alloy but it is thoroughly considered in theoretical studies of alloy ordering [21,27,28]. It is denoted “ A_2B_2 ” by Binder and coworkers [27] and “40 structure” by Lou and coworkers [31]. It is described by space group $I4_1/amd$ and, as suggested by Allen and Cahn [28], can also be regarded as the AuCuII ordered structure with a period 2, instead of 10, along the superlattice direction. Finally, structure 2(d) described by $Pm\bar{3}$ space group, involves molecular ordering analogue to the Au_3Cu ordered structure, being the unique structure considered here with different populations (stoichiometry) of the two standard orientations, in a 3:1 ratio. The first two and the last structures are stabilized, within the Ising model, by including second neighbor ferromagnetic interactions, while the third structure, 2(c), is stabilized by antiferromagnetic second neighbor interactions [27]. These structures were chosen as they are usually found in fcc binary alloys, as well as, in their theoretical simulations. Obviously, other fcc binary-alloy structures could be considered (for instance the Al_3Ti -type structure).

In all these structures, 56/56 2 + 2 cycloaddition bonds are formed between differently oriented molecules (orange bonds in Figs. 1 and 2) but no bonds are formed between similarly oriented molecules. The intermolecular bond lengths, ranging from 1.58 Å, in the “ A_2B_2 ”-type structure, to 1.69 Å, in the Au_3Cu -type structure, are typical of covalent bonds of known C_{60} polymer structures (Supplementary data contains the complete list of the observed bond lengths). The notation, taken from Ref. [13], is 56/56 cycloaddition, the bonded molecules having different orientations, and

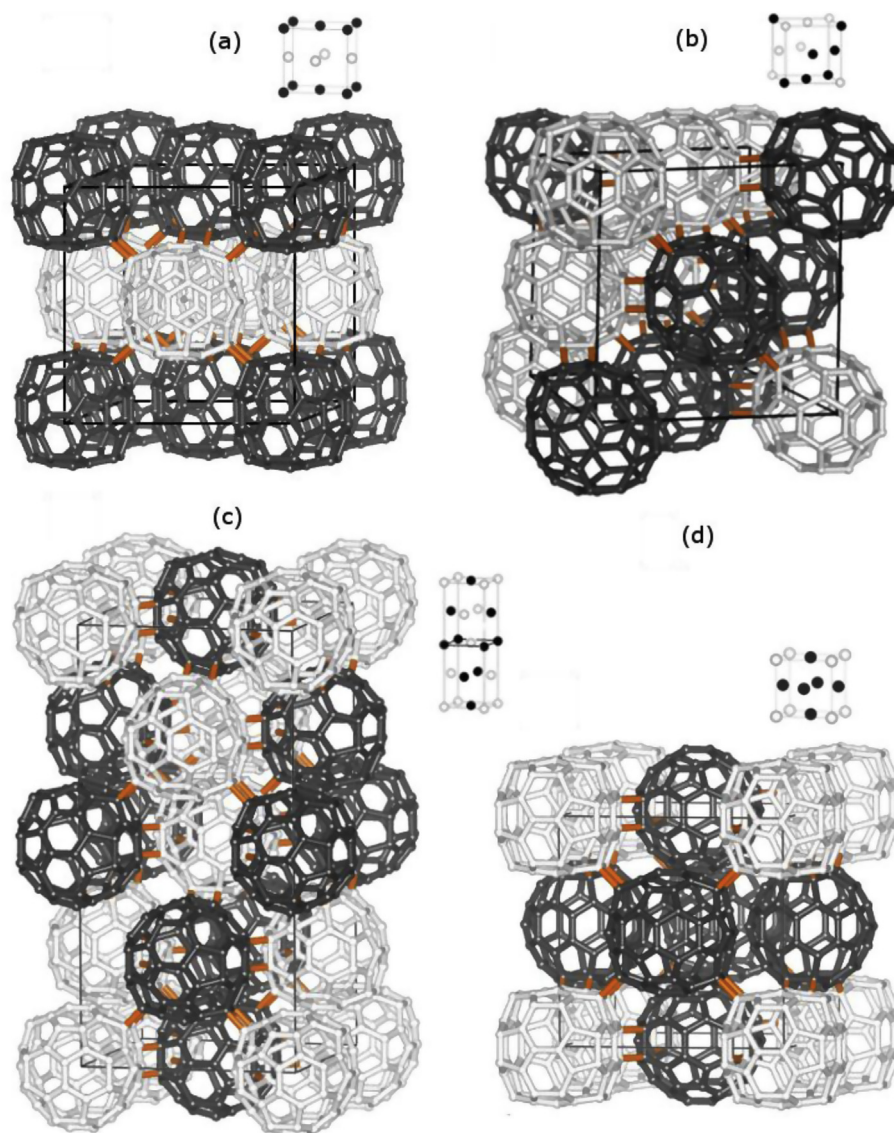


Fig. 2. 3D C_{60} polymer structures optimized at room pressure: (a) AuCuI-type; (b) CuPt-type; (c) “ A_2B_2 ”-type; (d) Au_3Cu -type. Differently oriented molecules are rendered in black/white structure and the polymeric bonds are rendered in orange. Corresponding binary-alloy structures are in the insets. (A colour version of this figure can be viewed online.)

Table 1

Optimized lattice constants (in Å). Hexagonal 3R cell constants are given for rhombohedral CuPt-type structure.

Space-group	Room pressure	9.5 GPa	Alloy-type structure
$P4_2/mnm$	$a = b = 9.32$; $c = 12.87$	$a = b = 9.07$; $c = 12.72$	AuCuI-type
$I4_1/amd$	$a = b = 12.99$; $c = 13.22 \times 2$	$a = b = 12.78$; $c = 12.83 \times 2$	“ A_2B_2 ”-type
R-3c	$a = b = 9.52$; $c = 22.35 \times 2$	$a = b = 9.19$; $c = 22.01 \times 2$	CuPt-type
Pm-3	$a = b = c = 13.15$	$a = b = c = 12.85$	Au_3Cu -type

not 56/65 as it was incorrectly named previously [11]. An ordered “ferromagnetic” structure with only one standard orientation, i.e. with only ferromagnetic interactions, was also considered, yet no bonds were formed in the final structure. All these results provide a robust confirmation that, in these structures, 56/56 2 + 2 cyclo-addition bonds are Ising-type antiferromagnetic interactions, giving additional evidence that the two-orientations C_{60} system can be mapped onto the Ising antiferromagnetic model. Relevantly, the “antiferromagnetic” bonding pattern extends in 3D space and, therefore, these structures are 3D C_{60} polymers.

$AuCuI$ and “ A_2B_2 ”-type structures are bonded to 8 neighboring molecules. Actually, these structures correspond to two configurations (ordered!) of the very large number ground state configurations of the frustrated Ising fcc antiferromagnet [32]. These configurations are characterized by 8 “antiferromagnetic” bonds and 4 frustrated interactions with nearest neighbors. They can easily be constructed by taking “antiferromagnetic” ordered (001) fcc planes and each time a plane is stacked two options can be taken, creating a stacking disorder along the [001] fcc direction [32].

Table 2

DFT total energies per atom for each structure.

Structure-type	Number of bonds per molecule	Energy/atom (eV) (room pressure)	Energy/atom (eV) (9.5 GPa)
AuCul	8	−8.725	−8.710
"A ₂ B ₂ "	8	−8.731	−8.715
CuPt	6	−8.756	−8.728
Au ₃ Cu	12; 4	−8.740	−8.714

In the CuPt-type rhombohedral structure each molecule has 6 bonded neighboring molecules and, within (111) fcc planes, 6 nonbonding neighbors. In the Au₃Cu-type structure the number of bonds are different for the two differently oriented molecules, A and B. The molecules with the less populated orientation have 12 polymeric bonds, each molecule being connected to all of its 12 nearest neighbors, while the molecules with the most populated orientation are bonded only to 4 neighboring molecules. The molecules of first type are strongly deformed, in an isotropic way, while those of the second type are deformed in the (001) fcc planes.

During the structural optimizations, all the structures evolved from the initial cubic metric to a metric according to their structural symmetry. In all cases, excluding obviously the cubic Au₃Cu-type structure, the fcc ratio *c/a* for the optimized structures is less than one. It is noted that for tetragonal structures, AuCul and "A₂B₂"-types, this evolution is minimal at high pressure, keeping a metric close to cubic. The lattice constants of these structures at high pressure are, thus, very close to the experimental ones, which could be related to the fact that these structures belong to the ground state configurations of the frustrated structure, presumably the true experimental structure [11].

The total energies per atom calculated for each structure, at room pressure and at 9.5 GPa, are shown in Table 2. As a reference, the calculated energy for the C₆₀ molecule is −8.850 eV/atom. Van der Waals interactions were not taken into account in the calculations, its effect being small [16]. The rhombohedral CuPt-type structure, which as the lowest number of bonds per molecule among all the structures considered, is the most stable polymer at room and high pressure. However, at high pressure the energies of the different structures become closer.

In addition, the second derivative of the energies was computed for all structures within the tight-binding formalism using the DFTB/3OB parametrization within the DFTB + software [33,34]. This yielded only positive frequencies, which confirms the dynamic stability of all the proposed structures. In order to characterize 56/56 bonds with respect to 66/66 bonds, we computed the stabilization energies and vibrational frequencies of related C₆₀ dimers. For this, we used the PBE-6-31g(d,p) Hamiltonian, which has been found to reproduce Raman frequencies on, the chemically similar, anthracene-C₆₀ adducts [35]. These computations were performed with Gaussian09 [36]. Four different C₆₀ dimers were computed, namely: dimers with 56/56 and 66/66 bonds, the single bond dimer, and an unbound dimer with no bonds between C₆₀ molecules. An analysis of the Hessian showed that the found geometries were minima with only positive frequencies in all cases. The

Table 3Calculated frequencies for the C₆₀ dimers.

Cyclo-butane breathing frequencies (cm ⁻¹)	
C ₆₀ -C ₆₀ 66/66 bonds	1064
C ₆₀ -C ₆₀ 56/56 bonds	1057
cyclobutane	1011
C-C stretching frequency (cm ⁻¹)	
ethane	1001

stabilization energies for 56/56 and 66/66 C₆₀ dimers were computed with respect to the chemically unbound dimer and are 0.77 and 0.03 eV respectively, which is coherent with observations from pericyclic reactions [37]. The dissociation barriers were estimated from the difference of energy with respect to the C₆₀ single bond dimer [38] and are 0.39 eV for 56/56 and 1.16 eV for 66/66, which matches remarkably well the 66/66 experimental estimation of 1.25 eV [39]. The lower energy needed to create 66/66 dimerized fullerenes together with the lower dissociation barrier for 56/56 dimerized fullerenes are probably the reason why at lower pressures the 66/66 bonding pattern is prevalent.

The vibrational frequencies for the symmetrical breathing of cyclobutane rings in the fullerene dimers with 66/66 and 56/56 bonds were computed within the harmonic approximation and are presented in Table 3. Interestingly, the frequencies of the 66/66 and 56/56 fullerene dimers are similar: 1064 and 1057 cm⁻¹ respectively, which indicates that 56/56 and 66/66 bonds are very similar. In comparison, the cyclobutane symmetrical breathing and the ethane C-C stretching, appear at ~50 cm⁻¹ lower frequencies indicating a higher double bond character for these bonds in polymerized fullerenes.

3.2. Electronic structure

Fullerite C₆₀ is a direct gap semiconductor at ambient conditions, with a 2.3–2.6 eV energy gap [40]. Local density approximation DFT calculations also point to semiconducting behavior for 1D and 2D polymerized fullerenes, with the electronic gap decreasing as the number of bonds in each molecule increases [20–22]. Xu and coworkers have obtained similar results using tight-binding methods [23]. Identical results were obtained using the methodology presented earlier in this paper. The electronic density of states (DOS) for the structures optimized at room pressure are shown in Fig. 3 (DOS for the structures optimized at high pressure are given as Supplementary data). As a point of comparison, DOS for "ferromagnetic" monomer is included in the same figure. All the structures have a finite non-zero number of states at the Fermi level and are, therefore, metallic (this is also observed at high pressure). We note that this metallic behavior is common to most 3D C₆₀ polymers studied so far, pointing to a gap closure induced by bonding patterns extended in 3D space [8–10,14–18]. The CuPt-type rhombohedral structure has the lowest density of states at the Fermi level, among the structures studied here, and it is barely metallic. This observation is probably directly connected to the intermolecular bonding since this structure shows the lowest number of polymeric bonds per molecule, 6.

Band structures of the 3D polymer structures optimized at room pressure are also shown in Fig. 3. In the monomer C₆₀, and, in a less extent, in the low-dimensional polymers, narrow energy bands derived from the molecular orbitals are observed. In the 3D polymer structures, the large number of sp³ carbons, symmetry reduction and the two molecular orientations involved, induces splitting and mixing of degenerate bands, creating states lying in a continuum of energy and leading to metallic behavior. Tetragonal AuCul and "A₂B₂"-type structures have an appreciable number of

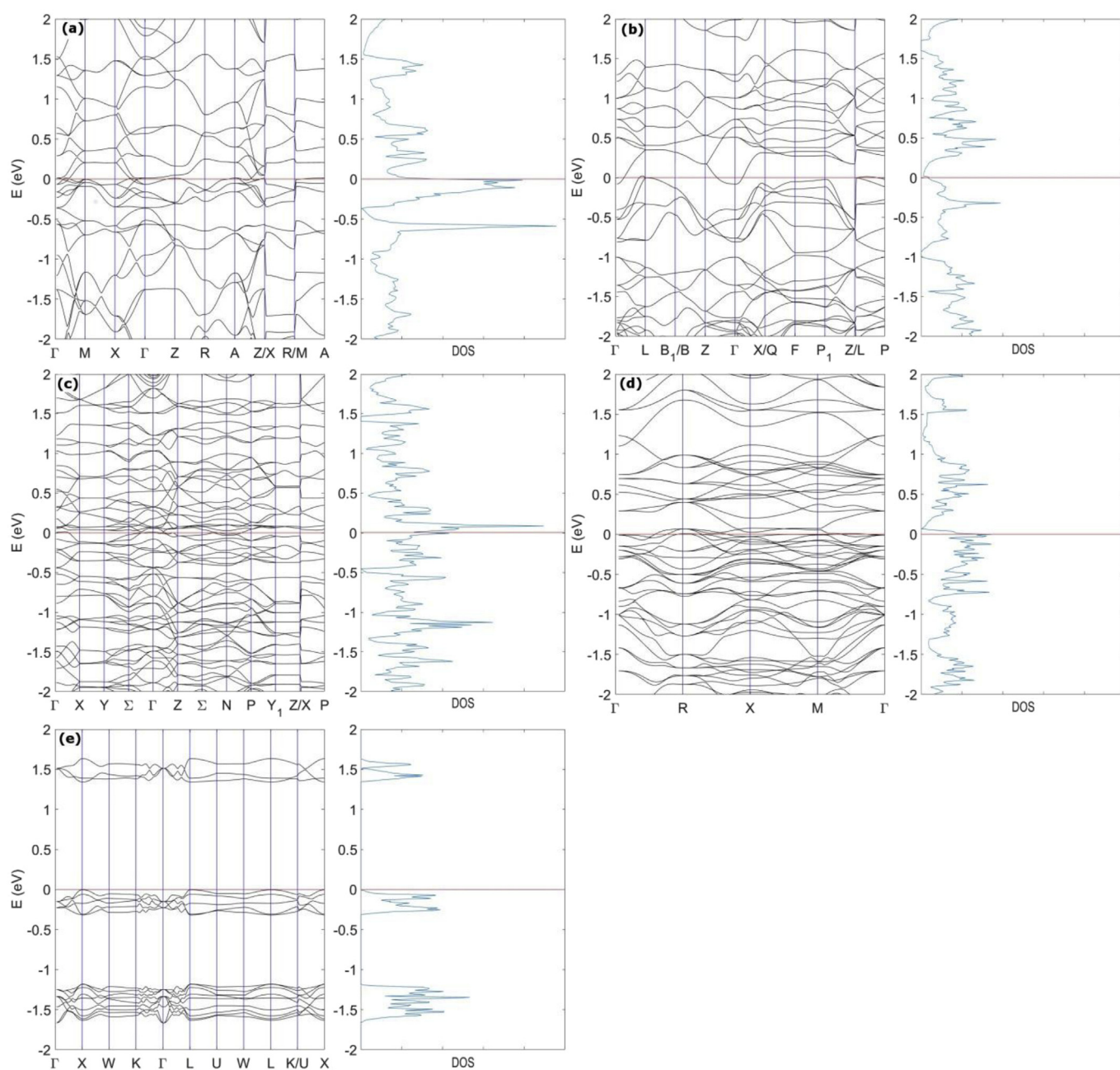


Fig. 3. Room pressure density of states (right panels) and band structures (left panels) of the polymeric structures, (a) AuCuI-type, (b) CuPt-type, (c) “A₂B₂”-type, (d) Au₃Cu-type and (e) of the “ferromagnetic” monomer structure. Red lines indicate the Fermi level. (A colour version of this figure can be viewed online.)

bands near the Fermi level. As a consequence, the Fermi level is located near a peak in the density of states. Yang and coworkers reported, for other 3D C₆₀ polymer structure, bands crossing the Fermi level with large dispersions that become flat near that energy, and they suggested that it could be a sign of superconductivity [14,15]. No similar bands were observed in the 3D polymer structures considered here. On the other hand, the CuPt-type rhombohedral structure, the structure with the lowest number of bonds per molecule, has fewer bands crossing the Fermi level, which, as referred, is at a local DOS minimum. At 9.5 GPa the polymer structures remain conductors and the band dispersions remain almost unchanged with respect to the scenario at ambient pressure.

In order to assess the reliability of these results, the computational methodology of this study was also explicitly benchmarked

against three different quantum chemistry methods ranging from tight-binding to different flavors of DFT with Gaussian and numeric basis sets for the AuCuI-type structure obtained with PW-PBE. The AuCuI-type structure has a $9.3 \times 9.3 \times 12.9 \text{ \AA}^3$ orthogonal unit cell containing 120 carbon atoms and is metallic at the PW-PBE level, and a relatively dense mesh of k points ($\geq 4 \times 4 \times 4$) was needed to correctly compute the electronic structure with all methods.

First, we computed AuCuI-type structure with the PBE functional with the “light” and “NAO-VCC-2Z” Numerical Atomic Orbitals (NAO) with a $4 \times 4 \times 4$ k-point grid ($8 \times 8 \times 8$ for DOS) with the program FHI-Aims [41–43]. The bands and density of states from NAO-PBE and PW-PBE are quite similar showing that both methodologies, as expected, give fundamentally the same results (see Fig. 4(b) and (c)).

Secondly, we computed the same properties with a hybrid Hamiltonian, HSE06, commonly used for periodic and molecular carbon systems [44]. For this, we used the program Crystal17 [45] with the STO-6G basis set on a $5 \times 5 \times 5$ k-point grid ($10 \times 10 \times 10$ for DOS). Note that probably STO-6G basis set is too small for this problem yet it was the largest that was computationally feasible on our resources. AuCuI-type structure is also metallic with the HSE06/STO-6G Hamiltonian, and the band structure looks fundamentally similar to the PBE, PW and NAO, Hamiltonians, although the bands show larger dispersion which is typical when hybrid and pure GGA functionals are compared. In addition, PBE shows a DOS peak below the Fermi energy, due to the low dispersion of frontier bands, which is not present in the HSE06 DOS (see Fig. 4 (d)).

Last, we computed AuCuI-type structure with a Density-

Functional-Tight-Binding (DFTB) Hamiltonian using the 3OB parameter [34] set on $8 \times 8 \times 8$ Monkhorst-Pack k-point grid ($8 \times 8 \times 8$ for DOS) with the DFTB + program [33]. The objective was to see how well more computationally efficient, semi-empirical, methods may address the electronic property of these materials. At the DFTB-OB level, the AuCuI-type structure is also metallic, and the bands are qualitatively similar to DFT models, yet the dispersion is different, appearing more similar to the HSE06 results (see Fig. 4 (e)).

Summing up, all methods coherently predict AuCuI-type structure to be metallic, which confirms the fundamental metallic nature of this structure. We did not find large differences between atom centered orbitals (numerical and Gaussian) and plane-wave calculations, showing that both methods give equivalent results

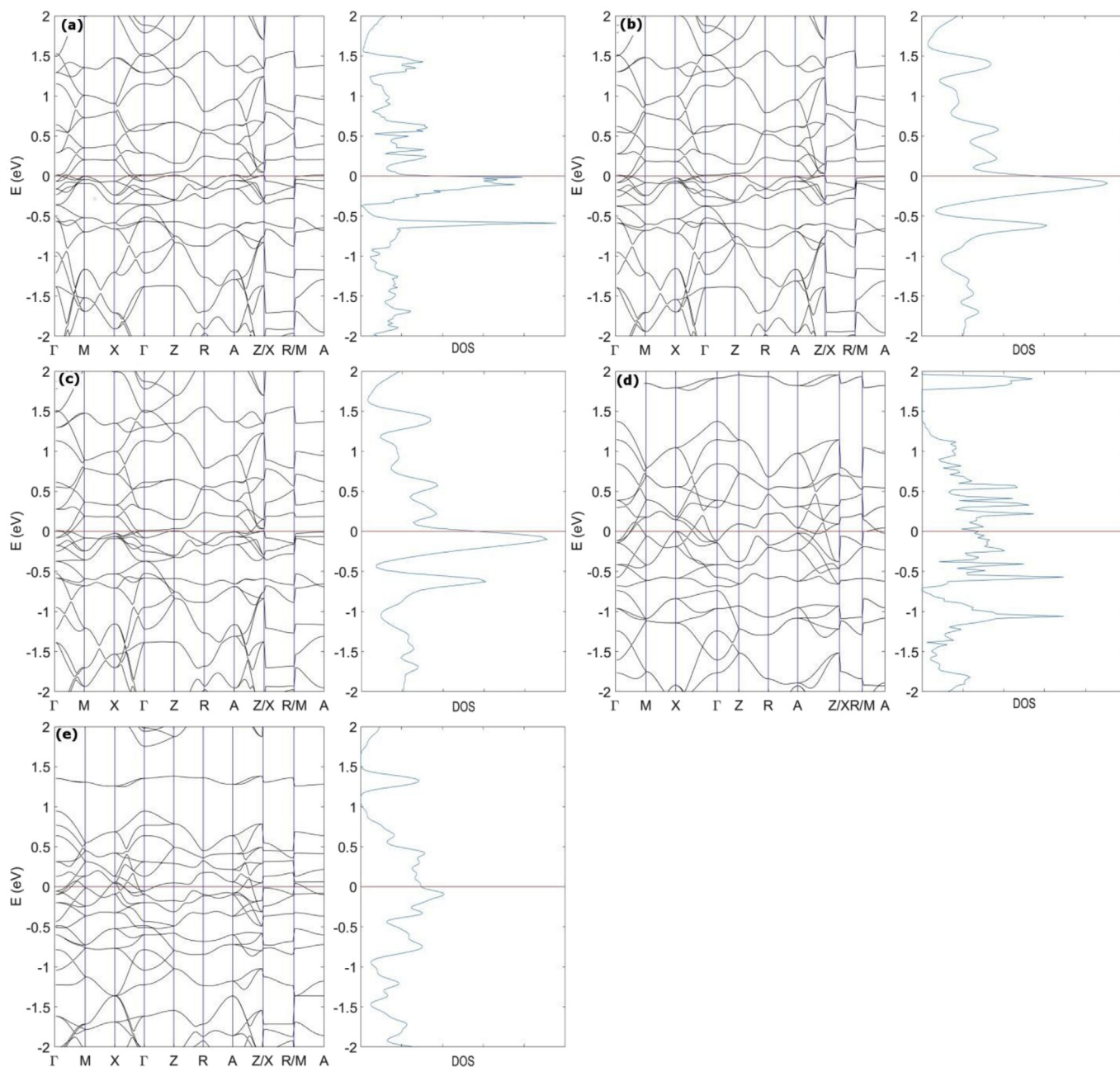


Fig. 4. Density of states (right panels) and band structures (left panels) of the polymeric AuCuI-type structure (optimized at 0 GPa) optimized with: (a) PW-PBE; (b) NAO-PBE/light, FHI-AIMS; (c) NAO-PBE/NAO-VCC-2Z, FHI-AIMS; (d) HSE06/STO-6G, Crystal17; (e) DFTB/3OB, DFTB+. Red lines indicate the Fermi levels. (A colour version of this figure can be viewed online.)

at the conditions computed. In addition, the simplified DFTB method seems to be applicable for this kind of materials.

4. Conclusions

We have shown that C_{60} molecules in the standard orientations form “antiferromagnetic” 56/56 cycloaddition bonds with differently oriented molecules, a robust finding which is independent of the configurations used. In the binary-alloy-type structures investigated here these polymeric bonds form a 3D network, displaying systematically metallic character. This bonding mechanism is involved in 3D C_{60} polymers found at 9.5 GPa and may also be present in some other 3D polymers whose structures have not yet been elucidated. The list of alloy ordered structures considered here is far from being exhaustive and thus other prototypes might be considered in forthcoming studies. These ordered alloy-type C_{60} structures are candidates to be observed experimentally once the observed frustration could be relieved.

Acknowledgements

This work was developed within the scope of the project CICECO-Aveiro Institute of Materials, POCI-01-0145-FEDER-007679 (FCT Ref. UID/CTM/50011/2013), financed by national funds through the FCT/MEC (UID/CTM/50011/2013) and when appropriate co-financed by FEDER (POCI-01-0145-FEDER-007679) under the PT2020 Partnership Agreement (JL, LM, MM-F, KS).

Appendix A. Supplementary data

Supplementary data related to this article can be found at <https://doi.org/10.1016/j.carbon.2018.05.070>.

References

- [1] P.A. Heiney, Structure, dynamics and ordering transition of solid C_{60} , *J. Phys. Chem. Solid.* 53 (1992) 1333–1352, [https://doi.org/10.1016/0022-3697\(92\)90231-2](https://doi.org/10.1016/0022-3697(92)90231-2).
- [2] M. Álvarez-Murga, J.-L. Hodeau, Structural phase transitions of C_{60} under high-pressure and high-temperature, *Carbon* 82 (2015) 381–407, <https://doi.org/10.1016/j.carbon.2014.10.083>.
- [3] M. Núñez-Regueiro, L. Marques, J.-L. Hodeau, O. Béthoux, M. Perroux, Polymerized fullerite structures, *Phys. Rev. Lett.* 74 (1995) 278–281, <https://doi.org/10.1103/PhysRevLett.74.278>.
- [4] V. Agafonov, V. Davydov, L. Kashevarova, A. Rakhmanina, A. Kahn-Harari, P. Dubois, R. Céolin, H. Szwarc, “Low-pressure” orthorhombic phase formed from pressure-treated C_{60} , *Chem. Phys. Lett.* 267 (1997) 193–198, [https://doi.org/10.1016/S0009-2614\(97\)00072-9](https://doi.org/10.1016/S0009-2614(97)00072-9).
- [5] V. Brazhkin, A. Lyapin, S. Popova, Y. Klyuev, A. Naletov, Mechanical properties of the 3D polymerized, sp^2 - sp^3 amorphous, and diamond-plus-graphite nanocomposite carbon phases prepared from C_{60} under high pressure, *J. Appl. Phys.* 84 (1998) 219–226, <https://doi.org/10.1063/1.368021>.
- [6] L. Marques, M. Mezouar, J.-L. Hodeau, M. Núñez-Regueiro, N. Serebryanaya, V. Ivdenko, V. Blank, G. Dubitsky, “Debye-Scherrer ellipses” from 3D fullerene polymers: an anisotropic pressure memory signature, *Science* 283 (1999) 1720–1723, <https://doi.org/10.1126/science.283.5408.1720>.
- [7] S. Buga, V. Blank, Å. Fransson, N. Serebryanaya, B. Sundqvist, DSC study of annealing and phase transformations of C_{60} and C_{70} polymerized under pressures in the range 9.5–13 GPa, *J. Phys. Chem. Solid.* 63 (2002) 331–343, [https://doi.org/10.1016/S0022-3697\(01\)00150-0](https://doi.org/10.1016/S0022-3697(01)00150-0).
- [8] S. Yamanaka, A. Kubo, K. Inumaru, K. Komaguchi, N. Kini, T. Inoue, T. Irifune, Electron conductive three-dimensional polymer of cuboidal C_{60} , *Phys. Rev. Lett.* 96 (2006), 076602, <https://doi.org/10.1103/PhysRevLett.96.076602>.
- [9] S. Yamanaka, N. Kini, A. Kubo, S. Jida, H. Kuramoto, Topochemical 3D polymerization of C_{60} under high pressure at elevated temperatures, *J. Am. Chem. Soc.* 130 (2008) 4303–4309, <https://doi.org/10.1021/ja076761k>.
- [10] Y. Sato, M. Terauchi, S. Yamanaka, Electronic structures of three-dimensional C_{60} polymers studied by high-energy-resolution electron energy-loss spectroscopy based on transmission electron microscopy, *Chem. Phys. Lett.* 626 (2015) 90–95, <https://doi.org/10.1016/j.cplett.2015.03.017>.
- [11] J. Laranjeira, L. Marques, M. Mezouar, M. Melle-Franco, K. Strutyński, Bonding frustration in the 9.5 GPa fcc polymeric C_{60} , *Phys. Stat. Sol. - RRL* 11 (2017), 1700343, <https://doi.org/10.1002/pssr.201700343>.
- [12] M. Mezouar, L. Marques, J.-L. Hodeau, V. Pischedda, M. Núñez-Regueiro, Equation of state of an anisotropic three-dimensional C_{60} polymer: the most stable form of fullerene, *Phys. Rev. B* 68 (2003), 193414, <https://doi.org/10.1103/PhysRevB.68.193414>.
- [13] D. Strout, R. Murry, C. Xu, W. Eckho, G. Odom, G. Scuseria, A theoretical study of buckminsterfullerene reaction products: $C_{60}+C_{60}$, *Chem. Phys. Lett.* 214 (1993) 576–582, [https://doi.org/10.1016/0009-2614\(93\)85686-1](https://doi.org/10.1016/0009-2614(93)85686-1).
- [14] J. Yang, J. Tse, T. Litaka, First-principles investigation on the geometry and electronic structure of the three-dimensional cuboidal C_{60} polymer, *J. Chem. Phys.* 127 (2007), 134906, <https://doi.org/10.1063/1.2771162>.
- [15] J. Yang, J. Tse, Y. Yao, T. Litaka, Structural and electronic properties of pristine and Ba-doped clathrate-like carbon fullerenes, *Angew. Chem.* 46 (2007) 6275–6277, <https://doi.org/10.1002/anie.200701555>.
- [16] F. Zipoli, M. Bernasconi, First principles study of three-dimensional polymers of C_{60} : structure, electronic properties, and Raman spectra, *Phys. Rev. B* 77 (2008), 115432, <https://doi.org/10.1103/PhysRevB.77.115432>.
- [17] Y. Yamagami, S. Saito, Polymerized sp^2 - sp^3 hybrid metallic phase of C_{60} as obtained via constant-pressure molecular dynamics, *Phys. Rev. B* 79 (2009), 045425, <https://doi.org/10.1103/PhysRevB.79.045425>.
- [18] S. Okada, S. Saito, A. Oshiyama, New metallic crystalline carbon: three dimensionally polymerized C_{60} fullerite, *Phys. Rev. Lett.* 83 (1999) 1986–1989, <https://doi.org/10.1103/PhysRevLett.83.1986>.
- [19] S. Berber, E. Osawa, D. Tománek, Rigid crystalline phases of polymerized fullerenes, *Phys. Rev. B* 70 (2004), 085417, <https://doi.org/10.1103/PhysRevB.70.085417>.
- [20] S. Okada, S. Saito, Electronic structure and energetics of pressure-induced two-dimensional C_{60} polymers, *Phys. Rev. B* 59 (1999) 1930–1936, <https://doi.org/10.1103/PhysRevB.59.1930>.
- [21] S. Okada, S. Saito, Rhombohedral C_{60} polymer: a semiconducting solid carbon structure, *Phys. Rev. B* 55 (1997) 4039–4041, <https://doi.org/10.1103/PhysRevB.55.4039>.
- [22] T. Miyake, S. Saito, Geometry and electronic structure of rhombohedral C_{60} polymer, *Chem. Phys. Lett.* 380 (2003) 589–594, <https://doi.org/10.1016/j.cplett.2003.09.067>.
- [23] C. Xu, G. Scuseria, Theoretical predictions for a two-dimensional rhombohedral phase of solid C_{60} , *Phys. Rev. Lett.* 74 (1995) 274–277, <https://doi.org/10.1103/PhysRevLett.74.274>.
- [24] I. Mazin, A. Liechtenstein, O. Gunnarsson, O. Andersen, V. Antropov, S. Burkov, Orientational order in A_3C_{60} : antiferromagnetic Ising model for the fcc lattice, *Phys. Rev. Lett.* 70 (1993) 4142–4145, <https://doi.org/10.1103/PhysRevLett.70.4142>.
- [25] T. Yildirim, S. Hong, A. Harris, E. Mele, Orientational phases for M_3C_{60} , *Phys. Rev. B* 48 (1993) 12262–12277, <https://doi.org/10.1103/PhysRevB.48.12262>.
- [26] Y. Takabayashi, K. Prassides, The renaissance of fullerene superconductivity, *Struct. Bond* 172 (2017) 119–138, https://doi.org/10.1007/430_2015_207.
- [27] K. Binder, J. Lebowitz, M. Phani, M. Kalos, Monte Carlo study of the phase diagrams of binary alloys with face centered cubic lattice structure, *Acta Metall.* 29 (1981) 1655–1665, [https://doi.org/10.1016/0001-6160\(81\)90048-1](https://doi.org/10.1016/0001-6160(81)90048-1).
- [28] S. Allen, J. Cahn, Ground state structures in ordered binary alloys with second neighbor interactions, *Acta Metall.* 20 (1972) 423–433, [https://doi.org/10.1016/0001-6160\(72\)90037-5](https://doi.org/10.1016/0001-6160(72)90037-5).
- [29] J. Perdew, K. Burke, M. Ernzerhof, Generalized gradient approximation made simple, *Phys. Rev. Lett.* 77 (1996) 3865–3868, <https://doi.org/10.1103/PhysRevLett.77.3865>.
- [30] G. Kresse, J. Furthmüller, Efficient iterative schemes for ab initio total-energy calculations using a plane-wave basis set, *Phys. Rev. B* 54 (1996) 11169–11186, <https://doi.org/10.1103/PhysRevB.54.11169>.
- [31] Z. Lu, S.-H. Wei, A. Zunger, S. Frota-Pessoa, L. Ferreira, First-principles statistical mechanics of structural stability of intermetallic compounds, *Phys. Rev. B* 44 (1991) 512–544, <https://doi.org/10.1103/PhysRevB.44.512>.
- [32] A. Danielian, Ground state of an Ising face-centered cubic lattice, *Phys. Rev. Lett.* 6 (1961) 670–671, <https://doi.org/10.1103/PhysRevLett.6.670>.
- [33] B. Aradi, B. Hourahine, T. Frauenheim, Dftb+, a sparse matrix-based implementation of the dftb method, *J. Phys. Chem. A* 111 (2007) 5678–5684, <https://doi.org/10.1021/jp070186p>.
- [34] M. Gaus, A. Goez, M. Elstner, Parametrization and benchmark of dftb3 for organic molecules, *J. Chem. Theor. Comput.* 9 (2013) 338–354, <https://doi.org/10.1021/ct300849w>.
- [35] R. Pfeiffer, C. Kramberger, H. Peterlik, H. Kuzmany, B. Kräutler, M. Melle-Franco, F. Zerbetto, FT-Raman characterization of the antipodal bis-adduct of C_{60} and anthracene, *Phys. Status Solidi B* 246 (2009) 2794–2797, <https://doi.org/10.1002/pssb.200982302>.
- [36] M.J. Frisch, G.W. Trucks, H.B. Schlegel, G.E. Scuseria, M.A. Robb, J.R. Cheeseman, G. Scalmani, V. Barone, G.A. Petersson, H. Nakatsuji, X. Li, M. Caricato, A. Marenich, J. Bloino, B.G. Janesko, R. Gomperts, B. Mennucci, H.P. Hratchian, J.V. Ortiz, A.F. Izmaylov, J.L. Sonnenberg, D. Williams-Young, F. Ding, F. Lipparini, F. Egidi, J. Goings, B. Peng, A. Petrone, T. Henderson, D. Ranasinghe, V.G. Zakrzewski, J. Gao, N. Rega, G. Zheng, W. Liang, M. Hada, M. Ehara, K. Toyota, R. Fukuda, J. Hasegawa, M. Ishida, T. Nakajima, Y. Honda, O. Kitao, H. Nakai, T. Vreven, K. Throssell, J.A. Montgomery Jr., J.E. Peralta, F. Ogliaro, M. Bearpark, J.J. Heyd, E. Brothers, K.N. Kudin, V.N. Staroverov, T. Keith, R. Kobayashi, J. Normand, K. Raghavachari, A. Rendell, J.C. Burant, S.S. Iyengar, J. Tomasi, M. Cossi, J.M. Millam, M. Klene, C. Adamo, R. Cammi, J.W. Ochterski, R.L. Martin, K. Morokuma, O. Farkas, J.B. Foresman, D.J. Fox, Gaussian 09, Revision A.02, Gaussian, Inc, Wallingford CT, 2016. <http://>

- gaussian.com/.
- [37] P. Plat, Y. Wang, M. Alcamí, Simple bond patterns predict the stability of Diels-Alder adducts of empty fullerenes, *Chem. Commun. (J. Chem. Soc. Sect. D)* 54 (2018) 4156–4159, <https://doi.org/10.1039/c8cc01709c>.
- [38] D. Porezag, M. Pederson, T. Frauenheim, T. Köhler, Structure, stability and vibrational properties of polymerized C₆₀, *Phys. Rev. B* 52 (1995) 14963–14970, <https://doi.org/10.1103/PhysRevB.52.14963>.
- [39] Y. Wang, J. Holden, X. Bi, P. Eklund, Thermal decomposition of polymeric C₆₀, *Chem. Phys. Lett.* 217 (1994) 413–417, [https://doi.org/10.1016/0009-2614\(93\)E1409-A](https://doi.org/10.1016/0009-2614(93)E1409-A).
- [40] W. Andreoni, P. Giannozzi, Structural and Electronic Properties of C₆₀ and C₇₀ Derivatives in the Solid Phases: Calculations Based on Density-functional Theory, *Physics of Fullerene-Based and Fullerene-Related Materials*, chap. 8, pg. 172, Springer, 2000, https://doi.org/10.1007/978-94-011-4038-6_8.
- [41] V. Blum, R. Gehrke, F. Hanke, P. Havu, V. Havu, X. Ren, K. Reuter, M. Scheffler, Ab initio molecular simulations with numeric atom-centered orbitals, *Comput. Phys. Commun.* 180 (2009) 2175–2196, <https://doi.org/10.1016/j.cpc.2009.06.022>.
- [42] A. Marek, V. Blum, R. Johanni, V. Havu, B. Lang, T. Auckenthaler, A. Heinecke, H.-J. Bungartz, H. Lederer, The ELPA library: scalable parallel eigenvalue solutions for electronic structure theory and computational science, *J. Phys. Condens. Matter* 26 (2014), 213201, <https://doi.org/10.1088/0953-8984/26/21/213201>.
- [43] V. Yu, F. Corsetti, A. García, W. Huhn, M. Jacquelin, W. Jia, B. Lange, L. Lin, J. Lu, W. Mi, A. Seifitokaldani, A. Vázquez-Mayagoitia, C. Yang, H. Yang, V. Blum, ELSA: a unified interface for Kohn-Sham electronic software solvers, *Comput. Phys. Commun.* 222 (2018) 267–285, <https://doi.org/10.1016/j.cpc.2017.09.007>.
- [44] M. Melle-Franco, Uthrene, a radically new molecule? *Chem. Commun. (J. Chem. Soc. Sect. D)* 51 (2015) 5387–5390, <https://doi.org/10.1039/c5cc01276g>.
- [45] A. Erba, J. Baima, I. Bush, R. Orlando, R. Dovesi, Large-scale condensed matter DFT simulations: performance and capabilities of the CRYSTAL code, *J. Chem. Theor. Comput.* 13 (2017) 5019–5027, <https://doi.org/10.1021/acs.jctc.7b00687>.

Supplementary data

K-point path

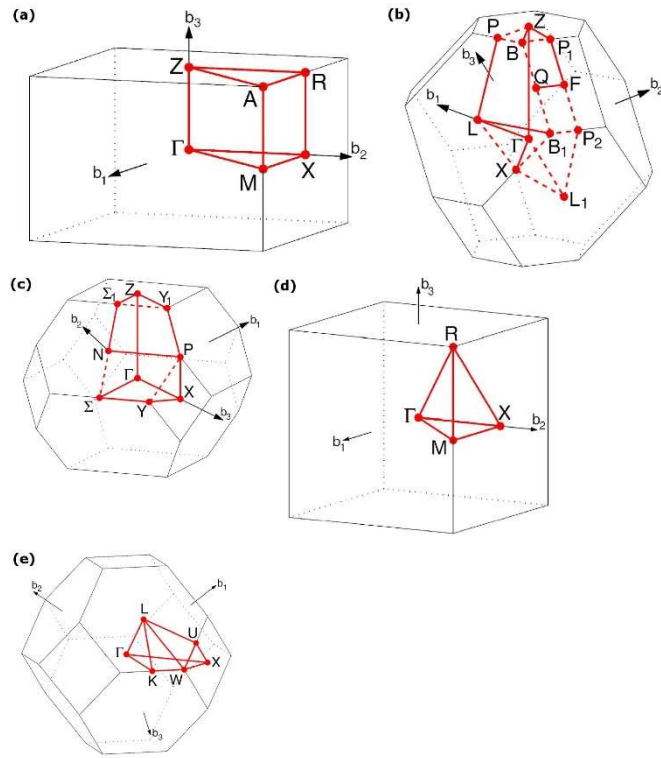


Figure 5. Considered structures first BZ and high symmetry K-Points. (a) AuCuI-type; (b) CuPt-type; (c) “ A_2B_2 ”-type; (d) Au_3Cu -type; (e) Monomer “Ferromagnetic” structure.

Optimized Atomic positions

Table 4. Fractional atomic coordinates of AuCuI-type structure after ionic, cell shape and volume relaxation at room pressure (left) and at 9.5GPa (right), and lattice parameters after relaxation.

atom	Room pressure			9.5 GPa		
	x	y	z	x	y	z
C(1)	-0.44444	-0.44444	0.24578	-0.44366	-0.44366	0.24294
C(2)	0.25711	0.25711	0.05548	0.26543	0.26543	0.05583
C(3)	0.31908	-0.21062	0.00000	-0.17299	-0.28390	0.50000
C(4)	-0.29941	-0.47775	0.26428	-0.29695	-0.47742	0.26449
C(5)	-0.18691	0.36119	0.38881	-0.17901	0.35709	0.38860
C(6)	-0.16263	-0.37503	0.40900	-0.15543	-0.37243	0.40886
C(7)	-0.22279	-0.34376	0.30460	-0.21953	-0.34249	0.30524
C(8)	-0.25081	0.37169	0.28120	-0.24820	0.37078	0.28213
C(9)	-0.14299	0.48167	0.44361	-0.13652	0.48100	0.44352
Lattice parameters	a(Å)	b(Å)	c(Å)	a(Å)	b(Å)	c(Å)
	9.32	9.32	12.87	9.07	9.07	12.72

Table 5. Fractional atomic coordinates of “ A_2B_2 ”-type structure after ionic, cell shape and volume relaxation at room pressure (left) and at 9.5GPa (right), and lattice parameters after relaxation.

atom	Room pressure			9.5 GPa		
	x	y	z	x	y	z
C(1)	0.00000	0.30486	0.49339	0.00000	0.30560	0.48909
C(2)	0.00000	0.30518	-0.24649	0.00000	0.30571	-0.24259
C(3)	0.00000	-0.01002	0.15455	0.00000	-0.01385	0.15465
C(4)	0.00000	-0.01200	0.09991	0.00000	-0.01735	0.09878
C(5)	-0.44403	0.00522	0.12738	-0.44355	0.01043	0.12645
C(6)	-0.40898	-0.14236	0.00957	-0.40861	-0.14106	0.00637
C(7)	-0.26294	-0.15957	0.06836	-0.26177	-0.15914	0.06771
C(8)	-0.38901	-0.47675	0.08232	-0.38806	-0.48022	0.08051
C(9)	-0.41131	-0.13910	0.23855	-0.41040	-0.13848	0.24127
C(10)	-0.26822	-0.16039	0.17711	-0.26541	-0.15978	0.17847
C(11)	-0.38707	-0.01479	0.17031	-0.38673	-0.01371	0.17018
C(12)	-0.44372	-0.06232	0.04190	-0.44335	-0.06015	0.03941
C(13)	-0.30430	-0.18830	0.01614	-0.30483	-0.18812	0.01502
C(14)	-0.28145	-0.05898	0.09456	-0.28097	-0.05835	0.09378
C(15)	-0.43802	-0.03131	0.22047	-0.43789	-0.03186	0.22070
C(16)	-0.32924	-0.19415	0.21851	-0.32754	-0.19375	0.22059
C(17)	-0.28163	-0.05700	0.15495	-0.28129	-0.05689	0.15522
Lattice parameters	a(Å)	b(Å)	c(Å)	a(Å)	b(Å)	c(Å)
	12.99	12.99	13.22x2	12.78	12.78	12.83x2

Table 6. Fractional atomic coordinates of CuPt-type structure after ionic, cell shape and volume relaxation at room pressure (left) and at 9.5GPa (right), and lattice parameters after relaxation.

atom	Room pressure			9.5 GPa		
	x	y	z	x	y	z
C(1)	-0.29835	-0.21593	0.20223	0.38462	0.12785	0.03613
C(2)	-0.49425	-0.23340	0.24144	0.17723	0.10514	0.07455
C(3)	-0.24363	-0.15471	0.17239	0.43740	0.18988	0.00585
C(4)	-0.36297	-0.38463	0.20214	0.31592	-0.04643	0.03577
C(5)	-0.37651	-0.00595	0.20932	0.29718	0.33982	0.04301
C(6)	0.41190	-0.14309	0.24722	0.07550	0.19082	0.07999
C(7)	0.49315	0.01303	0.22492	0.15811	0.35206	0.05826
C(8)	-0.32915	0.04537	0.18036	0.34378	0.39215	0.01372
C(9)	0.43432	0.07271	0.17207	0.09800	0.41571	0.00545
C(10)	-0.37050	-0.14482	0.22078	0.30829	0.19991	0.05467
Lattice parameters	a(Å)	b(Å)	c(Å)	a(Å)	b(Å)	c(Å)
	9.52	9.52	22.35x2	9.19	9.19	22.01x2

Table 7. Fractional atomic coordinates of Au₃Cu-type structure after ionic, cell shape and volume relaxation at room pressure (left) and at 9.5GPa (right), and lattice parameters after relaxation.

atom	Room pressure			9.5 GPa		
	x	y	z	x	y	z
C(1)	0.00000	0.05514	0.24443	0.00000	0.05582	0.25099
C(2)	0.22860	-0.08973	0.11085	0.23189	-0.09051	0.11196
C(3)	0.21697	-0.19159	0.06143	0.21814	-0.19225	0.06189
C(4)	0.00000	-0.23943	0.44512	0.00000	-0.23366	0.44439
C(5)	0.50000	0.26292	-0.44628	0.50000	0.27121	-0.44502
C(6)	0.50000	0.23432	0.05427	0.50000	0.22990	0.05548
C(7)	0.26856	0.38910	0.08769	0.26489	0.38813	0.08925
C(8)	-0.39304	-0.41237	0.22638	-0.39098	-0.41122	0.23228
C(9)	-0.41030	-0.26797	0.10641	-0.40966	-0.26548	0.10844
C(10)	0.30754	0.28239	0.06064	0.30679	0.28148	0.06155
C(11)	-0.30489	-0.44534	0.16915	-0.30191	-0.44458	0.17268
C(12)	-0.44497	-0.32770	0.18985	-0.44423	-0.32616	0.19362
Lattice parameters	a(Å)	b(Å)	c(Å)	a(Å)	b(Å)	c(Å)
	13.15	13.15	13.15	12.85	12.85	12.85

Intermolecular covalent bond lengths (calculated by DFT).

Table 8. Bond lengths

Alloy-type structure	Number of 2+2 cycloaddition intermolecular bonds per molecule	bond length (Å)
AuCuI	8	1.66
CuPt	6	1.64
Au ₃ Cu	12	1.69
	4	1.69
A ₂ B ₂	4 + 4	1.58; 1.60

Electronic structures at 9.5GPa

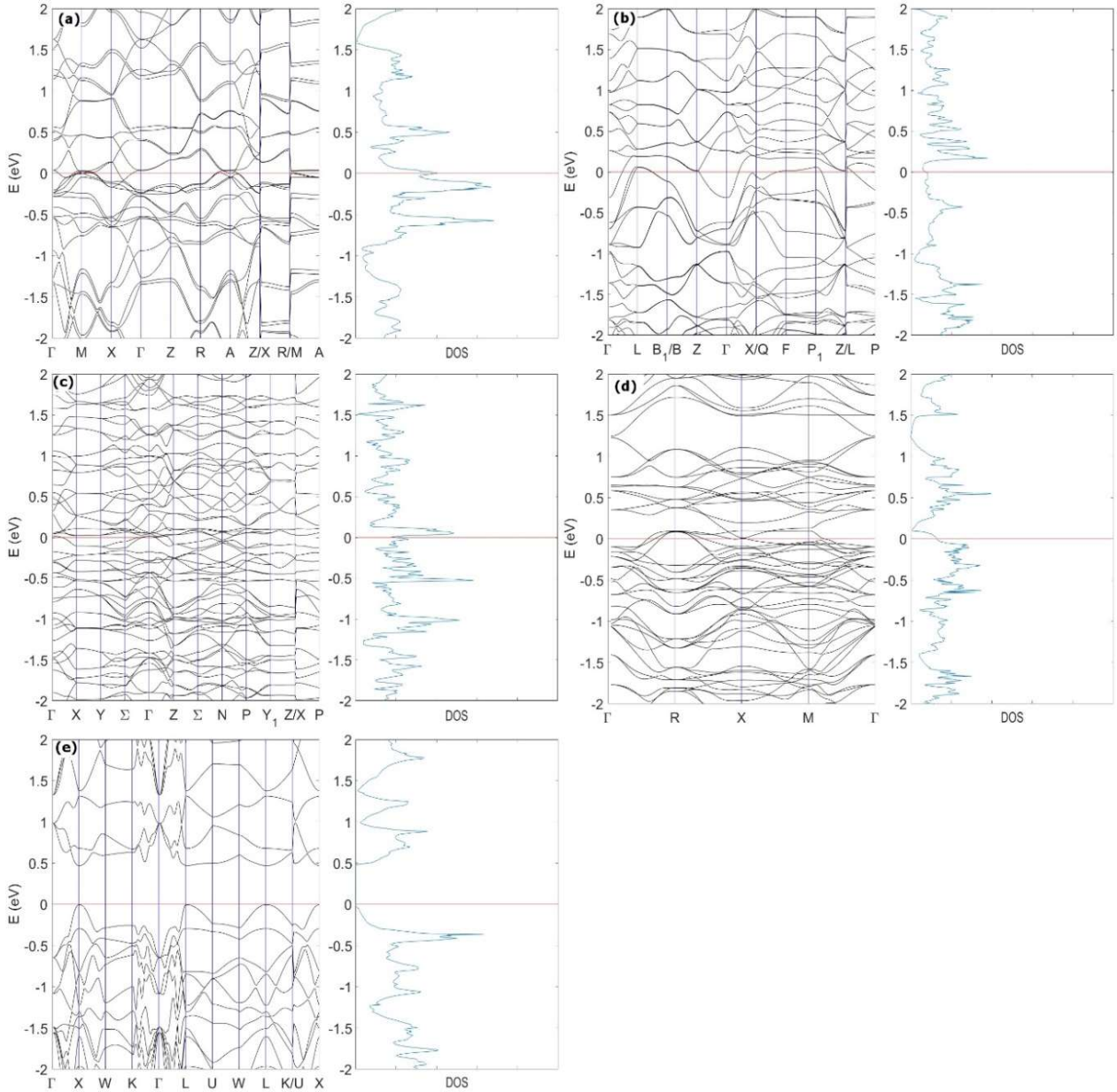
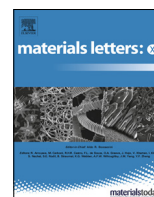


Figure 6. Density of states (right panels) and band structures (left panels) of the polymeric structures (optimized at 9.5 GPa): (a) AuCuI-type; (b) CuPt-type; (c) “A₂B₂”-type; (d) Au₃Cu-type; (e) Monomer “Ferromagnetic” structure. Red lines indicate the Fermi levels.

Chapter 5

A3 - Three-dimensional fcc C₆₀ polymer

© 2019 Elsevier Ltd.
Reprinted with permission.



Three-dimensional fcc C₆₀ polymer

J. Laranjeira^{a,*}, L. Marques^a, M. Melle-Franco^b, K. Strutyński^b, M. Mezouar^c, M. Barroso^d

^aDepartamento de Física and CICECO, Universidade de Aveiro, 3810-193 Aveiro, Portugal

^bDepartamento de Química and CICECO, Universidade de Aveiro, 3810-193 Aveiro, Portugal

^cE.S.R.F., BP220 38043 Grenoble, France

^dDepartamento de Física and I3N, Universidade de Aveiro, 3810-193 Aveiro, Portugal



ARTICLE INFO

Article history:

Received 15 August 2019

Received in revised form 20 August 2019

Accepted 17 September 2019

Available online 18 September 2019

Keywords:

Fullerene polymers

X-ray diffraction

DFT calculations

Ordered binary-alloy structures

ABSTRACT

A face-centered cubic (fcc) polymerized C₆₀ phase has been synthesized at 9.5 GPa and 550 °C. The observed short lattice constant, 13.19 Å, indicates that a three-dimensional (3D) polymer with adjacent C₆₀ molecules covalently bonded was obtained. Possible polymerized structures, with each molecule adopting one of the two standard orientations, have been investigated through density functional theory (DFT). It was found that intermolecular bonds, 56/56 2 + 2 cycloaddition, are formed between molecules with different orientations but no bonds are formed between molecules with the same orientation. The computed bulk moduli for these structures gave values ranging from 88 to 132 GPa. Although the distances between neighboring molecules and the volume per molecule from the models are close to the experimental values, the relaxed structures displayed symmetries lower than cubic, suggesting that the experimental fcc structure is likely disordered or frustrated.

© 2019 Published by Elsevier B.V. This is an open access article under the CC BY-NC-ND license (<http://creativecommons.org/licenses/by-nc-nd/4.0/>).

1. Introduction

At room conditions, C₆₀ is a Van der Waals solid with a face-centered cubic (fcc) structure, in which the molecules are rotating [1]. When compressed and heated, it forms extended polymerized networks with different dimensionalities and physical properties [2–9]. One-dimensional (1D) orthorhombic and two-dimensional (2D), tetragonal and rhombohedral, phases are synthesized at pressures below 8 GPa. These low-dimensional polymerized phases have a common type of intermolecular covalent bonds, 66/66 2 + 2 cycloadditions, which connects intramolecular double bonds of neighboring molecules [10].

Above 8 GPa, three-dimensional (3D) C₆₀ polymers are formed. They show outstanding physical properties for pure carbon phases, such as electron conductivity and low-compressibility [2–9]. Furthermore, a very high bulk modulus, superior to that of diamond, has been claimed from C₆₀ samples subjected to 13GPa and to temperatures above 700 °C [4].

3D polymeric structures, having exclusively 66/66 2 + 2 cycloaddition bonds, are not possible in ABC-stacked lattices and, thus, new bonding patterns need to be involved in such structures [7]. Previously, we have shown that 3D polymeric structures can

form with 56/56 2 + 2 cycloaddition bonds, which connects intramolecular single bonds of neighboring molecules. Here we present a brief description of our previous works regarding the 3D polymer phase obtained at 9.5GPa and 550 °C and its possible binary-alloy-type structures [7,8]. In addition, we report the bulk moduli computation for all proposed structures, which are consistent with experimental results.

2. Results and discussion

Fig. 1 shows in situ synchrotron diffraction patterns of C₆₀ under pressure and at room conditions, during the pressure-temperature cycle. The patterns of the transformed sample can be indexed in fcc lattices with constants 12.74 Å, at 9.5 GPa, and 13.19 Å, at room conditions. Experimental details were given elsewhere [7]. In comparison to the starting C₆₀, peak shifting to larger 2θ angles, reflecting a compressed structure, and peak broadening are observed for the transformed phase. The low resolution of these diffraction patterns impedes the determination of the detailed crystal structure. Therefore, plane-wave DFT calculations have been performed with VASP package, employing PBE functional, in order to understand the crystal structure of the polymerized phase [11]. Complete details of these computational methods employed were given in reference [8].

* Corresponding author.

E-mail address: jorgelaranjeira@ua.pt (J. Laranjeira).

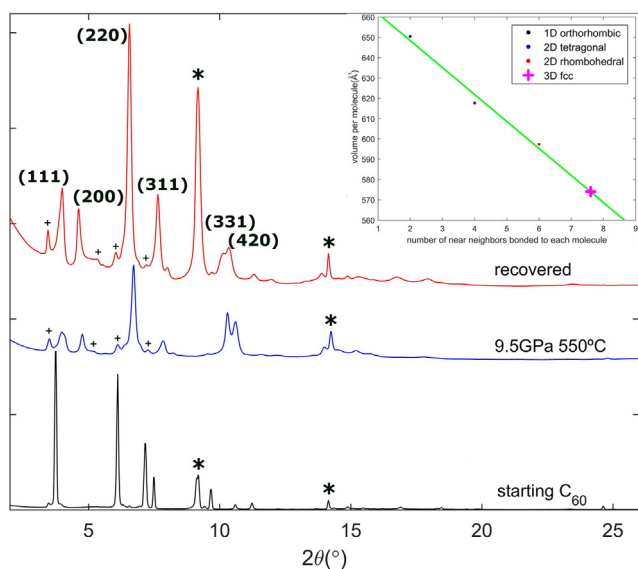


Fig. 1. 1D diffraction patterns obtained at different conditions along the pressure-temperature path ($\lambda = 0.53396 \text{ \AA}$). *: h-BN container diffraction peaks. +: gasket diffraction peaks. Inset: volume per molecule versus number of near-neighbors bonded to each molecule (see text).

In a first step, we have investigated the stability of polymerized structures built with molecules in the standard orientations, since these particular molecular orientations are compatible with the observed cubic symmetry [1]. These models show that no bond is formed by two neighboring molecules with the same orientation but occur under differently oriented molecules via 56/56 2+2 cycloaddition. These intermolecular bonds are analogous to an orientational “antiferromagnetic” interaction and the resulting polymer can be mapped onto an Ising antiferromagnet, where one of the standard orientations corresponds to spin up and the other to the spin down [7]. Similarly, the antiferromagnetic Ising model has also been applied to binary-alloys [12].

By using ordered binary-alloy structures as prototypes, several stable C_{60} structures have been constructed, shown in Fig. 2, and their stability analyzed [7,8]. Their optimized lattice constants at room conditions are given in Table 1 [8]. Structures 2(a) and 2(b) are analogous to tetragonal AuCuI and rhombohedral CuPt ordered alloy structures and involve orientational “antiferromagnetic” (001) and (111) fcc planes, respectively, which are in turn “ferromagnetically” ordered. The “antiferromagnetic” polymeric bonds are highlighted in red. Each molecule is bonded to eight nearest-neighbors in the AuCuI-type structure and six in the CuPt-type structure. Structure 2(c) is analogous to “ A_2B_2 ” structure, consisting of stacked “antiferromagnetic” ordered (001) fcc planes, with each molecule bonded to eight neighbors. Structure 2(d) is analogue to the Au_3Cu ordered cubic structure, in which less populated molecules bond to their twelve nearest-neighbors while the most populated molecules have four nearest-neighbor bonds. Furthermore, previous DFT calculations show that all these structures present states at the Fermi level and, therefore, they are metallic [8].

All computed structures, excluding the cubic Au_3Cu -type structure, have lower symmetry than the experimentally observed cubic symmetry and, thus, they cannot be directly assigned to the exper-

imental phase. Additionally, the Au_3Cu -type structure must be discarded since it would yield superlattice reflections missing in the experimental pattern. In contrast, the volume per molecule of these structures is close to the experimental one. Indeed, as Talyzin and coworkers pointed out, a linear correlation between the number of bonds per molecule and the volume per molecule is observed for the low-dimensional polymers [13]. Extending this correlation to the volume of the present phase, we obtain an average value of 7.6 molecules directly bonded to each molecule (see inset Fig. 1). This extrapolation can be made with confidence since the polymeric bonds arise all from 2 + 2 cycloadditions. Both AuCuI and “ A_2B_2 ”-type structures have eight near-neighbors bonded to each molecule, and their volumes are close to the experimental one. Thus, although we cannot assign the experimental 3D polymerized phase to a single calculated structure, the volume per molecules and also the distance between bonded molecules indicate that the polymeric bond present in the experimental polymerized phase is 56/56 2+2 cycloaddition. The observed cubic symmetry is then the result of disorder or frustrated polymerized structure with a number of bonded near-neighbors of 7.6. Indeed, as we have noted the system can be mapped onto the Ising fcc antiferromagnet, which is naturally frustrated with eight antiferromagnetic bonds per site [12].

Structural optimizations at different pressures were performed to compute the bulk modulus of each structure. The bulk modulus was then calculated by fitting the obtained volumes with the Birch-Murnaghan equation of state (EOS), shown in Fig. 3 [14]. The bulk modulus and its derivative are given in Table 1, for each structure. AuCuI and “ A_2B_2 ”-type structures have very similar bulk modulus, around 130GPa, and the same number of polymeric bonds per molecule. Au_3Cu -type structure has slightly lower bulk modulus, 117 GPa. The CuPt-type structure, with only six polymeric bonds per molecule, has the lowest bulk modulus, 88GPa. Thus, increasing the number of polymeric bonds increases the bulk modulus. An estimation from experimental data can be obtained for pressure-averaged bulk modulus from the molecular volumes at high and ambient pressures. This yields a value of 96GPa, in the range of the computed ones, thus confirming the correctness of bonding type. This range of values is larger than the bulk moduli of the low-dimensional C_{60} polymers but are smaller than those of 3D C_{60} polymers obtained at higher pressure [4,5,15]. The rise on the number of polymeric bonds and, concomitantly, on the number of sp^3 carbons, increases, as expected, the bulk moduli displayed by C_{60} polymers. A value, 217GPa, was reported for an identical 3D fcc polymer but this result is strongly influenced by the large dispersion of the experimental data [13].

3. Conclusions

A joint experimental and theoretical study of a 3D C_{60} polymer obtained at 9.5 GPa and 550 °C, was performed. This polymerized phase has a fcc symmetry with a frustrated structure, where the molecules are bonded through 56/56 2 + 2 cycloaddition.

Based on the 56/56 2 + 2 cycloaddition polymeric bond, several polymerized structures have been constructed and their stability investigated. These structures display bulk moduli ranging from 88 to 132GPa. These values are directly connected to the number of polymeric bonds per molecule, higher number of polymeric bonds leads to higher bulk modulus. Hence, higher pressures should induce more sp^3 bonds leading to even less compressible samples.

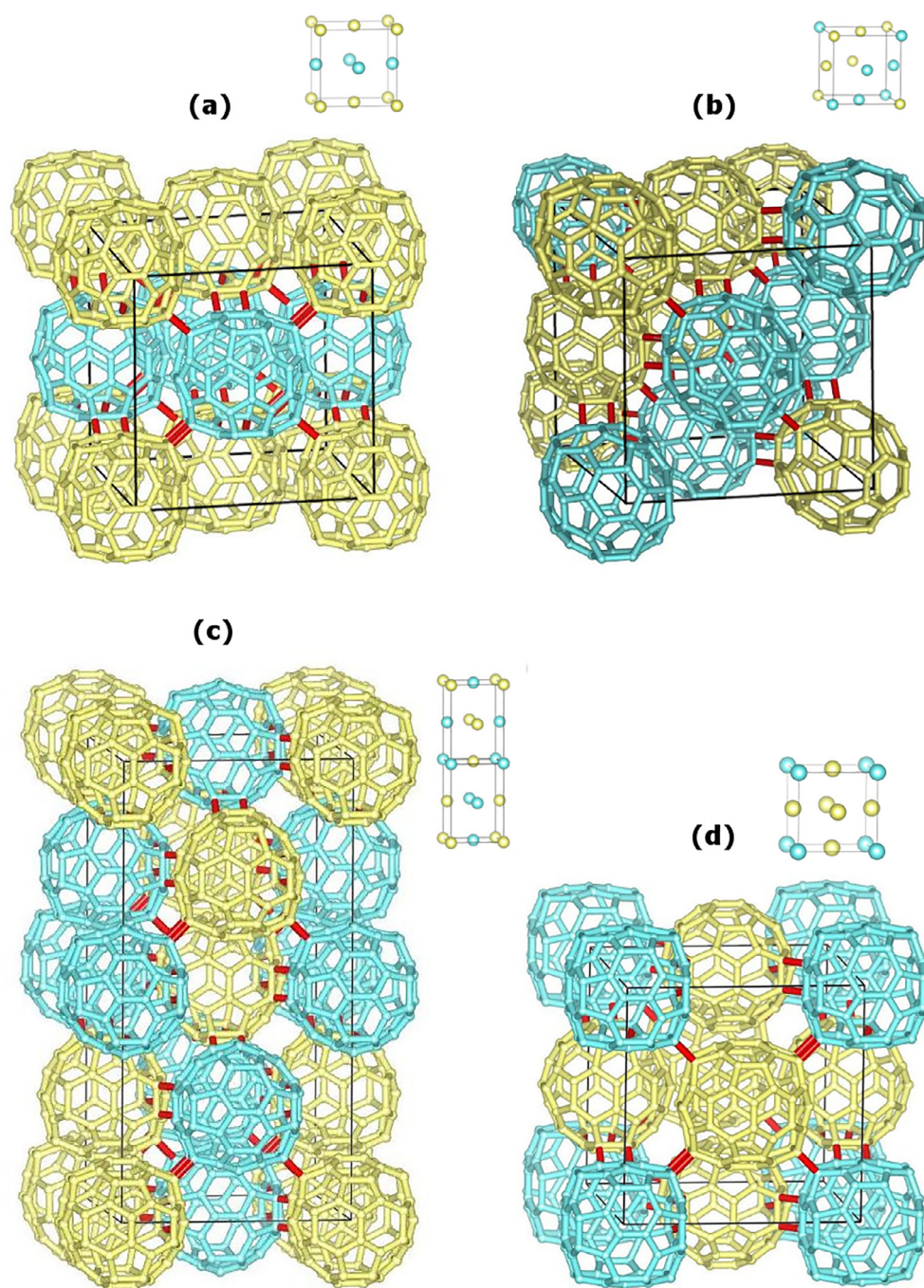


Fig. 2. C_{60} binary-alloy-type structures with binary-alloys as insets. (a) AuCuI-type; (b) CuPt-type; (c) “ A_2B_2 ”-type; (d) Au_3Cu -type. Differently oriented molecules are rendered in yellow/blue and the polymeric bonds are rendered in red. (For interpretation of the references to colour in this figure legend, the reader is referred to the web version of this article.)

Table 1

Binary-alloy-type structures optimized lattice constants, space group, bulk modulus B_0 and the respective pressure derivative B'_0 .

Alloy-type structure	Lattice constants (Å)	Space group	B_0 (GPa)	B'_0
AuCuI-type	$a = b = 9.32$; $c = 12.87$	$P4_2/mnm$	129.64	4.14
“ A_2B_2 ”-type	$a = b = 12.99$; $c = 13.22 \times 2$	$I4_1/amd$	132.29	4.25
CuPt-type	$a = b = 9.52$; $c = 22.35 \times 2$	$R\bar{3}c$	117.00	4.20
Au_3Cu -type	$a = b = c = 13.15$	$Pm\bar{3}$	88.77	4.76

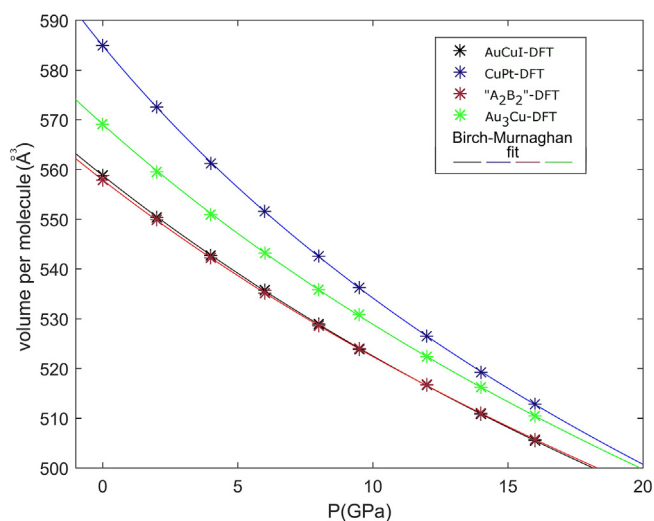


Fig. 3. Birch-Murnaghan EOS fits to calculated volumes per molecule for the different structures (indicated by stars).

Declaration of Competing Interest

The authors declare that they have no known competing financial interests or personal relationships that could have appeared to influence the work reported in this paper.

Acknowledgements

This work was supported by the projects POCI-01-0145-FEDER-031326 financed by the Portuguese Foundation for Science and Technology (FCT) and co-financed by FEDER. CICECO-Aveiro Institute of Materials, FCT Ref. UID/CTM/50011/2019, financed by national funds through the FCT/MCTES and IF/00894/2015 finances

by FCT. J. Laranjeira acknowledges a PhD grant from FCT (SFRH/BD/139327/2018).

References

- [1] P.A. Heiney, Structure, dynamics and ordering transition of solid C_{60} , *J. Phys. Chem. Solid.* 53 (1992) 1333–1352.
- [2] M. Álvarez-Murga, J.L. Hodeau, Structural phase transitions of C_{60} under high-pressure and high-temperature, *Carbon* 82 (2015) 381–407.
- [3] M. Núñez-Regueiro, L. Marques, J.L. Hodeau, O. Bethoux, M. Perroux, Polymerized fullerite structures, *Phys. Rev. Lett.* 74 (1995) 278–281.
- [4] V. Blank, S. Buga, G. Dubitsky, N.R. Serebryanaya, M. Popov, B. Sundqvist, High-pressure polymerized phases of C_{60} , *Carbon* 36 (1998) 319–343.
- [5] V. Brazhkin, A. Lyapin, S. Popova, Y. Klyuev, A. Naletov, Mechanical properties of the 3D polymerized, sp^2 - sp^3 amorphous, and diamond-plus-graphite nanocomposite carbon phases prepared from C_{60} under high pressure, *J. Appl. Phys.* 84 (1998) 219–226.
- [6] S. Yamanaka, A. Kubo, N. Kini, K. Inumaro, K. Komaguchi, T. Inoue, T. Irifune, Electron conductive three-dimensional polymer of cuboidal C_{60} , *Phys. Rev. Lett.* 96 (2006) 076602.
- [7] J. Laranjeira, L. Marques, M. Mezouar, M. Melle-Franco, K. Strutyński, Bonding frustration in the 9.5 GPa fcc polymeric C_{60} , *Phys. Stat. Sol.-RRL* 11 (2017) 1700343.
- [8] J. Laranjeira, L. Marques, N.M. Fortunato, M. Melle-Franco, K. Strutyński, M. Barroso, Three-dimensional C_{60} polymers with ordered binary-alloy-type structures, *Carbon* 137 (2018) 511–518.
- [9] J. Yang, J. Tse, T. Iitaka, First-principles investigation on the geometry and electronic structure of the three-dimensional cuboidal C_{60} polymer, *J. Chem. Phys.* 127 (2007) 134906.
- [10] D. Strout, R. Murry, C. Xu, W. Eckho, G. Odom, G. Scuseria, A theoretical study of buckminsterfullerene reaction products: $C_{60}+C_{60}$, *Chem. Phys. Lett.* 214 (1993) 576–582.
- [11] G. Kresse, J. Furthmüller, Efficient iterative schemes for ab initio total-energy calculations using a plane-wave basis set, *Phys. Rev. B* 54 (1996) 11169–11186.
- [12] K. Binder, J. Lebowitz, M. Phani, M. Kalos, Monte Carlo study of the phase diagrams of binary alloys with face centered cubic lattice structure, *Acta Metall.* 29 (1981) 1655–1665.
- [13] A. Talyzin, F. Langenhorst, N. Dubrovinskaia, S. Dub, L. Dubrovinsky, Structural characterization of the hard fullerite phase obtained at 13 GPa and 830K, *Phys. Rev. B* 71 (2005) 115424.
- [14] F. Birch, Finite elastic strain of cubic crystals, *Phys. Rev.* 71 (1974) 809–824.
- [15] J. Léger, J. Haines, V. Davydov, V. Agafonov, Irreversible amorphization of tetragonal two-dimensional polymeric C_{60} under high pressure, *Solid State Commun.* 121 (2002) 241–244.

Chapter 6

A4 - $C_{60}+C_{60}$ molecular bonding revisited and expanded

$C_{60}+C_{60}$ molecular bonding revisited and expanded

Jorge Laranjeira,^{1,*} Karol Strutyński,² Leonel Marques,¹ Emilio Martínez-Núñez,³ and Manuel Melle-Franco^{2,†}

¹*Departamento de Física and CICECO, Universidade de Aveiro, 3810-193 Aveiro, Portugal*

²*Departamento de Química and CICECO, Universidade de Aveiro, 3810-193 Aveiro, Portugal*

³*Departamento de Química Física, Universidade de Santiago de Compostela, 15782, Santiago de Compostela, Spain*

(Dated: February 21, 2023)

Several dimerization products of fullerene C_{60} are presented and thoroughly characterized with a quantum chemical DFT model augmented by dispersion. We reanalyze and expand significantly the number of known dimers from 12 to 41. Many of the novel bonding schemes were found by analyzing more than 2 nanoseconds of high energy molecular dynamics semiempirical trajectories with AutoMeKin, a methodology previously used to compute the reactivity of much smaller molecules. For completeness, this was supplemented by structures built by different geometric considerations. Also, spin-polarization was explicitly considered yielding 12 new bonding schemes with magnetic ground states. The results are comprehensively analyzed and discussed in the context of yet to be explained 3D fullerene structures and recent fullerene 2D systems.

Keywords: Fullerene Dimers, DFT calculations, AutoMeKin, HOMO-LUMO Gap

INTRODUCTION

At room temperature and atmospheric pressure, C_{60} is a van der Waals solid with a face-centered cubic (fcc) structure where the molecules are rotating freely [1]. When subjected to visible or ultraviolet light, or high-pressures high-temperatures (HPHT) treatments the C_{60} molecules bond to each other via 66/66 2+2 cycloaddition forming aggregates and dimers [2–4], see figure 1.

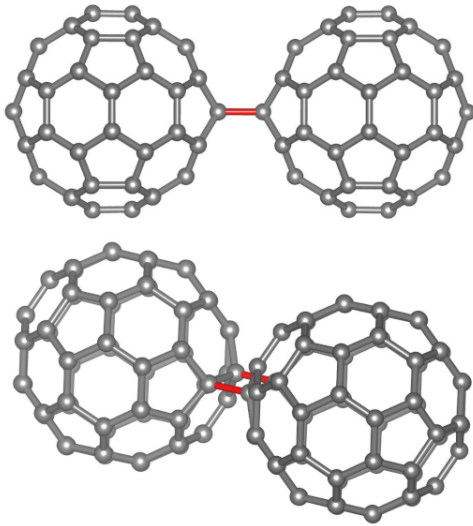


FIG. 1. Two views of the most stable and well studied C_{60} dimer with molecules bonded via 66/66 2+2 cycloaddition.

Increasing the pressure and temperature of the C_{60} HPHT treatment leads to the formation of extended

crystalline networks [5–11]. At pressures below 8 GPa the formation of low-dimensionality polymers occurs yielding 1D orthorhombic, 2D tetragonal and 2D rhombohedral phases. In all these low-dimensionality polymers, the molecules arrange themselves in covalently bonded chains (1D) or sheets (2D) formed exclusively by 66/66 2+2 cycloadditions.

It is above 8 GPa that fully 3D polymerized crystals are formed [8–11]. Here other bonding schemes, besides the 66/66 2+2 cycloaddition, start to play an important role, in fact, 3D polymers proposed to date have different bonding schemes such as the 56/56 2+2 cycloaddition [7, 8], the 6/6 3+3 cycloaddition and the double 66/66 4+4 cycloaddition [9], the 56/65 2+2 cycloaddition and the 5/5 3+3 cycloaddition [10] or even the double 5/5 2+3 cycloaddition [11].

Recently, other C_{60} polymers have been produced from a different route [12, 13]. This has yielded a pure carbon bulk material based on covalently linked fullerenes forming 2D sheets with hexagonal symmetry dubbed graphurelene [13]. These layers are bonded via single-bond and 56/65 2+2 cycloaddition, unlike any 2D polymers synthesized to date by HPHT treatment, showcasing the potential of alternative synthetic routes to produce new structures.

3D C_{60} polymers show quite remarkable physical properties for pure carbon phases, such as metallicity and low-compressibility which fosters interest in these materials [8–11]. Nevertheless, diffraction patterns from these phases lack the resolution needed to solve their crystalline structure. Thus, it is necessary to build complementary computational models fitting the overall symmetry and lattice parameters to the diffraction pattern and study their stability recurring to quantum simulation tools like Density Functional Theory (DFT) [7].

The distances between the two C_{60} covalently bonded molecules, i.e. a C_{60} dimer, computed from their molecular centers are similar to the corresponding

* jorgelaranjeira@ua.pt

† manuelmelle@ua.pt

distance in a bulk crystalline phase. For instance, the C_{60} molecular distance, we compute for the 66/66 2+2 cycloaddition dimer, is ~ 9.1 Å while in the low-dimensionality polymers it is found to be between 9.02 and 9.18 Å [5, 6]. Also, for the recent graphulere [12, 13], the computer dimer distances are 9.23 and 9.09 Å while the experimental bonding distance of 9.23 and 9.16 Å respectively. Hence, relating bonding distances to bonding schemes constitutes a simple yet accurate interpretation tool for the C_{60} crystal structure assignment, rendering covalent C_{60} dimers specifically relevant to compute and understand.

In the 90's and beginning of the 2000's, several studies regarding dimers were presented, nevertheless, to the best of our knowledge, no more than 12 dimers have been described altogether. Here, We consider, unless noted, C_{60} covalent dimers, that is dimers where the forming fullerene molecules are joined by intermolecular bonds. Strout et al. [4] performed probably the most extensive C_{60} dimerization study which addressed the 2+2 cycloadditions and a 2+4 cycloaddition. This last bonding scheme, following our notation, corresponds to a double 6/56 4+2 cycloaddition, since two 2+4 cycloaddition reactions, involving one hexagon (6) and one intramolecular single bond (56) each, are present.

Later, in 1994, Adams et al. [14] proposed three other bonding schemes, two bonding the molecules via their hexagons and one between their pentagons. In the bonding between hexagons, the six atoms from one hexagon bond to the six atoms of the other hexagon, which can be obtained in the following two ways: 1) the hexagons of the two molecules align with each other (as well as the pentagons); 2) the hexagons from one molecule align with the pentagons of the other. When possible, we will keep the cycloaddition notation for the formed dimers nomenclature thus, in this case the dimers will be named, for instance, "triple 66/66 2+2 cycloaddition" (or "triple 56/56 2+2 cycloaddition") and "triple 56/66 2+2 cycloaddition" respectively. In the bonding between pentagons the five atoms from one pentagon bond to the five atoms of the other, the dimer will be referred to as "double 56/56 2+2 cycloaddition plus single bond". More details about this bonding nomenclature are available in the supporting information (SI) section A. In 2007 Liu et al. [15] studied again the two dimers bonded via hexagons confirming that they are thermodynamically stable and thus, could be observed experimentally.

Osawa et al. [16] reported the two possible 6/6 4+4 cycloaddition bonded dimers, while Matsuzawa et al. [17] also considered the 6/6 4+4 cycloaddition dimers and

added one of the two 66/6 2+4 cycloaddition dimers to their calculations. Besides the mentioned dimers, the single bond dimer (SB) was also considered [18]. In all of the works mentioned so far, the lowest energy dimer was consistently found to be the 66/66 2+2 cycloaddition [4, 14, 15, 18].

Apart from dimers formed just with pristine, i.e. unfunctionalized, C_{60} , there have also been numerous studies of dimers formed with other intermediates as well as coalescence products [4, 19, 20]. In addition, there have been studies on the dimerization and coalescence of C_{60} inside carbon nanotubes [5, 21, 22]. Note that although some of these systems also did appear in our calculations, for simplicity, they were not considered in our analysis and will not be discussed. Nevertheless, coalescence products might improve the understanding of amorphous carbon phase formation from C_{60} [23] or other phases where the C_{60} cage is broken [24] and might be the object of future studies.

The new systems reported here have been obtained fundamentally with AutoMeKin [25–27], an automatic computational procedure to find and characterize chemical reaction paths, and extended by manual construction following geometric considerations. We report a total of 41 stable dimers computed at DFT level. From these, 25 were obtained with AutoMeKin, the others were built from geometric considerations or obtained from the literature. The molecular structure and relative stability of all dimers were computed at the TPSS-Def2-TZVPP/B3LYP-6-31G(d,p) theory level augmented by D3 dispersion with Becke–Johnson damping. All the dimers studied present C_{60} distances between 8.04 Å and 9.23 Å which renders some of these bridging patterns suitable candidates to be present in 3D C_{60} polymers.

METHODS

First, we performed a benchmark calculation of the dimer bonding energies for four different Hamiltonians, namely: TPSS-Def2-TZVPP-D3BJ/TPSS-6-31G(d,p)-D3BJ, TPSS-Def2-TZVPP-D3BJ/B3LYP-6-31G(d,p)-D3BJ, TPSS-6-31G(d,p)-D3BJ and B3LYP-6-31G(d,p)-D3BJ, on the lowest five energy C_{60} dimers, table I. The TPSS-Def2-TZVPP-D3BJ Hamiltonian was chosen after a recent benchmark study comparing the C_{60} isomerization energies with 115 methodologies which recommended this method based on its accuracy [28]. The bonding energy was computed by subtracting the energy of two isolated C_{60} to the energy of each dimer: $\Delta E_{Bond} = E_{dimer} - 2E_{C_{60}}$.

Theory level	Min1	Min2	Min3	Min4	Min5
B3LYP-6-31G(d,p)-D3BJ	-0.6541	0.2055	0.5839	1.0571	1.0934
TPSS-6-31G(d,p)-D3BJ	-0.5415	0.2125	0.5304	0.9635	0.9904
TPSS-Def2-TZVPP-D3BJ/TPSS-6-31G(d,p)-D3BJ	-0.2512	0.4931	0.7398	1.2428	1.2676
TPSS-Def2-TZVPP-D3BJ/B3LYP-6-31G(d,p)-D3BJ	-0.2494	0.4989	0.7440	1.2501	1.2771

TABLE I: Bonding energy of the five lowest energy $C_{60}+C_{60}$ dimers optimized with different levels of theory given in eV/dimer.

Theory level	ΔE_{Bond} (eV/dimer)	$\Delta E_{Bond} + BSSE$ (eV/dimer)
B3LYP-6-31G(d,p)-D3BJ	-0.4569	-0.3512
TPSS-Def2-TZVPP-D3BJ/B3LYP-6-31G(d,p)-D3BJ	-0.3604	-0.3460

TABLE II: Bonding energy of the non-covalent $C_{60}+C_{60}$ dimer optimized with different levels of theory and corrected by the basis set superposition error (BSSE), given in eV/dimer.

The Basis Set Superposition Error (BSSE) was evaluated in a non-covalent dimer, and found to be sizable, around 0.1 eV, for bonding energies with the smaller, DZP, basis sets, table II. After the BSSE correction, both levels of theory yielded values differing less than 5 meV. Interestingly, relative energies were very similar, and also similar results were found for all DFT functionals. Considering this, we selected the TPSS-Def2-TZVPP-D3BJ/B3LYP-6-31G(d,p)-D3BJ methodology as it yields a good compromise between accuracy and computational cost. Namely, we performed the geometry optimizations at the B3LYP-6-31G(d,p) [29, 30] level augmented by the D3 van der Waals correction [31, 32] with Becke–Johnson damping [33] (B3LYP-6-31G(d,p)-D3BJ) followed by a single point calculation with TPSS-Def2-TZVPP Hamiltonian [34, 35] also augmented by the D3 van der Waals correction with Becke–Johnson damping (TPSS-Def2-TZVPP-D3BJ) for the energies. Hessian calculations were performed in all presented geometries at the B3LYP-6-31G(d,p)-D3BJ level to explicitly check the absence of negative frequencies. All calculations were performed with Gaussian09 [36].

We explicitly analyzed the dispersion contribution to the bonding energy, as this contribution is missing in most early DFT and semiempirical studies. The dispersion correction shifts bonding energies to more binding values, for the B3LYP-6-31G(d,p) functional the maximum shift is 1.34 eV and the average one is 0.78 eV. For the TPSS-Def2-TZVPP functional the stabilization is lower, the maximum shift is 1.15 eV and the average 0.68 eV. This indicates that there is a consistent attractive dispersion contribution to the bonding interaction in all covalently bonded C_{60} dimers. In fact, without van der Waals correction, all dimers are metastable compared to the isolated C_{60} molecule, see SI table S1 and figures S1 and S2.

To systematically explore possible minima we employed AutoMeKin (AMK) [25–27], a software designed to find reaction mechanisms. AMK analyzes high-energy molecular dynamics trajectories via graph theory to search for structural transformations. When a structural transformation, such as bonds breaking or forming, is detected it finds and characterizes the transition state via its second-order derivatives. From the transition state, the intrinsic reaction coordinate (IRC) method is then used to obtain reactants and products. For this, 2.25 ns were run altogether via 4500, 500 fs long, independent molecular dynamics of two C_{60} molecules in a high energy bonding configuration. The dynamics were run with a specially modified version of MOPAC2016 [37] using the PM7 [38] Hamiltonian with a

time step of 0.5 fs. Note that AMK so far has been used in molecules ≤ 30 atoms [39], so this study, on a system with 120 atoms, showcases how the AMK methodology can be successfully extended to other problems.

In addition, for completeness, we have comprehensively searched for reported dimers in literature and also constructed other bonding schemes considering the geometric possibilities allowed by the molecule. In the tables, the following labels reveal the procedure followed for each minimum: L, literature, G, geometric considerations and AMK. To build dimers from geometric considerations, we went through the possibilities of bonding between each molecular element of geometry avoiding large deformations. Three geometry elements: chemical bonds, pentagons, or hexagons were considered with a maximum of two of these elements being combined at a time. For instance, the two "5/6 3+3" bonds may be constructed taking into consideration the bridging of one pentagon to one hexagon while the "double 66/66 4+4" takes into consideration the bridging of two hexagons from each molecule. For simplicity, we only considered systems with an even number of intermolecular bonds in this procedure.

We present the HOMO-LUMO gaps at the B3LYP-6-31G(d,p) level as this Hamiltonian is expected to yield closer values to experiment [40]. Note that all calculations were first run without spin polarization, and, in the cases where structures were found to be unstable under these conditions, they were then run considering triplet or quintuplet ground states. This procedure yielded 12 dimers with spin-polarized ground states. In all cases, no initial symmetry constraints were used in the geometry optimizations.

RESULTS AND DISCUSSION

The dimer structures found are comprehensively summarized in table III by increasing energy with their symmetry, number of intermolecular bonds, HOMO-LUMO gap, bonding energy, the distance between C_{60} molecules and a label indicating the minima origin. A graphical rendering for all the bonding schemes found on these dimers together with some others that were found by AMK but are not stable at the DFT level, can be found on the SI, table S3. Relevantly, of the 12 dimers previously reported just the 6/66 2+4 cycloaddition reported by Matsuzawa et al. [17] was found not to be stable in our study, although it was found by AMK (AMK minimum 3097) indicating that at the semiempirical PM7 level, this dimer is stable.

Only one covalent dimer with a bonding energy of

-0.25 eV was found to be thermodynamically more stable, i.e. exothermic, than the isolated C_{60} molecules. In comparison, the less stable dimer is considerably more endothermic with a bonding energy of 7.95 eV. As a reference, we also computed the energy of the non-covalent dimer, -0.36 eV, which is more stable than the isolated molecule and any covalent dimer. These results match experimental observations since the only, experimentally observed, covalent dimer is fruit of the

$66/66$ 2+2 cycloaddition [2–4] and at ambient conditions, C_{60} molecules are not covalently bound in the solid state. More exotic bonding configurations, for instance, corresponding to the $56/56$ 2+2 cycloaddition [8], can be found in three-dimensional crystals formed under high-pressure treatments, where the $66/66$ 2+2 cycloaddition bonding scheme alone cannot be used to bond all molecules in a three-dimensional extended system.

Minima order	Dimer name	Sym.	interm. bonds	HOMO-LUMO gap (eV)	ΔE_{Bond} (eV/dimer)	Mol. dist. Å	bond origin
	C_{60}	I_h	0	2.8523	-	-	-
	Non covalent	C_1	0	2.59561	-0.3604	9.88	-
Min1	66/66 2+2	D_{2h}	2	2.50562	-0.2494	9.05	AMK66/L [4, 14, 16–18]
Min2	56/66 2+2	C_s	2	1.81935	0.4989	9.07	AMK203/L [4]
Min3	SB	C_{2h}	1	1.9126*	0.7440	9.23	L [18]
Min4	56/65 2+2	C_{2h}	2	1.69636	1.2501	9.09	AMK1473/L [4]
Min5	56/56 2+2	C_{2v}	2	1.74996	1.2771	9.10	AMK1818/L [4]
Min6	double 66/66 2+2	C_{2v}	4	2.49311	1.4683	8.64	G
Min7	double 56/66 2+2 M2	C_s	4	2.45719	1.8367	8.65	AMK1269
Min8	5/66 3+2	C_s	2	1.8779*	2.1629	8.91	AMK3333
Min9	double 56/56 2+2	C_{2v}	4	2.34045	2.2527	8.66	G
Min10	AMK5678	C_1	3	1.5557*	2.3363	8.85	AMK5678
Min11	6/66 3+2	C_1	2	0.74614	2.3867	8.87	AMK3615
Min12	6/6 4+4 M1	C_{2v}	2	1.97527	2.6221	8.81	AMK2506/L [16, 17]
Min13	triple 66/65 2+2	D_{3d}	6	2.39487	2.6419	8.44	L [14, 15]
Min14	6/6 4+4 M2	C_1	2	1.79731	2.6441	8.81	AMK2507/L [16, 17]
Min15	triple 66/66 2+2	D_{3h}	6	2.4327	2.6783	8.44	L [14, 15]
Min16	6/6 3+4 M2	C_1	2	1.8916*	2.8918	8.80	AMK4004
Min17	6/6 3+3 M3	C_2	2	1.8632*	3.1388	8.77	AMK5325
Min18	double 56/66 2+2 M1	C_s	4	1.56792	3.2546	8.69	AMK2605
Min19	5/6 3+4 M2	C_s	2	1.01063	3.3104	8.87	AMK4307
Min20	5/6 3+4 M1	C_s	2	1.01798	3.3326	8.87	AMK4321
Min21	6/56 3+2 M2	C_1	2	1.6369*	3.3799	8.87	AMK4646
Min22	6/56 3+2 M1	C_1	2	1.6207*	3.4201	8.87	AMK4567
Min23	double 56/65 2+2	C_s	4	1.52057	3.6534	8.71	AMK3018
Min24	5/5 3+3 M1	C_{2h}	2	1.6465*	3.6760	8.89	G
Min25	6/6 3+4 M1	C_1	2	1.3896*	3.9138	8.77	AMK3893
Min26	double 56/56 2+2	C_{2v}	4	1.22506	4.4948	8.75	G
Min27	AMK6163	C_1	3	1.8342*	4.6261	8.41	AMK6163
Min28	double 56/56 2+2 plus SB	D_{5h}	5	0.74260	4.8285	8.68	L [14]
Min29	double 6/56 4+2	C_{2h}	4	2.34100	5.0253	8.62	L [4]
Min30	5/56 3+2 plus 6/56 4+2	C_s	4	1.52955	5.1168	8.67	G
Min31	double 5/5 2+3	C_{2h}	4	1.10995	5.2631	8.72	G
Min32	5/6 3+3 plus 56/6 2+3	C_1	4	1.4211*	5.5353	8.62	AMK5775
Min33	AMK7077	C_s	4	0.87974	6.3159	8.29	AMK7077
Min34	AMK6511	C_1	4	1.68194	6.4343	8.28	AMK6511
Min35	AMK7610	C_s	4	0.95349	6.7170	8.25	AMK7610
Min36	5/5 3+3 plus 6/6 4+4	C_{2v}	4	0.76546	6.8452	8.05	G
Min37	double 56/65 3+4	C_{2h}	4	0.7584*	6.9087	8.10	G/AMK_or
Min38	5/6 3+4 plus 6/6 4+4	C_s	4	0.94070	6.9973	8.04	G
Min39	double 66/66 4+4	D_{2h}	4	1.64030	7.0261	8.05	L
Min40	AMK8161	C_s	4	2.51216	7.5823	8.28	AMK8161
Min41	double 66/66 4+4 plus 66/66 2+2	D_{2h}	6	2.01174	7.9499	8.16	G

TABLE III: Energetics and distances of $C_{60}+C_{60}$ dimers computed at TPSS-Def2-TZVPP-D3BJ/B3LYP-6-31G(d,p)-D3BJ level. The HOMO-LUMO gaps presented were computed with B3LYP-6-31G(d,p)-D3BJ with * indicating that the presented value is an average of the α and β spin channels gaps (table S2 in SI has the used values). Letter L indicates a structure found in Literature while AMK and G indicate the structure was found using, respectively, AutoMeKin or geometric considerations. The number that follows AMK is an internal reference produced by AMK during the generation.

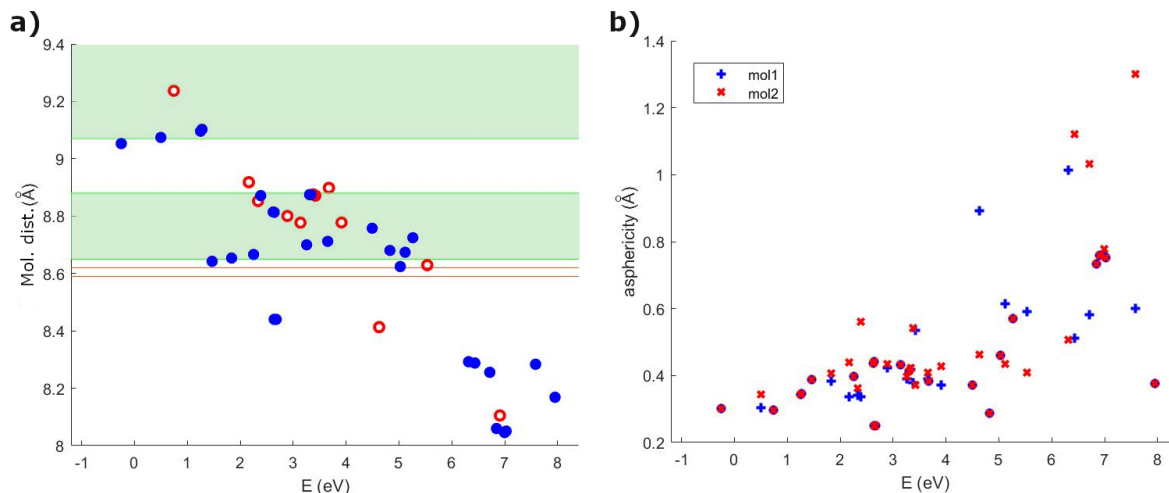


FIG. 2. a) Intermolecular distances as a function of the bonding energy computed at TPSS-Def2-TZVPP-D3BJ/B3LYP-6-31G(d,p)-D3BJ level of theory. Red circles indicate open-shell ground states and blue full circles closed-shell ground states. Red lines and green regions correspond to the experimental molecular distances reported by Yamanaka et al.[9] and Buga et al.[41] respectively. b) Asphericity as a function of the bonding energy. Blue cruces and red x represent the two different C_{60} molecules in each dimer.

Relevantly, with more extreme pressures, higher energy minima can be reached with reduced C_{60} distances, fitting the trend shown in figure 2 a) where the distances between molecules show a monotonous decrease with increasing bonding energies. Furthermore, several of our dimers have shorter distances than reported coalescence products, see for instance the report by Strout et al. [4]. This indicates, that very short distances, below 8.3 Å, may alternatively be explained by C_{60} molecules bonded by the patterns reported here. Also, it is important to notice that although all the bonding schemes yield lower HOMO-LUMO gaps compared to C_{60} , no clear trend between this quantity and energy, number of bonds or intermolecular distance was found.

Interestingly, some of the found dimers are minima only with spin-polarized, triplet or quintuplet, wavefunctions. If the minimization is performed without spin-polarization, the dimers either break into C_{60} molecules or transform into the more stable 66/66 2+2 cycloaddition dimer. Dimers with spin-polarized ground states, in table III, are marked with a star (*) in the HOMO-LUMO value. In addition, the value reported corresponds to the average gap for α and β electrons, all values are available on the SI, table S2. Minima 3, 8, 10, 27 and 37 have triplet ground states while minima 16, 17, 21, 22, 24, 25 and 32 have quintuplet ground states. This sheds light on the potential importance of spin-polarization in high-pressure polymerized C_{60} since some of these bonds may be present in high-pressure formed structures and thus, models built with them probably require spin-polarized Hamiltonians to be properly accounted for. In fact, Bernasconi et al. [42] took this into consideration while computing three-dimensional C_{60} polymers noticing that some of the modeled structures had more stable spin-polarized

ground states.

After the dimer formation, all the C_{60} molecules present some degree of deformation with respect to their original structure. To quantify the degree of molecular deformation we computed the asphericity of each molecule defined as the largest difference between the distance to the molecular center of mass for each atom and the same distance obtained for the pristine C_{60} , 3.51 Å. Asphericity values are summarized in table IV, relevantly, the dimers with higher symmetries than C_s have the same degree of deformation in both molecules, i.e. the same asphericity. In this case, asphericity values range from 0.25 Å for minima 13 and 15 to 0.75 Å for minima 37 and 39. Figure 2 b) shows the asphericity values as a function of the bonding energy. The asphericity qualitatively increases with increasingly endothermic bonding energies, indicating how higher deformation is clearly related to higher energetics and to the more extreme conditions needed for the synthesis of structures displaying these bonding schemes. In fact, the largest asphericity is found for one of the most energetic dimers, minimum 40, with a value of 1.30 Å.

AMK was crucial in finding exotic bonding schemes, like Minima 33 and 35 where one of the molecules is pinched allowing the bonding between one pentagon (for minimum 33 or hexagon for minimum 35) of one molecule to one hexagon and one pentagon of the other molecule, see figures 3 a) and b). This pinching implies a high asphericity value in the pinched molecule, ~ 1.0 Å, while the other molecule has nearly half that value in both dimers, see table IV. In both cases, this translates to remarkably short distances, ~ 8.25 Å, and is illustrative for dimers with short bonding distances, ≤ 8.4 Å. Furthermore, AMK found another peculiar bond, the double 5/5 2+3 cycloaddition (minimum 31), that was

Minima	asphericity of molecule 1 (Å)	asphericity of molecule 2 (Å)
Min1	0.3018	0.3018
Min2	0.3034	0.3431
Min3	0.2977	0.2977
Min4	0.3439	0.3439
Min5	0.3470	0.3470
Min6	0.3889	0.3889
Min7	0.3831	0.4056
Min8	0.3376	0.4389
Min9	0.3980	0.3980
Min10	0.3406	0.3617
Min11	0.3365	0.5613
Min12	0.4364	0.4364
Min13	0.2504	0.2504
Min14	0.4421	0.4421
Min15	0.2513	0.2513
Min16	0.4239	0.4353
Min17	0.4334	0.4334
Min18	0.3909	0.3971
Min19	0.4140	0.4147
Min20	0.4191	0.4241
Min21	0.3786	0.5421
Min22	0.5351	0.3725
Min23	0.3899	0.4091
Min24	0.3826	0.3826
Min25	0.3717	0.4273
Min26	0.3726	0.3726
Min27	0.8917	0.4637
Min28	0.2869	0.2869
Min29	0.4599	0.4599
Min30	0.6149	0.4343
Min31	0.5692	0.5692
Min32	0.5916	0.4099
Min33	1.0139	0.5077
Min34	0.5109	1.1206
Min35	0.5816	1.0315
Min36	0.7341	0.7341
Min37	0.7595	0.7595
Min38	0.7623	0.7786
Min39	0.7520	0.7520
Min40	0.6009	1.3002
Min41	0.3764	0.3764

TABLE IV. Asphericities of each molecule in the $C_{60}+C_{60}$ dimers.

already present in a novel clathrate structure with very similar distances to the ones presented here [11].

Buga et al. [41] presented a series of six experimental crystalline phases obtained by pressurizing C_{60} between 11.5 and 13 GPa. In their report, structures are body-centered orthorhombic with the $Immm$ space group ($\Gamma_6^v D_{2h}^{25}$ in Schönflies notation) and presented their lattice parameters although no actual structure was proposed. Since their structures are body-centered orthorhombic, each of them has three distinct C_{60} distances, table V. In figure 2 a), we show a green area where these intermolecular distances lie. The longest distance found in this study is ~ 9.2 Å, in minimum 3. Note that as distances by different computational methods

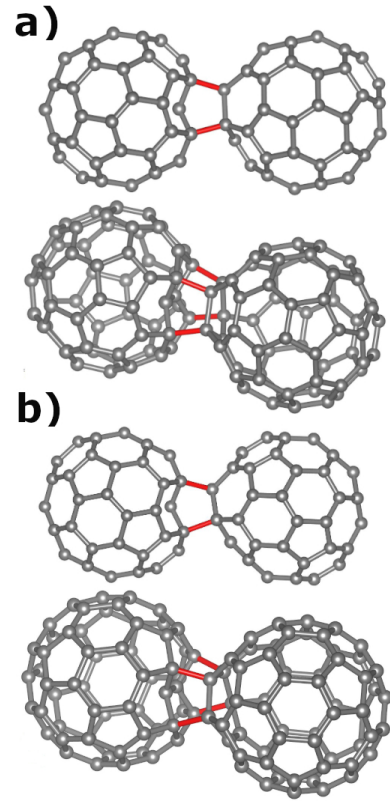


FIG. 3. Two distinct views of selected exotic bonding dimers found by AMK. a) Dimer AMK7077, min 33. b) Dimer AMK7610, min35.

Sample N ^o	1	2	3	4	5	6
distance 1 (Å)	9.07	8.73	8.69	8.68	8.67	8.65
distance 2 (Å)	9.47	9.16	8.88	8.84	8.81	8.78
distance 3 (Å)	9.19	9.05	8.88	8.85	8.83	8.79

TABLE V. Intermolecular distances from the structures reported in [41].

may differ, if slightly, we have considered a ± 0.2 Å of length "flexibility" to our intermolecular distance values. In addition, molecules may also have additional deformations while in the crystalline phase, therefore hindering the direct correspondence between dimer distances and crystalline distances. This is observed, for instance, in the 66/66 2+2 cycloaddition dimer that shows different experimental distances lying between 9.02 and 9.18 Å [5, 6]. Hence, experimental intermolecular distances larger than 9.3 Å in table V, may be due to either a single bond or no bond between neighboring molecules. Interestingly, several experimental distances between 8.65 and 8.80 Å in table V are common distances in our dimers. Considering this, it seems likely that some of our bonding schemes are responsible for the distances found in these experimental phases.

In addition, there are other structures in the literature still to be resolved, like the one reported by Yamanaka

et al. [9]. Although a complete crystalline structure was proposed, the structure changed considerably when optimized with DFT without constraints [42, 43]. Namely, Yamanaka et al. derived experimental lattice parameters of 7.86, 8.59 and 12.73 Å and a body-centered orthorhombic structure, with corresponding distances of 7.86, 8.59 and 8.62 Å, indicated in figure 2 a) by the red lines. The authors assigned these distances to double 66/66 4+4, no bond and 6/6 3+3 cycloaddition, respectively. Indeed, the 6/6 3+3 cycloaddition dimer, Min 17, and 66/66 4+4 cycloaddition dimer, min 39, have bonding distances in the appropriate range to explain this experimental data. Nevertheless, these bonding schemes were already used by Zipoli and Bernasconi [42] to construct crystalline structures and fail to reproduce the experimental lattice cell. Thus, other bonding schemes must be considered. We present here several potential alternatives within the observed range of distances.

Conversely, although the comparison of the distance is a simple, yet effective tool, we would like to emphasize that bonding patterns, which are stable in dimers may not be stable or not even geometrically possible in specific crystalline structures. For instance, minimum 4, although geometrically capable to bond to all the neighboring molecules in a crystalline fcc structure, turns out to be unstable in such configuration [7, 8]. On the other hand, the same minimum is present in other reported structures, such as in a 3D-rhombohedral phase [10] and in the recent graphullerene [13], proving that the molecular environment as a whole has to be considered to evaluate the existence of these patterns.

CONCLUSION

A comprehensive exploration and in-depth characterization of a large number of C_{60} dimers built from high energy molecular dynamics trajectories through the AMK methodology was performed. Several new C_{60} bonding schemes potentially relevant to understand polymeric phases were found and were energetically, structurally and electronically classified, increasing the number of known C_{60} dimers from 12 to 41. Some of the new dimers have bonding schemes matching experimental intermolecular distances observed on high-pressure high-temperature polymerized C_{60} yet to be understood, for instance in the works of Buga et al. or Yamanaka et al. [9, 41]. Relevantly,

12 of these dimers, i.e. 29 %, have spin-polarized ground states, which emphasizes that spin-polarization should be explicitly taken into consideration to properly model crystalline structures, especially with metallic or electronic exotic properties. This work paves the way for the exploration of novel extended 1D, 2D and 3D structures based on the bonding schemes presented here obtainable by HPHT treatment or more recent alternative routes [12, 13].

AUTHOR CONTRIBUTIONS

Conceptualization: M. Melle-Franco and J. Laranjeira; methodology: M. Melle-Franco, J. Laranjeira and E. Martínez-Núñez; software: M. Melle-Franco and E. Martínez-Núñez; validation: L. Marques, K. Strutyński and E. Martínez-Núñez; formal analysis: J. Laranjeira; investigation: J. Laranjeira; resources: M. Melle-Franco, E. Martínez-Núñez and J. Laranjeira; data curation: J. Laranjeira; writing-original draft preparation: J. Laranjeira; writing-review and editing: J. Laranjeira, M. Melle-Franco; visualization: J. Laranjeira; supervision: M. Melle-Franco; funding acquisition: M. Melle-Franco, E. Martínez-Núñez and J. Laranjeira. All authors have read and agreed to the published version of the manuscript.

ACKNOWLEDGMENTS

This work was developed within the scope of the project CICECO-Aveiro Institute of Materials, UIDB/50011/2020, UIDP/50011/2020 & LA/P/0006/2020, financed by national funds through the FCT/MCTES (PIDDAC) and IF/00894/2015 finances by FCT. J. Laranjeira acknowledges a PhD grant from FCT (SFRH/BD/139327/2018).

This work was partially supported by the Consellería de Cultura, Educación e Ordenación Universitaria (Grupo de referencia competitiva ED431C 2021/40), and the Ministerio de Ciencia e Innovación through Grant #PID2019-107307RB-I00.

The work has been performed under the project HPC-EUROPA3 (INFRAIA-2016-1-730897), with the support of the EC Research Innovation Action under the H2020 Programme; in particular, the author gratefully acknowledges the support of the computer resources and technical support provided by BSC.

-
- [1] A. Harris and R. Sachidanandam, *Phys. Rev. B* **46**, 4944 (1992).
- [2] A. Rao, P. Zhou, K.-A. Wang, G. Hager, J. Holden, Y. Wang, W.-T. Lee, X.-X. Bi, P. Eklund, D. Cornett, M. Duncan, and I. Amster, *Science* **259**, 955 (1993).
- [3] V. Davydov, L. Kashevarova, A. Rakhmanina, V. Senyavin, O. Pronina, N. Oleynikov, V. Agafonov, R. Céolin, H. Allouchi, and H. Szwarc, *Chem. Phys. Lett.* **333**, 224 (2001).
- [4] D. Strout, R. Murry, C. Xu, W. Eckhoff, G. Odom, and G. Scuseria, *Chem. Phys. Lett.* **214**, 576 (1993).
- [5] M. Álvarez-Murga and J. Hodeau, *Carbon* **82**, 381 (2015).

- [6] M. Núñez–Regueiro, L. Marques, J. L. Hodeau, O. Béthoux, and M. Perroux, *Phys. Rev. Lett.* **74**, 278 (1995).
- [7] J. Laranjeira, L. Marques, M. Mezouar, M. Melle-Franco, and K. Strutyński, *pss (RRL)* **11**, 1700343 (2017).
- [8] J. Laranjeira, L. Marques, N. Fortunato, M. Melle-Franco, K. Strutyński, and M. Barroso, *Carbon* **137**, 511 (2018).
- [9] S. Yamanaka, A. Kubo, K. Inumaru, K. Komaguchi, N. S. Kini, T. Inoue, and T. Irifune, *Phys. Rev. Lett.* **96**, 076602 (2006).
- [10] S. Yamanaka, N. S. Kini, A. Kubo, S. Jida, and H. Kuramoto, *J. Am. Chem. Soc.* **130**, 4303 (2008).
- [11] J. Laranjeira, L. Marques, M. Melle-Franco, K. Strutyński, and M. Barroso, *Carbon* **194**, 297 (2022).
- [12] L. Hou, X. Cui, B. Guan, S. Wang, R. Li, Y. Liu, D. Zhu, and J. Zheng, *Nature* **606**, 507 (2022).
- [13] E. Meirzadeh, A. Evans, M. Rezaee, M. Milich, C. Dionne, T. Darlington, S. T. Bao, A. Bartholomew, T. Handa, D. Rizzo, R. Wiscons, M. Reza, A. Zangiabadi, N. Fardian-Melamed, A. Crowther, J. Schuck, D. Basov, X. Zhu, A. Giri, P. Hopkins, P. Kim, M. Steigerwald, J. Yang, C. Nuckolls, and X. Roy, *Nature* **613**, 71 (2023).
- [14] G. Adams, J. Page, O. Sankey, and M. O’Keeffe, *Phys. Rev. B* **50**, 17471 (1994).
- [15] F.-L. Liu and X.-X. Zhao, *J. Mol. Struct.: THEOCHEM* **804**, 117 (2007).
- [16] S. Ōsawa, E. Ōsawa, and Y. Hirose, *Fullerene sci. technol.* **3**, 565 (1995).
- [17] N. Matsuzawa, M. Ata, D. Dixon, and G. Fitzgerald, *J. Phys. Chem.* **98**, 2555 (1994).
- [18] G. Scuseria, *Chem. Phys. Lett.* **257**, 583 (1996).
- [19] P. Fowler, D. Mitchell, R. Taylor, and G. Seifert, *J. Chem. Soc., Perkin Trans. 2*, 1901 (1997).
- [20] M. Diudea, C. Nagy, O. Ursu, and T. Balaban, *Fuller. Nanotub. Carbon Nanostructures* **11**, 245 (2003).
- [21] M. Koshino, Y. Niimi, E. Nakamura, H. Kataura, T. Okazaki, K. Suenaga, and S. Iijima, *Nat. Chem.* **2**, 7 (2010).
- [22] T. Shimizu, D. Lungerich, K. Harano, and E. Nakamura, *J. Am. Chem. Soc.* **144**, 9797 (2022).
- [23] S. Zhang, Z. Li, K. Luo, J. He, Y. Gao, A. Soldatov, V. Benavides, K. Shi, A. Nie, B. Zhang, W. Hu, M. Ma, Y. Liu, B. Wen, G. Gao, B. Liu, Y. Zhang, Y. Shu, D. Yu, X.-F. Zhou, Z. Zhao, B. Xu, L. Su, G. Yang, O. Chernogorova, and Y. Tian, *Natl. Sci. Rev.* **9**, 10.1093/nsr/nwab140 (2021), nwab140.
- [24] F. Pan, K. Ni, T. Xu, H. Chen, Y. Wang, K. Gong, C. Liu, X. Li, M.-L. Lin, S. Li, X. Wang, W. Yan, W. Yin, P.-H. Tan, L. Sun, D. Yu, R. Ruoff, and Y. Zhu, *Nature* **614**, 95 (2023).
- [25] E. Martínez-Núñez, *J. Comput. Chem.* **36**, 222 (2015).
- [26] E. Martínez-Núñez, *Phys. Chem. Chem. Phys.* **17**, 14912 (2015).
- [27] A. Rodríguez, R. Rodríguez-Fernández, S. Vázquez, G. Barnes, J. Stewart, and E. Martínez-Núñez, *J. Comput. Chem.* **39**, 1922 (2018).
- [28] A. Karton, S. Waite, and A. Page, *J. Phys. Chem. A* **123**, 257 (2019).
- [29] A. Becke, *J. Chem. Phys.* **98**, 1372 (1993).
- [30] C. Lee, W. Yang, and R. Parr, *Phys. Rev. B* **37**, 785 (1988).
- [31] S. Grimme, J. Antony, S. Ehrlich, and H. Krieg, *J. Chem. Phys.* **132**, 154104 (2010).
- [32] S. Grimme, S. Ehrlich, and L. Goerigk, *J. Comput. Chem.* **32**, 1456 (2011).
- [33] A. Becke and E. Johnson, *J. Chem. Phys.* **123**, 154101 (2005).
- [34] J. Tao, J. Perdew, V. Staroverov, and G. Scuseria, *Phys. Rev. Lett.* **91**, 146401 (2003).
- [35] F. Weigend and R. Ahlrichs, *Phys. Chem. Chem. Phys.* **7**, 3297 (2005).
- [36] M. Frisch, G. Trucks, H. Schlegel, G. Scuseria, M. Robb, J. Cheeseman, G. Scalmani, V. Barone, G. Petersson, H. Nakatsuji, X. Li, M. Caricato, A. Marenich, J. Bloino, B. Janesko, R. Gomperts, B. Mennucci, H. Hratchian, J. Ortiz, A. Izmaylov, J. Sonnenberg, D. Williams-Young, F. Ding, F. Lipparini, F. Egidi, J. Goings, B. Peng, A. Petrone, T. Henderson, D. Ranasinghe, V. Zakrzewski, J. Gao, N. Rega, G. Zheng, W. Liang, M. Hada, M. Ehara, K. Toyota, R. Fukuda, J. Hasegawa, M. Ishida, T. Nakajima, Y. Honda, O. Kitao, H. Nakai, T. Vreven, K. Throssell, J. Montgomery, J. Peralta, F. Ogliaro, M. Bearpark, J. Heyd, E. Brothers, K. Kudin, V. Staroverov, T. Keith, R. Kobayashi, J. Normand, K. Raghavachari, A. Rendell, J. Burant, S. Iyengar, J. Tomasi, M. Cossi, J. M. Millam, M. Klene, C. Adamo, R. Cammi, J. Ochterski, R. Martin, K. Morokuma, O. Farkas, J. Foresman, , and D. Fox, *Gaussian 09 revision A.02*, gaussian Inc. Wallingford CT, 2016.
- [37] J. Stewart, *Computational chemistry: Colorado springs, co.*, <http://openmopac.net> (2016). [accessed on 31/01/2023].
- [38] J. Stewart, *J. Mol. Model.* **19**, 1 (2013).
- [39] R. Jara-Toro, G. Pino, D. Glowacki, R. Shannon, and E. Martínez-Núñez, *ChemSystemsChem* **2**, e1900024 (2020).
- [40] K. Sohlberg and M. Foster, *RSC Adv.* **10**, 36887 (2020).
- [41] S. Buga, V. Blank, N. Serebryanaya, A. Dzwilewski, T. Makarova, and B. Sundqvist, *Diam. Relat. Mater.* **14**, 896 (2005).
- [42] F. Zipoli and M. Bernasconi, *Phys. Rev. B* **77**, 115432 (2008).
- [43] J. Yang, J. Tse, and T. Iitaka, *J. Chem. Phys.* **127**, 134906 (2007).

SUPPORTING INFORMATION

A. BONDING NOTATION

The naming of $C_{60}+C_{60}$ bonding schemes is done following the so-called cycloaddition rules which state how different rings react in organic chemistry in order to fuse. Considering the formation of a new ring of bonds between two molecules the bonding scheme is classified by the geometrical figure (or combination of geometrical figures) that is facing each molecule and by the number of atoms from each molecule that is involved in it. If we consider the more common, and stable, C_{60} dimer, the intermolecular bonding follows a 66/66 2+2 cycloaddition: 2+2 because from each molecule there are two bonds involved (one intramolecular and one intermolecular), and 66/66 since the two carbon atoms from each molecule are covalently bonded to the other by the two carbon atoms shared by two hexagons (hence 66 for each molecule). We may also consider that the alignment is done just by one geometrical figure from each molecule. If we consider the alignment between two hexagons, we will have a 6/6 n+m cycloaddition. With n, and m being integers smaller than 4.

B. VAN DER WAALS CORRECTION AND EXCHANGE-CORRELATION COMPARISON

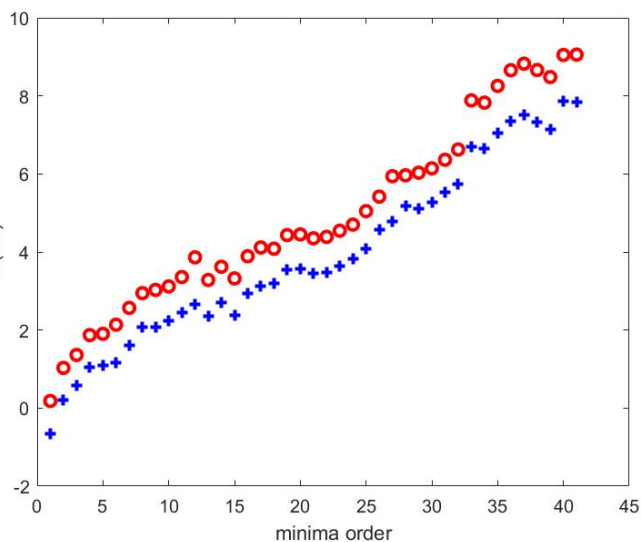


Figure S1. Minima bonding energy in eV per dimer vs minima order computed with B3LYP-6-31G(d,p) Hamiltonian (red circles) and augmented by the D3 van der Waals correction with finite Becke–Johnson damping (blue crosses) after optimization at B3LYP-6-31G(d,p)-D3BJ level.

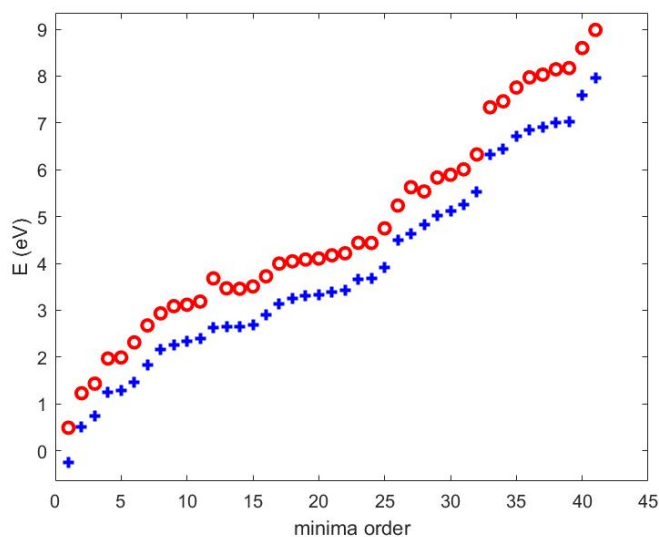


Figure S 2. Minima bonding energy in eV per dimer vs minima order computed with TPSS-Def2-TZVPP Hamiltonian (red circles) and augmented by the D3 van der Waals correction with finite Becke–Johnson damping (blue crosses) after optimization at B3LYP-6-31G(d,p)-D3BJ level.

Minima order	Dimer name	Sym.	interm. bonds	E_{Bond}^{B3LYP} (eV/dim)	$E_{Bond}^{B3LYP-D3BJ}$ (eV/dim)	$E_{Bond}^{TPSS-D3BJ}$ (eV/dim)	E_{Bond}^{TPSS} (eV/dim)
Min1	66/66 2+2	D _{2h}	2	0.1823	-0.6541	-0.2494	0.4900
Min2	56/66 2+2	C _s	2	1.0300	0.2055	0.4989	1.2269
Min3	SB	C _{2h}	1	1.3613	0.5839	0.7440	1.4314
Min4	56/65 2+2	C _{2h}	2	1.8711	1.0571	1.2501	1.9679
Min5	56/56 2+2	C _{2v}	2	1.9026	1.0934	1.2771	1.9906
Min6	double 66/66 2+2	C _{2v}	4	2.1376	1.1710	1.4683	2.3126
Min7	double 56/66 2+2 M2	C _s	4	2.5666	1.6022	1.8367	2.6752
Min8	5/66 3+2	C _s	2	2.9455	2.0740	2.1629	2.9319
Min9	double 56/56 2+2	C _{2v}	4	3.0279	2.0741	2.2527	3.0859
Min10	AMK5678	C ₁	3	3.1171	2.2272	2.3363	3.1170
Min11	6/66 3+2	C ₁	2	3.3582	2.4498	2.3867	3.1851
Min12	6/6 4+4 M1	C _{2v}	2	3.8631	2.6621	2.6221	3.6790
Min13	triple 66/65 2+2	D _{3d}	6	3.2816	2.3517	2.6419	3.4678
Min14	6/6 4+4 M2	C ₁	2	3.6203	2.6950	2.6441	3.4582
Min15	triple 66/66 2+2	D _{3h}	6	3.3219	2.3890	2.6783	3.5086
Min16	6/6 3+4 M2	C ₁	2	3.8909	2.9370	2.8918	3.7243
Min17	6/6 3+3 M3	C ₂	2	4.1152	3.1303	3.1388	3.9958
Min18	double 56/66 2+2 M1	C _s	4	4.0830	3.1872	3.2546	4.0437
Min19	5/6 3+4 M2	C _s	2	4.4326	3.5528	3.3104	4.0827
Min20	5/6 3+4 M1	C _s	2	4.4504	3.5723	3.3326	4.1037
Min21	6/56 3+2 M2	C ₁	2	4.3499	3.4470	3.3799	4.1725
Min22	6/56 3+2 M1	C ₁	2	4.3866	3.4796	3.4201	4.2159
Min23	double 56/65 2+2	C _s	4	4.5444	3.6441	3.6534	4.4392
Min24	5/5 3+3 M1	C _{2h}	2	4.7005	3.8357	3.6760	4.4361
Min25	6/6 3+4 M1	C ₁	2	5.0466	4.0917	3.9138	4.7480
Min26	double 56/56 2+2	C _{2v}	4	5.4181	4.5818	4.4948	5.2343
Min27	AMK6163	C ₁	3	5.9410	4.7803	4.6261	5.6268
Min28	double 56/56 2+2 plus SB	D _{5h}	5	5.9654	5.1727	4.8285	5.5361
Min29	double 6/56 4+2	C _{2h}	4	6.0320	5.1107	5.0253	5.8338
Min30	5/56 3+2 plus 6/56 4+2	C _s	4	6.1424	5.2653	5.1168	5.8918
Min31	double 5/5 2+3	C _{2h}	4	6.3630	5.5234	5.2631	6.0079
Min32	5/6 3+3 plus 56/6 2+3	C ₁	4	6.6255	5.7290	5.5353	6.3257
Min33	AMK7077	C _s	4	7.8846	6.7070	6.3159	7.3327
Min34	AMK6511	C ₁	4	7.8269	6.6398	6.4343	7.4601
Min35	AMK7610	C _s	4	8.2559	7.0520	6.7170	7.7550
Min36	5/5 3+3 plus 6/6 4+4	C _{2v}	4	8.6573	7.3448	6.8452	7.9718
Min37	double 56/65 3+4	C _{2h}	4	8.8244	7.5147	6.9087	8.0303
Min38	5/6 3+4 plus 6/6 4+4	C _s	4	8.6623	7.3213	6.9973	8.1441
Min39	double 66/66 4+4	D _{2h}	4	8.4821	7.1399	7.0261	8.1709
Min40	AMK8161	C _s	4	9.0487	7.8726	7.5823	8.5970
Min41	double 66/66 4+4 plus 66/66 2+2	D _{2h}	6	9.0574	7.8481	7.9499	8.9845

Table S1. Bonding energy of C₆₀+C₆₀ dimers optimized with B3LYP-6-31G(d,p) augmented with D3 van der Waals correction with finite Becke–Johnson damping and computed with B3LYP-6-31G(d,p) and TPSS-Def2-TZVPP/B3LYP-6-31G(d,p)-D3BJ, with and without D3 van der Waals correction with finite Becke–Johnson damping augmentation.

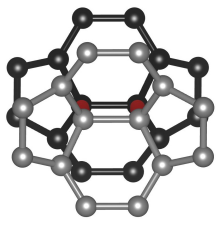
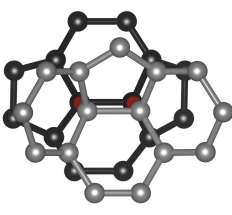
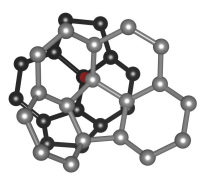
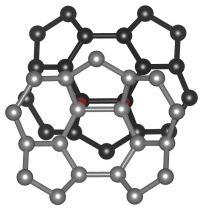
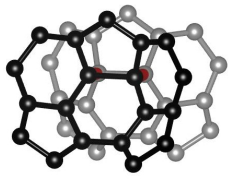
C. COMPLETE HOMO-LUMO GAP INFORMATION

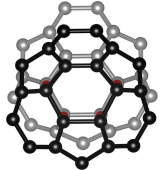
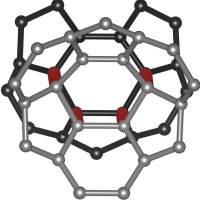
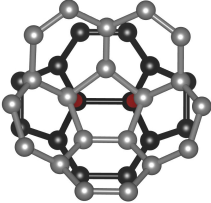
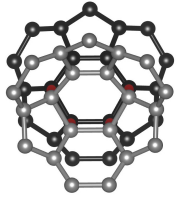
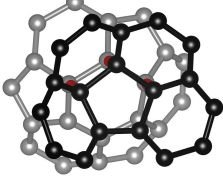
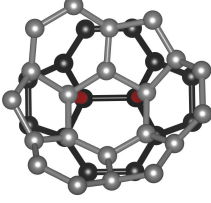
Minima order	Dimer name	Sym.	interm. bonds	HOMO-LUMO gap (eV)	ΔE_{Bond} (eV/dim)	Mol. dist. Å
	C_{60}	I_h	0	2.8523	-	
Min1	66/66 2+2	D_{2h}	2	2.50562	-0.6541	9.05
Min2	56/66 2+2	C_s	2	1.81935	0.2055	9.07
Min3	SB	C_{2h}	1	1.84359 1.98155	0.5839	9.23
Min4	56/65 2+2	C_{2h}	2	1.69636	1.0571	9.09
Min5	56/56 2+2	C_{2v}	2	1.74996	1.0934	9.10
Min6	double 66/66 2+2	C_{2v}	4	2.49311	1.1710	8.64
Min7	double 56/66 2+2 M2	C_s	4	2.45719	1.6022	8.65
Min8	5/66 3+2	C_s	2	1.91651 1.83923	2.0740	8.91
Min9	double 56/56 2+2	C_{2v}	4	2.34045	2.0741	8.66
Min10	AMK5678	C_1	3	1.41609 1.69528	2.2272	8.85
Min11	6/66 3+2	C_1	2	0.74614	2.4498	8.87
Min12	6/6 4+4 M1	C_{2v}	2	1.97527	2.6621	8.81
Min13	triple 66/65 2+2	D_{3d}	6	2.39487	2.3517	8.44
Min14	6/6 4+4 M2	C_1	2	1.79731	2.6950	8.81
Min15	triple 66/66 2+2	D_{3h}	6	2.4327	2.3890	8.44
Min16	6/6 3+4 M2	C_1	2	1.78589 1.99733	2.9370	8.80
Min17	6/6 3+3 M3	C_2	2	1.78318 1.94318	3.1303	8.77
Min18	double 56/66 2+2 M1	C_s	4	1.56792	3.1872	8.69
Min19	5/6 3+4 M2	C_s	2	1.01063	3.5528	8.87
Min20	5/6 3+4 M1	C_s	2	1.01798	3.5723	8.87
Min21	6/56 3+2 M2	C_1	2	1.53201 1.74182	3.4470	8.87
Min22	6/56 3+2 M1	C_1	2	1.51841 1.72304	3.4796	8.87
Min23	double 56/65 2+2	C_s	4	1.52057	3.6441	8.71
Min24	5/5 3+3 M1	C_{2h}	2	1.8637 1.4294	3.8357	8.89
Min25	6/6 3+4 M1	C_1	2	1.28058 1.49854	4.0917	8.77
Min26	double 56/56 2+2	C_{2v}	4	1.22506	4.5818	8.75
Min27	AMK6163	C_1	3	1.75270 1.91569	4.7803	8.41
Min28	double 56/56 2+2 plus SB	D_{5h}	5	0.74260	5.1727	8.68
Min29	double 6/56 4+2	C_{2h}	4	2.34100	5.1107	8.62
Min30	5/56 3+2 plus 6/56 4+2	C_s	4	1.52955	5.2653	8.67
Min31	double 5/5 2+3	C_{2h}	4	1.10995	5.5234	8.72
Min32	5/6 3+3 plus 56/6 2+3	C_1	4	1.39868 1.44358	5.7290	8.62
Min33	AMK7077	C_s	4	0.87974	6.7070	8.29
Min34	AMK6511	C_1	4	1.68194	6.6398	8.28
Min35	AMK7610	C_s	4	0.95349	7.0520	8.25
Min36	5/5 3+3 plus 6/6 4+4	C_{2v}	4	0.76546	7.3448	8.05
Min37	double 56/65 3+4	C_{2h}	4	0.85662 0.66015	7.5147	8.10
Min38	5/6 3+4 plus 6/6 4+4	C_s	4	0.94070	7.3213	8.04
Min39	double 66/66 4+4	D_{2h}	4	1.64030	7.1399	8.05
Min40	AMK8161	C_s	4	2.51216	7.8726	8.28
Min41	double 66/66 4+4 plus 66/66 2+2	D_{2h}	6	2.01174	7.8481	8.16

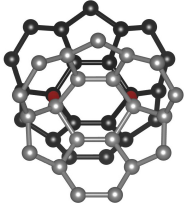
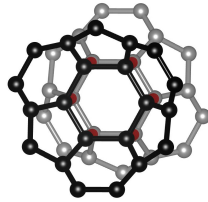
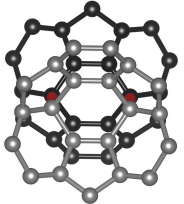
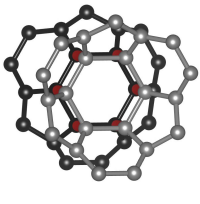
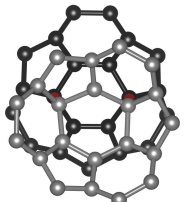
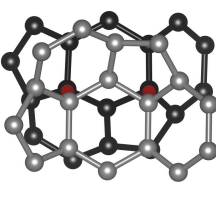
Table S2. Energetics and molecular distances of $C_{60}+C_{60}$ dimers computed at B3LYP-6-31G(d,p)-D3BJ level of theory. Letter L indicate structure found in Literature, AMK and G indicate the structure was found using, respectively, AutoMeKin or geometric considerations. The number that follows AMK is simple the energy order of the minimum given by AMK.

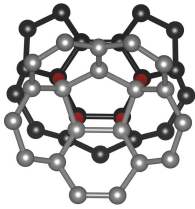
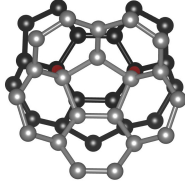
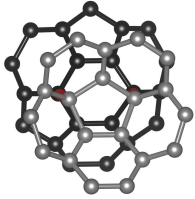
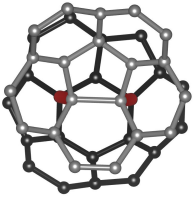
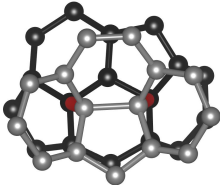
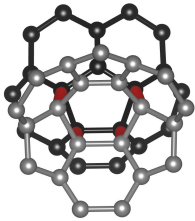
D. BONDING SCHEMES

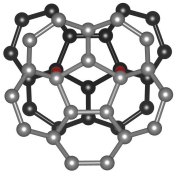
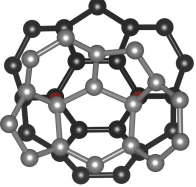
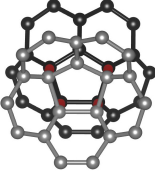
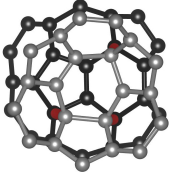
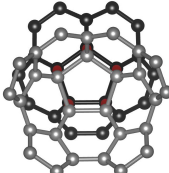
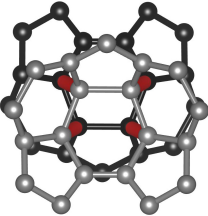
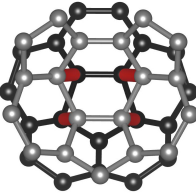
Table S3. $C_{60}+C_{60}$ dimer names, number of bonds, bonding schemes and origin of the bond. Letter L indicate structure found in Literature, AMK and G indicate that the structure was found using, respectively, AutoMeKin or geometric considerations. The number that follows AMK is simple the energy order of the minimum given by AMK.

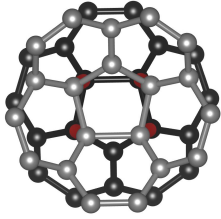
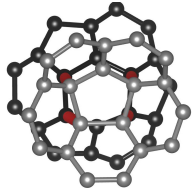
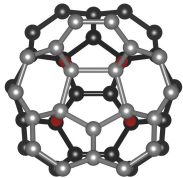
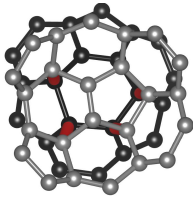
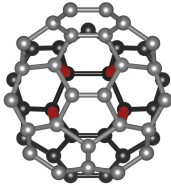
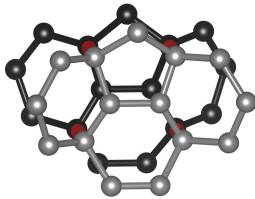
Isomer	intern. bonds	intermolecular bonding scheme	bond origin
C_{60}	0	-	-
Min1 66/66 2+2	2		AMK66/L [1-5]
Min2 56/66 2+2	2		AMK203/L [1]
Min3 single bond	1		L [3]
Min4 56/65 2+2	2		AMK1473/L [1]
Min5 56/56 2+2	2		AMK1818/L [1]

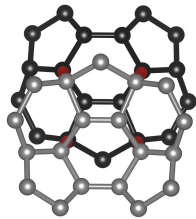
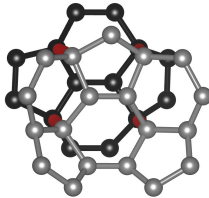
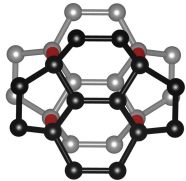
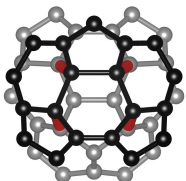
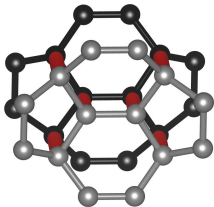
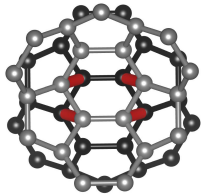
Min6 double 66/66 2+2	4		G
Min7 double 56/66 2+2 M2	4		AMK1269
Min8 5/66 3+2	2		AMK3333
Min9 double 56/56 2+2	4		G
Min10 AMK5678	3		AMK5678
Min11 6/66 3+2	2		AMK3615

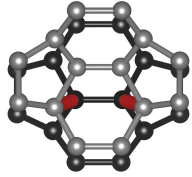
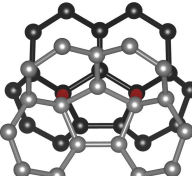
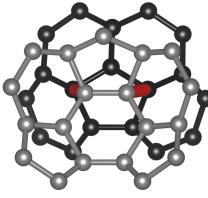
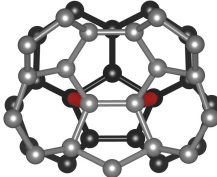
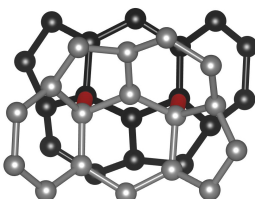
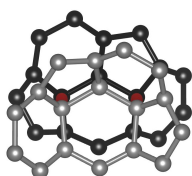
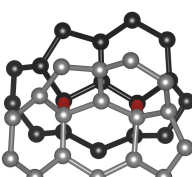
Min 12 6/6 4+4 M1	2		AMK2506/L [4, 5]
Min13 triple 66/65 2+2	6		AMK1372/L [2, 6]
Min 14 6/6 4+4 M2	2		AMK2507/L [4, 5]
Min15 triple 66/66 2+2	6		L [2, 6]
Min 16 6/6 3+4 M2	2		AMK4004
Min 17 6/6 3+3 M3	2		AMK5325

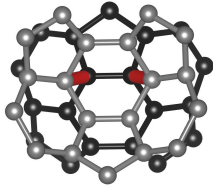
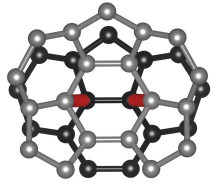
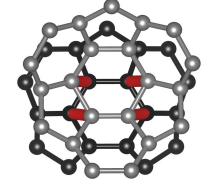
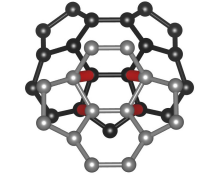
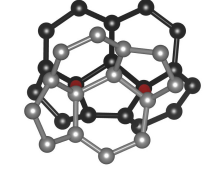
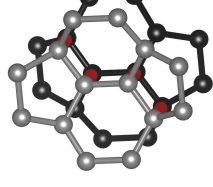
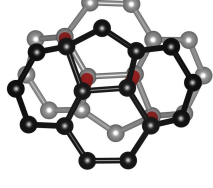
Min18 double 56/66 2+2 M1	4		AMK2605
Min 19 5/6 3+4 M2	2		AMK4307
Min 20 5/6 3+4 M1	2		AMK4321
Min 21 6/56 3+2 M2	2		AMK4646
Min22 6/56 3+2 M1	2		AMK4567
Min23 double 56/65 2+2	4		AMK3018

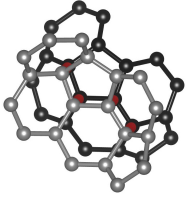
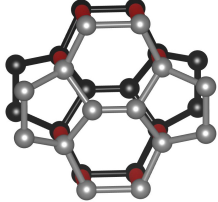
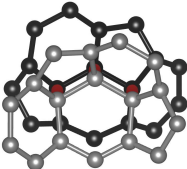
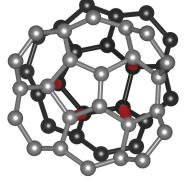
Min 24 5/5 3+3 M1	2		G
Min25 6/6 3+4 M1	2		AMK3893
Min 26 double 56/56 2+2	4		G
Min 27 AMK6163	3		AMK6163
Min 28 double 56/56 2+2 plus SB	5		L [2]
Min 29 double 6/56 4+2	4		L [1]
Min 30 5/56 3+2 plus			G
6/56 4+2	4		

Min 31 double 5/5 2+3	4		G
Min 32 5/6 3+3 plus 56/6 2+3	4		AMK5775
Min 33 AMK7077	4		AMK7077
Min 34 AMK6511	4		AMK6511
Min35 AMK7610	4		AMK7610
Min36 5/5 3+3 plus 6/6 4+4	4		G

Min37 double 56/65 3+4	4		S-AMK_or
Min38 5/6 3+4 plus 6/6 4+4	4		G
Min39 double 66/66 4+4	4		G
Min 40 AMK8161	4		AMK8161
Min41 double 66/66 4+4 plus 66/66 2+2	6		G
double 66/6 2+4	4		G

66/6 2+4	2		AMK3097/L [5]
5/5 3+3 M2	2		G
5/56 3+2	2		G
5/65 3+2	2		G
6/6 3+3 M1	2		G
6/6 3+3 M2	2		AMK5282
6/6 3+3 M4	2		G

6/56 4+2 M1	2		G
6/56 4+2 M2	2		G
6/56 4+2 plus 6/66 4+2	4		G
5/66 3+2 plus 6/56 4+2	4		G
5/6 3+3 M1	2		AMK5118
double 66/66 4+4 zig	4		G
double 56/65 3+4 zig	4		G

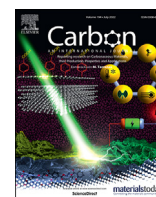
5/5 3+3 plus 6/6 4+4 zig	4		G
double 66/66 4+4 plus double 56/56 2+2	4		G
AMK5282	3		
AMK6480	4		AMK6480

-
- [1] D. Strout, R. Murry, C. Xu, W. Eckhoff, G. Odom, and G. Scuseria, Chem. Phys. Lett. **214**, 576 (1993).
 [2] G. Adams, J. Page, O. Sankey, and M. O’Keeffe, Phys. Rev. B **50**, 17471 (1994).
 [3] G. Scuseria, Chem. Phys. Lett. **257**, 583 (1996).
 [4] S. Ōsawa, E. Ōsawa, and Y. Hirose, Fullerene sci. technol. **3**, 565 (1995).
 [5] N. Matsuzawa, M. Ata, D. Dixon, and G. Fitzgerald, J. Phys. Chem. **98**, 2555 (1994).
 [6] F.-L. Liu and X.-X. Zhao, J. Mol. Struct.: THEOCHEM **804**, 117 (2007).

Chapter 7

A5 - Clathrate structure of polymerized fullerite C₆₀

© 2022 Elsevier Ltd.
Reprinted with permission.



Clathrate structure of polymerized fullerite C₆₀

Jorge Laranjeira ^{a,*}, Leonel Marques ^{a,**}, Manuel Melle-Franco ^b, Karol Strutyński ^b,
Manuel Barroso ^c

^a Departamento de Física and CICECO, Universidade de Aveiro, 3810-193, Aveiro, Portugal

^b Departamento de Química and CICECO, Universidade de Aveiro, 3810-193, Aveiro, Portugal

^c Departamento de Física and I3N, Universidade de Aveiro, 3810-193, Aveiro, Portugal



ARTICLE INFO

Article history:

Received 25 November 2021

Received in revised form

14 March 2022

Accepted 21 March 2022

Available online 23 March 2022

Keywords:

Carbon clathrates

Fullerite C₆₀

DFT Calculations

ABSTRACT

Investigations of clathrate structures have gained a new impetus with the recent discovery of room-temperature superconductivity in metal hydrides. Here we report the finding, through density functional theory calculations, of a clathrate phase in the fullerite C₆₀ system. Intermolecular bonds of the type 5/5 2+3 cycloaddition are induced between each C₆₀ molecule and its twelve nearest neighbors in the face centered cubic lattice. Remarkably, this bonding creates on octahedral sites new C₆₀ cages, identical to the original ones, and on tetrahedral sites distorted sodalite-like cages. The resulting carbon clathrate has a Pm $\bar{3}$ simple cubic structure with half of the original face centered lattice constant. Eighty percent of its atoms are sp³-hybridized, driving a narrow-gap semiconducting behavior, a moderate bulk modulus of 268 GPa and an estimated hardness of 21.6 GPa. This new phase is likely to be prepared by subjecting C₆₀ to high pressure and high temperature conditions.

© 2022 Elsevier Ltd. All rights reserved.

1. Introduction

Clathrates are open-framework structures with face-sharing polyhedral cages that can contain guest species, atoms or molecules [1–17]. Hydrates are an important group of clathrate structures, being the focus of intense investigations on the possibility of greenhouse gases storage [1]. Group IV elemental solids can also form clathrates and, in particular, silicon and germanium clathrates have been synthesized in both guest and guest-free forms [2,3]. Their properties can be tuned by inserting or exchanging guest atoms inside the polyhedral cages [14].

Carbon has exceptional flexibility as shown by the profusion of allotropes with distinct physical and chemical properties [3,13–40]. Despite the large number of geometries carbon constructs may adopt, no carbon clathrate has been synthesized so far, in contrast to other group IV elements. There have been several theoretical studies discussing the stability of different carbon clathrates, such as C₄₆, C₃₄ and C₂₄, whose construction is based on polyhedral cages and arrangements exhibited by clathrates of other chemical

elements [13–16]. A significant step towards the synthesis of carbon clathrates has been done recently with the high-pressure synthesis of mixed carbon-boron clathrates, where metal atoms, strontium or lanthanum, are trapped inside ordered sodalite-like cages formed by carbon and boron [9,10].

Notable candidates for the realization of carbon clathrates are some of the three-dimensional (3D) C₆₀ polymers prepared at high pressure and high temperature [3,22–40]. However, the crystal structures reported so far involve isolated C₆₀ cages bonded to each other through sp³ carbons. Here we show, through density functional theory (DFT) calculations, that indeed fullerite C₆₀ can also form an all-carbon clathrate structure through 3D polymerization of the molecules in the face centered cubic (fcc) lattice that creates two new polyhedral cages, sharing faces with each other and with the original C₆₀ molecules. This carbon clathrate structure is statically and dynamically stable, being somewhat less stable than the known 3D C₆₀ polymers and is a narrow-gap semiconductor with a predicted indirect gap of 1.33 eV. Despite a high ratio, eighty percent, of sp³ carbons, it displays moderate elastic moduli and a moderate hardness of 21.6 GPa, probably a consequence of the elastic flexibility of the big C₆₀ cages.

* Corresponding author.

** Corresponding author.

E-mail addresses: jorgelaranjeira@ua.pt (J. Laranjeira), lmarques@ua.pt (L. Marques).

2. Methods

DFT calculations were primarily performed using the Vienna ab-initio simulation package (VASP) [41] with the Perdew-Burke-Ernzerhof (PBE) generalized gradient approximation [42] which was used also to compute the elastic properties [43] and phonons [44]. Vibrational spectra were computed at the PBE-6-31G(d,p)-D3 level [45] as implemented on CRYSTAL17 [46], while additional HSE06-6-31G(d,p) level calculations [47] were performed with Gaussian 09 [48]. Fuller details of the calculations can be found in section A of the Supporting Information.

3. Results and discussion

The new C_{60} -based carbon clathrate structure was found stable at ambient pressure in DFT investigations of possible intermolecular bonds formed between C_{60} molecules in the fcc lattice. A new intermolecular bonding was considered, in which bonds are formed between pentagons of neighboring molecules. The new bonding has four intermolecular covalent bonds and is denoted “double 5/5 2+3 cycloaddition” joining two pentagonal rings in an antiparallel fashion, Fig. 1a). Its electron localization function around this bond and supporting its structural model is given in Fig. S1. Strout and coworkers reported a similar bonding, although it involves hexagons instead of pentagons [19]. A new polymeric structure is then constructed with each molecule adopting a standard molecular orientation and bonded, through the double 5/5 2+3 cycloadditions, to its twelve near neighbors (NN) in the fcc lattice, as illustrated in Fig. 1b).

An important consequence of having each molecule bonded to its neighbors via the double 5/5 2+3 cycloadditions, is that the resulting fcc polymeric structure has its octahedral interstitial sites enclosed by truncated icosahedron cages (identical to the original C_{60} molecular cages) and its tetrahedral interstitial sites enclosed by distorted truncated octahedron cages. These truncated octahedron cages, with 24 atoms arranged in 8 hexagons and 6 rhombi, i.e. 4^66^8 building block, are a distorted version of the sodalite-type cages displayed by numerous clathrates [9–13]. The original C_{60} molecular cages are strongly deformed and their double hexagonal rings, lying perpendicular to the cubic axes, are now perfectly planar. The C_{60} cages formed on the octahedral sites are exactly equal to the original C_{60} molecular cages, i.e. $5^{12}6^{20}$ building block. Hence, as it is illustrated in Fig. 2a), the resulting $Fm\bar{3}$ fcc structure can be described by a reduced $Pm\bar{3}$ simple cubic structure, with half of the lattice constant. The C_{60} cages share with each other the planar double hexagonal rings, while they share hexagons with the C_{24} sodalite-like cages, thus, forming a carbon clathrate structure. Fig. 2b) and c), illustrates the cages exhibited by this clathrate structure, emphasizing the different origins of the two C_{60} cages, one corresponding to the original molecules and the other, centered at the octahedral sites, resulting from the polymeric bonding.

The structural optimization carried out on the fcc lattice, at zero pressure and without symmetry constraints, gives a lattice constant of 12.42 Å, the standard molecular orientation remains unaltered during the optimization. A structural optimization conducted in the simple cubic cell gives exactly the same relaxed structure with a lattice constant of 6.21 Å, half of the relaxed fcc cell. The optimized atomic coordinates of the asymmetric cell, together with their Wyckoff positions, are given in Table 1 for the simple cubic structure. The C2 atoms are sp^2 -hybridized, whereas both C1 and C3 atoms are sp^3 -hybridized, and they are depicted in Fig. 2 b). Similar values were obtained from HSE06-6-31G(d,p) level calculations, Table S2. The resulting covalent 3D framework, having 80% of its

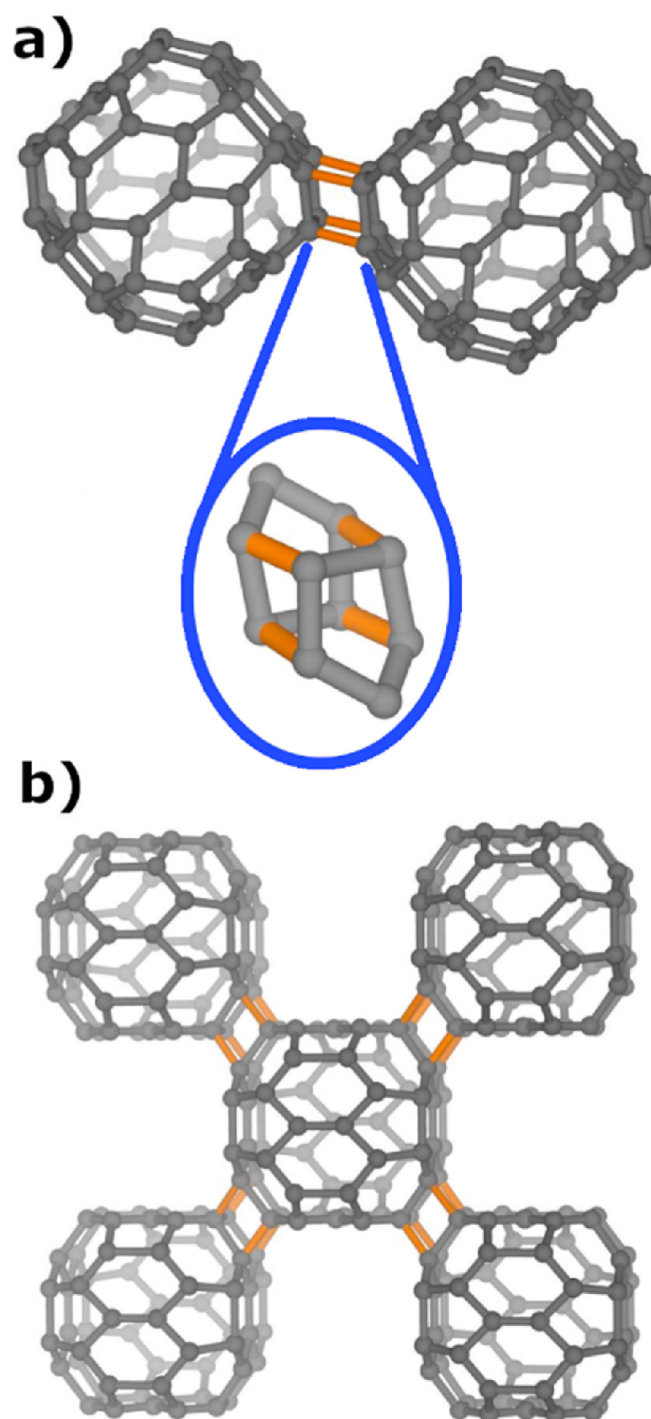


Fig. 1. a) Double 5/5 2+3 cycloaddition bond established between neighboring molecules and its expanded view. b) Molecules in the fcc (100) plane bonded through double 5/5 2+3 cycloadditions. Intermolecular bonds are drawn in orange. (A colour version of this figure can be viewed online.)

atoms in sp^3 hybridization, displays a bulk modulus $B_0 = 268$ GPa and a hardness of 21.6 GPa, which are moderate in comparison with those of full- sp^3 carbon clathrates [13–16]. The ideal ultimate tensile strength along [100] cubic direction, obtained from the calculated stress/strain curve given in the Supporting Information (section D, Fig. S2), is about 20 GPa, in agreement with the moderate elastic properties but much smaller than those displayed by the full- sp^3 carbon clathrates, ~100 GPa [49].

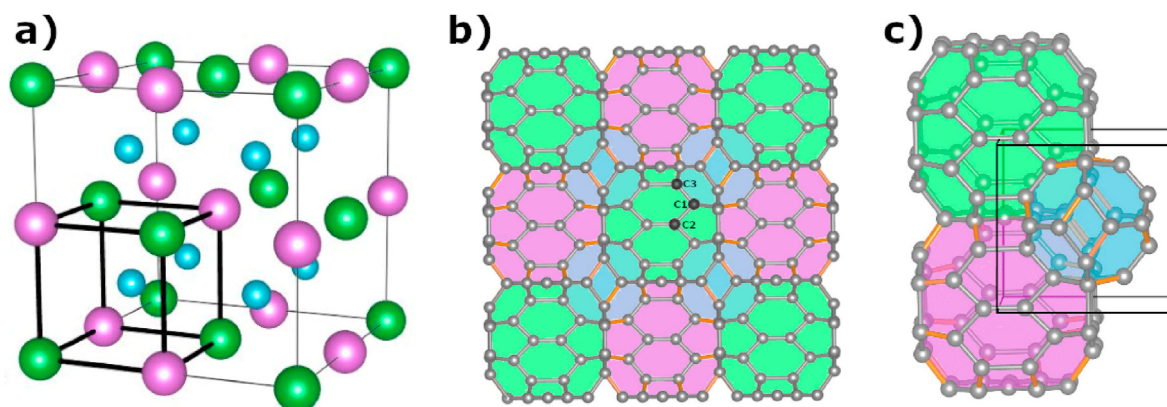


Fig. 2. a) Face centered cubic lattice with green spheres as lattice points, lilac spheres as octahedral interstitial sites and blue spheres as tetrahedral interstitial sites. A simple cubic lattice can be drawn when the fcc lattice points and octahedral fcc sites are considered as identical lattice points. b) The C_{60} -based clathrate structure viewed along the [100] direction. C_{60} cages enclosing fcc lattice points are green, C_{60} cages enclosing octahedral fcc interstitial sites are lilac, and C_{24} sodalite-like cages enclosing tetrahedral fcc interstitial sites are blue. c) C_{60} -based clathrate structure described in the simple cubic cell, viewed along [100] direction, with only two C_{60} cages shown and, at the center of the cell, a C_{24} sodalite-like cage (the colors have a correspondence as used before). Intermolecular bonds are drawn in orange. (A colour version of this figure can be viewed online.)

Table 1

Optimized atomic positions of the C_{60} -based clathrate structure in the $Pm\bar{3}$ simple cubic cell.

atom	X	Y	Z	Wyckoff Position
C1	0.50000	0.29165	-0.17136	12k
C2	-0.12132	0.00000	0.50000	6f
C3	0.50000	0.14222	0.34897	12k

The curve of the total energy per atom $E(V)$ as a function of volume for the new clathrate structure is given in Fig. S3. Its dynamic stability was also confirmed, since no negative frequencies were found (the phonon dispersion and phonon density of states are given in Fig. S5). The total energy calculated for the equilibrium clathrate structure is -7.93 eV/atom, significantly larger than the -8.85 eV/atom calculated for the C_{60} and larger than the other 3D polymerized C_{60} structures [27]. The enthalpy calculated as a function of pressure and shown in the Supporting Information (section E, Fig. S4), also points to a metastable structure. As it was reviewed in detail in Ref. [26], a huge number of 3D polymerized C_{60} phases, obtained at high energetic conditions of temperature and pressure, are highly metastable and they are often determined by non-thermodynamic factors (pressure-temperature path to the final conditions, uniaxial applied stress, time, etc), which is a typical situation in metastable systems like the C_{60} fullerite itself.

The new clathrate is a narrow-gap semiconductor with an indirect band gap of 1.33 eV, computed at the HSE06-6-31G(d,p) level, between the bottom of the conduction band at the M point and the top of the valence band at the X point. The electronic band structure and the density of states (DOS) shown in Fig. 3 were computed with PBE, yielding a bandgap of 0.68 eV. Upon tensile deformation, the bandgap first decreases and then closes (see Supporting Information D, Fig. S2), a trend also observed in full- sp^3 carbon clathrates [49].

The high proportion of sp^3 carbons present in this structure (80%) should be the reason for the observed semiconducting behavior. The three bands located just above the Fermi level and degenerate at the Γ point, are nearly flat and originate a sharp peak in DOS at 0.76 eV. The corresponding electronic density shown in Fig. S6 indicates that these three bands are nearly pure antibonding π^* orbitals of the sp^2 carbons (C2 atoms in Fig. 2b)). Doping, for instance with trivalent metallic atoms inside the C_{60} cages, would push the Fermi level to this peak, inducing metallic behavior.

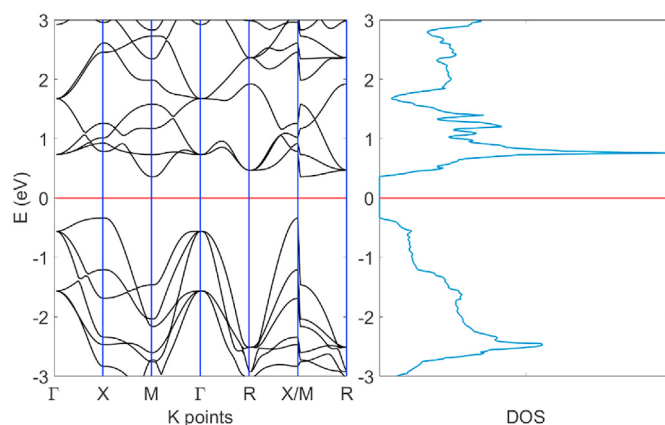


Fig. 3. Electronic density of states (right panel) and electronic band structure (left panel) of C_{60} -based clathrate. Red lines indicate the Fermi level. (A colour version of this figure can be viewed online.)

Furthermore, it might show superconductivity if the coupling of these π^* bands with modes stretching the C2–C2 double bonds turns out to be effective, as occurring in superconducting fullerenes [50,51].

High-pressure and high-temperature (HPHT) are known to induce ordered polymerization of C_{60} molecules. Indeed, with increasing pressure synthesis, one-dimensional and two-dimensional C_{60} polymers have been prepared [25,26]; inducing 3D polymerization requires higher pressures, above 8–9 GPa [26–32]. The clathrate structure reported here is, therefore, likely to be prepared by subjecting fullerite C_{60} to these HPHT conditions. In this sense and trying to establish an experimental connection to the new clathrate, we have compared its simulated X-ray diffraction pattern to those of experimental 3D C_{60} polymerized structures obtained at ambient conditions (see Fig. 4). These 3D C_{60} polymers comprise a fcc phase prepared at 9.5 GPa [28], an orthorhombic phase prepared at 13 GPa [29] and two phases prepared at 15 GPa: a fcc polymer [30] and a cuboidal orthorhombic polymer obtained from the compression of the 2D tetragonal C_{60} polymer [31]. From the X-ray diffraction patterns shown in Fig. 4, it is evident that the new clathrate is more compressed than the fcc phase obtained at 9.5 GPa, since its diffraction peaks are shifted to higher diffraction angles, but it is less compressed than the two phases obtained at

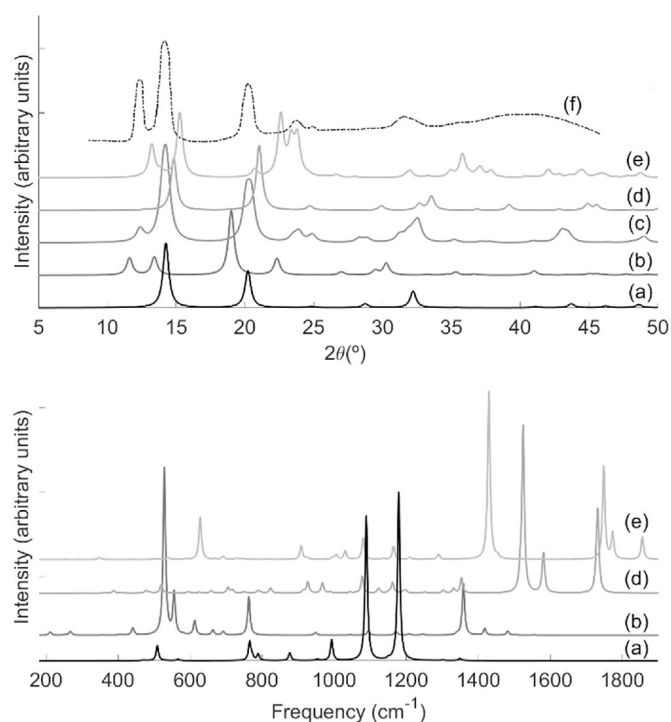


Fig. 4. (top panel) Simulated X-ray diffraction patterns, with wavelength $\lambda = 1.54 \text{ \AA}$ and crystallite size of 150 nm, at ambient pressure and (bottom panel) calculated Raman spectra, for the new clathrate phase (a) and for previously proposed structural models of 3D C_{60} polymers obtained at 9.5 GPa [28] (b), 13 GPa [29] (c), 15 GPa [30] (d) and 15 GPa using the 2D tetragonal C_{60} polymer as precursor [31] (e). An experimental X-ray diffraction pattern from Ref. [29] is also shown on the top panel (f).

15 GPa. Interestingly, the new clathrate is as compressed as the 3D polymer prepared at 13 GPa, indicating that molecule-molecule distances are similar in both phases. This 3D polymer has an orthorhombic symmetry, slightly distorted from fcc, with no splitting of fcc diffraction peaks [29]. The first peak, (111) in fcc indexation, is absent in the new clathrate because, as explained before, its structure is actually simple cubic. It deserves to be mentioned that Brazhkin and coworkers reported a series of fcc 3D polymerized phases of C_{60} obtained at 12.5 GPa, including one with lattice constant identical to the new clathrate and with an absent (111) diffraction peak [35], however, to the best of our knowledge, no structural models has been proposed to fit these observations to date. Another interesting result is that the {110} lattice planes of the new clathrate structure coincide with the (100) lattice planes of the orthorhombic distortion of a 3D polymerized phase prepared at 13 GPa [36]. Therefore, a 3D polymer with the clathrate structure described herein, or related to it, may be obtained by squeezing fullerite C_{60} at pressures of 12–13 GPa and high temperature.

The calculated Raman and infrared spectra for the clathrate structure and the other 3D C_{60} polymerized structures are shown in Fig. 4 and S7. These spectra refer to unpolarized light for polycrystalline specimens obtained after geometry optimization. These optimizations gave lattice constants significantly different from the experimental ones for the 3D C_{60} polymers prepared at 15 GPa, a result that was already emphasized by different authors [52,53], casting some doubts on the proposed structural models and implying some precaution on the simple comparison of the Raman and infrared spectra. In addition, the structure proposed for the 3D C_{60} polymer prepared at 13 GPa was found to be dynamically unstable, since it displays vibrational modes with negative frequencies, hence its Raman spectra is not presented. The Raman modes of the new clathrate arise between 450 and 1400 cm^{-1} , in an

energy region shorter than for C_{60} , indicating that upon polymerization the intermolecular modes harden, due to the formation of covalent intermolecular bonds, and the rigid intramolecular modes soften, due to the decrease in the strength and the number of the double bonds. The 9.5 GPa polymerized phase keeps the low-energy intermolecular modes, in agreement with experimental data, because some of weak Van der Waals interactions between neighboring molecules are preserved in this structure [54]. In contrast, the 15 GPa structures display high-energy modes, larger than 1700 cm^{-1} , associated with the short and strong double bonds ($\sim 1.30 \text{ \AA}$) present in these structures and resulting from the bonding type involved, as discussed in detail by Ref. [52]. Unfortunately, no experimental Raman and infrared spectra were reported for these polymers.

Other properties of the clathrate phase are also to be compared with experimental polymerized phases. Its density, 2.5 g/cm^3 , is close to densities reported for the 3D C_{60} polymers. However, its eighty percent sp^3 -hybridized atoms is higher than the experimental reported values for 3D polymers. Yamanaka and coworkers reported 49% and 45% of sp^3 carbons for the two 3D C_{60} polymers prepared at 15 GPa [30–32]. On the other hand, Lyapin and coworkers reported a cubic 3D C_{60} polymer obtained at 12.5 GPa with 60% of its atoms in sp^3 hybridization state [37]. Recently, Zhang and coworkers subjected fullerite C_{60} to 25 GPa to synthesize three amorphous phases with an estimated ratio of sp^3 carbons between 43% and 72% [22]. The elastic properties of the new clathrate, in particular the calculated bulk modulus of 268 GPa, are close to those reported for 3D C_{60} polymers obtained at pressures of 12–13 GPa. Lyapin and coworkers [37] reported a bulk modulus of 280 GPa for the polymer phase prepared at 12.5 GPa, although the published data has a significant uncertainty. Mezouar and coworkers [38] also reported a 3D polymer with a bulk modulus of 288 GPa for a 3D polymer prepared at 13 GPa.

Considering all this, it is plausible that C_{60} 3D polymer phases obtained at 12–13 GPa might consist or contain carbon clathrates related to the one reported here. Consequently, the present finding should lead to a reinterpretation, explicitly considering clathrate structures, of the structural models for polymerized phases prepared above 12 GPa, raising the strong possibility that these materials are in fact carbon clathrates, the long-missing member of the large carbon family.

4. Conclusion

In summary, a novel C_{60} -based carbon clathrate was predicted through DFT investigations of C_{60} polymerization in the solid state. To the best of our knowledge, this is the first proposed carbon clathrate structure with C_{60} molecular building blocks and, since it results from C_{60} polymerization, it could be prepared through high pressure high temperature treatment of fullerite C_{60} .

The high number of sp^3 carbons in this phase leads to a semi-conducting material with moderate elastic properties. In addition, appropriate doping, for instance, using endohedral metallofullerenes, may potentially render this phase metallic and superconducting with properties similar to barium silicon clathrate and the new metal hydrides, which display room-temperature superconductivity at megabar pressures [3–8].

CRediT authorship contribution statement

Jorge Laranjeira: Conceptualization, Methodology, Investigation, Visualization, Writing – original draft, Writing – review & editing. **Leonel Marques:** Conceptualization, Writing – review & editing, Supervision. **Manuel Melle-Franco:** Validation, Methodology, Writing – review & editing, Resources. **Karol Strutyński:**

Validation, Writing – review & editing. **Manuel Barroso:** Validation, Writing – review & editing, Resources.

Declaration of competing interest

The authors declare that they have no known competing financial interests or personal relationships that could have appeared to influence the work reported in this paper.

Acknowledgements

This work was supported by the projects POCI-01-0145-FEDER-031326 and IF/00894/2015 financed by the Portuguese Foundation for Science and Technology (FCT) and co-financed by FEDER. CICECO-Aveiro Institute of Materials, UIDB/50011/2020 & UIDP/50011/2020, financed by national funds through the FCT/MEC and when appropriate co-financed by FEDER under the PT2020 Partnership Agreement. J. Laranjeira acknowledges a PhD grant from FCT (SFRH/BD/139327/2018).

Appendix A. Supplementary data

Supplementary data to this article can be found online at <https://doi.org/10.1016/j.carbon.2022.03.055>.

References

- [1] A. Hassanpouryouzband, E. Joonaki, M. Farahani, S. Takeya, C. Ruppel, J. Yang, N. English, J. Schicks, K. Edlmann, H. Mehrabian, Z. Aman, B. Tohidi, Gas hydrates in sustainable chemistry, *Chem. Soc. Rev.* 49 (2020) 5225–5309, <https://doi.org/10.1039/C8CS00989A>.
- [2] A. Guloy, R. Ramlau, Z. Tang, W. Schnelle, M. Baitinger, Y. Grin, A guest-free germanium clathrate, *Nature* 443 (2006) 320–323, <https://doi.org/10.1038/nature05145>.
- [3] S. Yamanaka, Silicon clathrates and carbon analogs: high pressure synthesis, structure, and superconductivity, *Dalton Trans* 39 (2010) 1901–1915, <https://doi.org/10.1039/B918480E>.
- [4] Y. Sun, J. Lv, Y. Xie, H. Liu, Y. Ma, Route to a superconducting phase above room temperature in electron-doped hydride compounds under high pressure, *Phys. Rev. Lett.* 123 (2019), 097001, <https://doi.org/10.1103/PhysRevLett.123.097001>.
- [5] E. Snider, N. Dasenbrock-Gammon, R. McBride, M. Debessai, H. Vindana, K. Venkatasamy, K. Lawler, A. Salamat, R. Dias, Room-temperature superconductivity in a carbonaceous sulfur hydride, *Nature* 586 (2020) 373–377, <https://doi.org/10.1038/s41586-020-2801-z>.
- [6] M. Somayazulu, M. Ahart, A. Mishra, Z. Geballe, M. Baldini, Y. Meng, V. Struzhkin, R. Hemley, Evidence for superconductivity above 260 K in lanthanum superhydride at megabar pressures, *Phys. Rev. Lett.* 122 (2019), 027001, <https://doi.org/10.1103/PhysRevLett.122.027001>.
- [7] A. Drozdov, P. Kong, V. Minkov, S. Besedin, M. Kuzovnikov, S. Mozaffari, L. Balicas, F. Balakirev, D. Graf, V. Prakapenka, E. Greenberg, D. Knyazev, M. Tkacz, M. Erements, Superconductivity at 250 K in lanthanum hydride under high pressures, *Nature* 569 (2019) 528–531, <https://doi.org/10.1038/s41586-019-1201-8>.
- [8] C. Pickard, I. Errea, M. Erements, Superconducting hydrides under pressure, *Rev. Condens. Matter Phys.* 11 (2020) 57–76, <https://doi.org/10.1146/annurev-conmatphys-031218-013413>.
- [9] T. Strobel, L. Zhu, P. Guñka, G. Borstad, M. Guerette, A lanthanum-filled carbon–boron clathrate, *Angew. Chem. Int. Ed.* 60 (2020) 2877–2881, <https://doi.org/10.1002/anie.202012821>.
- [10] L. Zhu, G. Borstad, H. Liu, P. Guñka, M. Guerette, J.-A. Dolyniuk, Y. Meng, E. Greenberg, V. Prakapenka, B. Chaloux, A. Epshteyn, R. Cohen, T. Strobel, Carbon–boron clathrates as a new class of sp³-bonded framework materials, *Sci. Adv.* 6 (2020), <https://doi.org/10.1126/sciadv.aay8361>.
- [11] T. Zeng, R. Hoffmann, R. Nesper, N. Ashcroft, T. Strobel, D. Proserpio, Li-filled, B-substituted carbon clathrates, *J. Am. Chem. Soc.* 137 (2015) 12639–12652, <https://doi.org/10.1021/jacs.5b07883>.
- [12] Y. Liu, X. Jiang, Y. Huang, S. Zhou, J. Zhao, A new family of multifunctional silicon clathrates: optoelectronic and thermoelectric applications, *J. Appl. Phys.* 121 (2017) 85107–85115, <https://doi.org/10.1063/1.4977245>.
- [13] Z. Li, M. Hu, M. Ma, Y. Gao, B. Xu, J. He, D. Yu, Y. Tian, Z. Zhao, Superhard superstrong carbon clathrate, *Carbon* 105 (2016) 151–155, <https://doi.org/10.1016/j.carbon.2016.04.038>.
- [14] D. Connétable, V. Timoshevskii, B. Masenelli, J. Beille, J. Marcus, B. Barbara, A. Saitta, G.-M. Rignanesse, P. Mélinon, S. Yamanaka, X. Blase, Superconductivity in doped sp³ semiconductors: the case of the clathrates, *Phys. Rev. Lett.* 91 (2003), 247001, <https://doi.org/10.1103/PhysRevLett.91.247001>.
- [15] X. Blase, P. Gillet, A. San Miguel, P. Mélinon, Exceptional ideal strength of carbon clathrates, *Phys. Rev. Lett.* 92 (2004), 215505, <https://doi.org/10.1103/PhysRevLett.92.215505>.
- [16] D. Connétable, First-principles calculations of carbon clathrates: comparison to silicon and germanium clathrates, *Phys. Rev. B* 82 (2010), 075209, <https://doi.org/10.1103/PhysRevB.82.075209>.
- [17] D. Machon, V. Pischcheda, S. Le Floch, A. San-Miguel, Perspective: high pressure transformations in nanomaterials and opportunities in material design, *J. Appl. Phys.* 124 (2018), 160902, <https://doi.org/10.1063/1.5045563>.
- [18] J. Wang, S. Nie, H. Weng, Y. Kawazoe, C. Chen, Topological nodal-net semimetal in a graphene network structure, *Phys. Rev. Lett.* 120 (2018), 026402, <https://doi.org/10.1103/PhysRevLett.120.026402>.
- [19] D. Strout, R. Murry, C. Xu, W. Eckhoff, G. Odom, G. Scuseria, A theoretical study of buckminsterfullerene reaction products: C₆₀+C₆₀, *Chem. Phys. Lett.* 214 (1993) 576–582, [https://doi.org/10.1016/0009-2614\(93\)85686-1](https://doi.org/10.1016/0009-2614(93)85686-1).
- [20] M. Barhoumi, D. Rocca, M. Said, S. Lebégue, Elastic and mechanical properties of cubic diamond and silicon using density functional theory and the random phase approximation, *Solid State Commun.* 324 (2021), 114136, <https://doi.org/10.1016/j.ssc.2020.114136>.
- [21] A. Popov, S. Yang, L. Dunsch, Endohedral fullerenes, *Chem. Rev.* 113 (2013) 5989–6113, <https://doi.org/10.1021/cr300297r>.
- [22] S. Zhang, Z. Li, K. Luo, J. He, Y. Gao, A.V. Soldatov, V. Benavides, K. Shi, A. Nie, B. Zhang, W. Hu, M. Ma, Y. Liu, B. Wen, G. Gao, B. Liu, Y. Zhang, D. Yu, X.-F. Zhou, Z. Zhao, B. Xu, L. Su, G. Yang, O. Chernogorova, Y. Tian, Discovery of carbon-based strongest and hardest amorphous material, *Natl. Sci. Rev.* nwab140 (2021), <https://doi.org/10.1093/nsr/nwab140>.
- [23] C. Pei, L. Wang, Recent progress on high-pressure and high-temperature studies of fullerenes and related materials, *Matter Radiat. Extremes* 4 (2019), 028201, <https://doi.org/10.1063/1.5086310>.
- [24] B. Sundqvist, Carbon under pressure, *Phys. Rep.* 909 (2021) 1–73, <https://doi.org/10.1016/j.physrep.2020.12.007>.
- [25] M. Núñez-Regueiro, L. Marques, J.-L. Hodeau, O. Béthoux, M. Perroux, Polymerized fullerite structures, *Phys. Rev. Lett.* 74 (1995) 278–281, <https://doi.org/10.1103/PhysRevLett.74.278>.
- [26] M. Álvarez-Murga, J.-L. Hodeau, Structural phase transitions of C₆₀ under high-pressure and high-temperature, *Carbon* 82 (2015) 381–407, <https://doi.org/10.1016/j.carbon.2014.10.083>.
- [27] J. Laranjeira, L. Marques, N. Fortunato, M. Melle-Franco, K. Strutyński, M. Barroso, Three-dimensional C₆₀ polymers with ordered binary-alloy-type structures, *Carbon* 137 (2018) 511–518, <https://doi.org/10.1016/j.carbon.2018.05.070>.
- [28] J. Laranjeira, L. Marques, M. Mezouar, M. Melle-Franco, K. Strutyński, Bonding frustration in the 9.5 GPa fcc polymeric C₆₀, *Phys. Stat. Sol. - RRL* 11 (2017), 1700343, <https://doi.org/10.1002/pssr.201700343>.
- [29] L. Chernozatonskii, N. Serebryanaya, B. Mavrin, The superhard crystalline three-dimensional polymerized C₆₀ phase, *Chem. Phys. Lett.* 316 (2000) 199–204, [https://doi.org/10.1016/S0009-2614\(99\)01288-9](https://doi.org/10.1016/S0009-2614(99)01288-9).
- [30] S. Yamanaka, N. Kini, A. Kubo, S. Jida, H. Kuramoto, Topochemical 3D polymerization of C₆₀ under high pressure at elevated temperatures, *J. Am. Chem. Soc.* 130 (2008) 4303–4309, <https://doi.org/10.1021/ja076761k>.
- [31] S. Yamanaka, A. Kubo, K. Inumaru, K. Komaguchi, N. Kini, T. Inoue, T. Irifune, Electron conductive three-dimensional polymer of cuboidal C₆₀, *Phys. Rev. Lett.* 96 (2006), 076602, <https://doi.org/10.1103/PhysRevLett.96.076602>.
- [32] Y. Sato, M. Terauchi, S. Yamanaka, Electronic structures of three-dimensional C₆₀ polymers studied by high-energy-resolution electron energy-loss spectroscopy based on transmission electron microscopy, *Chem. Phys. Lett.* 626 (2015) 90–95, <https://doi.org/10.1016/j.cplett.2015.03.017>.
- [33] S. Berber, E. Osawa, D. Tománek, Rigid crystalline phases of polymerized fullerenes, *Phys. Rev. B* 70 (2004), 085417, <https://doi.org/10.1103/PhysRevB.70.085417>.
- [34] E. Burgos, E. Halac, R. Weht, H. Bonadeo, E. Artacho, P. Ordejón, New superhard phases for three-dimensional C₆₀-based fullerenes, *Phys. Rev. Lett.* 85 (2000) 2328–2331, <https://doi.org/10.1103/PhysRevLett.85.2328>.
- [35] V. Brazhkin, A. Lyapin, S. Popova, R. Voloshin, Y. Antonov, S. Lyapin, Y. Kluev, A. Naletov, N. Mel'nik, Metastable crystalline and amorphous carbon phases obtained from fullerite C₆₀ by high-pressure–high-temperature treatment, *Phys. Rev. B* 56 (1997) 11465–11471, <https://doi.org/10.1103/PhysRevB.56.11465>.
- [36] L. Marques, M. Mezouar, J.-L. Hodeau, M. Núñez-Regueiro, N. Serebryanaya, V.A. Ivdenko, V.D. Blank, G. Dubitsky, Debye-Scherrer ellipses” from 3D fullerene polymers: an anisotropic pressure memory signature, *Science* 283 (1999) 1720–1723, <https://doi.org/10.1126/science.283.5408.1720>.
- [37] A. Lyapin, Y. Katayama, V. Brazhkin, Order versus disorder: in situ high-pressure structural study of highly polymerized three-dimensional C₆₀ fullerite, *J. Appl. Phys.* 126 (2019), 065102, <https://doi.org/10.1063/1.5111370>.
- [38] M. Mezouar, L. Marques, J.-L. Hodeau, V. Pischcheda, M. Núñez-Regueiro, Equation of state of an anisotropic three-dimensional C₆₀ polymer: the most stable form of fullerene, *Phys. Rev. B* 68 (2003), 193414, <https://doi.org/10.1103/PhysRevB.68.193414>.
- [39] Y. Shang, Z. Liu, J. Dong, M. Yao, Z. Yang, Q. Li, C. Zhai, F. Shen, X. Hou, L. Wang, N. Zhang, W. Zhang, R. Fu, J. Ji, X. Zhang, H. Lin, Y. Fei, B. Sundqvist, W. Wang, B. Liu, Ultrahard bulk amorphous carbon from collapsed fullerene, *Nature* 599 (2021) 599–604, <https://doi.org/10.1038/s41586-021-03882-9>.
- [40] H. Tang, X. Yuan, Y. Cheng, H. Fei, F. Liu, T. Liang, Z. Zeng, T. Ishii, M.-S. Wang,

- T. Katsura, H. Sheng, H. Gou, Synthesis of paracrystalline diamond, *Nature* 599 (2021) 605–609, <https://doi.org/10.1038/s41586-021-04122-w>.
- [41] G. Kresse, J. Furthmüller, Efficient iterative schemes for ab initio total-energy calculations using a plane-wave basis set, *Phys. Rev. B* 54 (1996) 11169–11186, <https://doi.org/10.1103/PhysRevB.54.11169>.
- [42] J. Perdew, K. Burke, M. Ernzerhof, Generalized gradient approximation made simple, *Phys. Rev. Lett.* 77 (1996) 3865–3868, <https://doi.org/10.1103/PhysRevLett.77.3865>.
- [43] S. Singh, I. Valencia-Jaime, O. Pavlic, A. Romero, Elastic, mechanical, and thermodynamic properties of Bi–Sb binaries: effect of spin-orbit coupling, *Phys. Rev. B* 97 (2018), 054108, <https://doi.org/10.1103/PhysRevB.97.054108>.
- [44] A. Togo, I. Tanaka, First principles phonon calculations in materials science, *Scripta Mater.* 108 (2015) 1–5, <https://doi.org/10.1016/j.scriptamat.2015.07.021>.
- [45] S. Grimme, S. Ehrlich, L. Goerigk, Effect of the damping function in dispersion corrected density functional theory, *J. Comput. Chem.* 32 (2011) 1456–1465, <https://doi.org/10.1002/jcc.21759>.
- [46] R. Dovesi, A. Erba, R. Orlando, C. Zicovich-Wilson, B. Civalleri, L. Maschio, M. Rérat, S. Casassa, J. Baima, S. Salustro, B. Kirtman, Quantum-mechanical condensed matter simulations with crystal, *WIREs Comput. Mol. Sci.* 8 (2018) 1360, <https://doi.org/10.1002/wcms.1360>.
- [47] V. Barone, O. Hod, J. Peralta, G. Scuseria, Accurate prediction of the electronic properties of low-dimensional graphene derivatives using a screened hybrid density functional, *Acc. Chem. Res.* 44 (2011) 269–279, <https://doi.org/10.1021/ar100137c>.
- [48] M. Frisch, et al., Gaussian 09, Revision A.02, 2016, Gaussian Inc, Wallingford CT, 2016, <http://gaussian.com/>.
- [49] J. Zhu, K. Xu, Z. Zhang, X. Cao, S. Huang, J. Wu, Carbon clathrates as strong lightweight structures, 202–203, *Int. J. Mech. Sci.* (2021), 106509, <https://doi.org/10.1016/j.ijmecsci.2021.106509>.
- [50] C. Varma, J. Zaanen, K. Raghavachari, Superconductivity in the fullerenes, *Science* 254 (1991) 989–992, <https://doi.org/10.1126/science.254.5034.989>.
- [51] O. Gunnarsson, Superconductivity in fullerides, *Rev. Mod. Phys.* 69 (1997) 575–606, <https://doi.org/10.1103/RevModPhys.69.575>.
- [52] F. Zipoli, M. Bernasconi, First principles study of three-dimensional polymers of C₆₀: structure, electronic properties, and Raman spectra, *Phys. Rev. B* 77 (2008), 115432, <https://doi.org/10.1103/PhysRevB.77.115432>.
- [53] J. Yang, J. Tse, T. Iitaka, First-principles investigation on the geometry and electronic structure of the three-dimensional cuboidal C₆₀ polymer, *J. Chem. Phys.* 127 (2007), 134906, <https://doi.org/10.1063/1.2771162>.
- [54] A. Talyzin, F. Langenhorst, N. Dubrovinskaia, S. Dub, L. Dubrovinsky, Structural characterization of the hard fullerite phase obtained at 13 GPa and 830 K, *Phys. Rev. B* 71 (2005), 115424, <https://doi.org/10.1103/PhysRevB.71.115424>.

Supporting Information

A. Computational methods

DFT calculations were performed using the Vienna ab initio simulation package (VASP) [1]. Perdew-Burke-Ernzerhof generalized gradient approximation was used to calculate the exchange-correlation energy [2]. Electron core interaction was described by the projector augmented wave pseudo-potentials (PAW) supplied with VASP. The self-consistent-field process was stopped once the energy difference between two consecutive steps was smaller than 10^{-5} eV; the k-points were converged within 10^{-5} meV/atom. To achieve this convergence a $6 \times 6 \times 6$ k-point mesh was employed in the optimization of the atomic positions and lattice parameters. Gaussian smearing, with a standard deviation of 0.2 and an energy cutoff of 520 eV, was applied during all the optimizations.

Electron Density of States (DOS) calculations were performed using a $16 \times 16 \times 16$ k-point grid. An energy cutoff of 400 eV was employed and the tetrahedron method with Bloch corrections was used for electron smearing. For the electron band structure calculations, 20 k-points between the high symmetric k-points of the Brillouin zone associated to the primitive cubic cell with the same energy cutoff was used.

Elastic tensor calculations were performed with a $6 \times 6 \times 6$ k-point grid, an energy cutoff of 800 eV and a finite step size of 0.015 Å for the central differences. The strain-stress method as implemented on VASP was applied to the primitive unit cell [3]. Elastic properties were afterwards extracted using the MechElastic script [4]. The phonon dispersion and the phonon density of states were calculated using density functional perturbation theory as implemented in VASP to compute the Hessian matrix. A supercell of $2 \times 2 \times 2$ (regarding the primitive cubic cell) with a $3 \times 3 \times 3$ k-point grid were used and the phonon dispersion was then computed with the Phonopy code [5].

The Raman and infrared spectra of C_{60} polymeric systems were computed at the PBE-6-31G(d,p) level augmented with the classical D3 dispersion term [6] with Becke-Johnson damping as implemented on CRYSTAL17 [7]. The Raman intensity was computed with the Coupled-Perturbed-Hartree-Fock/Kohn-Sham (CPHF/KS) approach [8,9]. The Coulomb and exchange infinite lattice series is controlled by five numerical thresholds (Ti) which were set to 12 (T1-T4) and 24 (T5). The convergence threshold for the SCF was set $\leq 10^{-10}$ Hartree, a k-point grid with at least $6 \times 6 \times 6$ k-points was used. All the reported computed vibrational frequencies were scaled by a 0.98 factor previously derived to better fit experimental spectra for PBE-6-31G(d,p) calculations in PAH molecules [10]. A full optimization of all structures was done with CRYSTAL17 prior to the spectra computation. We have also employed CRYSTAL17 to compute the Birch-Murnaghan equation of states parameters for the different structures presented and for 2D tetragonal C_{60} polymer and graphite [11]. The Birch-Murnaghan $E(V)$ and $P(V)$ curves were then used to calculate the enthalpy curves presented in section I of this document.

In addition, periodic LCAO computations at the HSE06-6-31G(d,p) level [12] were performed with Gaussian09 [13] to obtain a better estimate of the bandgap. A full geometry optimization was also performed with Gaussian09.

Diagram 1 presents all the followed workflow and Table S1 shows the clathrate optimized lattice parameters with different methods.

Powder diffraction patterns were simulated using the RIETAN-FP package as implemented on VESTA software [14] using a wavelength of 1.54 Å, additionally the peaks were broadened to reproduce the experimental data.

Diagram 1: Workflow followed in this work, a different color refers to different DFT packages, namely: VASP is blue, Gaussian09 is yellow and CRYSTAL17 is green, while steps which do not include DFT calculations are pictured in grey. FCC meaning face centered cubic lattice, SC meaning simple cubic lattice and EOS meaning Equation of state.

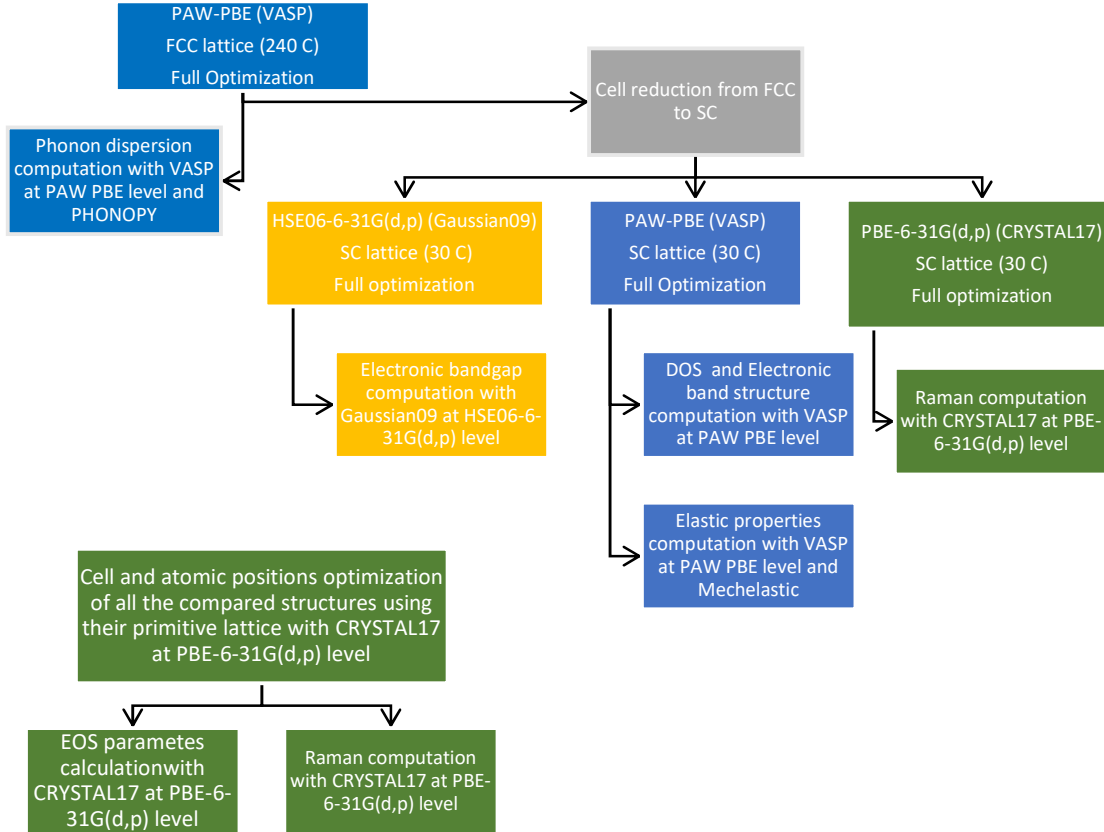


Table S1: Simple cubic lattice parameter of the C₆₀ clathrate structure after optimization with different DFT methods.

Method	Simple cubic lattice parameter (Å)
VASP PAW-PBE	6.21
CRYSTAL17 PBE-6-31G(d,p)	6.22
Gaussian09 PBE-6-31G(d,p)	6.22
Gaussian09 HSE06-6-31G(d,p)	6.17

B Gaussian09 geometry optimization

Table S2: Optimized atomic positions of the C₆₀-based clathrate structure in the $Pm\bar{3}$ simple cubic cell with lattice parameter 6.17 Å, at the HSE06-6-31G(d,p) level as implemented in Gaussian09.

Atom	x	Y	z	Wyckoff Position
C1	0.50000	0.34929	-0.14142	12k
C2	-0.12057	0.50000	0.00000	6f
C3	0.50000	-0.17123	-0.29200	12k

Table S3: Optimized atomic positions of the C₆₀-based clathrate structure in the $Pm\bar{3}$ simple cubic cell with lattice parameter 6.22 Å, at the PBE-6-31G(d,p) level as implemented in Gaussian09.

Atom	x	Y	z	Wyckoff Position
C1	0.50000	0.34890	-0.14228	12k
C2	-0.12129	0.50000	0.00000	6f
C3	0.50000	-0.17115	-0.29187	12k

C. Electron localization function (ELF)

The electron localization function (ELF) allows to analyze the location and strength of bonds between atoms from the integration of the electron density [15].

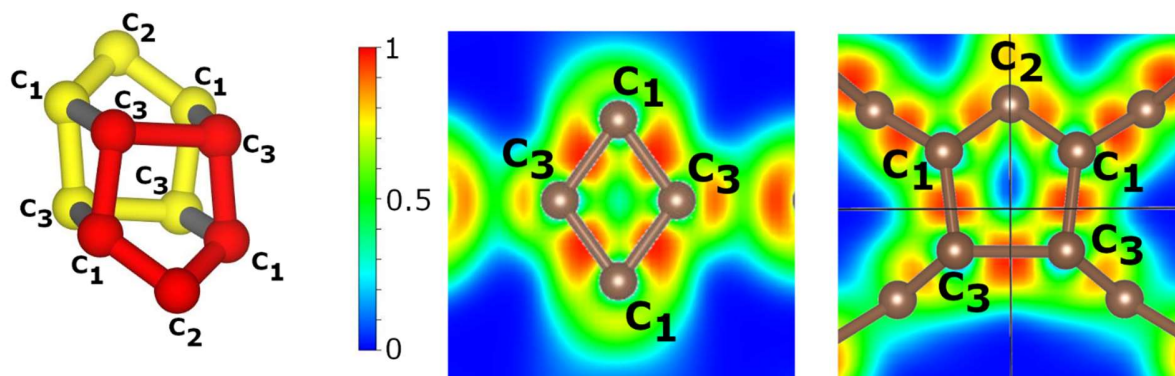


Figure S1: Detail on connecting bonds between two fullerenes and the 2D ELF cuts on the intermolecular bonding region for the C₆₀-based clathrate. The left panel shows the bonds connecting two fullerenes (in red and yellow) with its carbons labeled according to their atom label in table I. In the central panel the 2D ELF cut of the plane through rhombus showing that the C₃ atoms on the opposite sides of the rhombus are not chemically bonded. In contrast, the 2D map of ELF through the pentagon, right panel, shows that in this case the C₃ atoms are chemically bonded.

Table S4: Optimized atomic bond distances and bond angles of the C₆₀-based clathrate structure at the PAW-PBE level as implemented in VASP. The subscripts “y” and “r” are referring to the atom colors of the left image of figure S1, with y meaning that one can is an atom in the yellow-colored region and r one in the red colored region. (The atoms with * are not drawn)

Atoms	Bond distances (Å)	Bond angle (°)
C _{3y} -C _{1y} -C _{3r}	1.607, 1.440	127.159
C _{3y} -C _{1y} -C _{2y}	1.607, 1.499	119.166
C _{3r} -C _{1y} -C _{2y}	1.441, 1.499	95.098
C _{1y} -C _{2y} -C _{2y} *	1.499, 1.506	134.827
C _{1y} -C _{2y} -C _{1y}	1.499, 1.499	90.345
C _{1y} -C _{3y} -C _{1r}	1.607, 1.607	107.126
C _{1y} -C _{3y} -C _{3y}	1.607, 1.766	96.461
C _{1y} -C _{3y} -C _{1y} *	1.607, 1.441	111.951

D. Elastic and mechanical properties

The mechanical stability of the C_{60} -based clathrate structure was evaluated by computing the elastic tensor and checking the elastic stability criteria, which are the following for the cubic symmetry: $C_{11}-C_{12}>0$, $C_{11}+2C_{12}>0$, $C_{44}>0$ [16]. The computed values for these elastic constants are $C_{11} = 446$ GPa, $C_{12} = 179$ GPa and $C_{44} = 207$ GPa and therefore all the conditions of stability are satisfied. We used these values to compute the elastic properties, in the framework of Voigt-Reuss-Hill approximation, obtaining $B_0 = 268$ GPa, $G = 174$ GPa, $E = 429$ GPa and $\nu = 0.23$, for the bulk, shear and Young moduli, and the Poisson ratio, respectively [17].

We have also estimated the clathrate hardness using the macroscopic hardness model developed by Chen and coworkers, as implemented in MechElastic code [4, 18]. A value of 21.6 GPa was found, in agreement with the observed moderate elastic constants [19,20]. The C_{60} -based carbon clathrate with bigger cages and 20% of sp^2 carbons has a lower mechanical performance than the reported theoretical carbon clathrates, having smaller cages and being fully sp^3 -bonded.

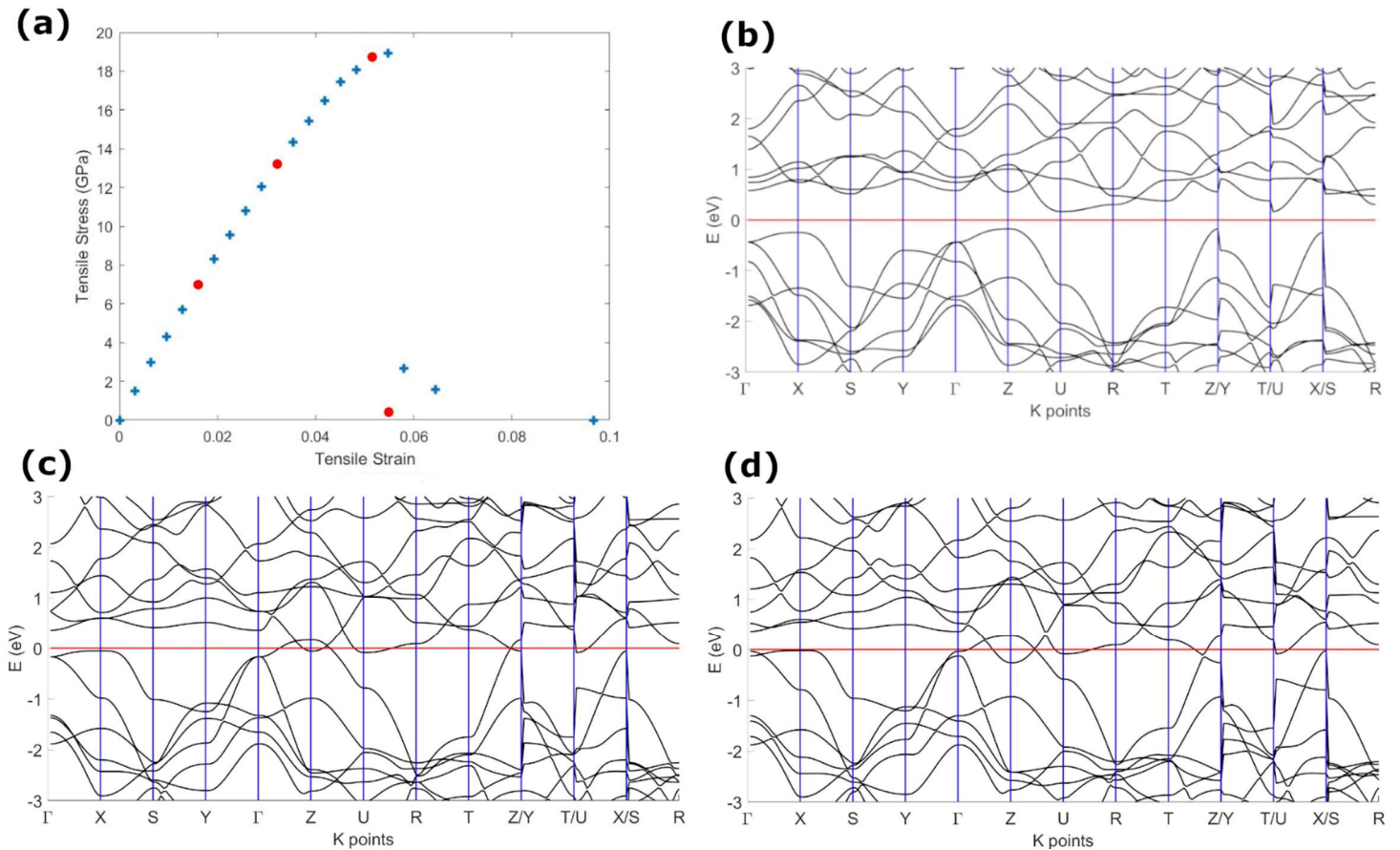


Figure S2: Tensile stress-strain curve for load along the [100] cubic direction (a) and electronic band structures at different strain indicated by red circles in the Stress-Strain plot by increasing strain (b)-(d).

E. DFT energy vs. volume and enthalpy-pressure relationship

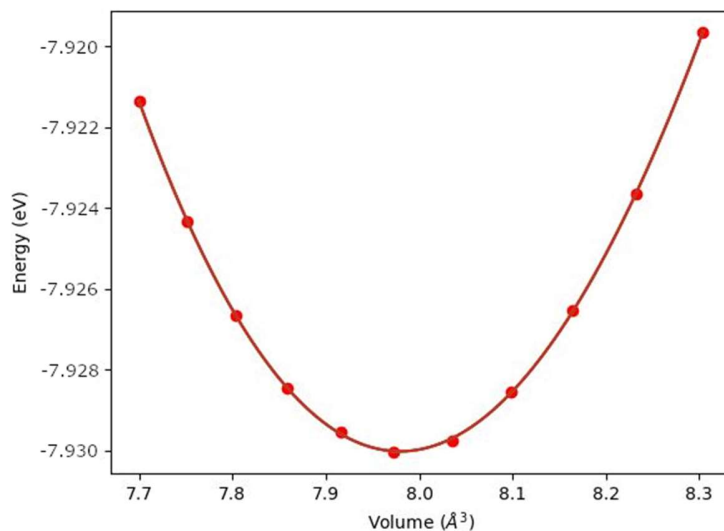


Figure S3: The total energy per atom for the C_{60} -based clathrate as a function of volume per atom.

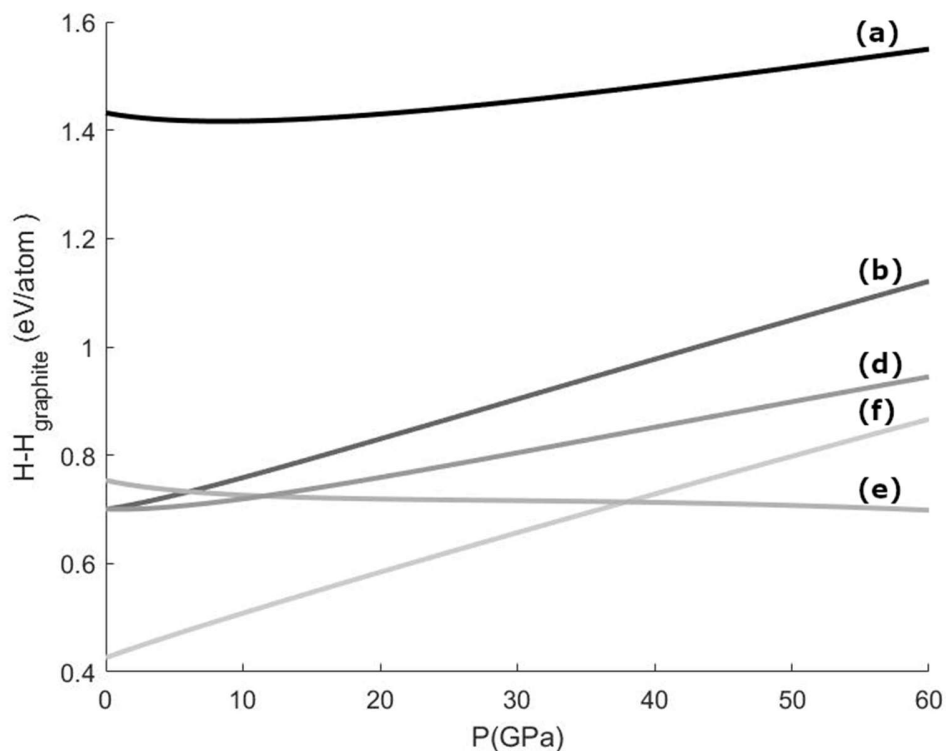


Figure S4: Enthalpy-pressure relationship between C_{60} polymers with respect to graphite for the new clathrate phase (a) and for experimentally based structural models of 3D C_{60} polymers obtained at 9.5 GPa (b), 15 GPa (d), 15 GPa using the 2D tetragonal C_{60} as precursor (e) and the 2D tetragonal C_{60} polymer (f) [11].

F. Phonon dispersion

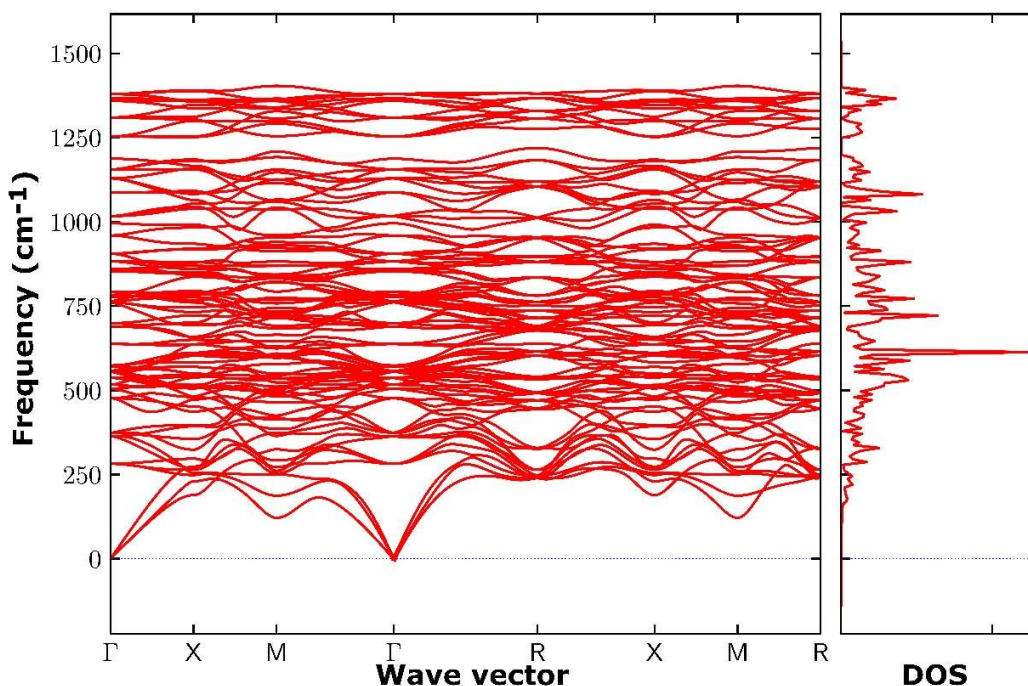


Figure S5: Phonon dispersion (left panel) and phonon density of states (right panel) of the C₆₀-based clathrate.

G. Partial electronic density of the most intense DOS peak

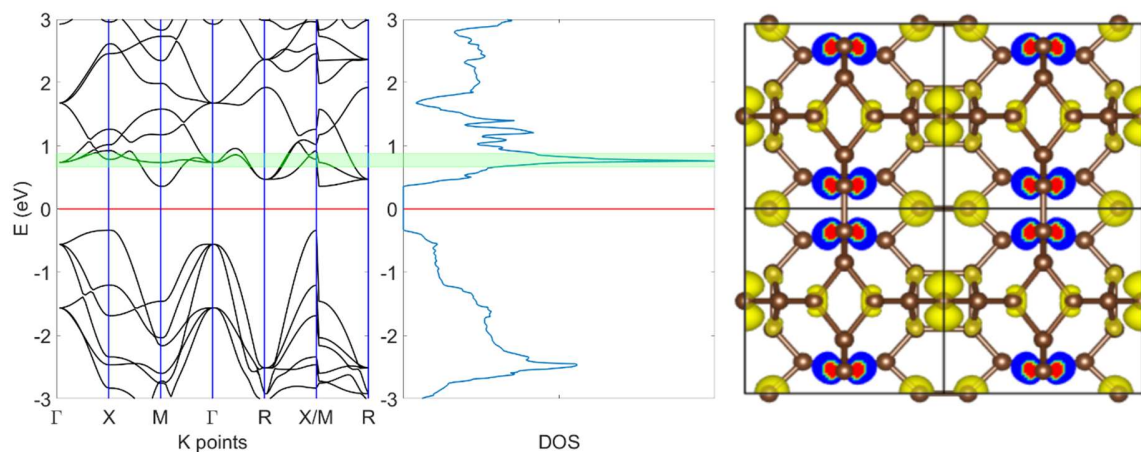


Figure S6: The electronic band structure (left panel), the electronic density of states, DOS, (center panel) and the partial electronic density near the DOS most intense peak (right panel), for the C₆₀-based clathrate. The red line indicates the Fermi level. The energy range where the partial electron density was integrated is highlighted in green, with the partial electronic density isosurface with $4.0 \times 10^{-3} \text{ e}/\text{\AA}^3$ superposed on ball-and-stick model oriented on the (100) crystallographic plane at the right panel.

H. Simulated infrared spectra

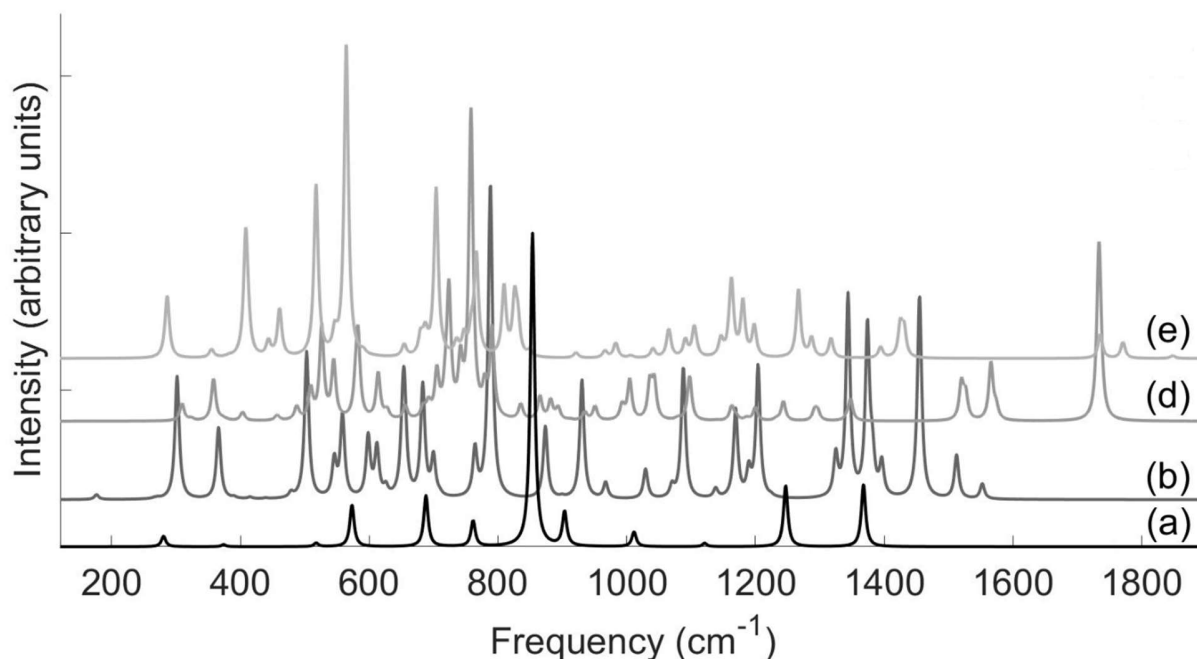


Figure S7: Calculated infrared spectra for the new clathrate phase (a) and for experimentally-based structural models of 3D C₆₀ polymers obtained at 9.5 GPa (b), 15 GPa (d) and 15 GPa using the 2D tetragonal C₆₀ as precursor (e).

I. References

- [1] G. Kresse, J. Furthmüller, Efficient iterative schemes for ab initio total-energy calculations using a plane-wave basis set, *Phys. Rev. B* 54 (1996) 11169-11186, <https://doi.org/10.1103/PhysRevB.54.11169>.
- [2] J. Perdew, K. Burke, M. Ernzerhof, Generalized gradient approximation made simple, *Phys. Rev. Lett.* 77 (1996) 3865-3868, <https://doi.org/10.1103/PhysRevLett.77.3865>.
- [3] X. Wu, D. Vanderbilt, D. Hamann, Systematic treatment of displacements, strains, and electric fields in density-functional perturbation theory, *Phys. Rev. B* 72 (2005) 035105, <https://doi.org/10.1103/PhysRevB.72.035105>.
- [4] S. Singh, I. Valencia-Jaime, O. Pavlic, A. Romero, Elastic, mechanical, and thermodynamic properties of Bi-Sb binaries: effect of spin-orbit coupling, *Phys. Rev. B* 97 (2018) 054108, <https://doi.org/10.1103/PhysRevB.97.054108>.
- [5] A. Togo, I. Tanaka, First principles phonon calculations in materials science, *Scr. Mater.* 108 (2015) 1-5 <https://doi.org/10.1016/j.scriptamat.2015.07.021>.
- [6] S. Grimme, S. Ehrlich, L. Goerigk, Effect of the damping function in dispersion corrected density functional theory, *J. Comput. Chem.* 32 (2011) 1456-1465, <https://doi.org/10.1002/jcc.21759>.
- [7] R. Dovesi, A. Erba, R. Orlando, C. Zicovich-Wilson, B. Civalleri, L. Maschio, M. Rérat, S. Casassa, J. Baima, S. Salustro, B. Kirtman, Quantum-mechanical condensed matter

simulations with crystal, WIREs Comput. Mol. Sci. 8 (2018) 1360

<https://doi.org/10.1002/wcms.1360>.

[8] L. Maschio, B. Kirtman, M. Rérat, R. Orlando, R. Dovesi, Ab initio analytical Raman intensities for periodic systems through a coupled perturbed Hartree-Fock/Kohn-Sham method in an atomic orbital basis. I. Theory, J. Chem. Phys. 139 (2013) 164101,

<https://doi.org/10.1063/1.4824442>.

[9] L. Maschio, B. Kirtman, M. Rérat, R. Orlando, R. Dovesi, Ab initio analytical Raman intensities for periodic systems through a coupled perturbed Hartree-Fock/Kohn-Sham method in an atomic orbital basis. II. Validation and comparison with experiments, J. Chem. Phys. 139 (2013) 164102, <https://doi.org/10.1063/1.4824443>.

[10] M. Laury, M. Carlson, A. Wilson, Vibrational frequency scale factors for density functional theory and the polarization consistent basis sets, J. Comput. Chem. 33 (2012) 2380- 2387,

<https://doi.org/10.1002/jcc.23073>.

[11] M. Núñez-Regueiro, L. Marques, J.-L. Hodeau, O. Béthoux, and M. Perroux, Polymerized Fullerite Structures, Phys. Rev. Lett. (1995) 74, 278-281,

<https://doi.org/10.1103/PhysRevLett.74.278>.

[12] V. Barone, O. Hod, J. Peralta, G. Scuseria, Accurate prediction of the electronic properties of low-dimensional graphene derivatives using a screened hybrid density functional, Acc. Chem. Res. 44 (2011) 269 –279, <https://doi.org/10.1021/ar100137c>.

[13] M. Frisch et al, Gaussian 09, Revision A.02 (2016), Gaussian Inc. Wallingford CT, 2016,

<http://gaussian.com/>.

[14] K. Momma, F. Izumi, VESTA 3 for three-dimensional visualization of crystal, volumetric and morphology data, J. Appl. Cryst. 44 (2011) 1272-1276,

<https://doi.org/10.1107/S0021889811038970>.

[15] K. Koumpouras, J. Larsson, Distinguishing between chemical bonding and physical binding using electron localization function (ELF), J. Phys.: Condens. Matter 32 (2020) 315502

<https://doi.org/10.1088/1361-648X/ab7fd8>.

[16] F. Mouhat, F.-X. Coudert, Necessary and sufficient elastic stability conditions in various crystal systems, Phys. Rev. B 90 (2014) 224104, <https://doi.org/10.1103/PhysRevB.90.224104>.

[17] R. Hill, The elastic behaviour of a crystalline aggregate Proc. Phys. Soc. Section A 65 (1952) 349-354, <https://doi.org/10.1088/0370-1298/65/5/307>.

[18] X.-Q. Chen, H. Niu, D. Li, and Y. Li, Modeling hardness of polycrystalline materials and bulk metallic glasses, Intermetallics 19 (2011) 1275

<http://dx.doi.org/10.1016/j.intermet.2011.03.026>.

[19] Z. Li, M. Hu, M. Ma, Y. Gao, B. Xu, J. He, D. Yu, Y. Tian, Z. Zhao, Superhard superstrong carbon clathrate, Carbon 105 (2016) 151-155, <https://doi.org/10.1016/j.carbon.2016.04.038>

[20] S. Zhang, Z. Li, K. Luo, J. He, Y. Gao, A. V. Soldatov, V. Benavides, K. Shi, A. Nie, B. Zhang, W. Hu, M. Ma, Y. Liu, B. Wen, G. Gao, B. Liu, Y. Zhang, D. Yu, X.-F. Zhou, Z. Zhao, B. Xu, L. Su, G. Yang, O. Chernogorova, Y. Tian, Discovery of carbon-based strongest and hardest amorphous material, Natl. Sci. Rev. nwab140 (2021),

<https://doi.org/10.1093/nsr/nwab140>.

Chapter 8

A6 - Superconductivity in the doped polymerized fullerite clathrate from first principles

Superconductivity in the doped polymerized fullerite clathrate from first principles

Jorge Laranjeira,^{1,*} Ion Errea,^{2,3,4} Đorđe Dangić,^{2,3} Leonel Marques,¹ Manuel Melle-Franco,⁵ and Karol Strutyński⁵

¹*Departamento de Física and CICECO, Universidade de Aveiro, 3810-193 Aveiro, Portugal*

²*Fisika Aplikatua Saila, Gipuzkoako Ingeniaritza Eskola, University of the Basque Country (UPV/EHU), Europa Plaza 1, 20018 Donostia/San Sebastián, Spain*

³*Centro de Física de Materiales (CSIC-UPV/EHU),*

Manuel de Lardizabal Pasealekua 5, 20018 Donostia/San Sebastián, Spain

⁴*Donostia International Physics Center (DIPC),*

Manuel de Lardizabal Pasealekua 4, 20018 Donostia/San Sebastián, Spain

⁵*Departamento de Química and CICECO, Universidade de Aveiro, 3810-193 Aveiro, Portugal*

(Dated: February 21, 2023)

Superconductivity in the new polymerized C₆₀ fullerite clathrate doped with simple metals was investigated through density functional theory methods. The phonon dispersion curves were systematically computed for the clathrate structures containing the guest dopants (Li, Na, K, Be, Mg, Ca, Al, Ga, Ge) in one of the two distinct cages, fullerene-like C₆₀ and sodalite-like C₂₄, exhibited by this structure. Only four of these structures, Li@C₂₄, Na@C₂₄, Ga@C₂₄ and Be@C₆₀, are dynamically stable in the harmonic approximation. They all show superconducting behavior, although their critical temperatures are predicted to be below 2 K.

Keywords: DFT Calculations, Carbon Clathrates, Superconductivity

INTRODUCTION

The achievement of room temperature superconductivity is extremely desirable for technological applications [1]. Very high superconducting critical temperature (T_c), ~ 200 K, was initially predicted from first principles density functional theory (DFT) for the H₃S compound [2], soon followed by its experimental observation [3] under a pressure of 150 GPa. These exciting results fostered huge efforts, led again by computational methods, to find new materials with even higher T_c by exploring hydrogen bearing compounds. A new lanthanum hydride, LaH₁₀, in which the hydrogen atoms form sodalite-like cages, was found at 140-220 GPa and displaying T_c of approximately 250 K [4, 5]. This near-room temperature superconducting phase is only stable under megabar pressures and cannot be quenched to room conditions, thus precluding practical applications. The focus of investigations is now directed to the search for superconducting materials that can operate at room pressure. One strategy to attain this goal is to consider other types of clathrate structures that still use a light element in its building blocks, a known key ingredient for high T_c conventional superconductivity [1], while being able to retain the clathrate structure at ambient pressure. Carbon clathrates are notable candidates since, besides containing a light element such as carbon, they exhibit strong covalent bonds that lead to large phonon frequencies, which is another key ingredient for high T_c superconductivity [6, 7].

Unfortunately, experimental carbon clathrates are yet to be synthesized, although an important step towards its realization was done recently with the high-

pressure synthesis of mixed carbon-boron clathrates, containing guest metallic atoms [8, 9]. Initial predictions based on DFT methods were again crucial to guide the investigations towards their experimental realization [10]. The mixed carbon-boron clathrate doped with strontium guest-atoms was hypothesized as a potential candidate for phonon-mediated superconductivity at ambient conditions, since its electronic structure showed the coexistence of steep and flat bands close to the Fermi level [9]. Indeed ab initio DFT simulations performed on the strontium and barium doped carbon-boron clathrates yield T_c 's of 40 K and 43 K, respectively, at room pressure [11]. Furthermore, an increase in T_c up to 88 K was predicted in this class of compounds for the potassium-lead binary-guest clathrate [6, 12].

A significant number of superconducting doped carbon allotropes have already been synthesized. Boron doped diamond yields a T_c of 4 K for a doping level of 2.5% [13] and 11.4 K for a doping level of 5% [14]. Graphite intercalation compounds such as YbC₆ and CaC₆, display T_c 's of 6.5 K and 11.5 K, respectively [15]. Also, the alkali-metal fulleride RbCs₂C₆₀ displays a T_c of 33 K at room pressure. The compound Cs₃C₆₀ presents a higher T_c 40 K, nevertheless, it requires a pressure of 1.5 GPa to stabilize the cubic superconducting phase [16, 17]. A theoretical study of a sodalite-like carbon clathrate, with a structure identical to that of the mixed carbon-boron clathrate, revealed that it could achieve high T_c , 116 K, at room pressure when doped with sodium [7].

Very recently, we have proposed a new carbon clathrate based on the polymerized fullerite, which is expected to be synthesized by subjecting fullerite C₆₀ to high-pressure and high-temperature (HPHT) treatment. Some experimental high-pressure C₆₀ phases found in the literature have interfullerene distances identical to that of the polymerized fullerite clathrate structure, showing evidence that it could be synthesized once the proper

* jorgelaranjeira@ua.pt

thermodynamic path is found [18]. Interestingly, its electronic structure has a narrow bandgap of 0.68 eV and its density of states (DOS), shown in Figure S1 of the Supporting Information (SI), displays a strong peak above (~ 0.7 eV) the Fermi level. We found that this peak is due to the three nearly-flat π^* bands from the remaining sp^2 carbons. The new clathrate also presents large phonon frequencies with the highest mode lying at ~ 1350 cm^{-1} , which suggests that it could be a good candidate for displaying superconductivity once properly doped. Here we explore this possibility by performing a systematic DFT study of the doping effect on the fullerite C_{60} clathrate structure. Nine simple metals were tested as guest-atoms being inserted in one of the two cages, fullerene-like C_{60} and sodalite-like C_{24} , exhibited by this clathrate structure. We compute the electronic structure and phonon dispersion curves and find that only four doped fullerite clathrates are dynamically stable, all of them showing metallic behavior. In addition, they display superconductivity but their T_c 's, computed using Migdal-Eliashberg theory, are predicted to be quite low.

METHODS

For each distinct doped fullerite clathrate we optimized its structure using the Perdew-Burke-Ernzerhof (PBE) exchange correlation functional [19, 20] as implemented in the ultrasoft pseudopotentials provided with the Quantum Espresso (QE) package [21, 22]. A k -space grid of $8 \times 8 \times 8$ was used and the self-consistent-field cycle was stopped once the energy difference between consecutive steps was smaller than 10^{-8} Ry. We also used a Methfessel-Paxton [23] smearing of 0.02 Ry, a kinetic energy cutoff of 60 Ry and a charge density cutoff of 600 Ry. Phonon dispersion and electron-phonon coupling calculations were performed with Density Functional Perturbation Theory (DFPT) [24] as implemented in QE. A q -grid of $2 \times 2 \times 2$ was used for the phonon dispersion calculation, when stability was found the q -space mesh was increased to $4 \times 4 \times 4$ prior to the electron-phonon matrix elements calculation. These parameters were converged within 1 cm^{-1} . To calculate the electron-phonon matrix elements we have used a smearing of 0.008 Ry for the double Dirac delta over the Fermi surface and a k -space mesh of $24 \times 24 \times 24$. To compute T_c , we solved isotropic Eliashberg equations [25]. We also evaluated T_c with the Allen-Dynes modified McMillan equation [26].

RESULTS AND DISCUSSION

The fullerite clathrate has a simple cubic cell, with a lattice constant of 6.21 Å, and belongs to the $Pm\bar{3}$ space group. The structure has three independent atoms, one at 6f and two at 12k Wyckoff positions [18]. This structure exhibits two different cages, sodalite-like C_{24} and fullerene-like C_{60} . Thus, doping may be achieved

by inserting guest atoms in either one or in both cages. Here we only studied the effect of doping in only one cage. Figure 1 a) shows the clathrate structure resulting from doping on the 1a Wyckoff position at the center of the C_{60} cage, hereafter denoted $M@C_{60}$ (M = guest atom), while Figure 1 b) shows the clathrate structure resulting from doping on the 1b Wyckoff position at the center of the C_{24} cage and hereafter denoted $M@C_{24}$. Note that the resulting stoichiometry, $M@C_{30}$, is the same for both insertion types. The optimized lattice constants of the differently doped structures and their relative stabilities are given in Tables S1 and S2.

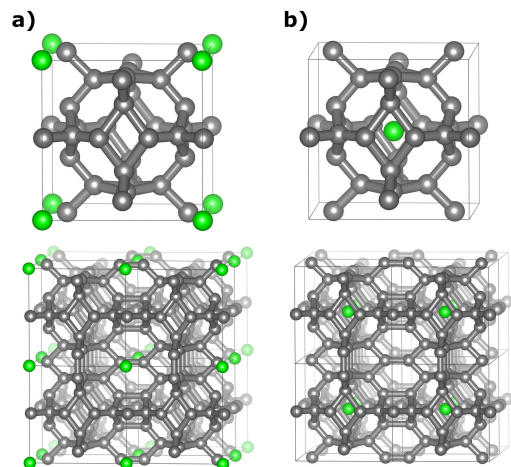


FIG. 1. Doped fullerite clathrate unit cells (top panels) and $2 \times 2 \times 2$ supercell depicting the C_{60} cages (bottom panels) with guest atoms at: a) C_{60} cages, 1a Wyckoff positions; b) C_{24} cages, the 1b Wyckoff positions. The grey atoms are carbons and the green ones are the dopants.

In an attempt to push the Fermi level to the strong DOS peak observed in the conduction band that arises from the three nearly-flat π^* bands, we initially considered doping with trivalent ions, yttrium and scandium, at the C_{60} cages, thus forming the $Y@C_{60}$ and $Sc@C_{60}$ clathrates. Inserting these guest atoms keeps the valence and conduction bands almost unchanged, while the Fermi level moves almost to the top of the DOS peak (see the left and middle panels of Figure S2). This rigid-band picture indicates a nearly-complete charge transfer from the metal guest to the carbon framework. The number of states at the Fermi level is around 0.3 and 0.2 states/eV/spin/atom for $Sc@C_{60}$ and $Y@C_{60}$ respectively, a significant number that is an important prerequisite for the observation of superconductivity. Unfortunately, filling the antibonding π^* states destabilizes the carbon framework and leads to large imaginary frequencies in the phonon dispersion curves, indicating that these doped clathrates are dynamically unstable (see the right panels of Figure S2). Moreover, we also found that they have spin-polarized ground states. The dynamical instabilities are an indication that these systems are prone to the

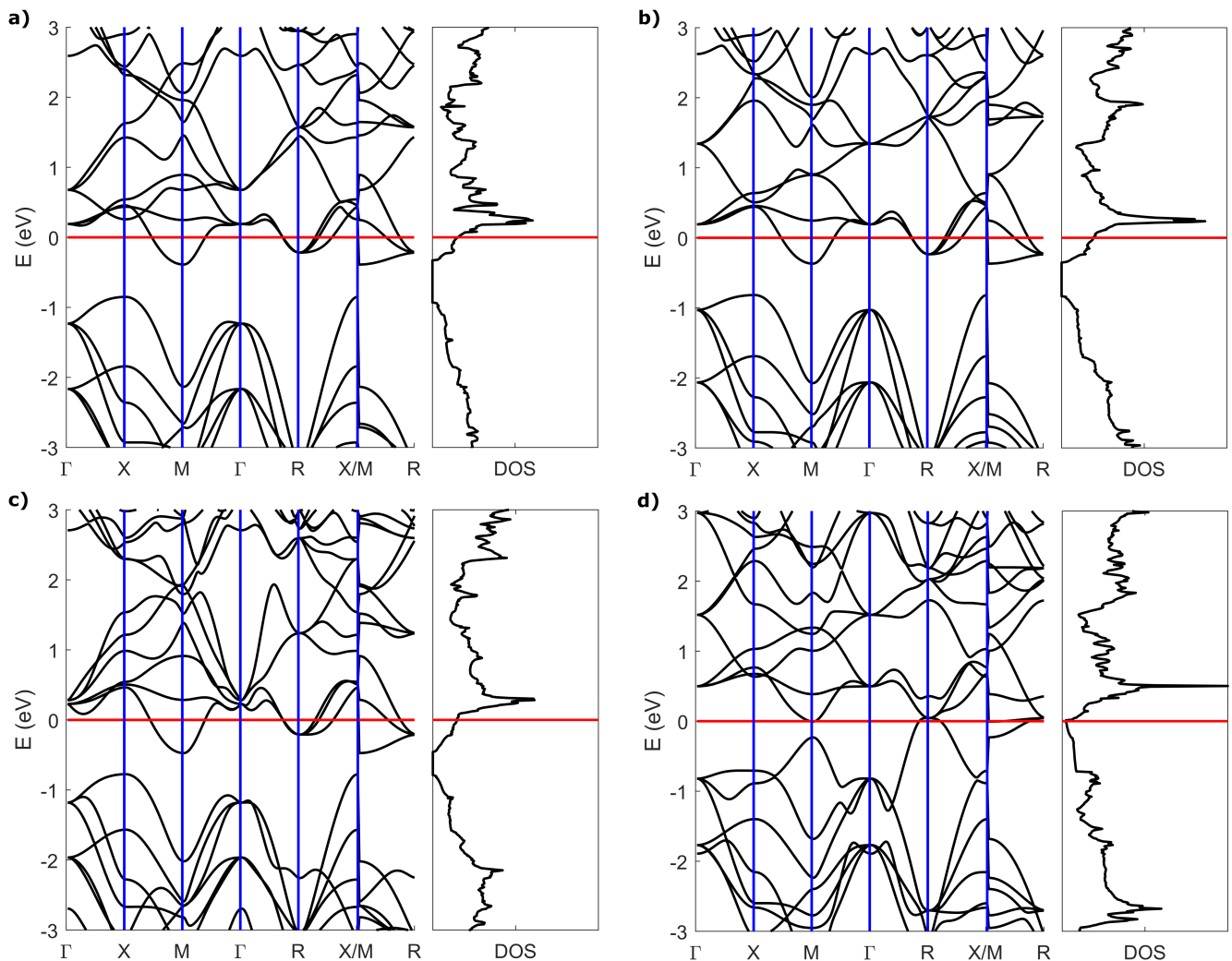


FIG. 2. Electronic band structure (left panels) and density of states (right panels) for the stable compounds: a) Li@C_{24} ; b) Na@C_{24} ; c) Ga@C_{24} ; d) Be@C_{60} . The red line indicates the Fermi level.

formation of a charge-density wave that lowers the DOS at the Fermi level and prevents a magnetic ground state.

Given the unfavorable results just described, the search for superconductivity was pursued through a systematic search of doped clathrate structures employing dopants from groups I, II and III (Li, Na, K, Be, Mg, Ca, Al, Ga) and also from group IV (Ge). As already mentioned, in the doped clathrates considered, the guest atoms are inserted in only one of the two cages available in the structure. The electronic bands, DOS and phonon dispersion curves for all the doped clathrates being studied are given in the SI, sections D and E, respectively. The electronic structures across the M@C_{60} series essentially follow a rigid-band model, in particular for the monovalent doped structures, the guest atom donates most of its charge to the carbon framework (see section D of the SI, Figures S3 and S4). The most noticeable exceptions are Be@C_{60} and Mg@C_{60} , shown

in Figure S3, where the metal states hybridize with the carbon states, thus changing deeply the electronic structure around the Fermi level. An interesting case is Ca@C_{60} where the charge transfer shifts the Fermi level to the DOS peak, inducing a high density of states (see the last panel of Figure S3). Concerning the electronic structure of the M@C_{24} series (also shown in section D of the SI, Figures S5 and S6) the rigid-band model is not followed, with the exceptions of the monovalent doped compounds ($\text{M}=\text{Li,Na,K}$) and Ca@C_{24} . The insertion of the dopant in the smaller C_{24} cage leads to the hybridization of the dopant and carbon framework states changing deeply the band structure.

The phonon dispersion curves for the studied doped fullerite clathrates are shown in the SI, section E. Only four doped clathrate structures do not display imaginary phonon modes and are dynamically stable, these structures being Li@C_{24} , Na@C_{24} , Ga@C_{24} and

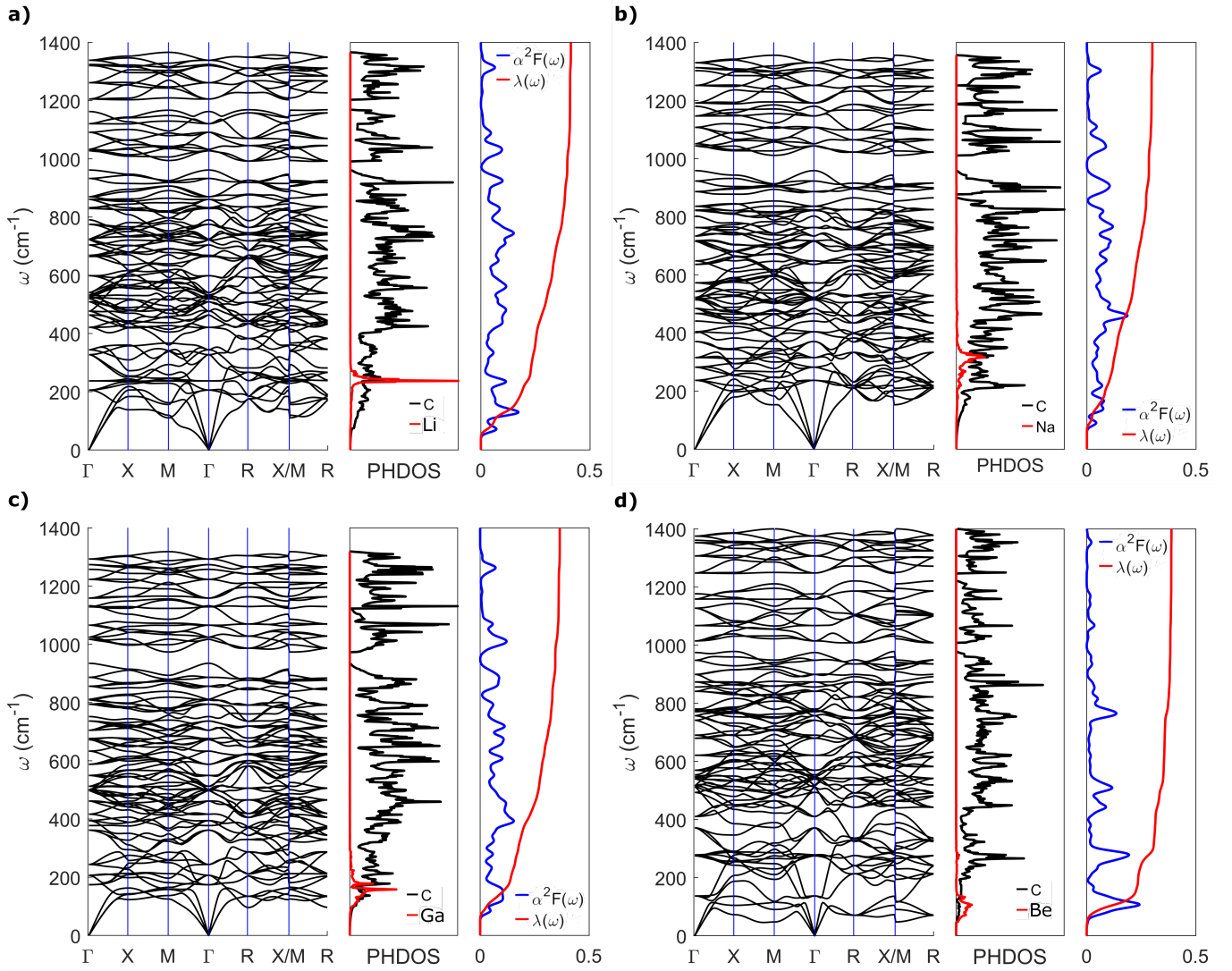


FIG. 3. Phonon dispersion curves (left panels), projected phonon density of states (middle panels), Eliashberg spectral function $\alpha^2F(\omega)$, blue line, and integrated electron-phonon coupling $\lambda(\omega)$, red line, (right panels) for the doped clathrate structures: a) Li@C₂₄; b) Na@C₂₄; c) Ga@C₂₄; d) Be@C₆₀.

Be@C₆₀. The imaginary phonon modes of unstable doped clathrates are either originated from the carbon framework or from mixed carbon-dopant vibrations. In the first case, the charge transfer from the guest atom to the carbon framework structure is observed to be nearly completed, while it is clearly uncompleted in the latter case.

Superconducting behavior was explored for the four stable clathrates. As referred above, the Be@C₆₀ clathrate shows a very different electronic band structure from that of the pristine fullerite clathrate (see Figure 2 d). In particular, the band that crosses the Fermi level is the result from the hybridization of beryllium and carbon framework states. Indeed, the incomplete charge transfer from the dopant to the carbon structure is confirmed from the integrated local DOS contours and the projected

DOS (PDOS) around the Fermi level (see Figures S11 and S12). The PDOS curve for the Be@C₆₀ shows electronic density from the dopant at the Fermi level, while no density is observed for the Li@C₂₄, Na@C₂₄, indicating in the latter case a complete charge transfer to the framework carbon structure. Ga@C₂₄ presents an intermediate case where ~ 1 electron is donated to the carbon framework but there is still a very low amount of states due to the dopant at the Fermi level. This picture is corroborated by the computed Bader charges given in Table S3.

The phonon dispersion curves shown in the left panels of Figure 3 present two distinct zones separated around 1000 cm⁻¹. A second gap around 1200 cm⁻¹ is also observed for Li@C₂₄ and Be@C₆₀ compounds. The middle panels in Figure 3 present the projected phonon

density of states (PHDOS) showing that the dopant atoms contribute only to lower frequencies, below 400 cm^{-1} . The calculated Eliashberg spectral function, $\alpha^2F(\omega)$, and the electron-phonon coupling constant, $\lambda(\omega)$, are also shown in Figure 3 (right panels). The strongest peaks in the Eliashberg spectral function arise at low energy, between 100 and 300 cm^{-1} , for Be@C_{60} and thus these are the phonon frequencies that will mostly contribute to the electron-phonon coupling ($\sim 80\%$) and concomitantly to the superconducting T_c , see Figure 3 d). For the other systems, the contribution to the Eliashberg spectral function is more evenly distributed over all frequencies leading to a smother growth of the integrated electron-phonon coupling curve, Figures 3 a), b) and c). Hence, beryllium is the only dopant that contributes significantly to the Eliashberg spectral function, which is in agreement with the fact that it is the sole dopant whose electronic states strongly hybridize with the carbon states. The integrated electron-phonon coupling constant is always lower than 0.5 , as indicated in Table I, considerably smaller than the 2.92 reported for the sodium doped sodalite-like carbon clathrate [7], and thus the T_c 's should not be high. Indeed, using the Allen-Dynes modified McMillan equation with a Coulomb screening potential $\mu^*=0.1$ the T_c 's obtained are quite low: 1.81 K , 0.23 K , 0.99 K and 0.88 K , respectively for Li@C_{24} , Na@C_{24} , Ga@C_{24} and Be@C_{60} clathrates. We also solved the isotropic Eliashberg equations obtaining the superconducting gaps for all the stable structures, shown in Figure 4. The calculated T_c 's are 2.03 K , 0.40 K , 1.29 K and 1.14 K for Li@C_{24} , Na@C_{24} , Ga@C_{24} and Be@C_{60} , respectively, in agreement with those referred above.

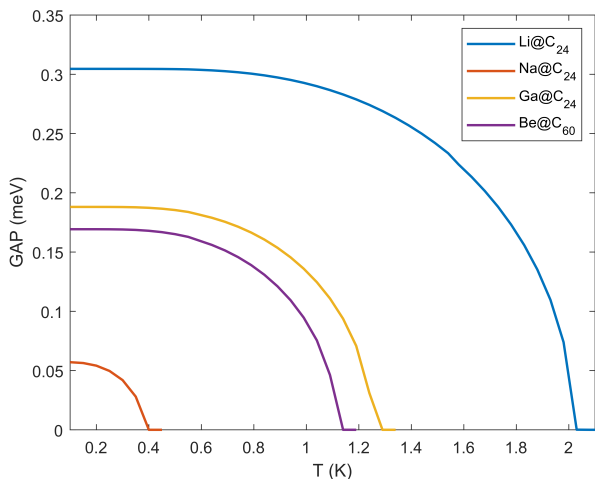


FIG. 4. Superconducting gap for the doped C_{60} clathrate structure: Li@C_{24} (blue curve); Na@C_{24} (orange curve); Ga@C_{24} (yellow curve); Be@C_{60} (purple curve).

The electron-phonon coupling constants, for each high-symmetry q-point, are given in Table I. The Na@C_{60} clathrate has been included in this list because, despite

being unstable, it has a higher electron-phonon coupling constant than all the stable doped clathrates at X and M q-points (excluding the X point for Be@C_{60} clathrate). In addition, it has, by far, the highest density of states at the Fermi level, $N(E_F)$. If this unstable structure could be turned dynamically stable, by accounting anharmonic [27–29] and/or pressure effects a serious increase in the T_c would then be expected. Considering that its softest phonon is barely imaginary, $56i \text{ cm}^{-1}$, it is possible that such effects will be sufficient to turn the structure stable, as was observed for the superconductor LaH_{10} [27] and for the ferroelectric SnTe [30].

TABLE I. Superconducting properties of a few selected systems. The electron-phonon coupling constant at R q-point is not present for Na@C_{60} due to the existence of imaginary modes. The number of density of states at the Fermi level $N(E_F)$ is given in state per spin per meV and per atom in the last column.

	λ X q-point	λ M q-point	λ R q-point	λ integrated	ω_{log} cm^{-1}	T_c K	$N(E_F)$ state/spin/eV/atom
Li@C_{24}	0.3740	0.3368	0.2801	0.41	254.69	1.81	63.0
Na@C_{24}	0.3170	0.2326	0.1597	0.30	342.87	0.23	63.3
Ga@C_{24}	0.3716	0.2263	0.3158	0.36	289.45	0.99	56.4
Be@C_{60}	0.9176	0.1835	0	0.39	178.34	0.88	21.4
Na@C_{60}	0.6142	0.7207	-	-	-	-	105.7

CONCLUSION

The stability and superconducting properties of the fullerite clathrate structures doped with simple metals has been explored. Only four structures were found to be stable: Li@C_{24} , Na@C_{24} , Ga@C_{24} and Be@C_{60} . They all show superconducting critical temperatures below 4 K , due to the weak electron-phonon coupling and the small number of states at the Fermi level. These two parameters, particularly the latter, are higher in the barely unstable Na@C_{60} , indicating that the stabilization of this compound would result in a superconductor with T_c much higher than those reported here. We are currently exploring this possibility by explicitly considering anharmonic and pressure effects.

ACKNOWLEDGMENTS

This work was developed within the scope of the project CICECO-Aveiro Institute of Materials, UIDB/50011/2020, UIDP/50011/2020 & LA/P/0006/2020, financed by national funds through the FCT/MCTES (PIDDAC) and IF/00894/2015 finances by FCT. J. Laranjeira acknowledges a PhD grant from FCT (SFRH/BD/139327/2018).

I.E. and D.D. acknowledge funding from the European Research Council (ERC) under the European Union's Horizon 2020 research and innovation program (Grant Agreement No. 802533) and the Department of Education, Universities and Research of the Eusko

Jaurilaritza and the University of the Basque Country UPV/EHU (Grant No. IT1527-22).

The work has been performed under the project HPC-EUROPA3 (INFRAIA-2016-1-730897), with the

support of the EC Research Innovation Action under the H2020 Programme; in particular, the author gratefully acknowledges the support of the computer resources and technical support provided by BSC.

-
- [1] C. Pickard, I. Errea, and M. Eremets, *Annu. Rev. Condens. Matter Phys.* **11**, 57 (2020).
- [2] D. Duan, Y. Liu, F. Tian, D. Li, X. Huang, Z. Zhao, H. Yu, B. Liu, W. Tian, and T. Cui, *Sci. Rep.* **4**, 6 (2014).
- [3] A. Drozdov, M. Eremets, I. Troyan, V. Ksenofontov, and S. Shylin, *Nature* **525**, 4 (2015).
- [4] M. Somayazulu, M. Ahart, A. Mishra, M. Geballe, Zacharyand Baldini, Y. Meng, V. Struzhkin, and R. Hemley, *Phys. Rev. Lett.* **122**, 027001 (2019).
- [5] A. Drozdov, P. Kong, V. Minkov, S. Besedin, M. Kuzovnikov, S. Mozaffari, L. Balicas, F. Balakirev, D. Graf, V. Prakapenka, E. Greenberg, D. Knyazev, M. Tkacz, and M. Eremets, *Nature* **569**, 528 (2019).
- [6] S. Di Cataldo, S. Qulaghasi, G. Bachelet, and L. Boeri, *Phys. Rev. B* **105**, 064516 (2022).
- [7] S. Lu, H. Liu, I. Naumov, S. Meng, Y. Li, J. Tse, B. Yang, and R. Hemley, *Phys. Rev. B* **93**, 104509 (2016).
- [8] T. Strobel, L. Zhu, P. Guńka, G. Borstad, and M. Guerette, *Angew. Chem. Int. Ed.* **60**, 2877 (2020).
- [9] L. Zhu, G. Borstad, H. Liu, P. Guńka, M. Guerette, J.-A. Dolyniuk, Y. Meng, E. Greenberg, V. Prakapenka, B. Chaloux, A. Epshteyn, R. Cohen, and T. Strobel, *Sci. Adv.* **6**, eaay8361 (2020).
- [10] T. Zeng, R. Hoffmann, R. Nesper, N. Ashcroft, T. Strobel, and D. Proserpio, *J. Am. Chem. Soc.* **137**, 12639 (2015).
- [11] J.-N. Wang, X.-W. Yan, and M. Gao, *Phys. Rev. B* **103**, 144515 (2021).
- [12] N. Geng, K. Hilleke, L. Zhu, X. Wang, T. Strobel, and E. Zurek, *J. Am. Chem. Soc.* **145**, 1696 (2023).
- [13] H. Amekura and N. Kishimoto, *Journal of Applied Physics* **104**, 063509 (2008).
- [14] Y. Takano, T. Takenouchi, S. Ishii, S. Ueda, T. Okutsu, I. Sakaguchi, H. Umezawa, H. Kawarada, and M. Tachiki, *Diam. Relat. Mater.* **16**, 911 (2007).
- [15] T. Weller, M. Ellerby, S. Saxena, R. Smith, and N. Skipper, *Nat. Phys.* **1**, 3 (2005).
- [16] O. Gunnarsson, *Rev. Mod. Phys.* **69**, 575 (1997).
- [17] T. Palstra, O. Zhou, Y. Iwasa, P. Sulewski, R. Fleming, and B. Zegarski, *Solid State Commun.* **93**, 327 (1995).
- [18] J. Laranjeira, L. Marques, M. Melle-Franco, K. Strutyński, and M. Barroso, *Carbon* **194**, 297 (2022).
- [19] J. Perdew, K. Burke, and M. Ernzerhof, *Phys. Rev. Lett.* **77**, 3865 (1996).
- [20] J. Perdew, K. Burke, and M. Ernzerhof, *Phys. Rev. Lett.* **78**, 1396 (1997).
- [21] P. Giannozzi, S. Baroni, N. Bonini, M. Calandra, R. Car, C. Cavazzoni, D. Ceresoli, G. Chiarotti, M. Cococcioni, I. Dabo, A. Dal Corso, S. De Gironcoli, S. Fabris, G. Fratesi, R. Gebauer, U. Gerstmann, C. Gougoussis, A. Kokalj, M. Lazzeri, L. Martin-Samos, N. Marzari, F. Mauri, R. Mazzarello, S. Paolini, A. Pasquarello, L. Paulatto, C. Sbraccia, S. Scandolo, G. Sclauzero, A. Seitsonen, A. Smogunov, P. Umari, and R. Wentzcovitch, *J. Phys. Condens. Matter* **21**, 395502 (2009).
- [22] P. Giannozzi, O. Andreussi, T. Brumme, O. Bunau, M. Nardelli, M. Calandra, R. Car, C. Cavazzoni, D. Ceresoli, M. Cococcioni, N. Colonna, I. Carnimeo, A. Dal Corso, S. De Gironcoli, P. Delugas, R. DiStasio, A. Ferretti, A. Floris, G. Fratesi, G. Fugallo, R. Gebauer, U. Gerstmann, F. Giustino, T. Gorni, J. Jia, M. Kawamura, H.-Y. Ko, A. Kokalj, E. Küçükbenli, M. Lazzeri, M. Marsili, N. Marzari, F. Mauri, N. Nguyen, H.-V. Nguyen, A. O. de-la Roza, L. Paulatto, S. Poncé, D. Rocca, R. Sabatini, B. Santra, M. Schlipf, A. Seitsonen, A. Smogunov, I. Timrov, T. Thonhauser, P. Umari, N. Vast, X. Wu, and S. Baroni, *J. Phys. Condens. Matter* **29**, 465901 (2017).
- [23] M. Methfessel and A. Paxton, *Phys. Rev. B* **40**, 3616 (1989).
- [24] S. Baroni, S. De Gironcoli, A. Dal Corso, and P. Giannozzi, *Rev. Mod. Phys.* **73**, 515 (2001).
- [25] G. Éliashberg, *Sov. Phys. JETP* **11**, 696 (1960).
- [26] P. Allen and R. Dynes, *Phys. Rev. B* **12**, 905 (1975).
- [27] I. Errea, F. Belli, L. Monacelli, A. Sanna, T. Koretsune, T. Tadano, R. Bianco, M. Calandra, R. Arita, F. Mauri, and J. Flores-Livas, *Nature* **578**, 66 (2020).
- [28] I. Errea, M. Calandra, C. Pickard, J. Nelson, R. Needs, Y. Li, H. Liu, Y. Zhang, Y. Ma, and F. Mauri, *Nature* **532**, 81 (2016).
- [29] I. Errea, M. Calandra, C. Pickard, J. Nelson, R. Needs, Y. Li, H. Liu, Y. Zhang, Y. Ma, and F. Mauri, *Phys. Rev. Lett.* **114**, 157004 (2015).
- [30] G. Ribeiro, L. Paulatto, R. Bianco, I. Errea, F. Mauri, and M. Calandra, *Phys. Rev. B* **97**, 014306 (2018).

SUPPORTING INFORMATION

A. ELECTRONIC STRUCTURE OF THE UNDOPED FULLERITE CLATHRATE

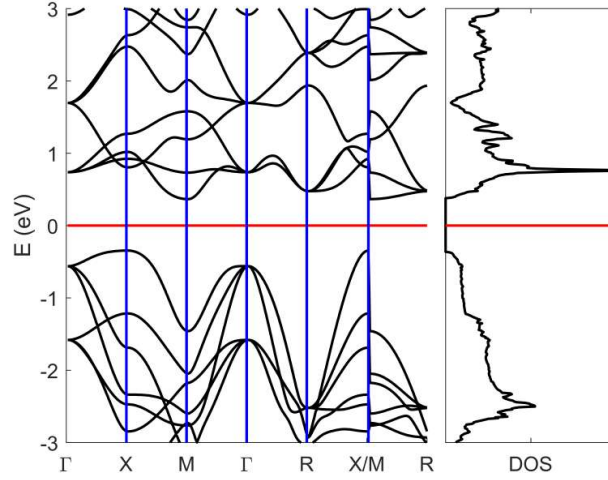


Figure S1. Electronic density of states (right panel) and electronic band structure (left panel) of the fullerite C_{60} clathrate. Red lines indicate the Fermi level.

B. ENERGY AND LATTICE PARAMETER EVOLUTION WITH DOPANT INSERTION

M(dopant)	@C ₆₀	@C ₂₄
Li	6.2211	6.2358
Na	6.2258	6.2565
K	6.2366	6.3039
Be	6.2067	6.2544
Mg	6.2187	6.2824
Ca	6.2359	6.2990
Al	6.2203	6.2872
Ga	6.2200	6.2926
Ge	6.2111	6.3087

Table S1. Simple cubic lattice parameters for all the doped systems after optimization, given in Å. The undoped system presents a lattice parameter of 6.2031 Å.

M(dopant)	@C ₆₀	@C ₂₄
Li	-7.5209	-7.4616
Na	-7.5161	-7.4089
K	-7.5200	-7.3202
Be	-7.4772	-7.3950
Mg	-7.4666	-7.3312
Ca	-7.5256	-7.3700
Al	-7.5179	-7.3455
Ga	-7.5189	-7.3270
Ge	-7.5256	-7.3076

Table S2. DFT formation energy for each structure in eV/atom. The formation energy, E_f , is computed by subtracting the energy per atom from the structure energy, $E_f = E_{struc} - (30E_c + E_M)$. The undoped system presents a ground state energy of -7.7327 eV/atom.

C. ELECTRONIC STRUCTURE AND PHONON DISPERSION CURVES OF THE Sc@C_{60} AND Y@C_{60} COMPOUNDS

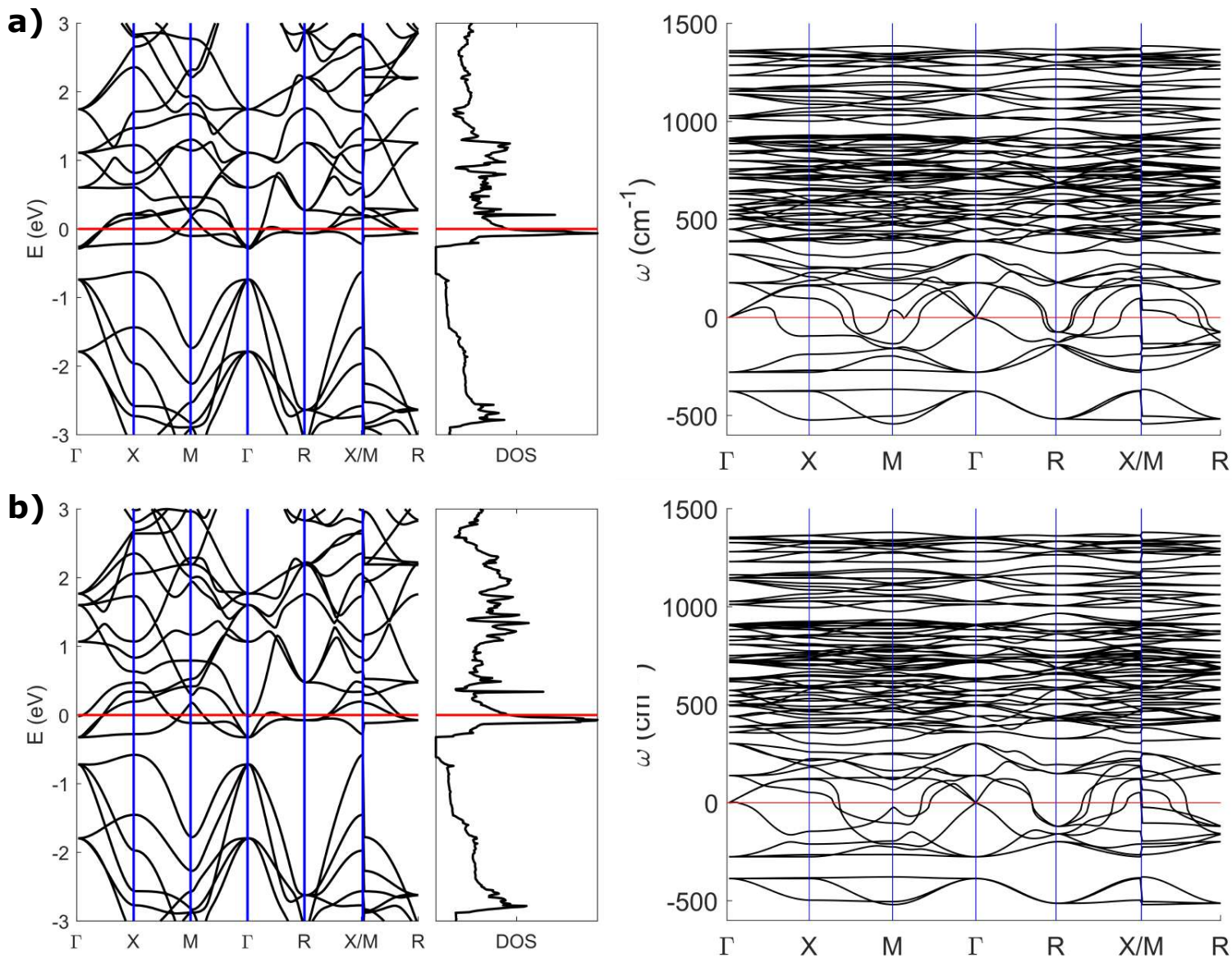


Figure S2. Electronic structure and phonon dispersion curves of fullerite C_{60} clathrate structure doped with two trivalent dopants: a) Sc@C_{60} ; b) Y@C_{60} . The left panels show the band structure and the electronic DOS, and the right panels show the phonon dispersion curves.

D. ELECTRONIC STRUCTURES OF THE DOPED FULLERITE CLATHRATES

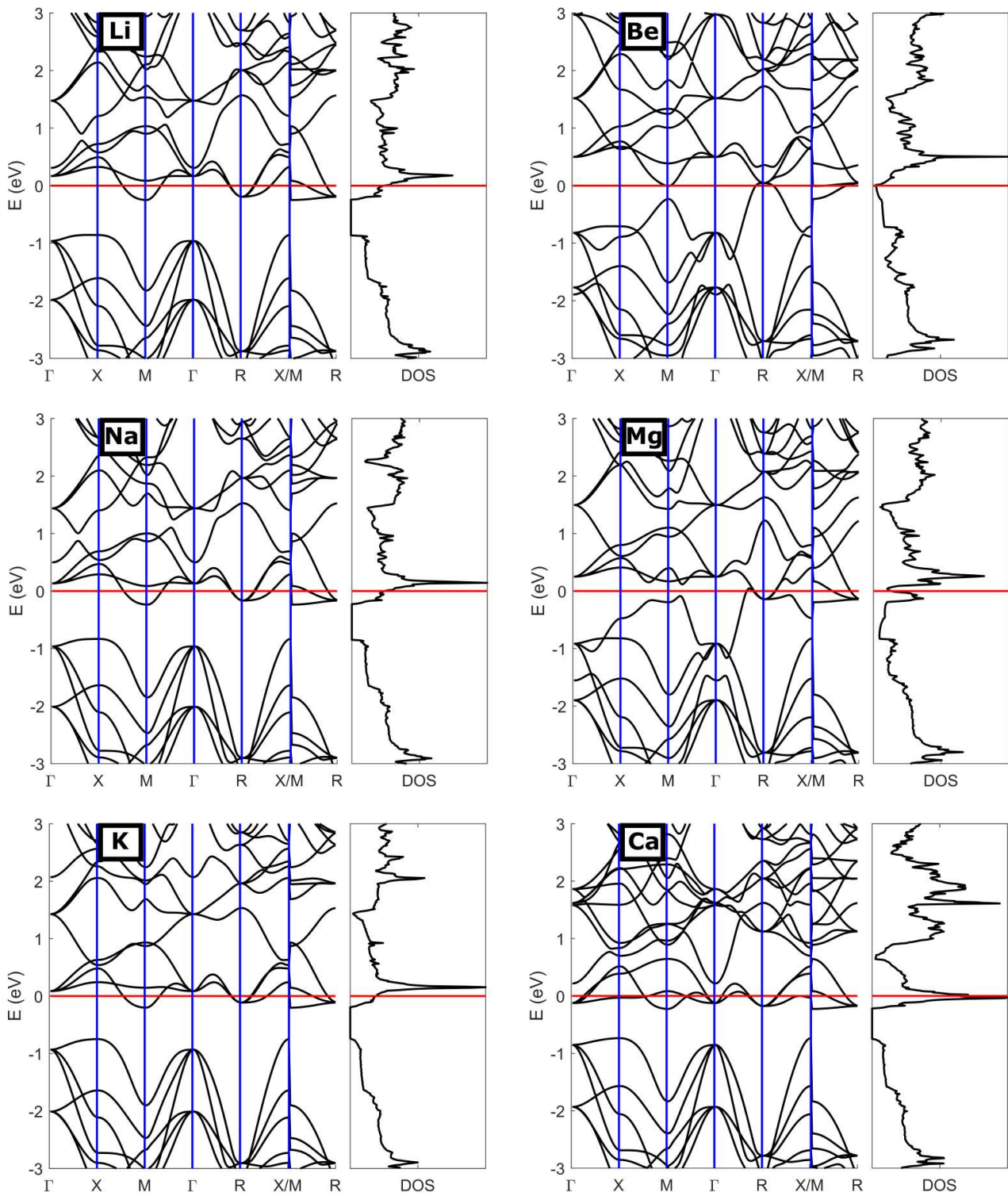


Figure S3. Electronic band structure and density of states of the doped fullerite clathrates containing the guest-dopant in the C_{60} cages. The left columns correspond to the monovalent dopants and the right columns correspond to the divalent ones.

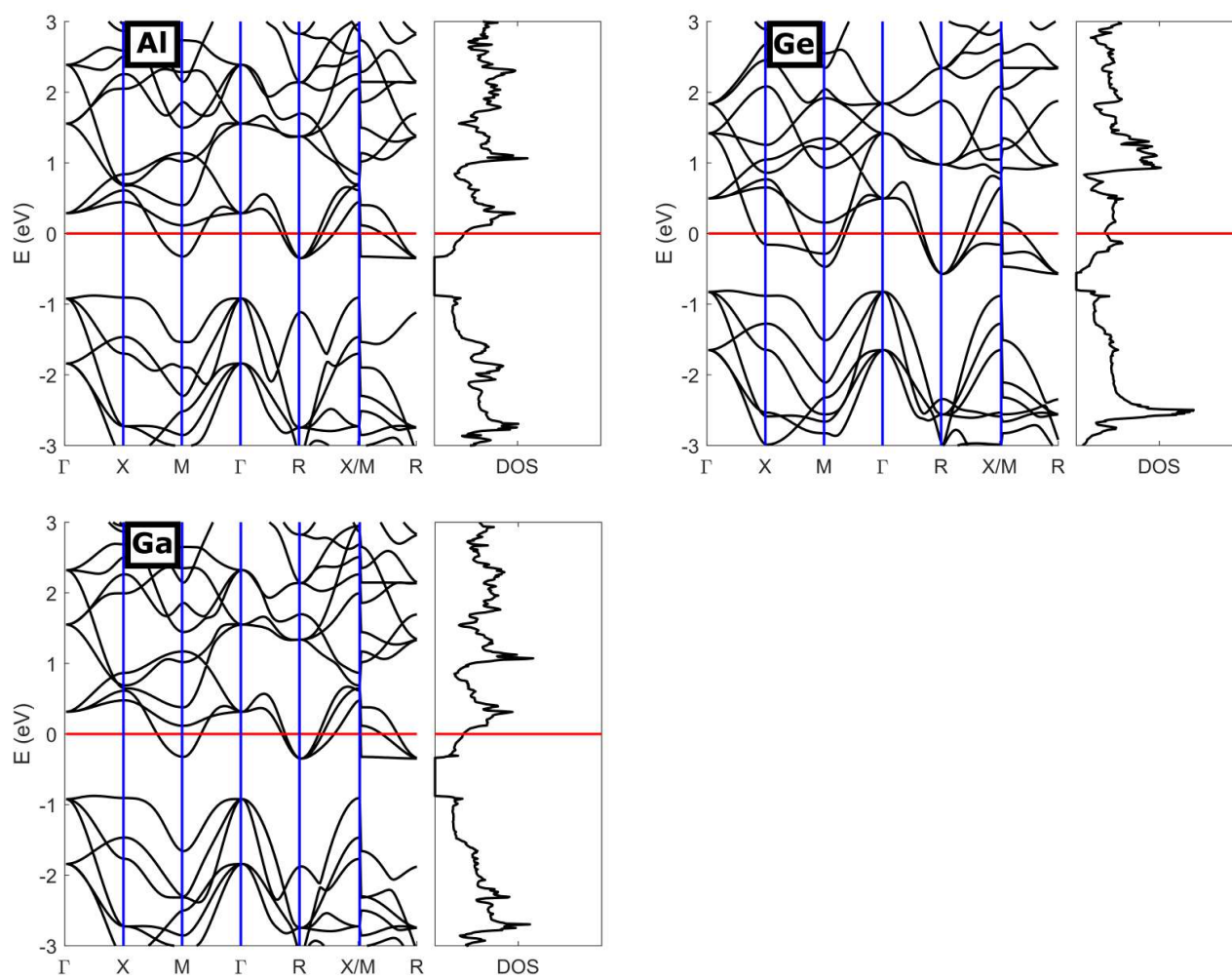


Figure S4. Electronic band structure and density of states of the doped fullerite clathrate containing the trivalent (left columns) or the tetravalent guest-dopants (right columns) in the C_{60} cages.

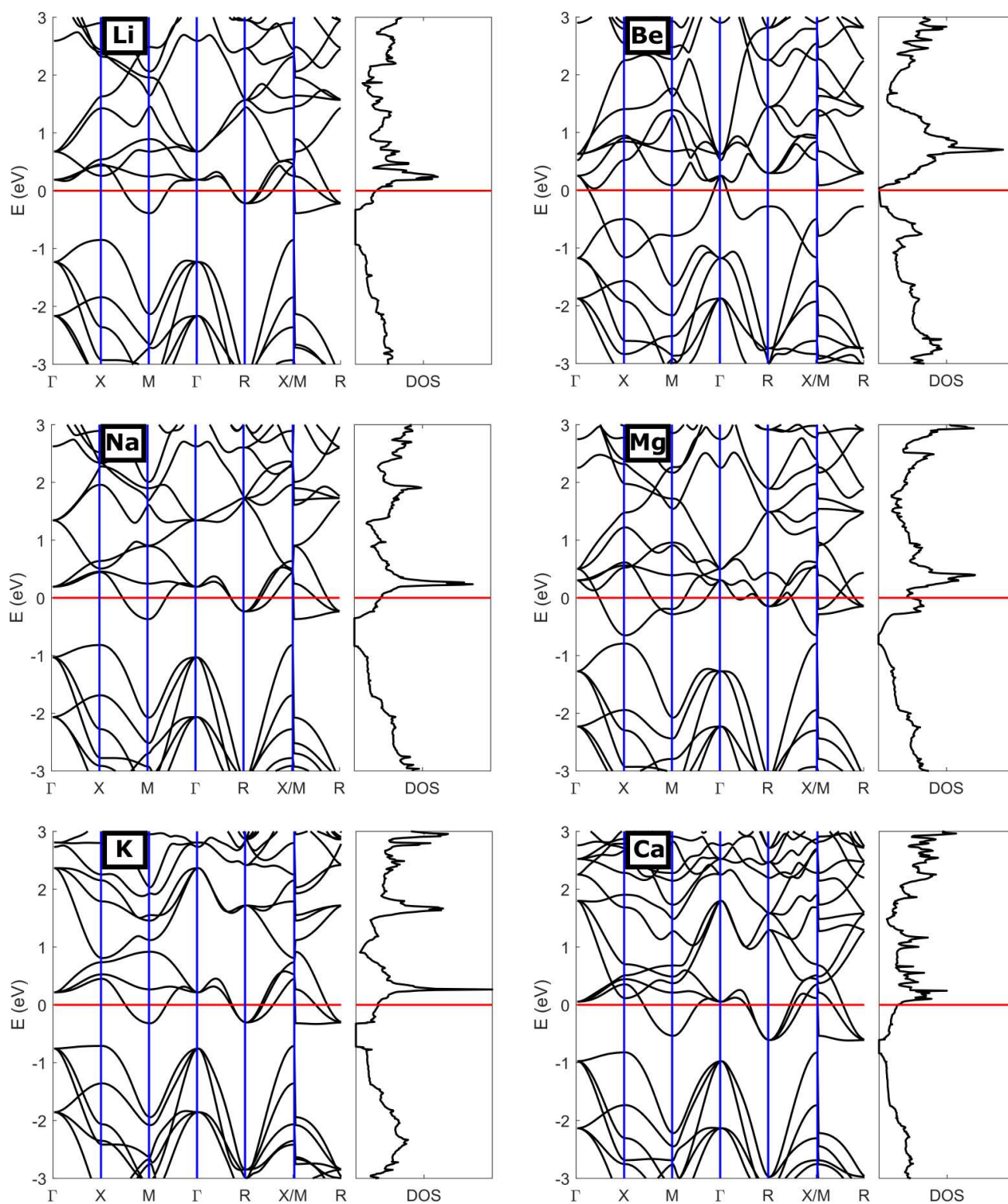


Figure S5. Electronic band structure and density of states of the doped fullerite clathrates containing the guest-dopants in the C_{24} cages. The left columns correspond to the monovalent dopants and the right columns correspond to the divalent dopants.

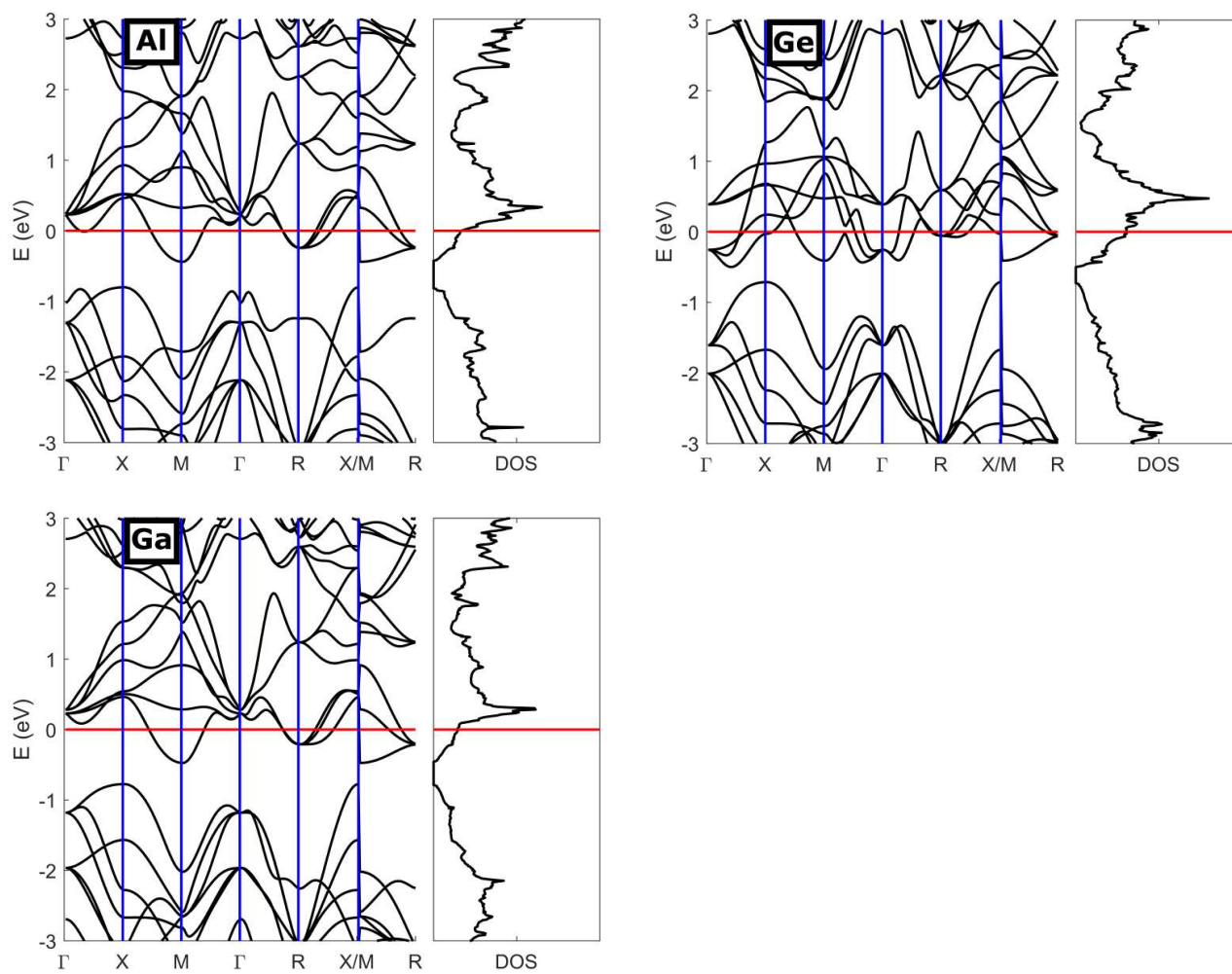


Figure S6. Electronic band structure and density of states of the doped fullerite clathrates containing the trivalent (left columns) or tetravalent (right columns) guest-dopants in the C_{24} cages.

E. PHONON DISPERSION CURVES FOR THE DOPED FULLERITE CLATHRATES

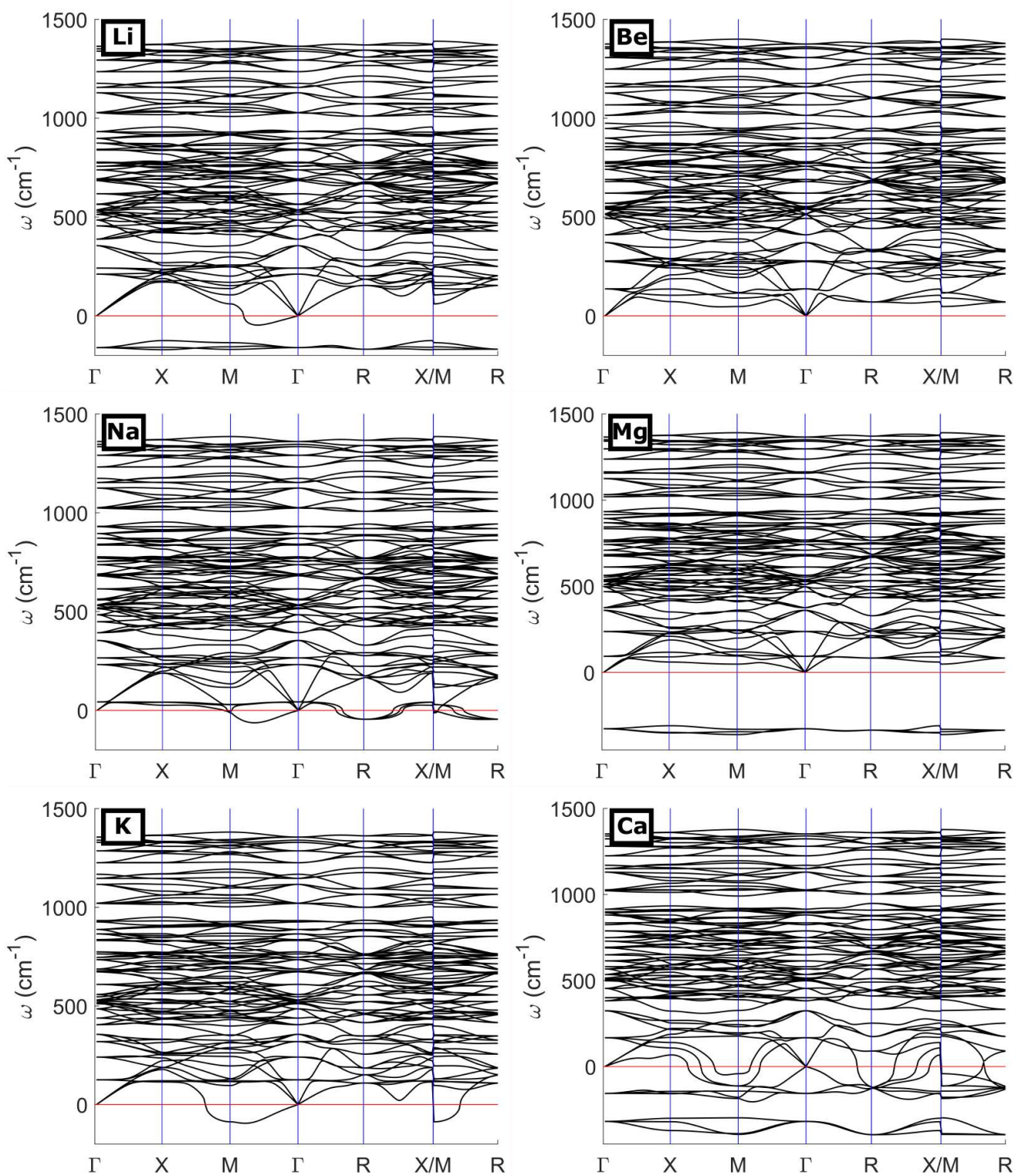


Figure S7. Phonon spectra of the doped fullerite clathrates containing the monovalent (left column) or divalent (right column) guest-dopants in the C_{60} cages.

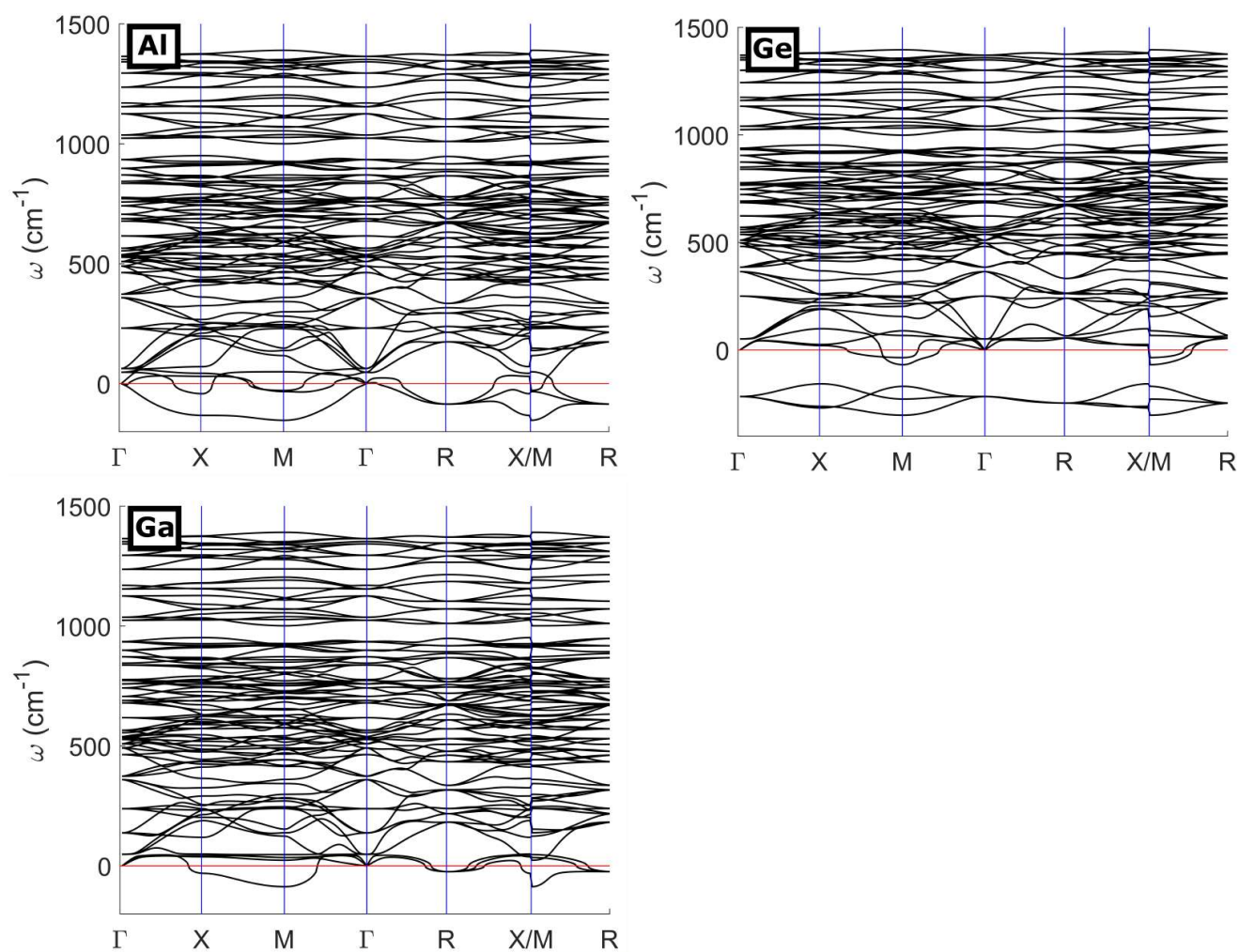


Figure S8. : Phonon spectra of the doped fullerite clathrates containing the trivalent (left column) or tetravalent (right column) guest-dopants in the C_{60} cages.

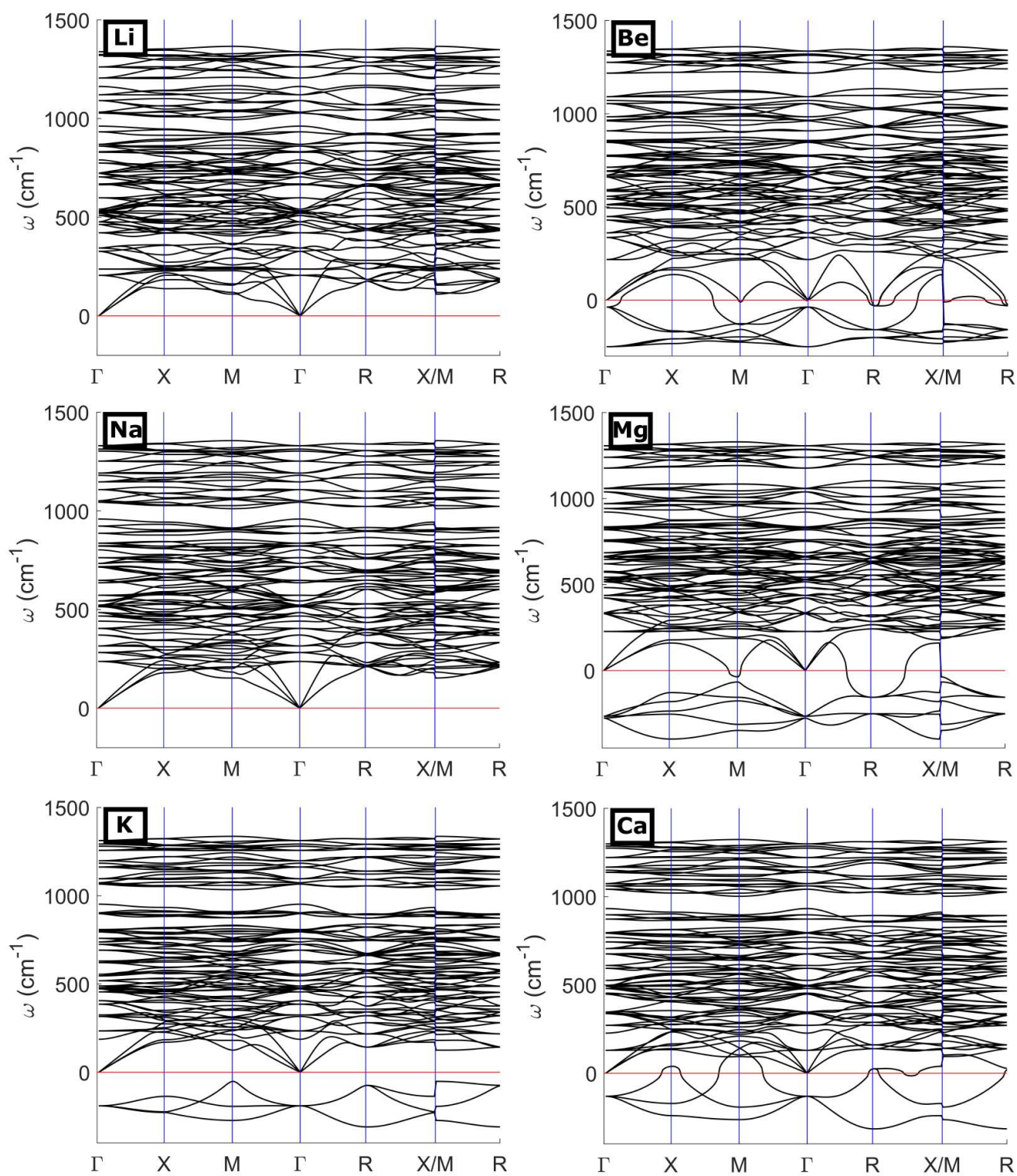


Figure S9. Phonon spectra of the doped fullerite clathrates containing the monovalent (left column) or divalent (right column) guest-dopants in the C_{24} cages.

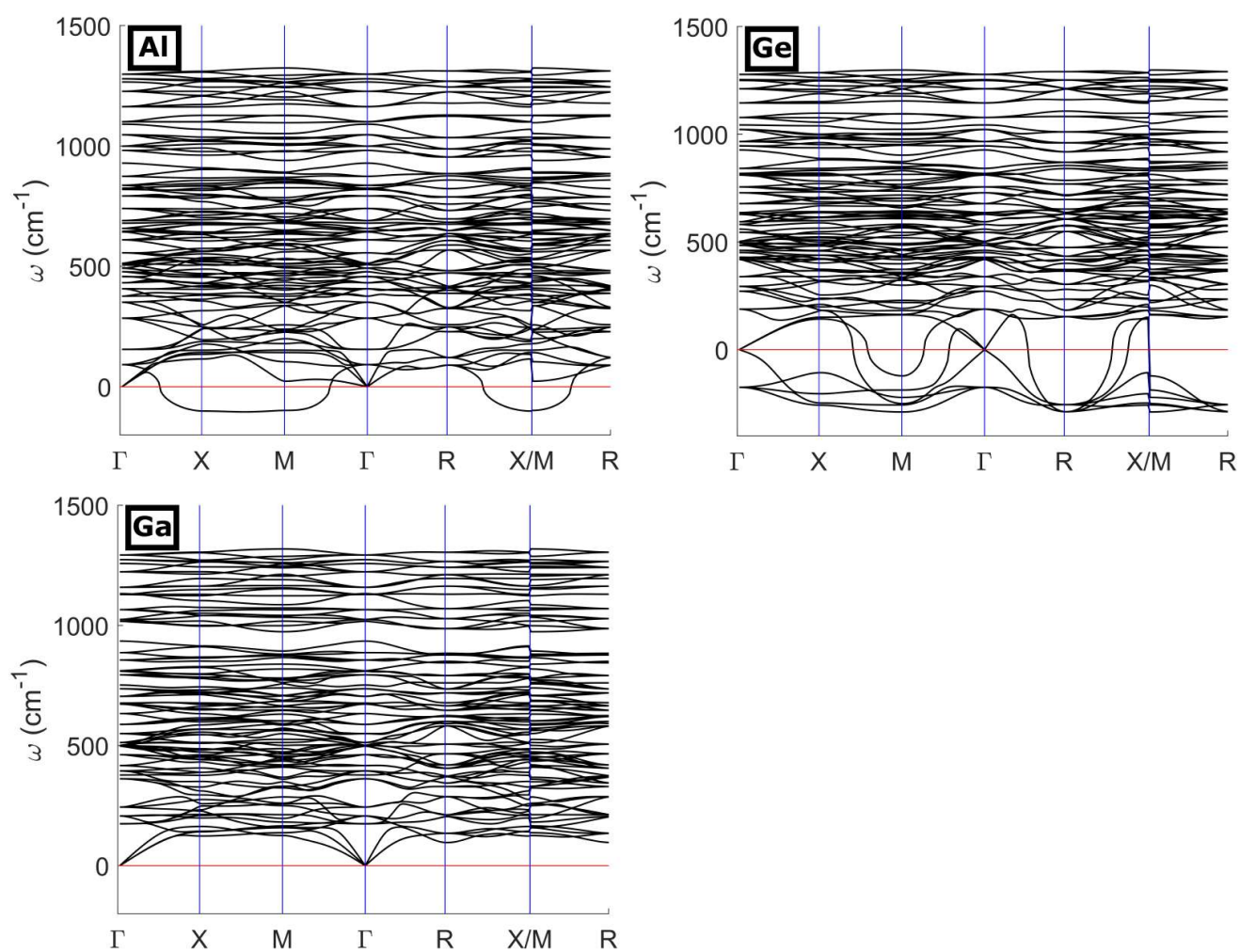


Figure S10. Phonon spectra of the doped fullerite clathrates containing the trivalent (left column) or tetravalent (right column) guest-dopants in the C_{24} cages.

F. INTEGRATED LOCAL ELECTRONIC DENSITY AROUND THE FERMI LEVEL FOR THE STABLE DOPED FULLERITE CLATHRATES

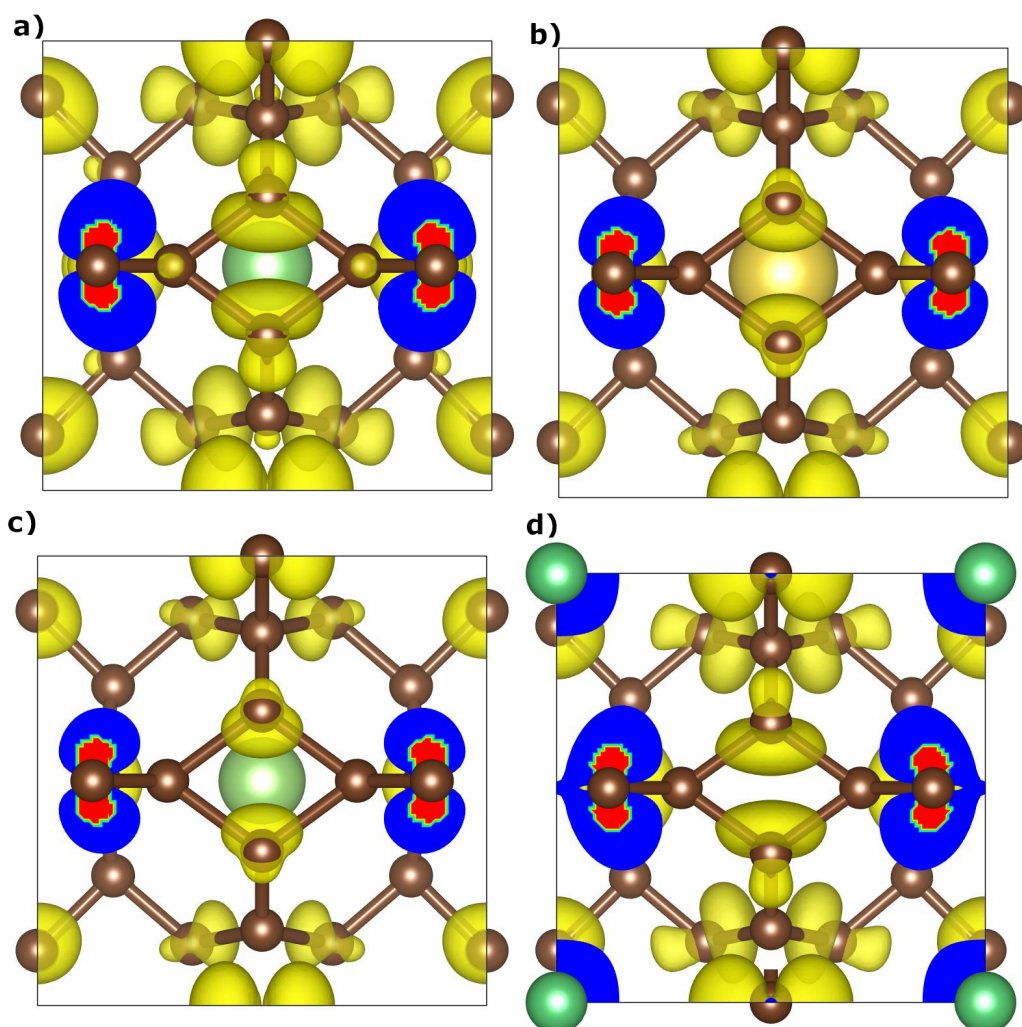


Figure S11. Integrated local electronic density around the Fermi level for: a) Li@C_{24} ; b) Na@C_{24} ; c) Ga@C_{24} and d) Be@C_{60} . The partial electron density was integrated 0.01 eV around the Fermi level, with the partial electronic density isosurface with $2.0 \times 10^{-4} \text{ e}/\text{\AA}^3$ ($5.0 \times 10^{-5} \text{ e}/\text{\AA}^3$ for Be@C_{60}) superposed on a ball-and-stick model for the (100) crystallographic plane.

G. PROJECTED ELECTRONIC DENSITY OF STATES FOR THE STABLE DOPED CLATHRATES

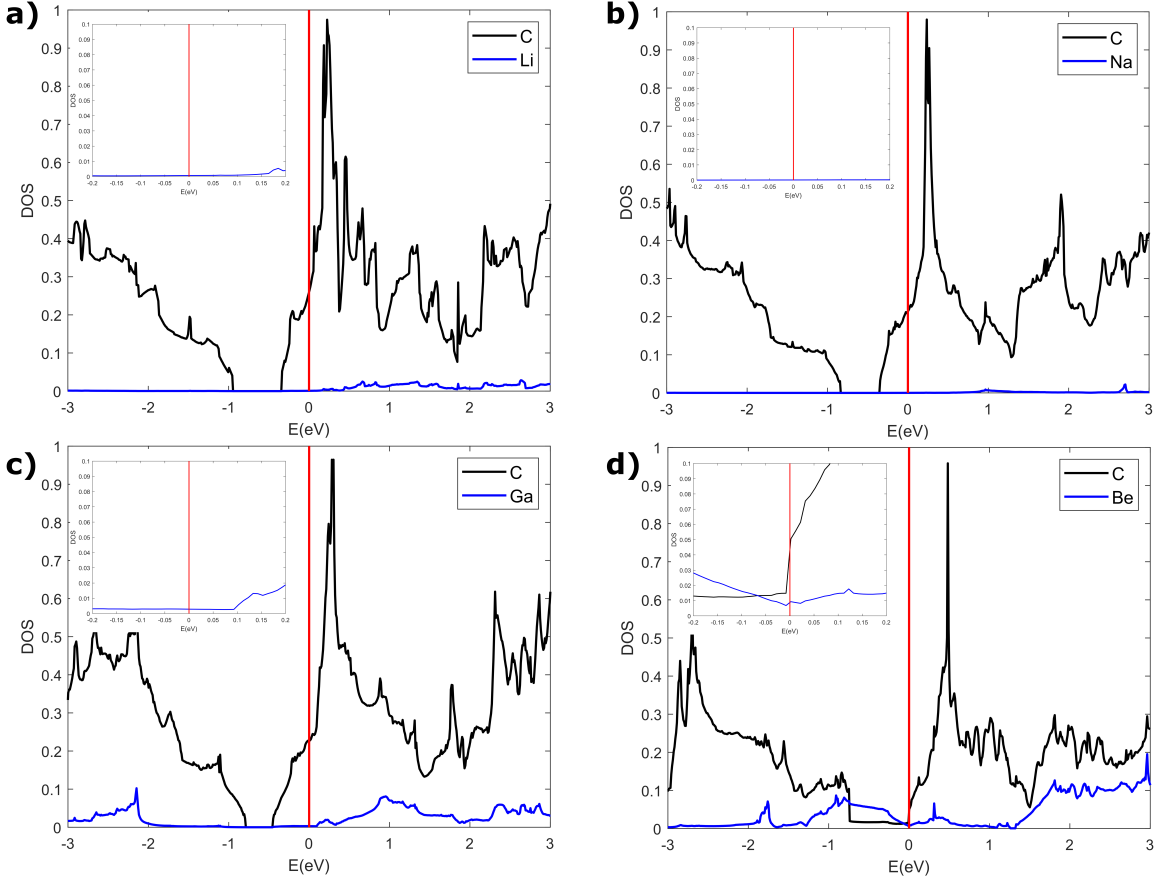


Figure S12. Projected electronic density of states for: a) $\text{Li}@C_{24}$; b) $\text{Na}@C_{24}$; c) $\text{Ga}@C_{24}$ and d) $\text{Be}@C_{60}$. The black always denotes carbon projected DOS while blue denotes the different dopant. Fermi level is denoted by a red line. All the plots are normalized to the highest peak found in carbon projected DOS.

H. BADER CHARGES FOR THE STABLE STRUCTURES

Structure	Atom	Wyckoff Position	Bader charge
$\text{Li}@C_{24}$	C1	12k	4.05
	C2	12k	3.99
	C3	6f	4.07
	Li	1b	0.11
$\text{Na}@C_{24}$	C1	12k	4.05
	C2	12k	3.99
	C3	6f	4.06
	Na	1b	0.16
$\text{Ga}@C_{24}$	C1	12k	4.06
	C2	12k	3.99
	C3	6f	4.06
	Ga	1b	2.08
$\text{Be}@C_{60}$	C1	12k	4.02
	C2	12k	3.95
	C3	6f	4.08
	Be	1a	1.92

Table S3. Bader charges of the inequivalent atoms.

Chapter 9

Polymeric C_{60} electronic structure evolution

9.1 A7 - C_{60} structures: Structural, electronic and elastic properties

© 2020 Elsevier Ltd.
Reprinted with permission.



C₆₀ structures: Structural, electronic and elastic properties

Jorge Laranjeira, Leonel Marques*

Departamento de Física and CICECO, Universidade de Aveiro, 3810-193, Aveiro, Portugal



ARTICLE INFO

Keywords:

Fullerene polymers
DFT calculations
Electronic density of states
Bulk moduli

ABSTRACT

A systematic investigation, using density functional theory (DFT) methods, of the physical properties of one-dimensional (1D), two-dimensional (2D) and three-dimensional (3D) pressure-induced polymerized C₆₀ structures, was performed. The optimized crystal structures, the electronic density of states (DOS) and the bulk moduli B₀ were calculated for such polymerized structures, showing how these properties change with the degree of polymerization and providing an overview of the properties of this class of materials. The increasing number of intermolecular bonds, across the low-dimensional polymers, induces a decrease of the electronic bandgap, which in turn vanishes for the metallic 3D polymers. The compressibility behavior of these materials also shows a monotonous dependence on the degree of polymerization: the rise in the number of polymeric bonds induces an expected increase of the bulk modulus. From semiconducting to metallic and from soft to low-compressibility, this class of materials is shown to display an enormous range of electronic and elastic properties.

1. Introduction

At room conditions, C₆₀ fullerite is a Van der Waals solid with a face-centered cubic (fcc) structure, in which the molecules are rotating [1]. It is a wide-gap semiconductor with an indirect bandgap of 2.3 eV, and it is a soft solid with bulk modulus of about 10 Giga-pascal (GPa) [2,3]. When compressed at high temperatures C₆₀ fullerite transforms to a variety of polymerized structures, with different dimensionalities, depending on the magnitude of the applied pressure [4]. These high-pressure polymerized phases can be quenched to ambient conditions and, thus, they constitute a class of nanostructured pure-carbon materials.

At pressures below 8 GPa low-dimensional polymers are synthesized: 1D orthorhombic polymer, a 2D polymer, with tetragonal or pseudo-tetragonal symmetry, and a second 2D polymer, with rhombohedral symmetry and more compressed than the previous ones [5]. These low-dimensional polymerized phases have the same type of intermolecular covalent bond, 66/66 2 + 2 cycloaddition, which bridges intramolecular double bonds of neighboring molecules. Above 8 GPa, 3D C₆₀ polymers are synthesized [6,7]. Although several 3D polymerized phases have been claimed, only a few crystal structures have been reported so far. A disordered face centered cubic (fcc) 3D polymer, involving 56/56 2 + 2 cycloaddition bonds that bridges intramolecular single bonds of neighboring molecules, is synthesized at 9.5 GPa and 550 °C [8]. By compressing the 2D tetragonal polymer at 15 GPa and 600 °C, an orthorhombic 3D polymer was obtained, where the planes

initially polymerized are bonded through 3 + 3 cycloaddition bonds, inducing a cuboid-shape molecular deformation [9].

Although each one of these phases has been studied individually, a systematic investigation of this class of nanostructured materials is lacking. In this sense, we employed DFT methods to calculate the optimized crystal structures, which in general agree with experiments, and some of their electronic and elastic properties. We show how these properties change, in a very broad range, with the polymerization degree across these polymeric materials.

2. Methods

DFT calculations were performed using the Vienna ab initio simulation package (VASP) [10]. Perdew-Burke-Ernzerhof (PBE) generalized gradient approximation (GGA) was used to calculate the exchange-correlation energy [11]. Electron core interaction was described by the projector augmented wave pseudo-potentials supplied with VASP. The self-consistent-field process was stopped once the energy difference between two consecutive steps was smaller than 10⁻⁵ eV; the k-points were converged within 10⁻⁵ meV/atom.

All the crystalline structures had their atomic positions and lattice constants optimized using a 6 × 6 × 6 k-points mesh and a Gaussian smearing with standard deviation of 0.2. An energy cutoff of 520 eV was employed. Van der Waals dispersive interactions were accounted in 1D and 2D polymerized C₆₀ structures through the Tkatchenko-Scheffler method with iterative Hirshfeld partitioning correction [12].

* Corresponding author.

E-mail address: lmарques@ua.pt (L. Marques).

<https://doi.org/10.1016/j.mtcomm.2020.100906>

Received 1 November 2019; Accepted 7 January 2020

Available online 21 January 2020

2352-4928/ © 2020 Elsevier Ltd. All rights reserved.

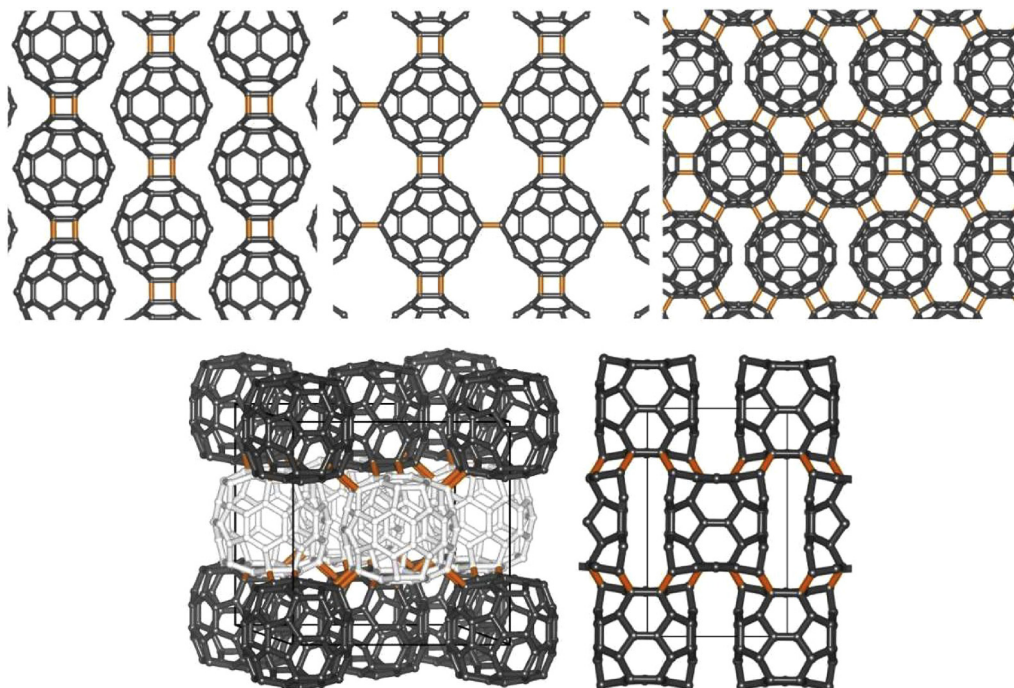


Fig. 1. Polymerized C_{60} structures: (top panel) 1D, 2D-T, 2D-R; (bottom panel) 3D AuCuI-type, on the left, and 3D cuboidal, on the right.

Optimizations were stopped once all forces were smaller than 0.01 eV/Å.

DOS calculations were performed using a k-point grid of $6 \times 6 \times 6$ for the low-dimensional polymers, $12 \times 12 \times 10$ for the 3D AuCuI-type structure and $8 \times 8 \times 8$ for the 3D cuboidal structure. An energy cutoff of at least 400 eV was employed.

Bulk moduli of the different structures were obtained by fitting the optimized volumes per molecule at different pressures with the third order Birch-Murnaghan equation of state. The molecular volumes were calculated at different pressures employing the same method of structural optimization mentioned above.

3. Results and discussion

Fig. 1 shows the crystal structures of 1D, 2D and 3D C_{60} polymers. Note that there are two 2D polymers, the first one, denoted 2D-T, has tetragonal or pseudo-tetragonal symmetry and the second one, denoted 2D-R, has rhombohedral symmetry. As shown in Table 1, the preparation of polymers with increased dimensionality, that is, with increased polymerization degree, require higher pressures. Table 1 also shows the cell constants obtained from full structural relaxations and their comparison with experimental values. Their agreement improved by taking

into account Van der Waals interactions in the calculation. Nevertheless, a poor agreement remains for the c cell constant of the 1D polymer. The calculated 3D AuCuI-type structure is the ordered analogue of the experimental disordered fcc 3D polymer, in which alternating planes stacked along the c axis are populated with molecules adopting one of the two standard orientations. Considering the experimental cell constants referred to the body centered tetragonal setting one gets $a = b = 9.32 \text{ \AA}$ and $c = 13.19 \text{ \AA}$ ($a = b = c = 13.19 \text{ \AA}$, in the fcc setting), which compares relatively well with calculated values $a = b = 9.32 \text{ \AA}$ and $c = 12.87 \text{ \AA}$. For the cuboidal 3D structure, in which the molecules strongly deform into cuboid-shape, the relaxed cell constants agree with identical DFT calculations [13]. However, the agreement with experiment is quite poor and that should indicate that the structural model considered is not the ultimate one.

Atoms involved in polymeric bonds change their hybridization from sp^2 to sp^3 . Thus, increasing the number of polymeric bonds imply increasing the number of sp^3 carbon atoms and, naturally, they occur in largest number on 3D phases, particularly on cuboidal polymer. Note that the 3D polymerized structures exhibit new bonding types, other than the 66/66 2 + 2 cycloaddition characteristic of low-dimensional polymers. The 3D AuCuI-type structure has 2 + 2 cycloaddition bonds originating from a reaction between single intramolecular bonds and

Table 1

DFT optimized cell constants of polymerized C_{60} structures compared to experimental ones. The total energies are given with respect to the total energy of graphite. Pressure synthesis and experimental cell constants were retrieved from [4].

	1D	2D-T	2D-R	3D	3D cuboidal
Pressure synthesis (GPa)	1.2-1.5 GPa	2.2-3.5 GPa	5-8 GPa	9-10 GPa	15 GPa
# sp^3 carbons/molecule	4	8	12	16	24
Experimental cell constants (Å)	a = 9.09 b = 9.83 c = 14.72 $\alpha = \beta = \gamma = 90^\circ$	a = 9.03 b = 9.08 c = 15.07 $\alpha = \beta = \gamma = 90^\circ$	a = 9.17 b = 9.17 c = 24.57 $\alpha = \beta = 90^\circ; \gamma = 120^\circ$	a = 9.32 b = 9.32 c = 13.19 $\alpha = \beta = \gamma = 90^\circ$	a = 7.86 b = 8.59 c = 12.73 $\alpha = \beta = \gamma = 90^\circ$
DFT-optimized cell constants (Å)	a = 9.08 b = 10.06 c = 14.38 $\alpha = \beta = \gamma = 90^\circ$	a = 9.02 b = 9.12 c = 15.03 $\alpha = \beta = \gamma = 90^\circ$	a = 9.16 b = 9.16 c = 24.72 $\alpha = \beta = 90^\circ; \gamma = 120^\circ$	a = 9.32 b = 9.32 c = 12.87 $\alpha = \beta = \gamma = 90^\circ$	a = 8.63 b = 8.51 c = 13.15 $\alpha = \beta = \gamma = 90^\circ$
DFT-total energy (eV/atom)	0.3943	0.3922	0.3998	0.6085	0.6886

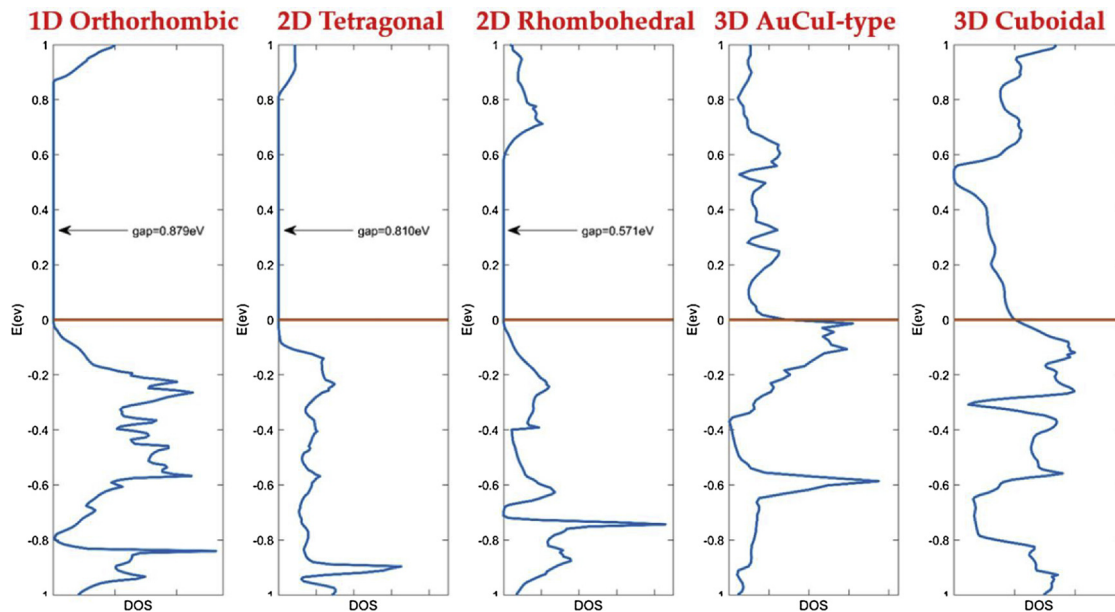


Fig. 2. Calculated DOS for the polymerized structures.

thus named 56/56, while the 3D cuboidal structure has 3 + 3 cycloaddition bonds between the planes initially polymerized and 4 + 4 cycloaddition bonds along the orthorhombic b axis.

Fig. 2 shows the calculated electronic density of states (DOS) for the polymerized structures considered. Their bandgaps are given in Table 2 together with the bandgap of the monomeric fullerite, given for comparison. Its value, 1.5 eV, is underestimated with respect to the experimental gap of 2.3 eV [2]. Therefore, and as expected for this type of calculation, the bandgaps reported here for the low-dimensional polymers are underestimated, although they are higher than those obtained in a previous DFT-LDA study, which also gave a small value of 1 eV for monomeric fullerite [14]. Across the low-dimensional polymer series, the bandgap decreases with the increasing number of polymeric bonds on each molecule, that is, from C₆₀ monomer to 2D-R structure (see Table 2). This trend extends to 3D structures, for which the bandgap closes and a finite number of states at the Fermi level is observed, i.e. metallic behavior. In fact, electron conduction was observed experimentally in the 3D cuboidal phase, although the rising of conductivity with temperature, attributed to variable range hopping, is in contrast with the metallic behavior.

A wide range of electronic behavior is found across the polymeric structures considered, from semiconducting low-dimensional polymers to metallic 3D polymers. As the formation of polymeric bonds removes

Table 2
Calculated electronic bandgap and bulk moduli for the polymerized structures as a function of the number of sp³ carbon atoms and the volume per molecule.

Polymerized Structure	Bandgap(eV)	# sp ³ carbons/molecule	Volume/molecule (Å ³)	Bulk Modulus (GPa)
0D Van der Walls monomer	1.5	0	711	10 ^a
1D Orthorhombic	0.879	4	657	24 (22 ^b)
2D Tetragonal	0.810	8	618	36 (35 ^b)
2D Rhombohedral	0.571	12	599	55 (45-50 ^a)
3D AuCuI-type	-	16	559	130
3D Cuboidal	-	24	483	178 ^b

^a Experimental values from [3,17–19].

^b DFT calculation from [13].

electronic charge from the cage, this trend should stop at some critical degree of polymerization, when the cage becomes non-conducting. Indeed, the resurgence of semiconducting behavior was observed in a 3D polymer obtained at 15 GPa and 500–600 °C. Unfortunately important disagreements remain between the proposed structural model and experiment and this polymer is not considered here [15].

In order to compute the bulk moduli, structural optimizations at different pressures were performed for each structure. The bulk modulus B₀ was then calculated by fitting the optimized molecular volumes with the Birch-Murnaghan equation of state (EOS), as shown in Fig. 3 [16].

B₀ values obtained for each phase are indicated in Table 2. The experimental bulk modulus B₀ for monomeric fullerite is also indicated for comparison. The bulk moduli calculated for the low-dimensional polymers agree with the experimental values of 22 GPa (1D polymer), 35 GPa (2D-T polymer) and 45–50 GPa (2D-R polymer) [17,18,19]. The 3D polymers, consisting of rigid 3D networks, have bulk moduli noticeably higher. The value of B₀ for the AuCuI-type structure is consistent with the experimental data [20]. The highest B₀ value is displayed, as expected, by the 3D cuboidal polymer, which has the

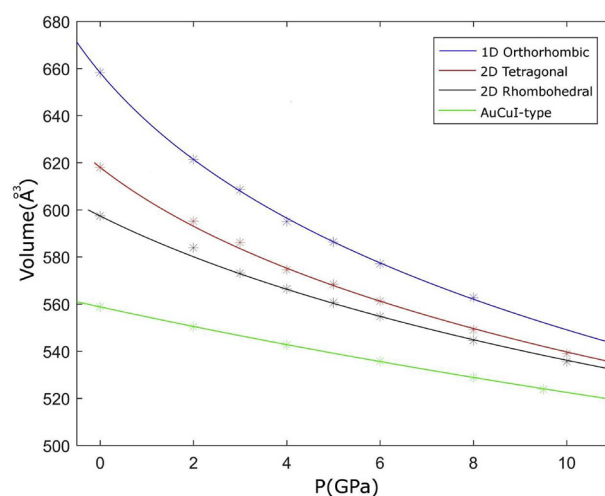


Fig. 3. Birch-Murnaghan EOS fits (lines) to calculated volumes per molecule (asterisks) for the polymerized structures considered.

largest number of sp^3 carbon atoms. Its value shown in the Table 2 was borrowed from similar DFT studies [13].

The increase in the number of polymeric bonds and, concomitantly, in the number of sp^3 carbons, increases the bulk moduli displayed by C_{60} polymers, as expected. This tendency is expected to extend to other 3D polymerized structures having more sp^3 -hybridized atoms than the ones considered here. A 3D C_{60} polymer synthesized at 12.5 GPa and 450 °C, having 60% of sp^3 carbon atoms, a percentage determined from the radial distribution function, displays a very high bulk modulus of 280 GPa [21]. Another 3D polymer, synthesized at 13 GPa and 550 °C, has a B_0 of 288 GPa [22]. An hypothetical cage structure with only sp^3 carbons should have an even larger bulk modulus. These extremely large bulk moduli indicate that the highly polymerized 3D phases are superhard.

4. Conclusions

Polymerized C_{60} structures with varying dimensionalities, 1D, 2D and 3D, were investigated using DFT methods. These polymers display a broad range of electronic properties, from semiconducting to metallic, and of elastic properties, from soft to incompressible, combined with their characteristic low-density. The magnitude of the pressure synthesis can be used to easily control the sp^3/sp^2 carbon ratio and, thus, to prepare the polymer phase having the desired physical properties. Although these materials have remained in the shadow in the field of carbon nanomaterials, they show many potential applications and clearly deserve a much more intense research effort. Novel polymerized structures, with an even higher degree of polymerization, are much awaited, which would extend the range of the outstanding physical properties presented here.

Declaration of Competing Interest

The authors declare that they have no known competing financial interests or personal relationships that could have appeared to influence the work reported in this paper.

Acknowledgements

This work was supported by the projects POCI-01-0145-FEDER-031326 financed by the Portuguese Foundation for Science and Technology (FCT) and co-financed by FEDER. CICECO-Aveiro Institute of Materials, FCT Ref. UID/CTM/50011/2019, financed by national funds through the FCT/MCTES and IF/00894/2015 finances by FCT. J. Laranjeira acknowledges a PhD grant from FCT (SFRH/BD/139327/2018)

References

- [1] P. Heiney, Structure, dynamics and ordering transition of solid C_{60} , *J. Phys. Chem. Solid.* 53 (1992) 1333–1352, [https://doi.org/10.1016/0022-3697\(92\)90231-2](https://doi.org/10.1016/0022-3697(92)90231-2).
- [2] W. Andreoni, P. Giannozzi, Structural and Electronic Properties of C_{60} and C_{60} Derivatives in the Solid State: Calculations Based on Density-functional Theory, the Physics of Fullerene-based and Fullerene-related Materials, Kluwer Academic Publishers, 2000, pp. 291–329, <https://doi.org/10.1007/978-94-011-4038-6>.
- [3] a) L. Pintschovius, O. Blaschko, G. Krexner, N. Pyka, Bulk modulus of C_{60} studied by single-crystal neutron diffraction, *Phys. Rev. B* 59 (1999) 11020–11026, <https://doi.org/10.1103/PhysRevB.59.11020>;
- b) O. Yagafarov, E. Gromintskaia, A. Lyapin, V. Brazhkin, M. Kondrin, Elasticity of molecular fullerite C_{60} under pressure, Fullerenes, Nanotubes and carbon nanostructures. 16 (2008) 499–506, <https://doi.org/10.1080/15363830802282458>.
- [4] M. Álvarez-Murga, J. Hodeau, Structural phase transitions of C_{60} under high-pressure and high-temperature, *Carbon* 82 (2015) 381–407, <https://doi.org/10.1016/j.carbon.2014.10.083>.
- [5] M. Núñez-Regueiro, L. Marques, J. Hodeau, O. Bethoux, M. Perroux, Polymerized fullerite structures, *Phys. Rev. Lett.* 74 (1995) 278–281, <https://doi.org/10.1103/PhysRevLett.74.278>.
- [6] V. Blank, S. Buga, G. Dubitsky, N. Serebryanaya, M. Popov, B. Sundqvist, High-pressure polymerized phases of C_{60} , *Carbon* 36 (1998) 319–343, [https://doi.org/10.1016/S0008-6223\(97\)00234-0](https://doi.org/10.1016/S0008-6223(97)00234-0).
- [7] V. Brazhkin, A. Lyapin, S. Popova, Y. Klyuev, A. Naletov, Mechanical properties of the 3D polymerized, sp^2 - sp^3 amorphous, and diamond-plus-graphite nanocomposite carbon phases prepared from C_{60} under high pressure, *J. Appl. Phys.* 84 (1998) 219–226, <https://doi.org/10.1063/1.368021>.
- [8] a) J. Laranjeira, L. Marques, M. Mezouar, M. Melle-Franco, K. Strutyński, Bonding frustration in the 9.5 GPa fcc polymeric C_{60} , *Phys. Stat. Sol. RRL* 11 (2017) 1700343, <https://doi.org/10.1002/pssr.201770365>;
- b) J. Laranjeira, L. Marques, N. Fortunato, M. Melle-Franco, K. Strutyński, M. Barroso, Three-dimensional C_{60} polymers with ordered binary-alloy-type structures, *Carbon* 137 (2018) 511–518, <https://doi.org/10.1016/j.carbon.2018.05.070>.
- [9] S. Yamanaka, A. Kubo, N. Kini, K. Inumaro, K. Komaguchi, T. Inoue, T. Irifune, Electron conductive three-dimensional polymer of cuboidal C_{60} , *Phys. Rev. Lett.* 96 (2006) 076602, <https://doi.org/10.1103/PhysRevLett.96.076602>.
- [10] G. Kresse, J. Furthmüller, Efficient iterative schemes for ab initio total-energy calculations using a plane-wave basis set, *Phys. Rev. B* 54 (1996) 11169–11186, <https://doi.org/10.1103/PhysRevB.54.11169>.
- [11] J. Perdew, K. Burke, M. Ernzerhof, Generalized gradient approximation made simple, *Phys. Rev. Lett.* 77 (1996) 3865–3868, <https://doi.org/10.1103/PhysRevLett.77.3865>.
- [12] G. Kresse, M. Marsman, J. Furthmüller, VASP The Guide, (2016) <https://cms.mpi.univie.ac.at/vasp/vasp/vasp.html>.
- [13] a) J. Yang, J. Tse, T. Iitaka, First-principles investigation on the geometry and electronic structure of the three-dimensional cuboidal C_{60} polymer, *J. Chem. Phys.* 127 (2007) 134906, <https://doi.org/10.1063/1.2771162>;
- b) F. Zipoli, M. Bernasconi, First principles study of three-dimensional polymers of C_{60} : structure, electronic properties, and Raman spectra, *Phys. Rev. B* 77 (2008) 115432, <https://doi.org/10.1103/PhysRevB.77.115432>.
- [14] S. Okada, S. Saito, Electronic structure and energetics of pressure-induced two-dimensional C_{60} polymers, *Phys. Rev. B* 59 (1999) 1930–1936, <https://doi.org/10.1103/PhysRevB.59.1930>.
- [15] S. Yamanaka, N. Kini, A. Kubo, S. Jida, H. Kuramoto, Topochemical 3D polymerization of C_{60} under high pressure at elevated temperatures, *J. Am. Chem. Soc.* 130 (2008) 4303–4309, <https://doi.org/10.1021/ja076761k>.
- [16] F. Birch, Finite elastic strain of cubic crystals, *Phys. Rev.* 71 (1947) 809–824, <https://doi.org/10.1103/PhysRev.71.809>.
- [17] R. Papoular, V. Dimitriev, V. Davydov, A. Rakhmanina, H. Allouchi, V. Agafonov, Study of the orthorhombic polymeric phase of C_{60} under high pressure using synchrotron x-ray powder diffraction, Fullerenes, nanotubes and carbon nanostructures. 18 (2010) 392–395, <https://doi.org/10.1080/1536383X.2010.487438>.
- [18] J. Léger, J. Haines, V. Davydov, V. Agafonov, Irreversible amorphisation of tetragonal two-dimensional polymeric C_{60} under high pressure, *Sol. St. Comm.* 121 (2002) 241–244, [https://doi.org/10.1016/S0038-1098\(01\)00503-8](https://doi.org/10.1016/S0038-1098(01)00503-8).
- [19] V. Levin, V. Blank, V. Prokhorov, J. Soifer, N. Kobelev, Elastic modules of solid C_{60} : measurement and relationship with nanostructure, *J. Phys. Chem. Sol.* 61 (2000) 1017–1024, [https://doi.org/10.1016/S0022-3697\(99\)00357-1](https://doi.org/10.1016/S0022-3697(99)00357-1).
- [20] J. Laranjeira, L. Marques, M. Melle-Franco, K. Strutyński, M. Mezouar, M. Barroso, Three-dimensional fcc C_{60} polymer, *Mater. Lett.X* 4 (2019) 100026, <https://doi.org/10.1016/j.mblux.2019.100026>.
- [21] A. Lyapin, Y. Katayama, V. Brazhkin, Order versus disorder: in situ high-pressure structural study of highly polymerized three-dimensional C_{60} fullerite, *J. Appl. Phys.* 126 (2019) 065102, <https://doi.org/10.1063/1.5111370>.
- [22] a) M. Mezouar, L. Marques, J. Hodeau, V. Pischedda, M. Núñez-Regueiro, Equation of state of an anisotropic three-dimensional C_{60} polymer: the most stable form of fullerene, *Phys. Rev. B* 68 (2003) 193414, <https://doi.org/10.1103/PhysRevB.68.193414>;
- b) L. Marques, M. Mezouar, J. Hodeau, M. Núñez-Regueiro, N. Serebryanaya, V. Ivdenko, V. Blank, G. Dubitsky, Debys-Scherrer ellipses from 3D fullerene polymers: An anisotropic pressure memory signature, *Science* 283 (1999) 1720–1723, <https://doi.org/10.1126/science.283.5408.1720>.

9.2 A8 - Reentrant semiconducting behavior in polymerized fullerites with increasing sp^3 content

Reentrant semiconducting behavior in polymerized fullerites with increasing sp^3 content

Jorge Laranjeira,^{1,*} Leonel Marques*,¹ Manuel Melle-Franco,² and Karol Strutyński²

¹*Departamento de Física and CICECO, Universidade de Aveiro, 3810-193 Aveiro, Portugal*

²*Departamento de Química and CICECO, Universidade de Aveiro, 3810-193 Aveiro, Portugal*

(Dated: February 28, 2023)

Density functional theory calculations with the hybrid Heyd–Scuseria–Ernzerhof (HSE) functional were used to study the electronic structure of polymerized fullerites, ranging from one-dimensional to three-dimensional polymerized structures. We found that the bandgap across these structures decreases with the rise of the number of sp^3 carbons until metallic behavior is observed. Further increase of the sp^3 carbon content induces a reopening of the bandgap, showing a reentrant semiconducting behavior in this class of materials.

Keywords: DFT Calculations, Carbon Nanostructures, Bandgap Engineering

INTRODUCTION

The electronic bandgap is responsible for the optical and electronic properties of materials, making it an important parameter to tune in view of possible applications [1, 2]. Bandgap engineering of materials is, therefore, a powerful tool to obtain new physical and chemical properties with possible high technological impact [3, 4].

Carbon materials present distinct electronic properties, from semi-metallic behavior in graphite [5, 6] to the wide bandgap in diamond [7]. Several other carbon allotropes such as peapods, nanotubes and nanoribbons, present a wide range of electronic bandgaps, depending on their structures [8–10]. Solid C_{60} (fullerite) is a semiconductor and its bandgap decreases under pressure up to 20 GPa, followed by a sudden increase on further compression [11–14]. Saito and coworkers suggested that the initial bandgap decrease is the result of the increasing interaction between π electrons belonging to neighboring molecules induced by the reduction of the molecular distance [11]. Conversely, the sudden rise of the bandgap at 20 GPa is due to the molecular collapse with the formation of an amorphous carbon phase having a high content of sp^3 hybridized atoms [11–13]. Similar behavior has been recently observed in *m*-xylene solvated C_{60} [15].

A family of carbon allotropes that have been less studied regarding the electronic structure are the fullerene C_{60} polymers. Most of these phases have been produced recurring to high-pressure high-temperature (HPHT) treatments of fullerite monomer. Low-dimensional polymers are formed at pressures below 8 GPa. In particular, one-dimensional (1D) orthorhombic polymer and two two-dimensional (2D), tetragonal and rhombohedral, polymers are synthesized with all of them containing 66/66 2+2 cycloaddition bonds, with van der Waals interactions remaining in the non-bonding

directions [16, 17]. Above 8 GPa, three-dimensional (3D) polymerized phases are synthesized [17–23]. Although several 3D phases were reported, very few crystalline structures have been proposed so far. A face-centered cubic (fcc) 3D polymer was synthesized at 9.5 GPa and 550 °C, where the molecules, being in either one of two C_{60} standard orientations, are bonded through 56/56 2+2 cycloaddition, the cubic structure resulting from the frustrated arrangement of these bonds in the fcc lattice [18, 19]. A cuboidal 3D polymerized phase was synthesized by subjecting the 2D tetragonal polymer to 15 GPa and 600 °C; its proposed orthorhombic structure involves 6/6 3+3 cycloadditions bonds between neighboring molecules belonging to adjacent (a,b) planes and double 66/66 4+4 cycloadditions along the shortest lattice parameter of the (a,b) planes [21]. At the same HPHT conditions, an fcc 3D polymer was synthesized from the fullerite monomer, but it was proposed that it results from the disordering of rhombohedral domains, in which hexagonal planes of molecules are bonded via 5/5 3+3 cycloadditions and 56/65 2+2 cycloadditions are formed between these hexagonal planes [22].

In addition to these fullerite structures, a computationally hypothesized polymerized fullerite clathrate [24] is also to be mentioned since its lattice parameter matches that of an fcc 3D polymer obtained at 12.5 GPa by Brazhkin and coworkers [25]. This clathrate structure is constructed by bonding each molecule, adopting a standard orientation, to the twelve nearest neighbors in the fcc lattice through double 5/5 2+3 cycloaddition bonds.

Here, we report a systematic electronic structure calculations of polymerized fullerite structures ranging from the 1D to 3D polymers, expanding our previous study [26] and performing more accurate electronic structure calculations via the Heyd–Scuseria–Ernzerhof (HSE) hybrid functional [27]. We show that initially, the bandgap progressively decreases with the increasing number of sp^3 carbons until metallic behavior is observed. Then, a further increase in the number of the sp^3 atoms leads to a bandgap reopening in a reentrant behavior, fundamentally similar to the

* jorgelaranjeira@ua.pt, lmarques@ua.pt

behaviour observed with oxygen functionalized carbon nanotubes [28].

METHODS

Polymerized fullerite structures were first optimized without any constrain with the Perdew–Burke–Ernzerhof (PBE) [29, 30] exchange-correlation functional augmented with the classical D3 dispersion term [31] with Becke–Johnson damping and a 6-31G(d,p) atomic Gaussian basis set, PBE-6-31G(d,p)-D3, as implemented in CRYSTAL17 [32]. For this, the Coulomb and exchange infinite lattice series is controlled by five numerical thresholds (Ti), which were set to 12 (T1-T4) and 24 (T5). The convergence threshold for the self-consistent field (scf) cycle was set to be smaller than 10^{-8} Hartree and an energy difference of 10^{-4} Hartree was enforced between consecutive geometric steps. A k-point grid with at least $6 \times 6 \times 6$ points was used for the calculations in bulk systems. In addition, when we computed lower dimensionality systems, namely 1D or 2D self-standing chains, a minimum of 6 points along each periodic direction was used.

As PBE functional systematically underestimates experimental bandgaps [33, 34], the electronic density of states (DOS) and band structures calculations were computed at the HSE06-6-31G(d,p) level [27], which produces improved bandgap values yet with at a feasible computational cost [34]. A denser $24 \times 24 \times 24$ Monkhorst-Pack [35] grid and a lower scf convergence threshold, 10^{-10} Hartree, were employed for these calculations. Then, band structure calculations were performed with paths from AFLOW [36].

RESULTS AND DISCUSSION

Table I gives a summary of the optimized structural properties and electronic bandgap values of the polymerized fullerites considered in this study. The optimized polymerized structures are shown in figure S1; their Wyckoff positions are also given in the Supporting Information (SI), section B. The van der Waals fullerite monomer at room conditions is also considered, mainly as a reference, and for simplicity is denoted as 0D [37]. The 3D-AuCu-type and 3D-CuPt-type are ordered structures that have been proposed to be present in the frustrated fcc 3D polymer synthesized at 9.5 GPa and that are described in detail elsewhere [38].

The electronic band structures and densities of states (DOS) for all the polymerized structures being studied are presented in section C of the SI. The low dimensionality polymers bandgap show a strong dependence on the distance between polymeric chains (or layers). We have explicitly investigated the influence of these van der Waals distances on the calculated bandgap for the 1D orthorhombic polymer. Whenever

the distance between the chains is reduced, the bandgap is also reduced and, similarly, when the distance between chains increases the bandgap increases, this being illustrated in figure S11. Moreover, the electronic properties also depend on the orientation adopted by the chains but this was not investigated in this study [17]. To further evaluate the extent to which the van der Waals description influences the bandgaps of low-dimensional polymers, they were computed for the corresponding self-standing polymers, namely: for one molecule, one chain, one quadratic polymerized plane and one hexagonal polymerized plane. The bandgap evolution with the number of sp^3 carbons in the self-standing polymers is shown at the top of figure 1. There is an increase in the bandgaps of the self-standing chains with respect to the bulk system but this difference is reduced when the number of van der Waals interactions decreases. Thus, for the 1D polymerized structure, this has a high impact with its bandgap, 1.85 eV, being now larger than that of the 2D tetragonal polymerized structure, 1.55 eV. This indicates that the smaller bandgap in the bulk 1D polymer is probably an artifact from the chosen theory level description of the van der Waals interaction used here and, indeed, the bandgap decreases monotonously with the number of sp^3 carbons in the low-dimensional polymers. Furthermore, it also allows one to conclude that the observed reduction in the electronic bandgaps of the low-dimensional polymers with the number sp^3 atoms rise is primarily a consequence of the reduction of the intermolecular distance induced by the formation of covalent bonds between the monomers. The reduction in the intermolecular distance leads to a stronger interaction of the molecular wave functions of neighboring molecules leading to an increased dispersion of the bands and the concomitant reduction in the bandgap. In fact, a similar effect has been observed experimentally in compressed monomeric C_{60} at room temperature [11].

The binary-alloy type structures, 3D-CuPt-type and 3D-AuCu-type, that have been proposed as ordered configurations of the frustrated 3D fcc polymer synthesized at 9.5 GPa, both display metallic behavior at the PBE level [38]. Relevantly, the 3D-CuPt-type polymerized structure has the same number of sp^3 carbons as the 2D-rhombohedral polymerized structure but displays a much smaller bandgap. This is due to the fact that the bonding in this structure being three-dimensional yields a higher band dispersion and a lower molecular volume than that of the 2D-rhombohedral structure, which in turn, induces a stronger interaction of the molecular wave functions, as discussed above.

The 3D-AuCu-type structure, where each molecule is bonded to eight nearest neighbors and has sixteen sp^3 carbons, displays metallic behavior. It is noteworthy to compare this electronic behavior with that of monomeric C_{60} fullerite compressed at 20 GPa at room temperature, which has about the same volume but is a low-gap semiconductor with a gap of 0.35 eV [14]. This simple comparison indicates that the sp^3 bonding states, absent

TABLE I. Optimized lattice parameters and volume per molecule for the polymerized fullerite structures, at the PBE-6-31G(d,p)-D3 level. The space group of each structure, number of sp^3 carbons per molecule and the electronic bandgap for each structure calculated at the HSE-6-31G(d,p) theory level, are also presented. The hexagonal 3R lattice parameters are used for the rhombohedral structures.

structure	space group	DFT cell constants (Å)	$V(\text{Å}^3/C_{60})$	# sp^3 atoms/ C_{60}	Bandgap (eV)
0D	$Fm\bar{3}$	a=14.08 b=14.08 c=14.08 $\alpha = \beta = \gamma = 90$	698.26	0	1.5407
1D	Immm	a=9.11 b=10.29 c=13.99 $\alpha = \beta = \gamma = 90$	655.68	4	1.2580
2D-tetragonal	Immm	a=9.05 b=9.15 c=14.91 $\alpha = \beta = \gamma = 90$	617.96	8	1.3771
2D-rhombohedral	$R\bar{3}m$	a=9.19 b=9.19 c=24.65 $\alpha = \beta = 90; \gamma = 120$	601.45	12	1.1479
3D-CuPt-type	$R\bar{3}c$	a=9.45 b=9.45 c=2x22.34 $\alpha = \beta = 90; \gamma = 120$	576.22	12	0.0628
3D-AuCu-type	$P4_2/mnm$	a=9.27 b=9.27 c=12.87 $\alpha = \beta = \gamma = 90$	553.10	16	–
3D-cuboidal	Immm	a=8.50 b=8.62 c=13.16 $\alpha = \beta = \gamma = 90$	481.92	24	–
3D-rhombohedral	$R\bar{3}$	a=8.92 b=8.92 c=22.35 $\alpha = \beta = 90; \gamma = 120$	513.48	24	1.3796
3D-clathrate	$Pm\bar{3}$	a=12.41 b=12.41 c=12.41 $\alpha = \beta = \gamma = 90$	478.31	48	1.2806

in the compressed C_{60} , are fundamental for closing the bandgap in polymerized structures driving its metallic behavior. This is further corroborated by the results shown in figure S12 where the bandgap of the monomeric fullerite closes at a lattice length of 11.9 Å. However, this gap closure, and the corresponding metallicity, cannot be observed experimentally on compressions at room temperature because the cages collapse into an amorphous phase at 20 GPa for a lattice parameter of about 13 Å [12]. In the frustrated 3D fcc polymer each molecule has on average 7.6 bonded near-neighbors, indicating that the molecules adopted more frequently the 3D-AuCu-type configuration (eight bonded nearest-neighbors) than the 3D-CuPt-type configuration (six bonded nearest-neighbors) [19]. Considering this, a metallic behavior would be expected for this 3D fcc phase prepared at 9.5 GPa and 550 °C and, indeed, it was actually experimentally found by Buga and coworkers

[39, 40].

Another 3D polymerized fullerite showing metallic behavior is the so-called cuboidal structure [21]. However, the 3D-rhombohedral polymerized structure is semiconducting, despite having the same number of sp^3 carbons [22]. The optimized 3D-cuboidal structure has a smaller volume per molecule, which is an important parameter to induce metallic behavior through a strong interaction of wave functions from neighboring molecules. These two 3D polymerized structures have been proposed for the C_{60} polymers synthesized from the 2D tetragonal polymer compressed at 15 GPa and 600 °C (the 3D-cuboidal) and from the fullerite monomer subjected to the same conditions (the 3D-rhombohedral) [21, 22]. Yet, the lattice parameters from calculations are significantly different from the experimental ones for both cases, as it was thoroughly discussed for the 3D-cuboidal case [41, 42]. Nevertheless, the metallic nature of the 3D-cuboidal

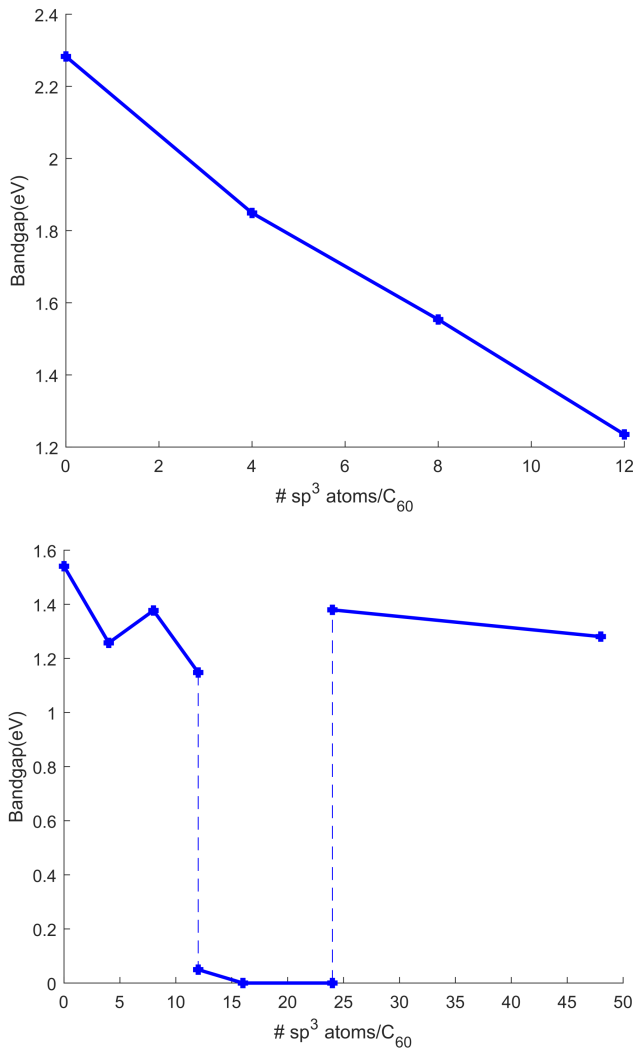


FIG. 1. Top panel: electronic bandgap of the polymerized fullerite structures against the number of sp^3 carbons on each molecule for the self-standing low-dimensional polymers. Bottom panel: same plot for the bulk polymeric systems. The blue line serves only as a guide to the eye.

polymerized phase and the semiconducting behavior of the 3D-rhombohedral polymer were experimentally observed [21, 22].

The last polymerized structure being addressed is the polymerized fullerite clathrate, 3D-clathrate, where most of the atoms are sp^3 - hybridized, forty-eight out of sixty. Thus, likely the σ -like states start to dominate the electronic structure while the few remaining π -like states are highly localized contributing to the semiconducting nature of this structure [24]. It is to be noted that other polymerized structures with higher sp^3 content, having fifty-two, fifty-six and sixty sp^3 -hybridized atoms per molecule, proposed by Burgos and coworkers [43] are also semiconductors, confirming thus the reentrant

semiconducting behavior in polymerized fullerites. These polymerized structures were not investigated by us because they are derived from the body-centered cubic packing, while the experimental structures are based on the fcc packing.

The overall electronic behavior of the polymerized fullerite structures is given in figure 1, bottom panel, where their bandgaps are plotted against their number of sp^3 carbons on each molecule. Initially, the bandgap decreases with the rise of sp^3 -hybridized atoms until its closure, as has been discussed. However, further increase in the number of sp^3 atoms, and concomitantly on the number of polymeric bonds, drives the electronic structure to become dominated by σ -like states, while the remaining π -like states become highly localized, leading to a reopening of the bandgap and a reentrant semiconducting behavior. Although the evolution of the electronic bandgap is dominated by the number of sp^3 carbons on each molecule, the molecular volume alone is also seen to influence the electronic behavior. Polymerized structures with the same number of sp^3 carbons show a considerable reduction in the bandgap, or even its closure, for structures with smaller volumes.

CONCLUSION

Polymerized fullerite structures present a wide range of electronic behavior from semiconducting to metallic. This behavior is clearly dependent on the number of sp^3 hybridized carbons present in each structure.

The initial reduction of the bandgap with the increment in the number of sp^3 carbons should be a consequence of the C_{60} intermolecular distance reduction, and concomitantly of the increase in the interaction of the wave functions of neighboring molecules. The bandgap closure is seen to be also determined by the formation of a 3D network of polymeric bonding. Increasing further the number of sp^3 carbons induces a bandgap reopening in a reentrant fashion. This reentrant semiconducting behavior is due to the fact that σ -like states start to dominate the electronic structure, while the remaining π -like states become highly localized.

ACKNOWLEDGMENTS

This work was developed within the scope of the project CICECO-Aveiro Institute of Materials, UIDB/50011/2020, UIDP/50011/2020 & LA/P/0006/2020, financed by national funds through the FCT/MCTES (PIDDAC) and IF/00894/2015 financed by FCT. J. Laranjeira acknowledges a PhD grant from FCT (SFRH/BD/139327/2018).

-
- [1] M. Peplow, *Nature* **503**, 327 (2013).
- [2] M. Kang, B. Kim, S. Ryu, S. Jung, J. Kim, L. Moreschini, C. Jozwiak, E. Rotenberg, A. Bostwick, and K. Kim, *Nano Lett.* **17**, 1610 (2017), pMID: 28118710.
- [3] F. Capasso, *Science* **235**, 172 (1987).
- [4] V. Zeghbroeck, *Principles of Semiconductor Devices and Heterojunctions* (Prentice Hall PTR, 2007).
- [5] S. Trickey, F. Müller-Plathe, G. Diercksen, and J. Boettger, *Phys. Rev. B* **45**, 4460 (1992).
- [6] B. Partoens and F. Peeters, *Phys. Rev. B* **74**, 075404 (2006).
- [7] R. Strong, C. Pickard, V. Milman, G. Thimm, and B. Winkler, *Phys. Rev. B* **70**, 045101 (2004).
- [8] M. Otani, S. Okada, and A. Oshiyama, *Phys. Rev. B* **68**, 125424 (2003).
- [9] K. An and Y. Lee, *Nano* **1**, 115 (2006).
- [10] V. Barone, O. Hod, and G. Scuseria, *Nano Lett.* **6**, 2748 (2006).
- [11] Y. Saito, H. Shinohara, M. Kato, H. Nagashima, M. Ohkohchi, and Y. Ando, *Chem. Phys. Lett.* **189**, 236 (1992).
- [12] W. Qiu, S. Chowdhury, R. Hammer, N. Velisavljevic, P. Baker, and Y. Vohra, *High Press. Res.* **26**, 175 (2006).
- [13] F. Moshary, N. Chen, I. Silvera, C. Brown, H. Dorn, M. de Vries, and D. Bethune, *Phys. Rev. Lett.* **69**, 466 (1992).
- [14] M. Núñez–Regueiro, P. Monceau, A. Rassat, P. Bernier, and A. Zahab, *Nature* **354**, 289 (1991).
- [15] Z. Wu, G. Gao, J. Zhang, A. Soldatov, J. Kim, L. Wang, and Y. Tian, *Nano Res.* **15**, 3788 (2022).
- [16] M. Núñez–Regueiro, L. Marques, J.-L. Hodeau, O. Béthoux, and M. Perroux, *Phys. Rev. Lett.* **74**, 278 (1995).
- [17] M. Álvarez–Murga and J.-L. Hodeau, *Carbon* **82**, 381 (2015).
- [18] J. Laranjeira, L. Marques, M. Mezouar, M. Melle-Franco, and K. Strutyński, *Phys. status solidi -RRL* **11**, 1700343 (2017).
- [19] J. Laranjeira, L. Marques, M. Mezouar, M. Melle-Franco, and K. Strutyński, *Mater. Lett.: X* **4**, 100026 (2019).
- [20] L. Marques, M. Mezouar, J.-L. Hodeau, M. Núñez-Regueiro, N. Serebryanaya, V. Ivdenko, V. Blank, and G. Dubitsky, *Science* **283**, 1720 (1999).
- [21] S. Yamanaka, A. Kubo, K. Inumaru, K. Komaguchi, N. Kini, T. Inoue, and T. Irifune, *Phys. Rev. Lett.* **96**, 076602 (2006).
- [22] S. Yamanaka, N. Kini, A. Kubo, S. Jida, and H. Kuramoto, *J. Am. Chem. Soc.* **130**, 4303 (2008).
- [23] V. Blank, S. Buga, G. Dubitsky, N. Serebryanaya, M. Popov, and B. Sundqvist, *Carbon* **36**, 319 (1998).
- [24] J. Laranjeira, L. Marques, M. Melle-Franco, K. Strutyński, and M. Barroso, *Carbon* **194**, 297 (2022).
- [25] V. Brazhkin, A. Lyapin, S. Popova, R. Voloshin, Y. Antonov, S. Lyapin, Y. Kluev, A. Naletov, and N. Mel’nik, *Phys. Rev. B* **56**, 11465 (1997).
- [26] J. Laranjeira and L. Marques, *Mater. Today Commun.* **23**, 100906 (2020).
- [27] V. Barone, O. Hod, J. Peralta, and G. Scuseria, *Acc. Chem. Res.* **44**, 269 (2011).
- [28] S.-H. Jhi, S. Louie, and M. Cohen, *Phys. Rev. Lett.* **95**, 226403 (2005).
- [29] J. Perdew, K. Burke, and M. Ernzerhof, *Phys. Rev. Lett.* **77**, 3865 (1996).
- [30] J. Perdew, K. Burke, and M. Ernzerhof, *Phys. Rev. Lett.* **78**, 1396 (1997).
- [31] S. Grimme, S. Ehrlich, and L. Goerigk, *J. Comput. Chem.* **32**, 1456 (2011).
- [32] R. Dovesi, A. Erba, R. Orlando, C. M. Zicovich-Wilson, B. Civalieri, L. Maschio, M. Rérat, S. Casassa, J. Baima, S. Salustro, and B. Kirtman, *WIREs Comput. Mol. Sci.* **8**, e1360 (2018).
- [33] K. Sohlberg and M. Foster, *RSC Adv.* **10**, 36887 (2020).
- [34] P. Borlido, J. Schmidt, A. Huran, F. Tran, M. Marques, and S. Botti, *Npj Comput. Mater.* **6**, 96 (2020).
- [35] H. Monkhorst and J. Pack, *Phys. Rev. B* **13**, 5188 (1976).
- [36] W. Setyawan and S. Curtarolo, *Comput. Mater. Sci.* **49**, 299 (2010).
- [37] R. Fleming, T. Siegrist, P. Marsh, B. Hessen, A. Kortan, D. Murphy, R. Haddon, R. Tycko, G. Dabbagh, A. Mujsce, M. Kaplan, and S. Zahurak, *MRS Proceedings* **206**, 10.1557/PROC-206-691 (1990).
- [38] J. Laranjeira, L. Marques, N. Fortunato, M. Melle-Franco, K. Strutyński, and M. Barroso, *Carbon* **137**, 511 (2018).
- [39] S. Buga, V. Blank, G. Dubitsky, L. Edman, X.-M. Zhu, E. Nyeanchi, and B. Sundqvist, *J. Phys. Chem. Solids* **61**, 1009 (2000).
- [40] S. Buga, V. Blank, N. Serebryanaya, A. Dzwilewski, T. Makarova, and B. Sundqvist, *Diamond and Related Materials* **14**, 896 (2005), proceedings of Diamond 2004, the 15th European Conference on Diamond, Diamond-Like Materials, Carbon Nanotubes, Nitrides and Silicon Carbide.
- [41] F. Zipoli and M. Bernasconi, *Phys. Rev. B* **77**, 115432 (2008).
- [42] J. Yang, J. Tse, and T. Iitaka, *J. Chem. Phys.* **127**, 134906 (2007).
- [43] E. Burgos, E. Halac, R. Weht, H. Bonadeo, E. Artacho, and P. Ordejón, *Phys. Rev. Lett.* **85**, 2328 (2000).

Supporting Information

A. C_{60} Polymeric structures schemes

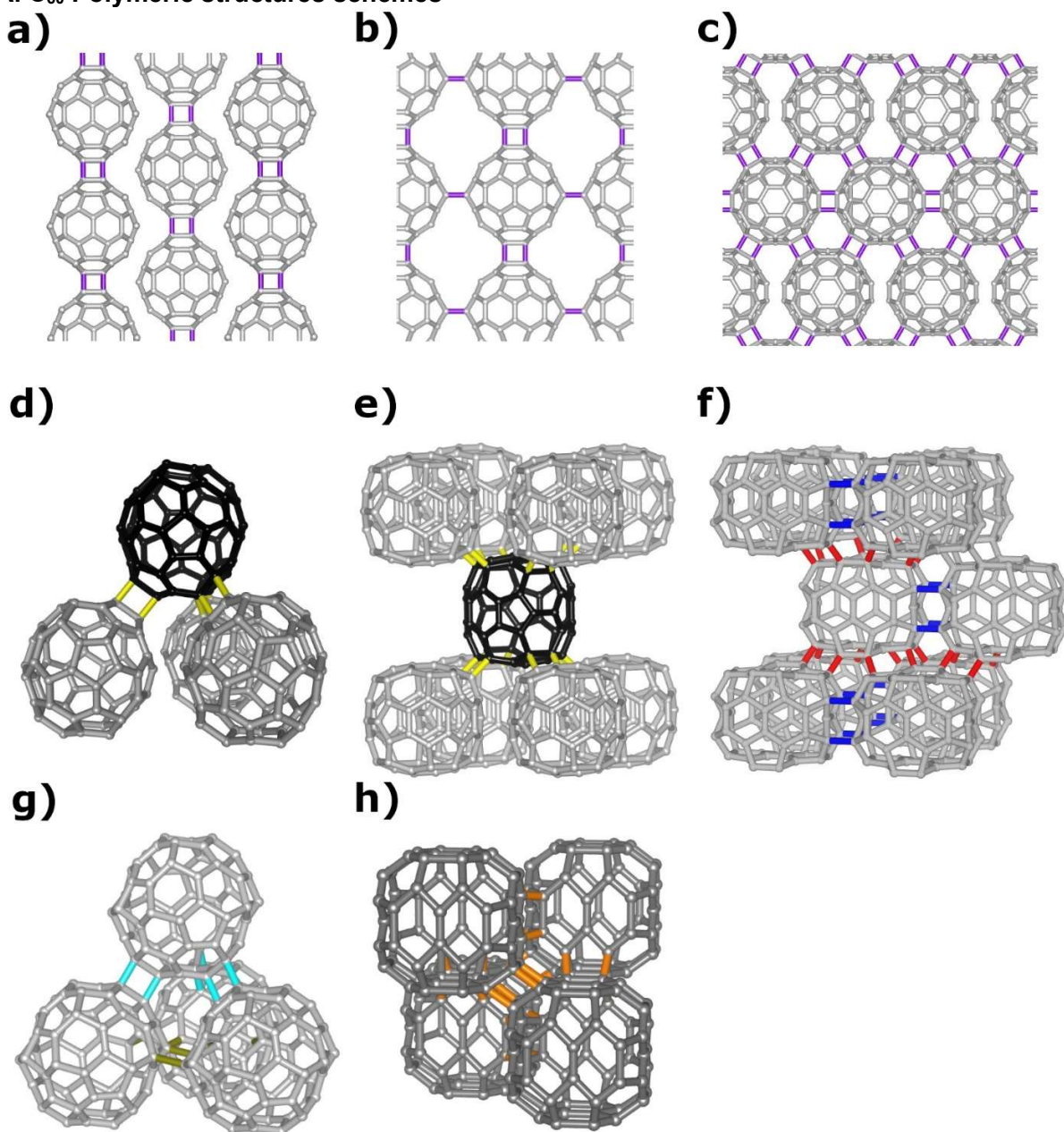


Figure S1. Polymerized C_{60} structures: Figures a, b and c) show the low dimensionality polymers 1D, 2D-tetragonal and 2D-rhombohedral structures, respectively. The 66/66 2+2 cycloaddition intermolecular bonds are drawn in purple; Figures d and e) show the 3D-CuPt-type and the 3D-AuCu-type polymerized structures, respectively, with the 56/56 2+2 cycloaddition shown in yellow and differently oriented molecules represented by different colors (grey and black); f) 3D-cuboidal structure with the double 66/66 4+4 cycloaddition blue-colored bonds within the (a,b) lattice planes and with 6/6 3+3 cycloaddition bonds drawn in red connecting (a,b) planes; g) 3D-rhombohedral structure having 5/5 3+3 cycloaddition green-colored bonds within the (a,b) lattice plane and 56/65 2+2 cycloaddition bonds drawn in light blue connecting (a,b) planes; h) Polymerized fullerite clathrate structure with orange-colored double 5/5 2+3 cycloaddition intermolecular bonds.

B. Wyckoff positions of the polymeric structures optimized at the PBE-6-31G(d,p)-D3 level as implemented in CRYSTAL17

Table S1: Optimized atomic positions of the 0D C₆₀ fullerite in the Fm $\bar{3}$ fcc cell with lattice parameter 14.08 Å.

Atom	x	Y	z	Wyckoff Position
C1	0.00000	0.24854	-0.04995	48h
C2	0.41636	0.21621	0.39844	96i
C3	0.33588	0.18513	0.44830	96i

Table S2: Optimized atomic positions of the 1D-orthorhombic C₆₀ polymer in the Immm orthorhombic cell with lattice parameters a=9.11 Å, b=10.29 Å and c=13.99 Å.

Atom	x	Y	z	Wyckoff Position
C1	0.00000	0.34127	0.05013	8l
C2	-0.07981	0.22607	0.18569	16o
C3	-0.07706	0.00000	-0.24647	8m
C4	-0.12921	0.29729	0.10228	16o
C5	-0.15707	0.11448	0.21478	16o
C6	-0.25372	0.25324	0.05206	16o
C7	-0.28669	0.07203	0.16314	16o
C8	-0.33562	0.14159	0.08425	16o
C9	-0.41294	0.07784	0.00000	8n

Table S3: Optimized atomic positions of the 2D-tetragonal C₆₀ polymer in the Immm orthorhombic cell with lattice parameters a=9.15 Å, b=9.05 Å and c=14.91 Å.

Atom	x	Y	z	Wyckoff Position
C1	0.25304	-0.08036	0.17281	16o
C2	0.33601	-0.13045	0.09734	16o
C3	0.12802	-0.15776	0.20144	16o
C4	0.28609	-0.25313	0.04958	16o
C5	0.08075	-0.28746	0.15320	16o
C6	0.15991	-0.33485	0.07886	16o
C7	0.08786	-0.41227	0.00000	8n
C8	0.00000	-0.07743	0.23170	8l
C9	0.41324	0.00000	0.05358	8m

Table S4: Optimized atomic positions of the 2D-rhombohedral C₆₀ polymer in the R $\bar{3}m$ orthorhombic cell with lattice parameters a= 9.19 Å and c= 24.65 Å.

Atom	x	Y	z	Wyckoff Position
C1	-0.46085	-0.09440	0.01134	36i
C2	-0.39267	-0.11897	0.06419	36i
C3	-0.19042	0.19042	0.07376	18h
C4	-0.22636	0.22636	0.02366	18h
C5	-0.01675	0.27540	0.09507	36i
C6	-0.15686	-0.00176	0.12788	36i

Table S5: Optimized atomic positions of the 3D-CuPt-type C₆₀ polymer in the R $\bar{3}c$ hexagonal cell with lattice parameters a=9.45 Å and c=2x22.35 Å.

Atom	x	Y	z	Wyckoff Position
C1	-0.29318	-0.21429	0.20245	36f
C2	-0.49252	-0.23244	0.24147	36f
C3	-0.23825	-0.15243	0.17240	36f
C4	-0.35953	-0.38487	0.20228	36f
C5	-0.37286	-0.00211	0.20951	36f
C6	0.41196	-0.14261	0.24713	36f
C7	0.49421	0.01546	0.22501	36f
C8	-0.32538	0.04957	0.18044	36f
C9	0.43562	0.07754	0.17206	36f
C10	-0.36659	-0.14238	0.22100	36f

Table S6: Optimized atomic positions of the 3D-AuCu-type C₆₀ polymer in the P4₂/mnm orthorhombic cell with lattice parameters a=9.27 Å and c=12.87 Å.

Atom	x	Y	z	Wyckoff Position
C1	0.05594	0.05594	-0.24503	8j
C2	-0.23903	-0.23903	-0.05568	8j
C3	0.28721	-0.17760	0.00000	8i
C4	0.02251	0.20186	-0.26413	16k
C5	-0.14075	0.31687	-0.38859	16k
C6	0.12608	0.34041	-0.40886	16k
C7	0.15707	0.27892	-0.30455	16k
C8	-0.12887	0.25058	-0.28128	16k
C9	-0.01889	0.36042	-0.44348	16k

Table S7: Optimized atomic positions of the 3D-cuboidal C₆₀ polymer in the Immm orthorhombic cell with lattice parameters a=8.62 Å, b=8.50 Å and c= 13.16 Å.

Atom	x	Y	z	Wyckoff Position
C1	0.10070	0.33614	0.19633	16o
C2	0.17353	0.39781	0.09340	16o
C3	0.30264	0.28343	0.05537	16o
C4	0.13508	0.16536	0.21394	16o
C5	0.20464	0.40641	0.28497	16o
C6	0.33584	0.14174	0.10712	16o
C7	0.35104	0.00000	0.05204	8m
C8	0.00000	0.08244	0.22460	8l
C9	0.07662	-0.36649	0.00000	8n

Table S8: Optimized atomic positions of the 3D-rhombohedral C₆₀ polymer in the R $\bar{3}$ hexagonal cell with lattice parameters a=8.92 Å and c=22.35 Å.

Atom	x	Y	z	Wyckoff Position
C1	0.19421	0.10380	0.15786	18f
C2	0.08942	0.18453	0.14625	18f
C3	0.30531	0.16074	0.21750	18f
C4	0.26651	0.02046	0.26248	18f
C5	0.29994	0.32879	0.30628	18f
C6	0.33986	0.32450	0.24911	18f
C7	0.18171	0.00480	0.32577	18f
C8	-0.48496	-0.16077	0.00910	18f
C9	0.36255	-0.06069	0.26252	18f
C10	0.14477	0.32145	0.10761	18f

Table S3: Optimized atomic positions of the C₆₀-based clathrate structure in the Pm $\bar{3}$ simple cubic cell with lattice parameter 6.21 Å.

Atom	x	Y	z	Wyckoff Position
C1	0.50000	0.34897	0.14222	12k
C2	0.12132	0.50000	0.00000	6g
C3	0.50000	-0.17136	0.29165	12k

C. Electronic structures for the polymerized structures at the HSE-6-31G(d,p) level as implemented in CRYSTAL17

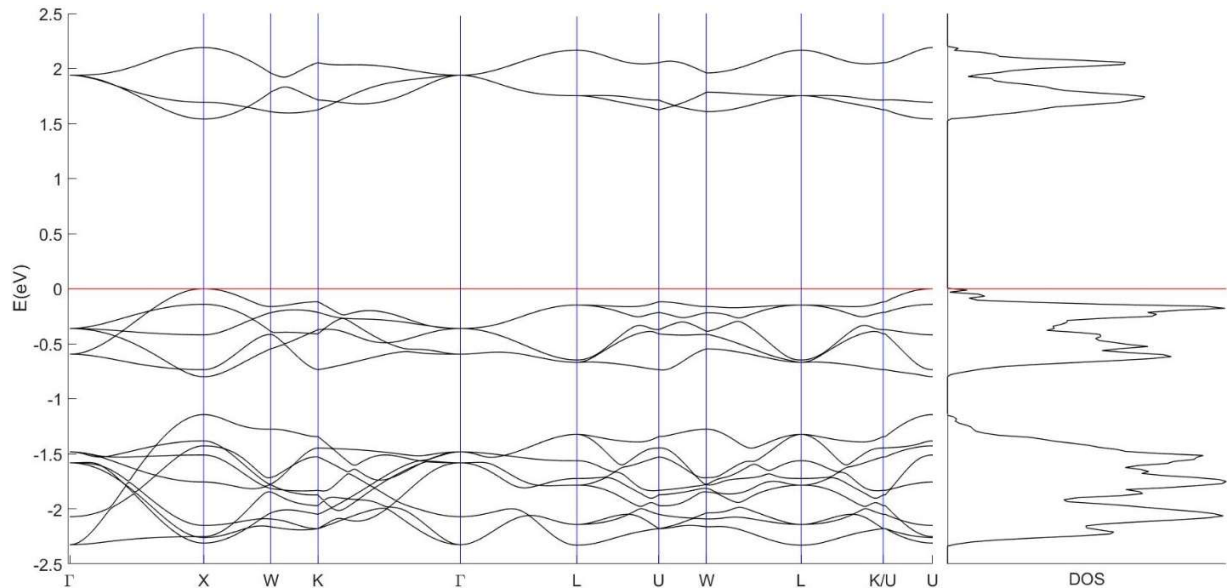


Figure S2. Electronic density of states (right panel) and electronic band structure (left panel) of the van der Waals fullerite C₆₀, 0D. Red line indicates the Fermi level.

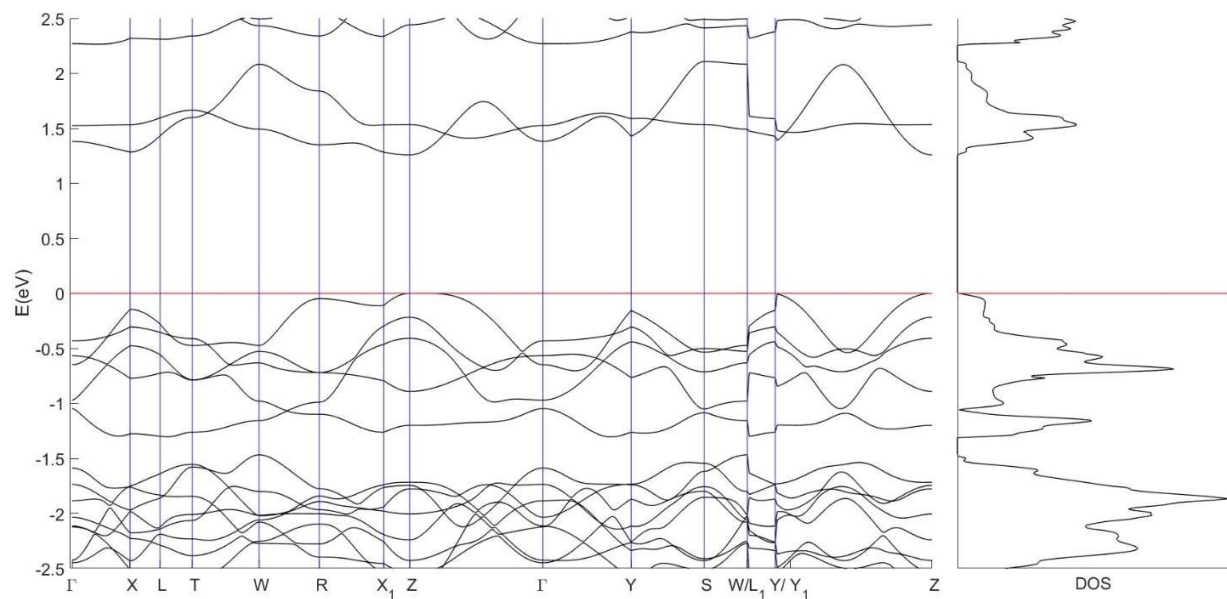


Figure S3. Electronic density of states (right panel) and electronic band structure (left panel) of the 1D orthorhombic C₆₀ polymer. Red line indicates the Fermi level.

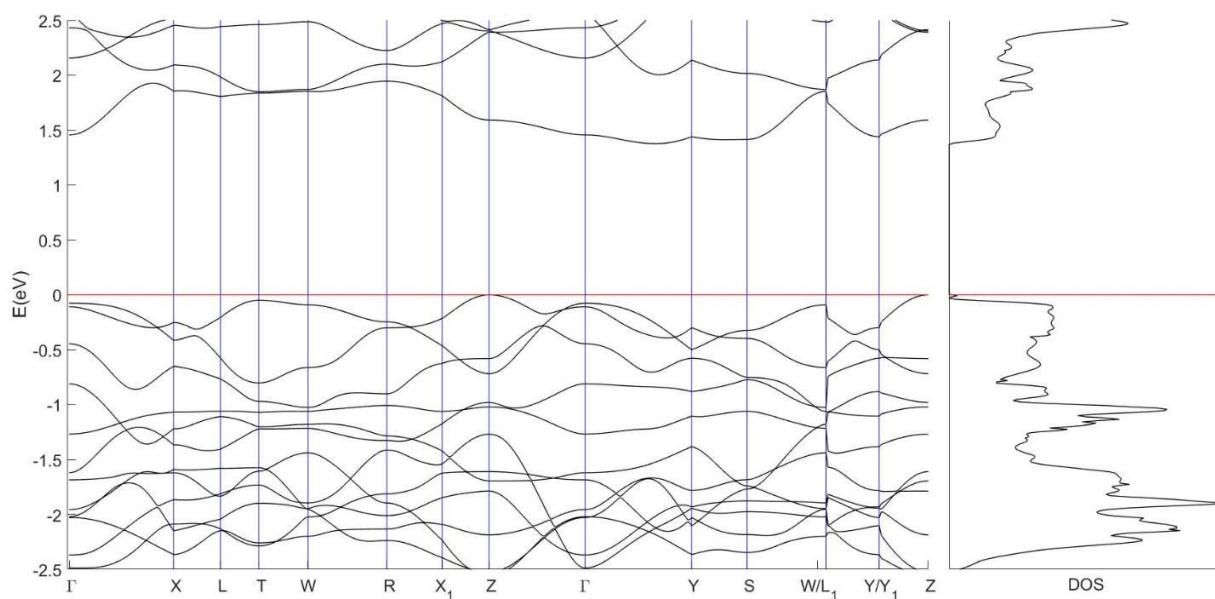


Figure S4. Electronic density of states (right panel) and electronic band structure (left panel) of the 2D tetragonal C_{60} polymer. Red line indicates the Fermi level.

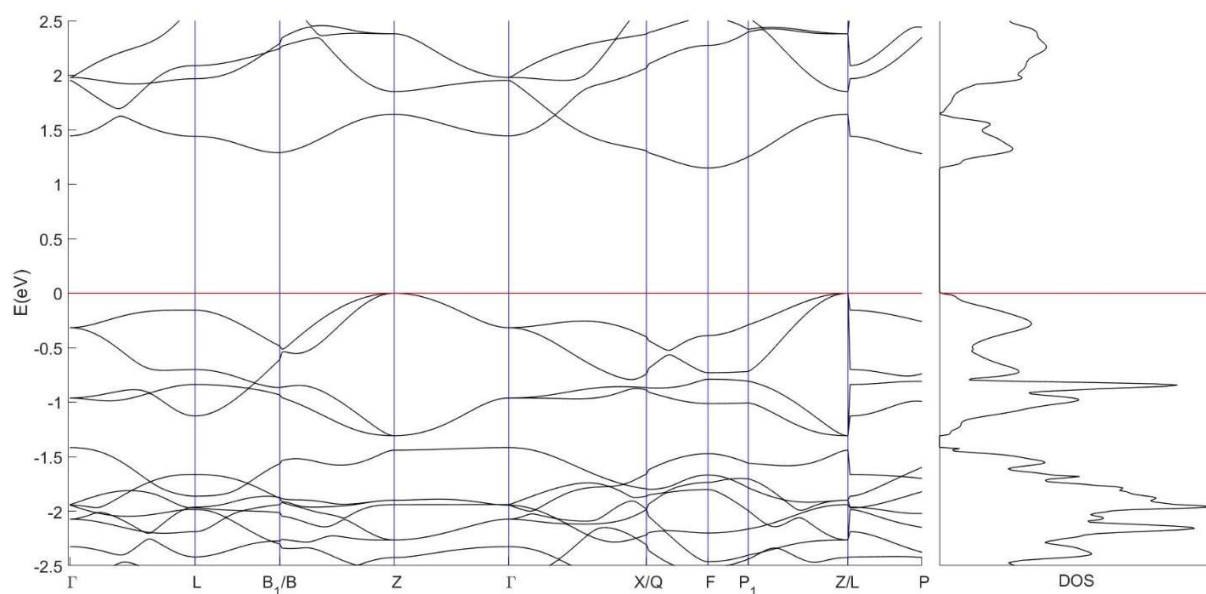


Figure S5. Electronic density of states (right panel) and electronic band structure (left panel) of the 2D rhombohedral C_{60} polymer. Red line indicates the Fermi level.

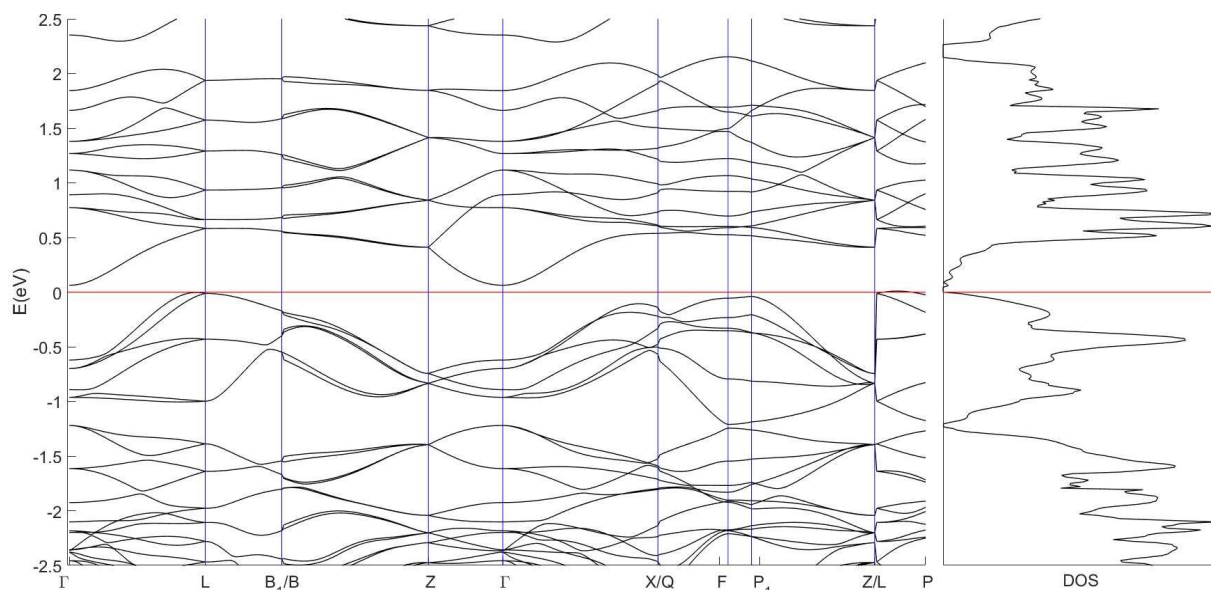


Figure S6. Electronic density of states (right panel) and electronic band structure (left panel) of the 3D-CuPt-type C_{60} polymer. Red line indicates the Fermi level.

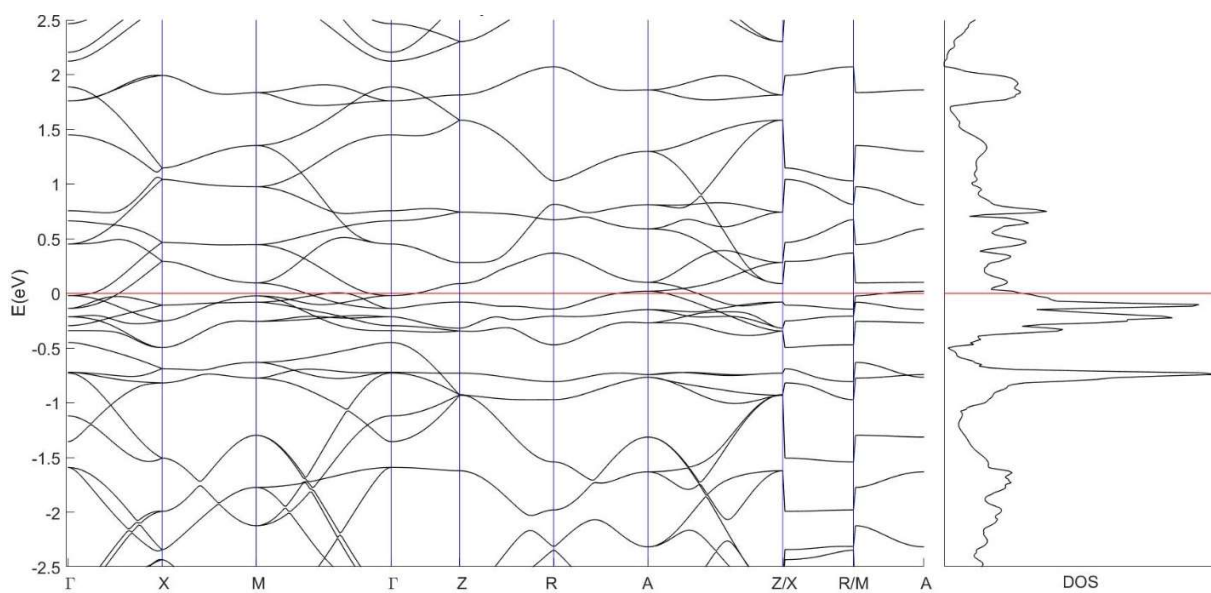


Figure S7. Electronic density of states (right panel) and electronic band structure (left panel) of the 3D-AuCu-type C_{60} polymer. Red line indicates the Fermi level.

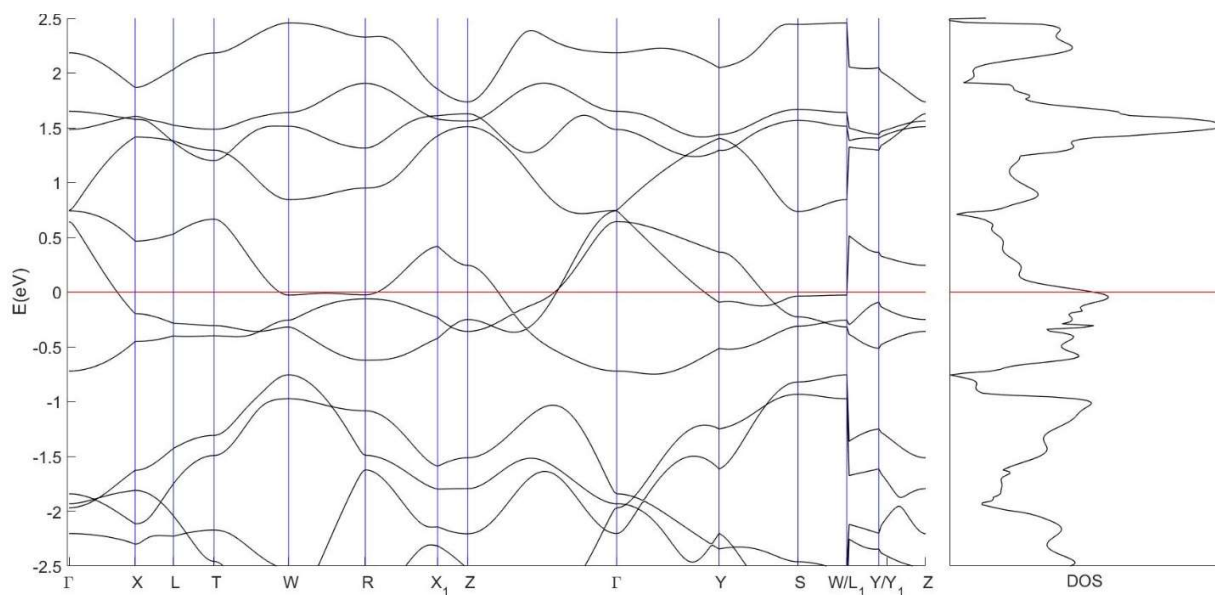


Figure S8. Electronic density of states (right panel) and electronic band structure (left panel) of the 3D-cuboidal C_{60} polymer. Red line indicates the Fermi level.

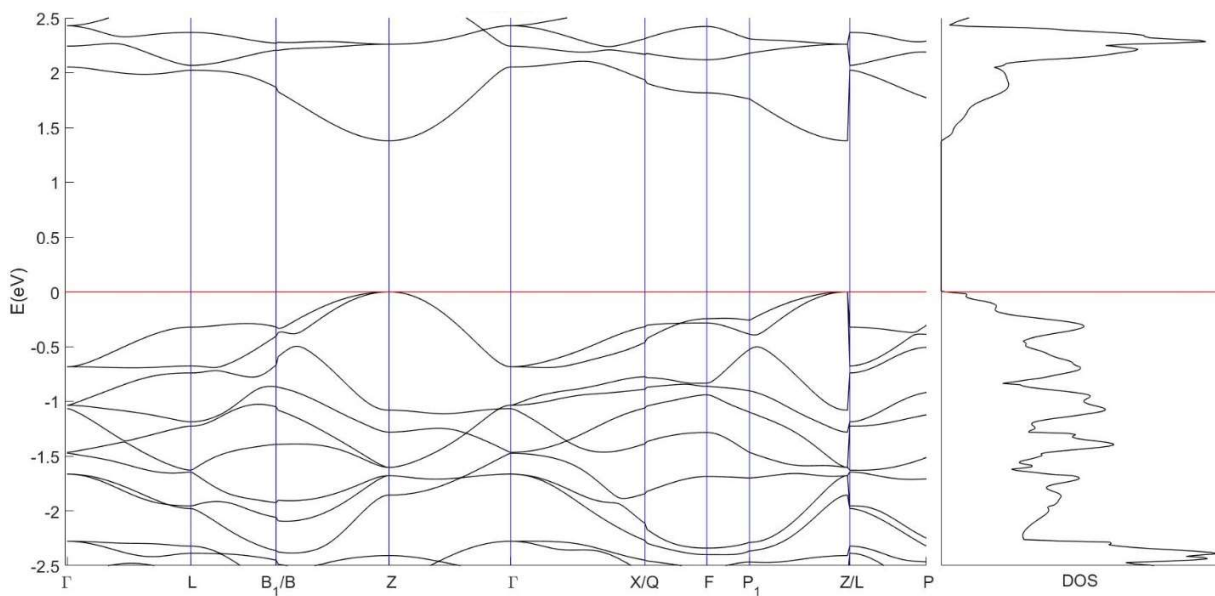


Figure S9. Electronic density of states (right panel) and electronic band structure (left panel) of the 3D-rhombohedral C_{60} polymer. Red line indicates the Fermi level.

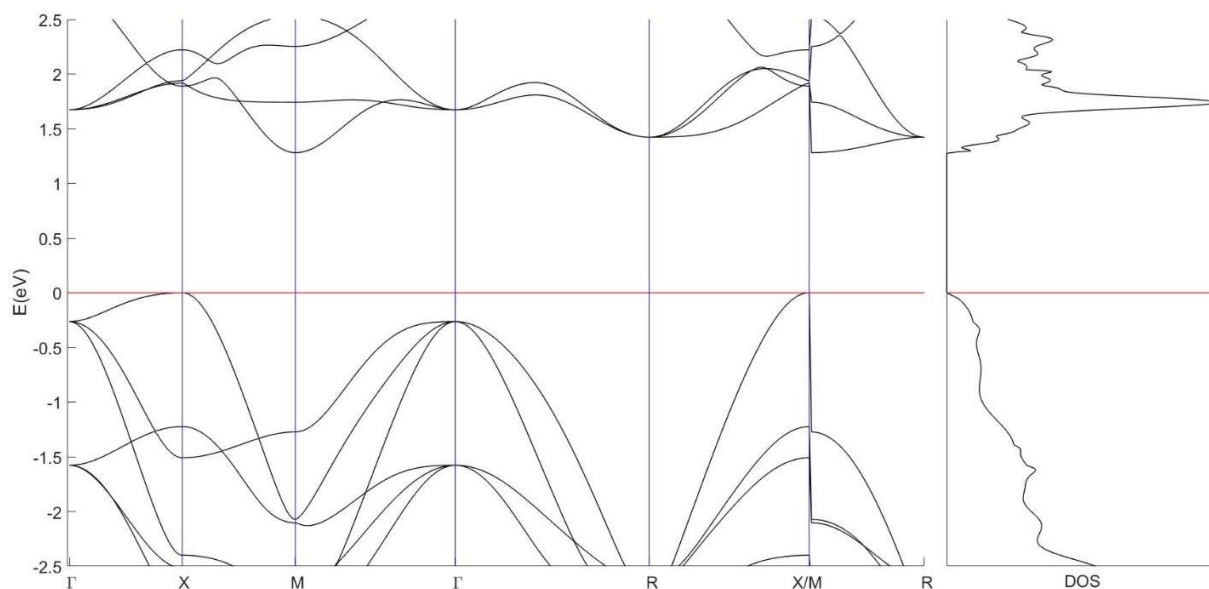


Figure S10. Electronic density of states (right panel) and electronic band structure (left panel) of the 3D-clathrate C_{60} polymer. Red line indicates the Fermi level.

D. Electronic gap evolution with volume change for the 1D polymerized structure

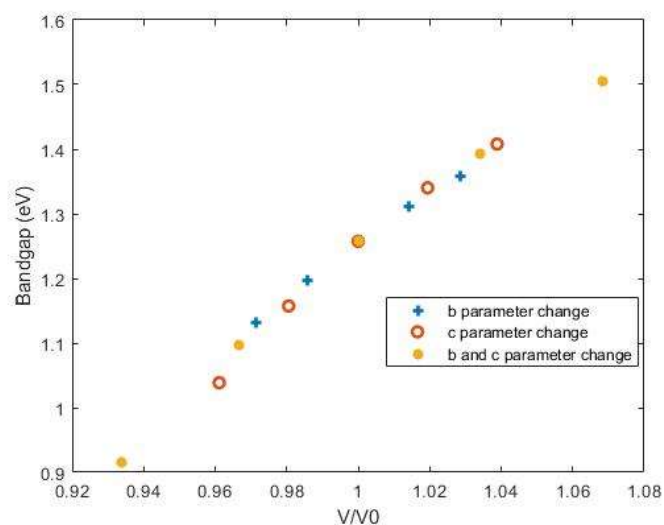


Figure S11. Electronic gap evolution, computed at HSE06-6-31-G(d,p) theory level, for variations of the van der Waals directions (b and c parameters) as a function of the volume change regarding the PBE-6-31G(d,p) minimum. The volume change is made by compressing/extending the lattice parameters corresponding to van der Waals directions.

E. Electronic gap evolution with lattice parameter change for the 0D fullerite

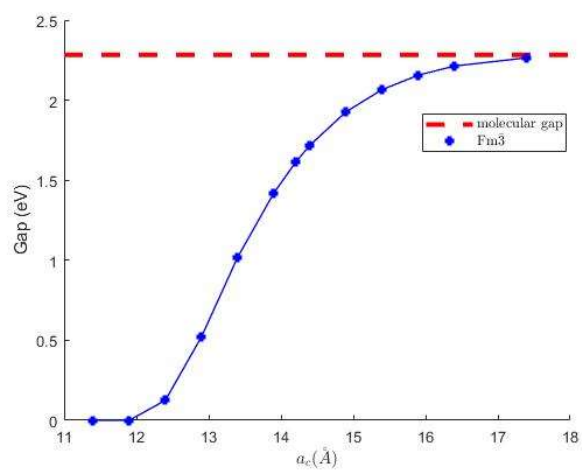


Figure S12. Electronic gap evolution with the cubic lattice parameter for the 0D van der Waals fullerite belonging to the $Fm\bar{3}$ space group computed at HSE06-6-31G(d,p) level of theory. The dashed red line indicates the electronic gap for the self-standing molecule.

Chapter 10

Conclusions

The main objective of this thesis was to investigate the crystal structures of 3D polymerized C_{60} phases, obtained from high-pressure high-temperature treatments, that could not be solved by traditional x-ray diffraction techniques due to resolution effects. Density functional theory (DFT) techniques have been used, in first place, to evaluate the stability of our structural models, but their application quickly evolved to compute meaningful physical properties that often could be compared to experimental data. Using this approach, we were able to elucidate the structure of a 3D polymerized C_{60} phase, as well as, to propose a novel and quite unique polymerized fullerite clathrate structure and study their properties. A summary of the main conclusions and proposals of future work, will be presented in the remainder of this chapter.

In the first three articles, we have modeled one experimental 3D polymerized C_{60} phase obtained at 9.5 GPa and 550 °C, recurring to different structural models, and predicted its electronic properties and bulk modulus. This phase has a face-centered cubic (fcc) structure resulting from a frustrated arrangement of 56/56 2+2 cycloaddition bonds in the fcc lattice. These bonds are formed between C_{60} molecules oriented in either one of the two standard orientations. If the molecules have different orientations this polymeric bond, 56/56 2+2 cycloaddition, is formed, otherwise no bond formation occurs. We have mapped the bond formation to an "antiferro" interaction and non-bonding to a "ferro" interaction, which allowed us to perceive the polymeric fcc structure as frustrated, analogous to the well-known fcc Ising antiferromagnet, which also serves as model for ordering in binary alloys. We have studied four ordered structures based on 56/56 2+2 cycloadditions and found that they show metallic behavior and a bulk modulus identical to the experimental one, which proves the validity of our model. These studies highlight the importance of molecular orientational disorder in the crystal structures exhibited by 3D polymerized fullerite phases obtained above 8 GPa.

In article A4, a search of different C_{60} bonding schemes was conducted, using AMK [1–3] to study the $C_{60}+C_{60}$ dimerization. Remarkably, the C_{60} dimers are the largest system studied with this package up to now. Besides the AMK calculations and the dimers already found in the literature, we have also considered C_{60} bonding schemes from geometrical considerations. After finding new dimers we have optimized them with DFT at TPSS-Def2-TZVPP-D3BJ/B3LYP-6-31G(d,p)-D3BJ level of theory in Gaussian09 [4], confirming forty-one stable dimers and expanding the universe of known C_{60} dimers from twelve to forty-one. Eleven of these forty-one dimers present a spin-polarized ground state, breaking apart or transforming into another dimer if spin polarization is not considered. This turns possible the hypothesis of magnetism exhibition by polymerized C_{60} structures containing these bonding schemes, as previously noted by Zipoli and Bernasconi [5] and experimentally claimed by Makarova et al. [6]. Relevant to our subsequent investigations, the observed distance between the two C_{60} molecules is about the same in the new dimers and in C_{60} polymers having the same bond, thus, allowing

identification of bonding types occurring in the experimental fullerite polymers and facilitating their modeling. Nevertheless, much work is still needed to develop new structural models, this being an open question that we will leave for future work. The simulation of Raman and infrared spectra of the new dimers should also be investigated in future work and, in particular, the low-energy vibrations, originated by intermolecular bonds, should be compared with the same vibrations found in the spectra of experimental polymerized phases, facilitating the bond assignment. Furthermore, in this article, A4, we ignored coalescence products, although they might improve the understanding of amorphous carbon products also formed in HPHT treatments of C_{60} [7] and, thus, should be studied in future works.

Article A5 presents another breakthrough in carbon nanostructure research, just as had already occurred with the first three articles. Here, we predict a polymerized fullerite clathrate, with this being the first carbon clathrate constructed without analogy to clathrate structures already displayed by other elements, such as clathrates of group IV. This structure is the result of each molecule in the fcc lattice being bonded to all its nearest neighbors via the double 5/5 2+3 cycloadditions, a new polymeric bond that was also found stable in our study of dimers, article A4. As a consequence of this extensive bonding, new C_{60} cages are generated on the octahedral interstitial sites and new C_{24} cages are generated in the interstitial tetrahedral sites, leading to a continuum of face-sharing polyhedral cages, thus forming a clathrate. Although highly energetic, this structure proved to be dynamically stable. This clathrate structure presents moderate elastic and mechanical properties and an interesting electronic structure, with a strong peak in the density of states (DOS), appearing in the conduction band right above the Fermi level. This peak is originated by three nearly-flat bands, having π^* -like nature, and could lead to high-temperature superconductivity, once properly doped. It also presents similar features to the existing experimental phases. Thus, it should lead to a reinterpretation of some 3D polymerized C_{60} phases as possibly the experimental realization of long-awaited carbon clathrates.

We have explored, recurring to ab initio techniques, the superconductivity in the doped polymerized fullerite clathrate, which is described in our next work, article A6. This study was driven by the observation of the huge DOS peak right above the Fermi level and the fact that the clathrate structure is formed only by carbon, a light element that forms strong covalent bonds, both key ingredients in conventional superconductivity. We have attempted to dope the clathrate structure with several dopants and evaluated its dynamic stability. Since the clathrate structure has three nearly-flat bands to be filled, we started our doping efforts with trivalent ions, scandium and yttrium, in either one of the available cages of the primitive cell, C_{60} or C_{24} , but we quickly showed that these dopants leave the structure dynamically unstable, even presenting spin-polarized groundstates. Thus, we have used other dopants, from groups I, II, III and one from group IV. Unfortunately, from all the nine dopants inserted in either the C_{24} cages or the C_{60} cages, totaling eighteen different guest atom insertions, just four structures have been found stable: beryllium inserted in the C_{60} cages ($Be@C_{60}$) and lithium, sodium and gallium inserted in the smaller C_{24} cages ($Li@C_{24}$, $Na@C_{24}$ and $Ga@C_{24}$, respectively). The electronic structure of $Be@C_{60}$ is highly changed with respect to pristine clathrate, while in the other structures it is mostly kept, the charge being simply transferred from the dopant to the carbon framework. These four stable structures presented low superconducting temperatures, against our expectations. Nevertheless, some of the unstable structures were barely unstable and show promising electron-phonon coupling constants, thus a strong increase in the superconducting temperatures is expected if the small instabilities are proven to be an artifact from the harmonic approximation used within standard DFT techniques. These effects may be corrected recurring to the stochastic self-consistent harmonic approximation (SSCHA) [8–11], which we would like to apply in these structures in a future study. Pressure may also

turn stable some of the unstable structures and this should also be explored in future work. Furthermore, simultaneous doping in both cages, mixing dopants and doping only the C_{60} cages that correspond to fcc lattice points, also deserve to be explored in future works. The latter case would have particular relevance since it would lead to the simulation of a doped structure that could be experimentally realized recurring to endohedral fullerenes.

Finally, in chapter 9, we presented two articles where a systematic exploration of the electronic properties of polymerized C_{60} structures is conducted. In the first article, A7, we have performed calculations, employing the PBE functional and plane waves, on the low-dimensional polymers and on two 3D polymerized structures, the 3D cuboidal structure and the AuCu-type structure, computing their DOS and their bulk moduli. From the DOS analysis, a decrease of the bandgap with the increase in the number of the sp^3 -hybridized atoms is observed, with metallic behavior being observed for all the studied 3D polymerized structures. Regarding the bulk modulus, the increment of sp^3 carbons leads to higher bulk moduli. In article A8, we present new calculations performed employing a more accurate Hamiltonian for bandgap computations, the HSE-6-31G(d,p), thus using linear combination of atomic orbitals (LCAO) instead of plane waves, since this calculation is computationally more feasible. We have also expanded the number of polymerized structures analyzed, computing the bandgaps for three more 3D polymerized structures. As expected, we observed larger bandgaps than in any of our previous PBE calculations. The main results of article A7 were corroborated with the bandgap decreasing as the increase on the number of sp^3 carbons until metallic behavior is achieved. Nevertheless, further increase of the sp^3 content leads to the reopening of the bandgap and a reentrant semiconducting behavior is observed. The volume per C_{60} molecule of each polymer is also an important factor to be considered. Structures with the same number of sp^3 carbons are seen to show semiconducting behavior and metallicity, the latter being observed in structures with smaller volumes while the former is observed in structures with larger volumes. These different electronic behaviors should be the result of the stronger overlap of molecular orbitals occurring at smaller volumes. Further work should be done to better understand this possible molecular overlapping effect, such as analyzing the nature of the bands around the Fermi level and how they change with the type of bonding pattern exhibited by the polymerized structures. Relevantly, the content of sp^3 -hybridized carbons in C_{60} polymers strongly correlates to their synthesis pressure, thus there is a clear path to produce structures with desired electronic bandgaps for technological applications.

In summary, we have successfully elucidated the crystal structure of a 3D C_{60} polymer and studied its electronic and elastic properties. Several new C_{60} bonding schemes were also studied in C_{60} dimers that could open the path to design new polymerized C_{60} structures. We have also found the first clathrate structure in the C_{60} system and studied its physical properties. The doped clathrate structures had their superconducting properties computed. To finalize our studies, an overview of the electronic and elastic properties is given for the most relevant polymerized C_{60} structures, ranging from the van der Waals fullerite to the 3D polymerized fullerite clathrate, with these structures showing a semiconducting reentrant behavior with the growing number of sp^3 -hybridized atoms.

Besides all the future work that we have been describing in this chapter, we also would like to perform a careful study of C_{60} pressure-temperature phase diagram, through a method similar to that presented in reference [12], that employs a machine learning potential, namely GAP20 [13], to perform molecular dynamics calculations. However, we propose to refine the parameters in order to capture the different dimensionalities of the polymer formation.

Bibliography

- [1] E. Martínez-Núñez. An automated method to find transition states using chemical dynamics simulations. *Journal of Computational Chemistry*, 36(4):222–234, 2015. doi: 10.1002/jcc.23790.
- [2] E. Martínez-Núñez. An automated transition state search using classical trajectories initialized at multiple minima. *Physical Chemistry Chemical Physics*, 17(22):14912–14921, 2015. doi: 10.1039/C5CP02175H.
- [3] A. Rodríguez, R. Rodríguez-Fernández, S. Vázquez, G. Barnes, J. Stewart, and E. Martínez-Núñez. tsscds2018: A code for automated discovery of chemical reaction mechanisms and solving the kinetics. *Journal of Computational Chemistry*, 39(23):1922–1930, 2018. doi: 10.1002/jcc.25370.
- [4] M. Frisch, G. Trucks, H. Schlegel, G. Scuseria, M. Robb, J. Cheeseman, G. Scalmani, V. Barone, G. Petersson, H. Nakatsuji, X. Li, M. Caricato, A. Marenich, J. Bloino, B. Janesko, R. Gomperts, B. Mennucci, H. Hratchian, J. Ortiz, A. Izmaylov, J. Sonnenberg, D. Williams-Young, F. Ding, F. Lipparini, F. Egidi, J. Goings, B. Peng, A. Petrone, T. Henderson, D. Ranasinghe, V. Zakrzewski, J. Gao, N. Rega, G. Zheng, W. Liang, M. Hada, M. Ehara, K. Toyota, R. Fukuda, J. Hasegawa, M. Ishida, T. Nakajima, Y. Honda, O. Kitao, H. Nakai, T. Vreven, K. Throssell, J. Montgomery, J. Peralta, F. Ogliaro, M. Bearpark, J. Heyd, E. Brothers, K. Kudin, V. Staroverov, T. Keith, R. Kobayashi, J. Normand, K. Raghavachari, A. Rendell, J. Burant, S. Iyengar, J. Tomasi, M. Cossi, J. M. Millam, M. Klene, C. Adamo, R. Cammi, J. Ochterski, R. Martin, K. Morokuma, O. Farkas, J. Foresman, , and D. Fox. Gaussian 09 revision A.02. Gaussian Inc. Wallingford CT, 2016.
- [5] F. Zipoli and M. Bernasconi. First principles study of three-dimensional polymers of C₆₀: Structure, electronic properties, and raman spectra. *Physical Review B*, 77(11):115432, 2008. doi: 10.1103/PhysRevB.77.115432.
- [6] T. Makarova, B. Sundqvist, R. Höhne, P. Esquinazi, Y. Kopelevich, P. Scharff, V. Davydov, L. Kashevarova, and A. Rakhmanina. Magnetic carbon. *Nature*, 413(6857):716–718, 2001. doi: 10.1038/35099527.
- [7] S. Zhang, Y. Wu, K. Luo, B. Liu, Y. Shu, Y. Zhang, L. Sun, Y. Gao, M. Ma, Z. Li, B. Li, P. Ying, Z. Zhao, W. Hu, V. Benavides, O. Chernogorova, A. Soldatov, J. He, D. Yu, B. Xu, and Y. Tian. Narrow-gap, semiconducting, superhard amorphous carbon with high toughness, derived from C₆₀ fullerene. *Cell Reports Physical Science*, 2(9):100575, 2021. doi: 10.1016/j.xcrp.2021.100575.
- [8] I. Errea, M. Calandra, and F. Mauri. First-principles theory of anharmonicity and the inverse isotope effect in superconducting palladium-hydride compounds. *Physical Review Letters*, 111(17):177002, 2013. doi: 10.1103/PhysRevLett.111.177002.
- [9] I. Errea, M. Calandra, and F. Mauri. Anharmonic free energies and phonon dispersions from the stochastic self-consistent harmonic approximation: Application to platinum and palladium hydrides. *Physical Review B*, 89(6):064302, 2014. doi: 10.1103/PhysRevB.89.064302.
- [10] R. Bianco, I. Errea, L. Paulatto, M. Calandra, and F. Mauri. Second-order structural phase transitions, free energy curvature, and temperature-dependent anharmonic phonons

in the self-consistent harmonic approximation: Theory and stochastic implementation. *Physical Review B*, 96(1):014111, 2017. doi: 10.1103/PhysRevB.96.014111.

- [11] L. Monacelli, I. Errea, M. Calandra, and F. Mauri. Pressure and stress tensor of complex anharmonic crystals within the stochastic self-consistent harmonic approximation. *Physical Review B*, 98(2):024106, 2018. doi: 10.1103/PhysRevB.98.024106.
- [12] Y. Zhao, C. Qian, V. Gladkikh, and F. Ding. Diagram of new carbon materials derived by high-temperature and high-pressure treatment of C₆₀ bulk. *Carbon*, 2022. doi: 10.1016/j.carbon.2022.11.007.
- [13] P. Rowe, V. Deringer, P. Gasparotto, G. Csányi, and A. Michaelides. An accurate and transferable machine learning potential for carbon. *The Journal of Chemical Physics*, 153(3):034702, 2020. doi: 10.1063/5.0005084.